# COLLECTIVE DYNAMICS OF MATTER WITH GRANULARITY

A Thesis
Presented to
The Academic Faculty

by

Nicholas G. Gravish

In Partial Fulfillment
of the Requirements for the Degree
Doctor of Philosophy in the
School of Physics

Georgia Institute of Technology
May 2013

# COLLECTIVE DYNAMICS OF MATTER WITH GRANULARITY

Approved by:

**Dr. Daniel I. Goldman**, Advisor
School of Physics
*Georgia Institute of Technology*

**Dr. Michael F. Schatz**
School of Physics
*Georgia Institute of Technology*

**Dr. Michael A.D. Goodisman**
School of Biology
*Georgia Institute of Technology*

**Dr. Andrew Zangwill**
School of Physics
*Georgia Institute of Technology*

**Dr. David L. Hu**
School of Mechanical Engineering
*Georgia Institute of Technology*

Date Approved: March 15, 2013

*To my parents Jeff & Cathy.*

# ACKNOWLEDGEMENTS

My family has been a great source of inspiration and support for me. Most importantly my parents, Jeff & Cathy Gravish, have been an endless source of love, support, and help. I can't thank them enough for the encouragement and trust they gave me to pursue my interests. Additionally I would like to thank my grandparents Gene & Adele Muzzio for getting me out of the house and into the garage woodshop. Lastly I would like to thank Danielle Wagner for her patience with me throughout my graduate career. She has suffered through me telling her *I am making just one more plot* countless times.

I could not have gotten to where I am right now without the help and support of professor Kellar Autumn. My work with Kellar at Lewis & Clark college was extremely rewarding, challenging, enriching, and best of all fun. I learned a great deal from Kellar which really helped me in my graduate research. I am deeply indebted to him for his mentorship and friendship.

I have made a great many of friends along the way and I would especially like to thank my fellow lab mates. Of these I would like to single out Ryan Maladen and Chen Li and thank them for their help in getting me started in the lab early on. I greatly respect them both as scientists and friends. Additionally I would like to thank Yang Ding, Sarah Sharpe, and Nicole Mazouchova for there help and friendship. I want to specially thank Andrei Savu for all his help in constructing (and deconstructing) experiments. Special thanks to to Feifei Qian, Tingnan Zhang, Jeff Aguilar, and Mark Kingsbury for making this lab a fun place to work. I would like to thank Mateo Garcia who played a role in many of the projects I have worked on. Lastly I am very grateful for having the opportunity to work with and learn from Dr. Paul Umbanhowar.

Most importantly I want to thank my advisor Prof. Dan Goldman for the role he has played in shaping almost every facet of my graduate and future career. I have learned an immense amount from working with Dan. His passion and excitement spurned me on in the beginning of my graduate career. He has instilled in me the same passion and excitement for scientific discovery which I will strive to pursue for the rest of my life. I have many wonderful experiences in the CRAB lab and I am incredibly thankful for all the opportunities Dan has given me.

# TABLE OF CONTENTS

# LIST OF TABLES

# LIST OF FIGURES

# SUMMARY

Granular materials are abundant in the natural and industrial environments. Typical granular materials are collections of inert, passive particles in which the constituent grains of the material are macroscopic; thus they fill space, are a-thermal, and interact through only local contact forces. This definition can be broadened to include non-inert particles as well–active particles–in which the grains of an active granular material possess an internal energy source which drives motion. Active granular materials are found in many areas of the biological world, from cattle stampedes and pedestrian traffic flow, to the subterranean world of ant colonies and their collective motion within the nest.

We study the rheology and dynamics of inert granular material, and an active granular system of collections of fire-ants, which together we call *matter with granularity.* In both of these systems we observe bifurcations in the force and flow dynamics which results from confinement effects of the effectively rigid granular materials. In inert granular systems, the onset of flow among particles that are closely packed together causes them to dilate as particles must separate away from each other to accommodate flow. Dilation is a property unique to *matter with granularity* and other complex fluids in which particles interact locally and occupy space. We explore how dilation influences the inert granular system in situations of local and global forcing: drag of an immersed intruder and avalanche flow respectively. We next study collections of fire ants which also interact with each other locally through contact forces and exclude volume. We study the construction of, and locomotion within subterranean tunnels by groups of fire ants. We find that the traffic dynamics of ants within confined tunnels are significantly affected by tunnel diameter. Reducing tunnel diameter increases the formation of traffic jams due to the inability of ants to pass each other easily. However, we show that jamming within tunnels may have beneficial effects on subterranean locomotion. Individual ants jam there their bodies, limbs and antennae against the walls of vertical tunnels to resist falling. From biophysical studies of fire ant mobility in confined spaces, we show that subterranean tunnel size has a significant effect on the stability and mobility of ants within these environments.

# CHAPTER I

# INTRODUCTION

## *1.1 Matter with granularity*

We interact with systems of inert, macroscopic particles almost everyday. For example, at breakfast we may shake salt, grind coffee, and pour cereal into a bowl (Fig. 1.1). These systems—which we define as granular materials—have the common properties that they are composed of macroscopic, discrete, dissipative, and athermal particles. Granular materials are interesting to scientists and engineers alike because they exhibit complex rheological properties while consisting of potentially simple individual elements with simple interactions [1, 2, 3, 4]. As such, research in granular materials has been performed across a broad range of disciplines.

Granular materials have significant importance in industry, engineering, and fundamental science study. Granular matter is the second-most-manipulated material by man (behind water) [5]. It is estimated that the processing of granular materials such as phamaceuticals, coal, and other raw materials, accounts for 10% of the worlds energy consumption [4]. Because of the prevalence of granular materials in industry and life, advancing our knowledge of the granular state of matter has much practical industrial importance. Additionally, granular materials are a paradigmatic non-equilibrium system [5]. Physics studies of granular materials have advanced our understanding of numerous fundamental non-equilibrium physics processes such as self-organized criticality [6, 7, 8, 9], pattern formation [10, 11, 12, 13], and the glass transition [14, 15, 16, 17].

Increasingly—through both biological and industrial inquiry—granular materials research has turned its focus on particles that move through their own internal energy sources [19, 20, 21, 18]. In contrast to dissipative, passive, granular materials, "active" granular materials operate according to both their interactions with the external environment, and their internal degrees of freedom [20]. Many examples of of active materials are found in the

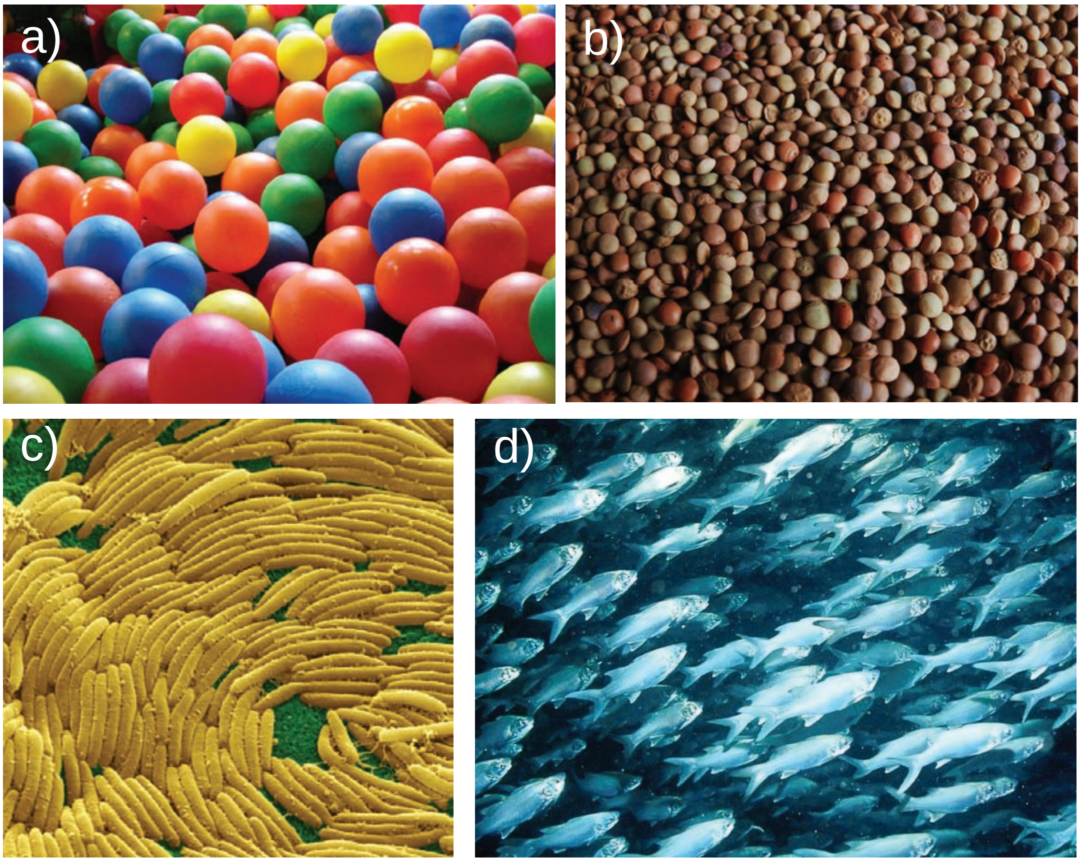

**Figure 1.1:** Examples of passive and active granular materials. a) Balls from a children's playground b) Lentil grains c) The bacteria *Myxococcus*. Image reproduced from [18] d) A school of fish. Image courtesy of the *National Oceanic and Atmospheric Administration*.

natural world: bacteria aggregations, bird flocks, and fish schools (Fig. 1.1). Thus, physics study of active granular materials may have increasing significance in the understanding of group animal behavior, across many scales of organism size [22, 23, 24, 25]. Furthermore, collective biological systems inspire more than just scientific curiosity and the processes that lead to collective behavior such as self-organization and system robustness may lead to new design paradigms for engineered systems [26, 27, 28].

The work presented in this thesis is focused on the study of collective, particulate, systems—both active and passive—which we define as **matter with granularity**.

## *1.2 A case study in active and passive granular materials*

To begin to acquaint ourselves with granular phenomena, and to illustrate the symbiotic relationship between active and passive granular materials, we begin with the following case study. A common phenomena experienced when handling granular media is the flow and jamming of particles as they exit through a small hole. When we invert a salt shaker to flavor our food we experience this phenomena (Fig. 1.2). The inert salt grains begin to flow from the small holes until without fail the flow is halted by particles that jam in the holes. To relieve this jam we shake the salt shaker which removes the jammed particles and re-initiates flow.

In a similar fashion to that of the inert salt grains, panicked crowds of humans (and in recent analogous experiments, ants [29]) also experience jams when attempting to exit from a larger room through a narrow corridor (Fig. 1.2) [30, 31]. Such jams have been illustrated in laboratory experiment [32], field observation [33, 34], and computer simulations [30, 31] of pedestrian traffic flow (Fig. 1.2). The consequences for jam formation in pedestrian flow through an exit can be devastating and lead to injuries or even fatalities.

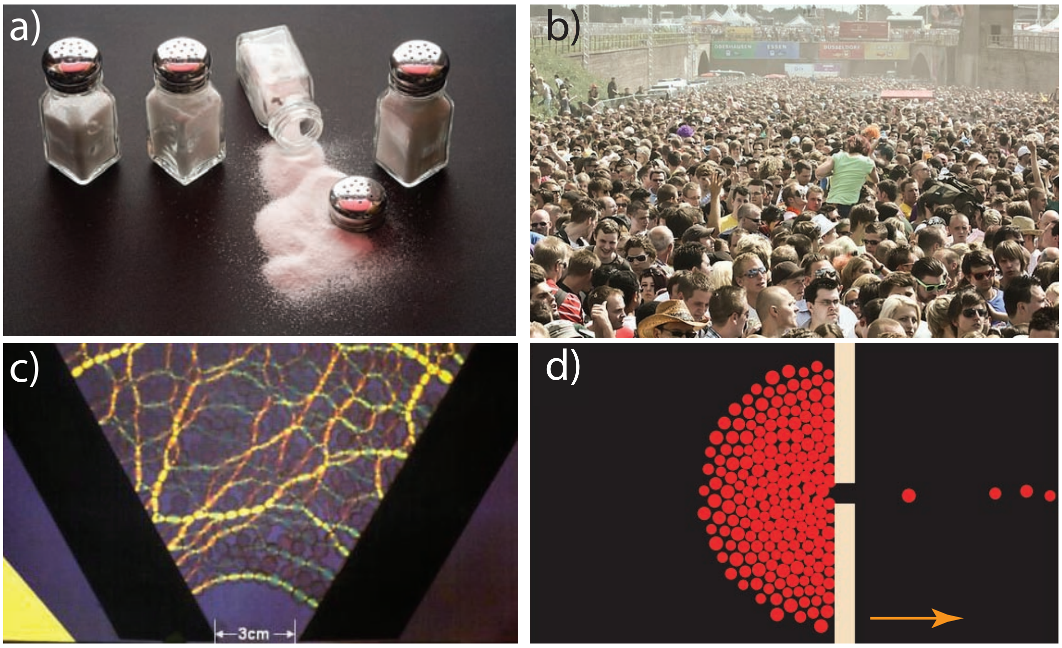

**Figure 1.2:** Examples of identical jamming phenomena in active and passive granular systems. a) Flow of inert granular salt through small holes can lead to particle jams. b) An example of a jammed granular flow in a 2D experiment. Colored particles indicate high stress. c) Jams are also formed by pedestrian crowds egressing through narrow exits) [35], b) Jammed active particles simulating a crowd exiting a narrow exit [30]

Granular jamming is a phenomena in which through small changes in "particle" density smooth flow of the material can be arrested and resist further motion. In the previous two examples of jamming of active and passive systems, the situations are nearly identical: a large system of similarly shaped “particles” interact locally through contact forces, exclude volume from each other, and thus squeeze together and form force-chains which jam the flow (Fig. 1.2). The similarity of these situations suggests that to mitigate the formation of potentially harmful human traffic jams, we may draw on insights learned from the study of passive granular materials flowing through narrow exits.

Hoppers and silos are used frequently in industry to transport and store granular materials. These structures are large containers which slope at the base leading to a narrow exit (Fig. 1.2). Hoppers suffer similar problems of jam formation during outflow of granular media [36] and the physics of spontaneous jam formation of granular flow through a narrow exit has been a frequently-studied problem in granular materials [35, 4, 3]. A solution to counteract the formation of exit jams in hopper flow has been to place a small obstruction immediately prior to the outflow region of the aperture [37, 38, 39]. The obstruction directs granular flow near the exit to resist the formation of arching jams. Recent physics studies of this phenomena have shown that with the appropriate choice of obstructor geometry and positioning, the probability to form an outflow jam is reduced by a factor of 100[37].

Inspired from the results of jam mitigation in passive granular materials this design was employed in active granular systems. Computer simulations [40], experiments with human subjects, and experiments with model organisms (ants leaving a nest [41]) have all demonstrated that the placement of an obstructor near an egress alleviated pedestrian jams as well. Thus architects have begun to employ this design in pedestrian walkways [] inspired from the studies of passive granular materials.

Here I have illustrated an example of the symbiotic relationship between active and passive granular systems research. The discovery of core principles of **matter with granularity** benefits from the simultaneous study of many different types of materials.

## *1.3 Organization of this thesis*

The over-arching theme of the research presented here is that of the dynamics of granular systems in which the grains exclude volume. When particles interact through rigid, nearly hard-wall, contact forces, their phases of matter display interesting phenomena. Granular dilation, mechanical particle entanglement, and ant traffic-jams are all examples of phenomena that occur because the constituent "particles" cannot freely pass through each other. Instead these "particles" effectively interact with each other through local, hard-wall contact forces and experience segregation, slowing down, and jams. In this thesis we explore how particle shape, size, confinement, and forcing, influence the response of matter with granularity.

I outline a program of research in which I study the principles of active and passive matter with granularity to discover properties of biological systems that interact with, or are composed of matter with granularity. In chapter 2, with a review of important phenomena in active and passive granular systems. We then describe two complementary series of experiments in which we study the properties of active and passive granular systems:

- In **chapters 3-5** we study passive granular media
- In **chapter 6** we study a passive granular material that is inspired by phenomena observed in collections of living fire-ants, an active granular material.
- In **chapters 7-9** we study the collective dynamics of collections of living fire-ant groups.
- In **chapter 10** we discuss and summarize our findings and outline areas for future investigation.

# CHAPTER II

# REVIEW OF MATTER WITH GRANULARITY

In chapters 3-9 we describe experiments to study the dynamics of active and passive granular materials; collectively denoted as **matter with granularity**. We define matter with granularity as collections of *discrete, rigid objects that exclude volume and (typically) interact only through local contact forces.* In this chapter we introduce the basic phenomena associated with active and passive granular materials.

## *2.1 Passive granular phenomena*

### 2.1.1 Introduction

Passive granular materials are assemblies of macroscopic particles that are typically of size greater than 10 $\mu m$ [5]. Particles smaller than 10 $\mu m$ are subject to thermal effects while granular materials are athermal [5]. and These particle assemblies are easily studied in table-top experiments. Being of macroscopic size, granular materials are readily visualized in the laboratory which allows for quantitative flow characterization through particle tracking and image velocimetry. However, due to their opaque nature, imaging the three-dimensional structure and flow of granular materials requires the use of X-ray [42, 43], magnetic resonance imaging, or immersion in index of refraction matched liquid.

Granular materials come in many shapes and sizes [44], however in the majority of physics studies granular materials are considered as convex (often spherical) particles (Fig. 2.1)[*]. Dry granular materials consist of particles that interact through frictional and repulsive normal forces only [1, 2, 3, 4]. Because of the absence of particle-particle attraction, dry, spherical, granular material cannot support tensile loading [3]. Since grain-grain interactions are frictional, the force laws of granular flows are typically rate insensitive at low speeds [3]. At higher flow speeds however, momentum transfer between particles becomes

---

[*] In chapter 6 we will discuss how deviations from a convex shape affects behavior.

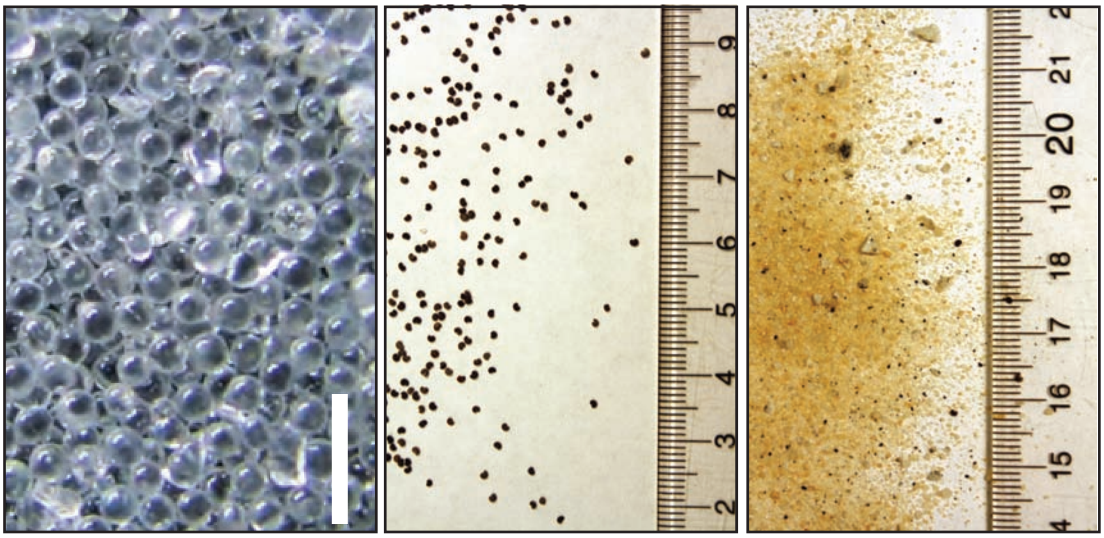

**Figure 2.1:** (Left) Spherical 210 $\mu$m diameter glass beads. Scale bar is 1 mm. (Middle) Poppy seeds. (Right) Beach sand from Jekyll Island, GA, USA. Photo credit (a) Sarah Sharpe.

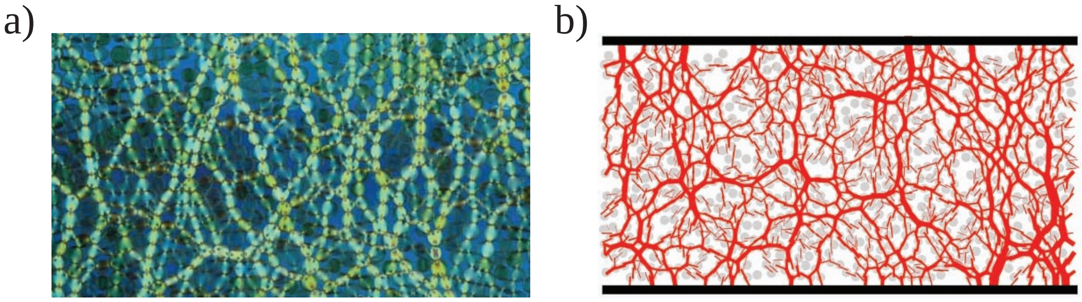

**Figure 2.2:** Heterogeneous force chains in a granular material. a) Experiment demonstrating force chains in granular material using photo-elastic disks. Photo courtesy of Bob Behringer. b) Simulation of force chains (red lines) in a granular material using the discrete element method.

important and force laws take on a velocity dependence (with a force law dependent upon the packing density of the material [45]).

In certain cases grains may cohere, through electrostatic interaction between charged grains [4], or through capillary forces from an intermediate wetting fluid [4]. The physics of cohesive granular materials is of fundamental importance in many applications, such as the study of soil stability for civil engineering. However in this thesis we focus only on the study of dry granular materials. Dry granular material is well suited to experimental study as it can be prepared in repeatable initial states in the laboratory.

Because grains are of finite size, forces within a granular material are heterogeneously distributed through filamentary force chains (See Fig. 2.2 and [46, 47]). These force chains have been studied in two-dimensional granular materials using photo-elastic particles which are bi-refringent and thus change the polarization of transmitted light in areas of high stress (Fig. 2.2). The heterogeneous stress distribution within granular materials has made the development of continuum mechanics models difficult [48, 49]. As such, computational simulation of granular materials using the Discrete Element Method (DEM) [50] or other energy-minimization based methods have made major advances in understanding and modeling granular flows (Fig. 2.2). Computer simulation is an essential tool in granular physics which we discuss further in chapter 6.

### 2.1.2 Phases of granular matter

A fundamental feature of granular materials is their ability to act like solids, fluids, or gases [2]. The "phase" of the granular material may spontaneously change under perturbations. A feature of granular flows is the rapid transition between the three phases [2]. For example, a pile of granular materials (Fig. 2.3a) is considered a solid. Thermal effects of granular materials are negligible because of their large size [5, 2] and thus the solid state will persist until an external perturbation is applied. When a granular flow down a slope occurs, rapidly moving grains are located on the surface while immobile grains remain solid below the surface. Thus the granular flow exhibits a co-existence between the fluid-like surface flow and the solid-like below supporting material below (Fig. 2.3b).

The phase-change and resultant flow in granular material induces a change in the microstructure of the grain contact network within the flowing region. This change in grain contacts in turn alters the rheological properties of the granular material in the flowing region, which creates a feedback process between granular flow and internal microstructure. Dependent upon the conditions of forcing, this feedback feedback process can result in granular flows which reach a quiescent steady-state (See section 2.1.4) or alternatively exhibit bifurcations and pattern formation (Fig. 2.3c and section 4).

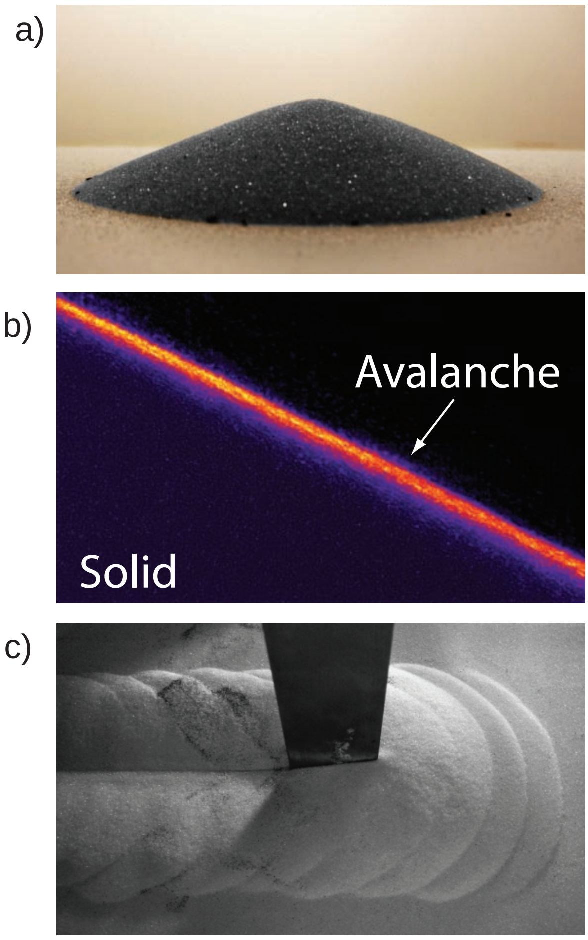

**Figure 2.3:** a) A granular slope. b) False color image of an avalanche down a slope. The color corresponds to the speed of granular flow with orange being high speed flow and black being low speed flow. c) Drag of an immersed intruder (translated from the left to the right) through closely packed granular media.

### 2.1.3 Packing of granular material

One of the simplest granular experiments that can be performed is to pour particles of a known density and mass into a container and measure the volume occupied by the assembly. This experiment provides a measure of packing efficiency of the granular particles. We measure packing of granular material as the fraction of total volume, $V$, occupied by solid particles, $V_p$. We define volume fraction as

$$\phi = \frac{V_p}{V} \tag{2.1}$$

The volume fraction, $\phi$, represents the fraction of filled space. $\phi$ is intimately related to the dynamical response of the media when it is subjected to external perturbations such as vibration [51, 52], shear [53], penetrator impact [45], or intruder drag [54].

Mechanically stable ensembles of spherical, monodisperse granular materials are found in a range of $\phi$ from random loose-pack $\phi_{rlp} = 0.55$ [55, 4] to random close-pack volume fraction $\phi_{rcp} = 0.64$ [4]. The term random in these definitions represents the fact that these are not ordered configurations of grains. The maximum $\phi$ for ordered, uniform, spheres is that of a face-centered-cubic lattice in which $\phi_{fcc} = 0.77$. A loose, ordered, packing is that of a simple-square lattice with $\phi_{ssl} = 0.52$. Although the packing fraction of ordered ensembles (i.e. on a lattice) may be analytically solved for, the calculation of the maximum $\phi$ of randomly distributed particles of arbitrary shape must be done computationally [56].

Physics study of the packing of granular media under mechanical [51] or air-fluidized [52] perturbation has revealed that the evolution of $\phi$ is dependent upon the forcing parameters such as peak mechanical acceleration, or air pressure (Fig. 2.4). The relaxation dynamics of granular material are complex, exhibiting signatures of two-time scales (Fig. 2.4a and [52]) or stretched exponential behavior (Fig. 2.4b and [51]). The common feature of these experiments is that compaction of granular material, and subsequently the increase in $\phi$, occurs slowly, over many thousands of iterations. We will discuss in section 3 how the packing of granular materials can be controlled rapidly for experimental application.

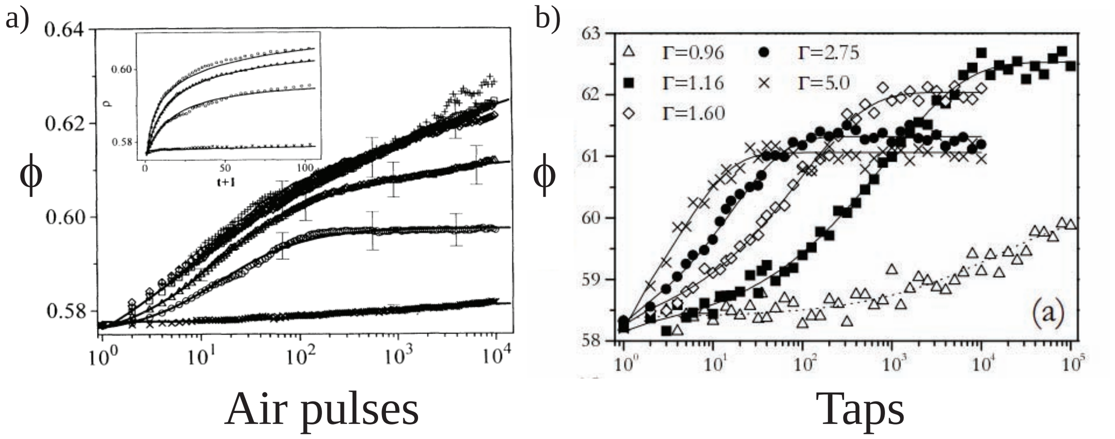

**Figure 2.4:** Results from packing experiments of granular media. a) Results from an air-fluidized experiment. $\phi$ versus number of air pulses. Reproduced from [52]. b) Results from a mechanical tapping experiment. $\phi$ versus tap number. Reproduced from [51]

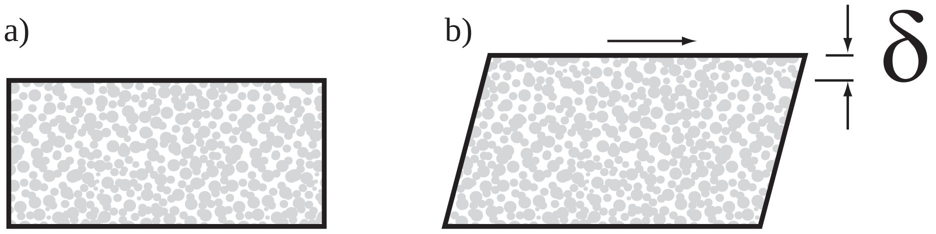

**Figure 2.5:** Simple shear of a granular media. a) Before shearing. b) After shearing.

### 2.1.4 Critical state

As discussed at the end of section 2.1.1, granular flow induces a change in the microstructure of the contact network between grains, which in turn may alter the flow in that region through a feedback process. Thus we may ask whether this feedback process will result in a stationary-state of granular flow? This is the subject of critical-state soil mechanics [53, 57]. Critical-state theory is an important tool in soil mechanics yet has not fully been appreciated by granular physicists.

In the prototypical critical-state experiment we subject granular material, placed between two (semi-) infinite, horizontal, planes to a simple shear (Fig. 2.5) while keeping the top plate under constant pressure. The vertical height change of the top plate during shear, $\delta$, corresponds to an associated change in average $\phi$ of the granular material contained within. The height changes according to the amount of free-space within the material and

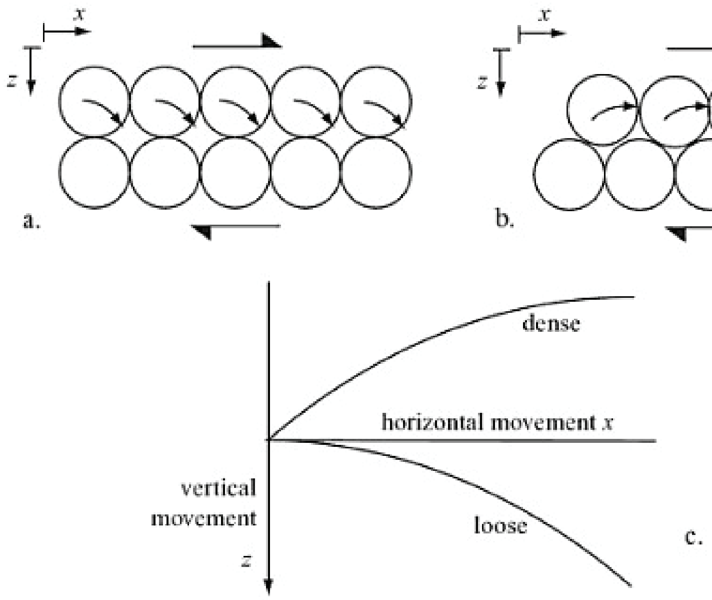

**Figure 2.6:** Cartoon model of dilation and compaction. a) Shearing a low $\phi$ material compacts grains. b) Shearing a high $\phi$ material dilates grains. c) Expected height change as a function of shear. Figure reproduced from [57]

may either increase or decrease depending on initial $\phi$ (Fig. 2.6).

Experiments show that independent of the initial $\phi_0$ the granular material is prepared at, under shear it will evolve to a steady state $\phi_c$ which is only dependent on the grain properties and the confining stress (Fig. 2.7 and [53]). In the evolution from $\phi_0$ to $\phi_c$, the net change in volume fraction, $\Delta\phi$, may be either positive or negative. Negative $\Delta\phi$ indicates that the granular media underwent compaction during shear as grains moved closer together to fill voids. Positive $\Delta\phi$ indicates that the granular media underwent dilation during shear in which the material expanded to accommodate the motion of the granular media. The critical state volume fraction, $\phi_c$, is the state in which the granular material neither expands nor contracts under further shearing. As we will see in subsequent chapters, the initial volume fraction of the granular material strongly determines the response of the media under forcing.

The value of $\phi_c$ is not a universal constant of the granular material but is instead a function of both the magnitude of the normal stress on the material [53], and the coefficient of friction between particles [59]. The relationship between $\phi_c$ and stress is given by the

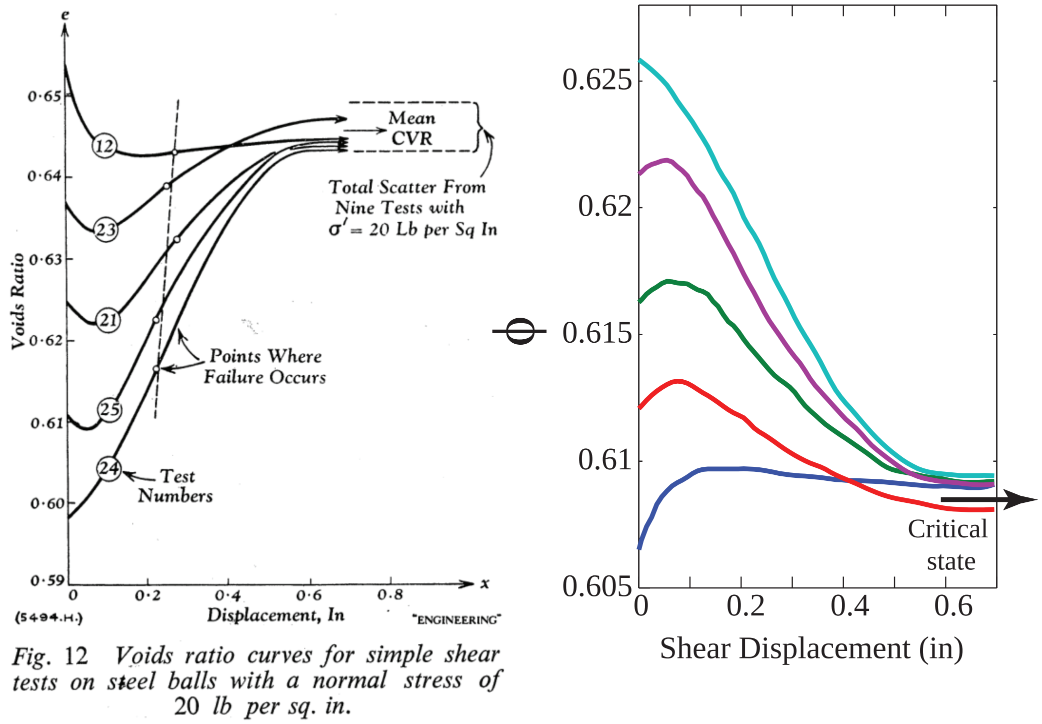

**Figure 2.7:** Evolution of granular volume fraction under shear. a) Original experiments from Wroth, et al. [58] reported as voids-ratio, $e$, versus shear. b) Data re-plotted in terms of $\phi = \frac{1}{1+e}$.

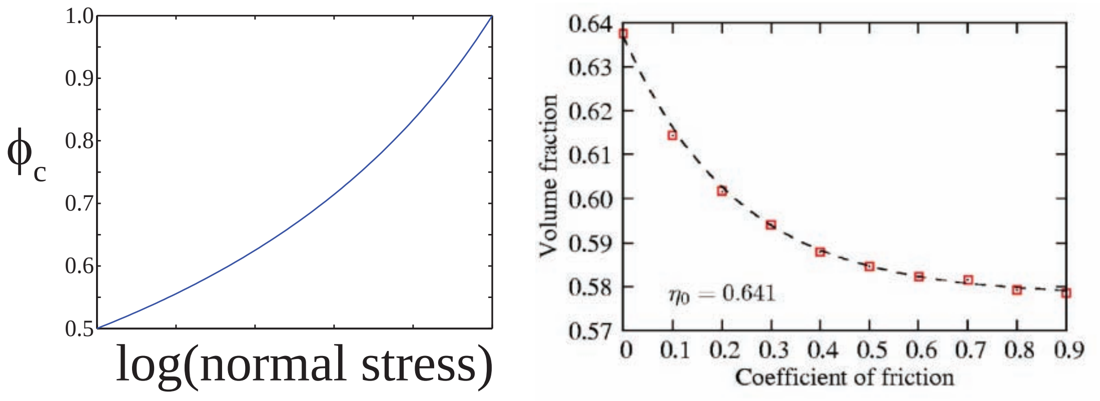

**Figure 2.8:** Effect of stress and coefficient of friction on $\phi_c$. a) Cartoon sketch of the relationship between $\phi_c$ and the logarithm of the mean confining stress. b) DEM simulation tri-axial tests on a dry granular material with varied particle-particle coefficient of friction. Coefficient of friction influence on $\phi_c$. Reproduced from [59]

Cam-Clay model of critical state soil mechanics in terms of the critical voids ratio $e_c$. Voids ratio is defined as the ratio of pore volume to solid volume and is related to volume fraction by the relationship $\phi = \frac{1}{1+e}$. The Cam-Clay model states

$$e_c = e_\Gamma - \lambda \log(p) \tag{2.2}$$

where $e_c$ and $e_0$ are the critical-state and zero-pressure voids ratios respectively, $\lambda$ is a compression parameter of the soil, and $p$ is the confining pressure. Substituting $\phi$ for $e$ we arrive at the relationship

$$\phi_c = \frac{\phi_\Gamma}{1 - \phi_\Gamma \lambda \log(p)} \tag{2.3}$$

where as with the voids ratio, $\phi_c$ is the critical state volume fraction at pressure $p$, and $\phi_\Gamma$ is the zero-stress critical state volume fraction. In figure 2.8a we plot equation 2.3. $\phi_c$ increases monotonically with the confining and is a function of the logarithm of the confining pressure.

Experiments and DEM simulation also have found that $\phi_c$ is sensitive to the grain-grain coefficient of friction, $\mu$, in the granular material [59]. In 2.8b we show results from DEM simulation which illustrate that $\phi_c$ decreases exponentially as a function of increasing $\mu$. The value of $\phi_c$ approaches that of random close pack as $\mu \to 0$. As $\mu \to \infty$, $\phi_c \to 0.578$ which the authors define as a *dynamic random loose pack* to distinguish this state from the lower $\phi$ random loose pack.

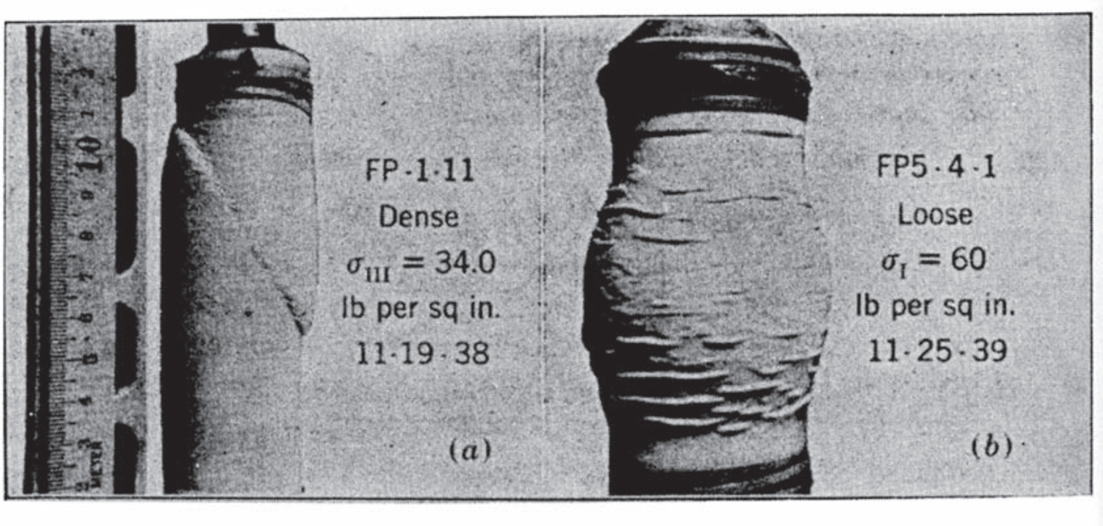

**Figure 2.9:** Shear localization in granular materials. a) Results from two triaxial tests: $\phi > \phi_c$ (right) and $\phi < \phi_c$ (left). Figure reproduced from [60].

### 2.1.5 Shear localization

A novel feature of granular flows is the strong localization of flow that may occur when the material is sheared. An example of shear localization is the formation of a narrow "shear-band" in the material along which the flow (and shear) is concentrated. In figure 2.9 we show granular material deformed in a tri-axial test exhibiting a shear band (left panel). A tri-axial test is a measurement from soil-mechanics in which the granular material is placed into a cylindrical rubber sleeve and immersed in a fluid held at constant pressure. Two plates on the top and bottom push inwards at a constant stress and the plate displacement is recorded. From this measurement a stress-strain profile of the granular material is measured.

As illustrated in figure 2.9 the formation of shear-bands is sensitive to the initial $\phi$. The left image of figure 2.9 is of a granular material prepared at $\phi > \phi_c$ while the right image of figure 2.9 is a material prepared at $\phi < \phi_c$. The crucial feature to the formation of shear bands as stated in a recent review is "a mutual coupling between local flow and local organization, in which flow induces the microscopic organization of the constituent units, which feeds back on the flow properties and can cause instabilities" [61].

From granular rheology experiments, the formation of shear bands can be understood as a bi-stability in the stress-strain rate relation (Fig. 2.10). In shear experiments in which

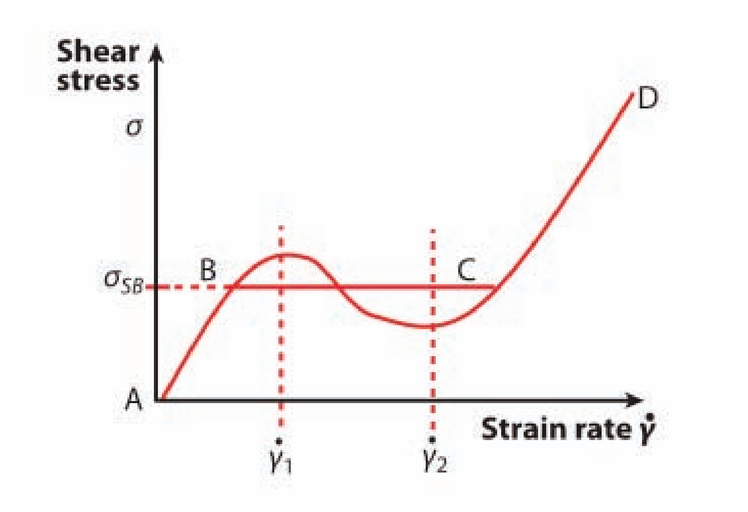

**Figure 2.10:** Stress-strain is non-mononotic as a function of stress. Shear bands in granular material can be understood through rheological measurements of the stress-strain relation.

the shear rate is between the range $\gamma_1 - \gamma_2$ (Fig. 2.10) stable flow will occur at either $\gamma_1$ or $\gamma_2$ and thus the flow separates into two regions, one at $\gamma_1$ and one at $\gamma_2$. Within this shear band revion the stress is constant at $\sigma_{sb}$ (Fig. 2.10). This process can is similar to the Maxwell construction for phase transition in a Van der Waals gas.

A feature of shear-bands that has been relatively unexplored is the stability of these flow regions. This is because most experiments of shear-band formation either probe the initial shear-band bifurcation (like in tri-axial tests) or the steady-state shear band flow (like in standard periodic boundary condition geometries such cone-plate rheology). We will demonstrate in chapter 4 new studies to explore the stability of shear bands through the use of drag measurements.

### 2.1.6 Vibrated granular materials

As introduced in section 2.1.3, the repeated mechanical agitation of granular materials is a useful experimental method to explore the phases and relaxation dynamics of granular material [51, 52]. Uniform sinusoidal vibration is employed to repeatedly inject kinetic energy into the granular material. High-intesity vibration is essential for the study of granular gases, pattern formation, and relaxation. Additionally it is possible to condense vibrated granular systems from the gaseous state to an aggregated liquid or solid state using

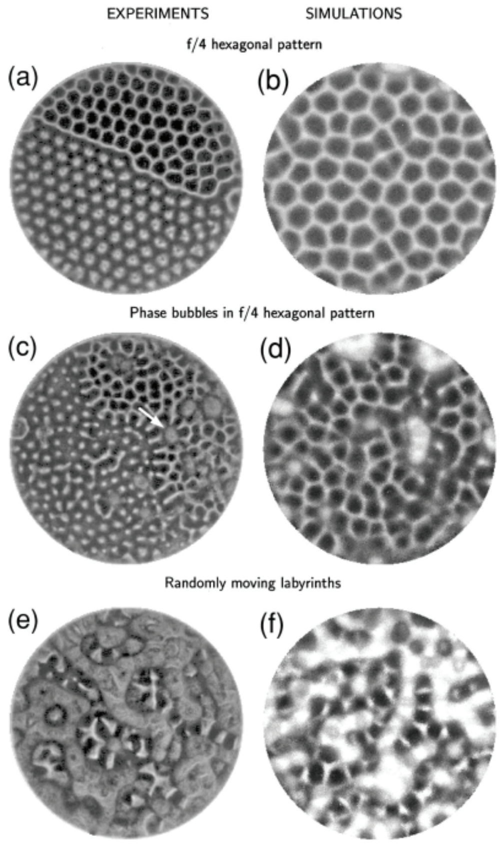

**Figure 2.11:** Pattern formation in granular materials. Left and right columns show experiment and simulation results of surface patterns formed in sinusoidally vibrated granular material. Image reproduced from [64].

vibration [62, 63].

Two parameters may be varied during vertical, sinusoidal vibration of a granular material: the oscillation frequency, $f$, and the peak-peak amplitude of the oscillator, $A$. We non-dimensionalize the peak vibration acceleration as

$$\Gamma = \frac{A(2\pi f)^2}{g} \tag{2.4}$$

In oscillation conditions of $\Gamma < 1$ the object(s) being vibrated will remain in contact with the oscillator as the peak acceleration does not exceed $g$. In conditions of $\Gamma > 1$ the object(s) will experience a ballistic period in which they lose contact with the oscillator. In this case the object(s) will repeatedly collide with the oscillator.

Analogous to Faraday waves observed in vibrated fluids, granular materials also exhibit surface patterns when a thin shallow layer is vibrated (See Fig. 2.11 and [64]). Vibration induced fluidization has been used to study the properties of wet cohesive beads by exploring the solid-liquid, and liquid-gas phase transitions that occur as a function of oscillation amplitude and frequency [65, 66, 67]. In wet cohesive granular material the energy scale required to separate particles is set by the particle radius and surface tension of the liquid forming the bridge. A liquid to gaseous phase transition occurs in wet cohesive granular media when the injected energy from vibration exceeds the capillary bond energy [65] and thus vibration induced fluidization is an effective means to explore the phases of granular materials. Lastly, in avalanche experiments with dry granular media, vibration has been used to mobilize particles and thus cause the granular materials to avalanche at lower slope angles, dependent upon the amplitude and frequency of vibration [68, 69]. In one of these experiments the authors showed that the vibration [68] was analogous to a thermal energy source and illustrated that the granular slope relaxation followed a Boltzman-like exponential function.

In chapter 6 we describe how we use sinusoidal vibration of a “u-shaped” granular material to study the relaxation and stability of u-particle piles.

### 2.1.7 Force and flow surrounding intruders in GM

The drag and lift force experienced by intruders submerged within a granular material have been of interest since the invention of the plow. The force and flow of a granular material experienced by a submerged intruder is interesting from a physicists viewpoint because it is a localized forcing. As discussed in section 2.1.4 shearing a granular material will induce a change in the microstructure (and local $\phi$) and this change will thus result in a change in the rheology of the media in that location. By constantly translating an object through a granular material which has been prepared at $\phi$, we continually advect undisturbed granular material into the shearing region and frustrate this feedback process. Physics study of the forces on a submerged intruder in granular media have explored how the shape of the intruder affects drag and lift force (Fig. 2.12). Force-fluctuations during periodic stick-slip flow [70], or aperiodic self-organized criticality like flow [71, 72], have also been studied to explore the statistics of un-jamming in granular material.

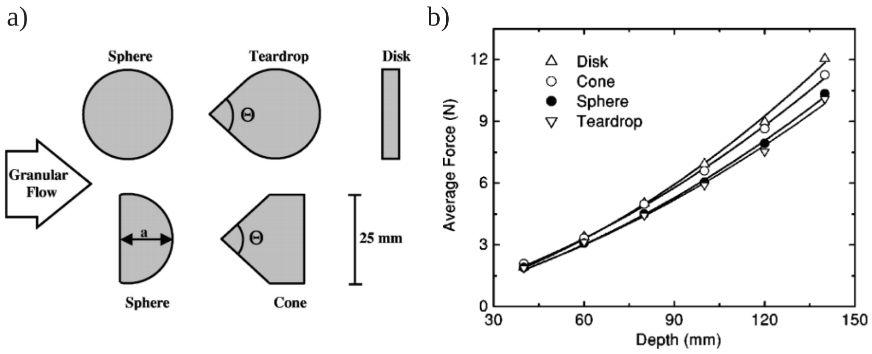

**Figure 2.12:** Localized intruder experiments in granular media. a) Different shapes of submerged intruders dragged within a granular media. b) Depth dependence of drag force for four different shapes of intruder. Shape had a small effect on drag force.

In general the shape of the intruder dragged through granular material did not have a large effect on the drag force experienced [73] as compared to the comparable shape effects in a fluid. Instead in a granular material what is important in determining drag important is largely the intruder depth. Since granular flow is frictional the increase in hydrostatic pressure as the intruder is submerged deeper increases the drag force proportionally [3]. Furthermore because granular material is frictional the drag force is velocity independent below speeds of ≈ 0.5 m/s [74, 3].

### 2.1.8 Grain shape

The study of grain shape effects on granular materials has typically focused on convex particles (See Fig. 2.1 and Fig. 2.13). These studies have practical application as many granular materials found in nature are not perfect spheres [44]. Instead sand and gravel particles typically have angular surfaces (Fig. 2.13). This angularity increases the peak shear-strength of the granular material from that of ideal spheres[44, 75]. This can be understood because the angular surfaces allow for particles to interlock, effectively increasing the bulk friction of the granular material.

The packing properties of non-spherical granular material is also of fundamental interest. Packing experiment, simulation, and numerics have been performed for regular platonic and achrimedean solids [76, 77], ellipsoids of revolution [78, 79], and both oblate and prolate spherocylinders [80, 81]. In a recent comprehensive study of particle packing, an effective

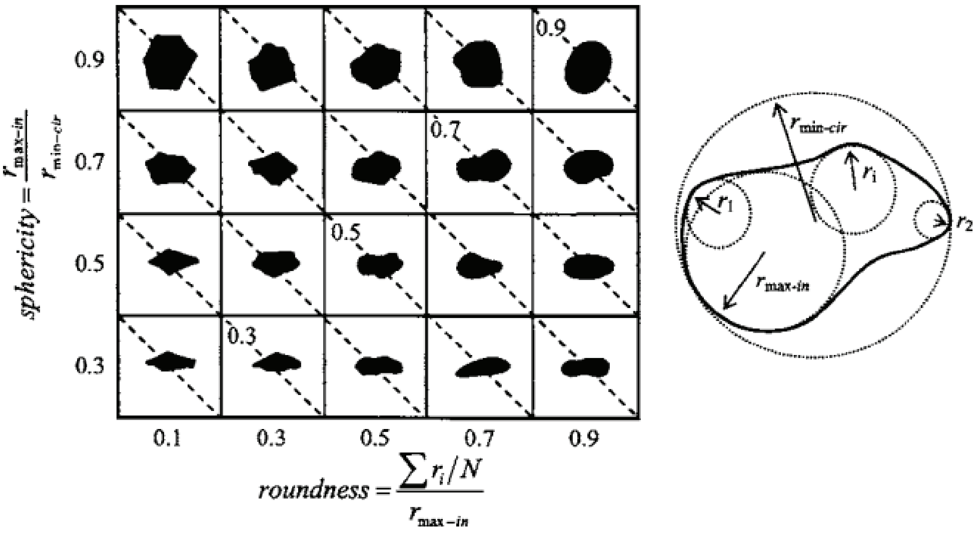

**Figure 2.13:** Table illustrating granular materials of various angularity and roundness. Figure reproduced from [44]

dictionary of shape effects on packing fraction has been constructed [56].

Numerous experiments have also been performed to study the packing of rods of length $L$, and diameter $D$ [82, 83, 84, 85, 86, 87, 88, 89]. Rods with large aspect ratio, defined as $\alpha = L/W$, are able to be formed into sandcastle-like vertical towers (Fig. 2.14). Thus adding fluid to dry granular media is not the only way to create cohesive effects. Rods within an ensemble lack rotational freedom and thus experience a rotational caging effect, which generates an effective tensile strength in the granular material. The random contact model is an important mean-free theory which describes the relationship between $\phi$ and particle shape for rod-like granular material (Fig. 2.14). We will discuss non-spherical particles and the random contact model at length in chapter 6.

## *2.2 Active granular phenomena*

### 2.2.1 Introduction

The physics of swarm behavior [24], an emergent feature of many biological systems such as slime molds [90], bacteria colonies [91, 92, 93], and bird flocks [94, 95], is a nascent field of study (Fig. 2.15). Large collections of living, interacting, organisms are interesting from the standpoint of physics because they may display emergent, seemingly coordinated behaviors

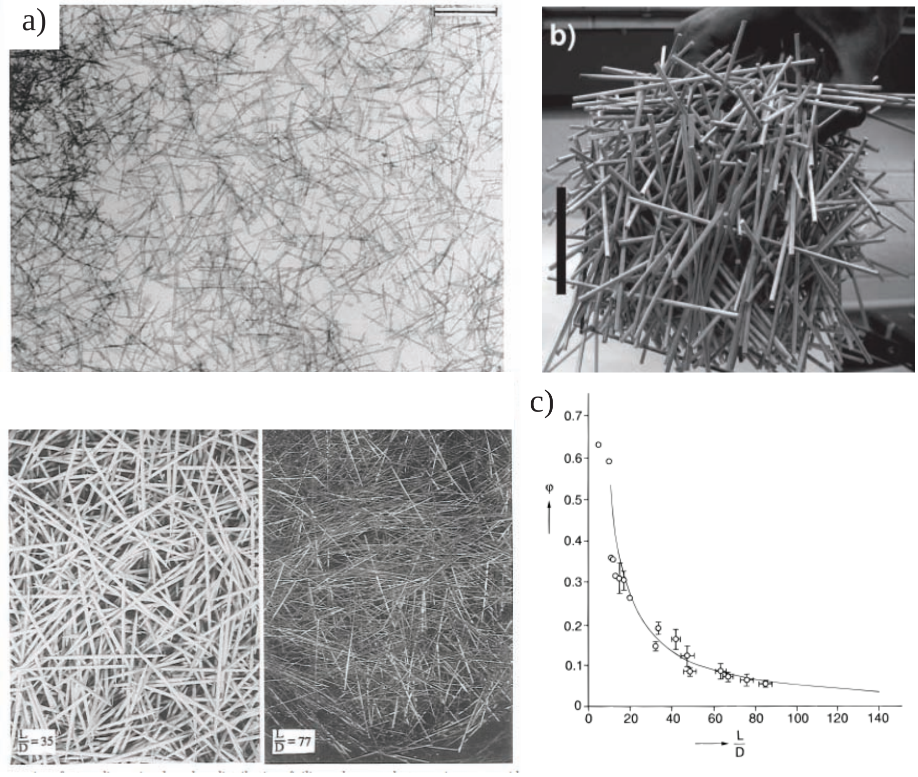

**Figure 2.14:** Examples of rod packing experiments. a) Three images from [82]; Silica rods (top), toothpicks (bottom left), and copper wire (bottom middle). b) Ensemble of wooden rods used to measure rod-contact numbers [83]. c) Prediction of $\phi$ versus aspect ratio from random contact model (line) and measurements from experiment [82].

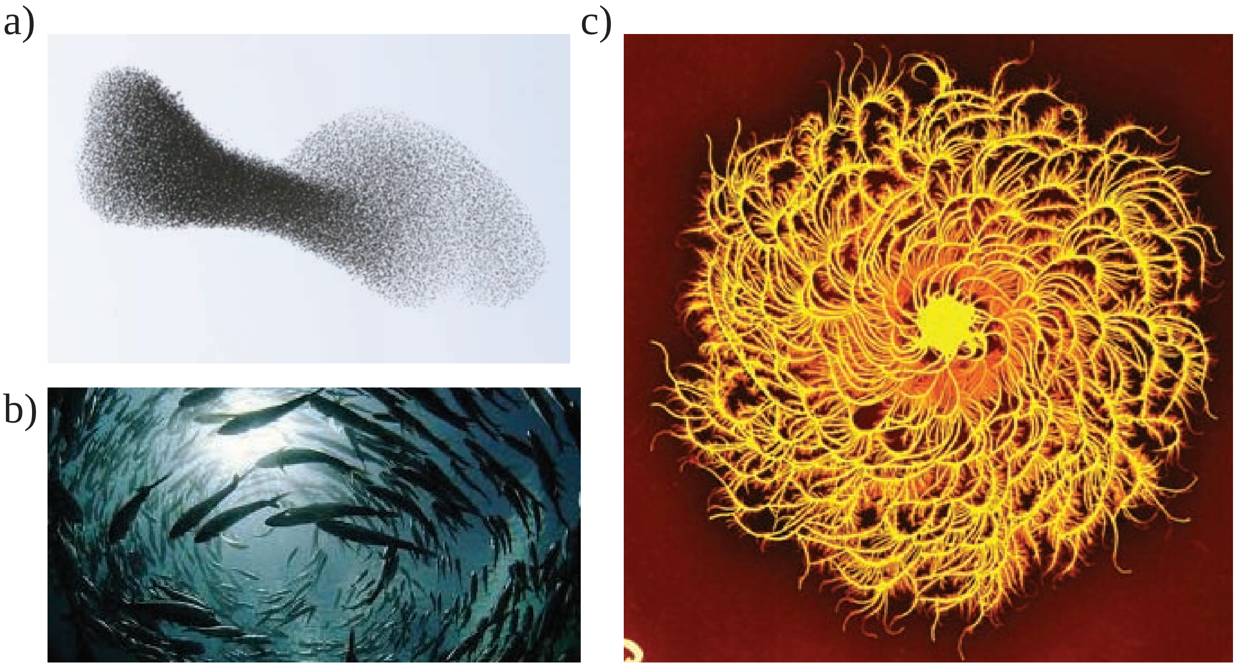

**Figure 2.15:** Examples of collective behavior in biology. a) A starling flock. b)A school of fish. c) A culture of the bacteria *Paenibacillus dendritiformis*.

that often stem from simple behavioral rules among individuals (For comprehensive reviews see [96, 24, 18, 20]). In this sense biological collectives such as fish schools, bird flocks, and fire-ant colonies can be considered a form of active granular matter. Active matter is a branch of soft matter physics which involves the study of non-equilibrium particulate systems in which the particles have internal degrees of freedom [18].

Because many biological systems are intrinsically macroscopic, grainy, and non-equilibrium, traditional thermodynamic descriptions of the phases and phase transition within active materials may not be sufficient. This is especially the case in macroscopic biological collectives (ants, fish, birds) in which the constituent organisms in the group exhibit complex behaviors that are likely not fully described by simplistic ideal-gas derived models [97]. For such systems state machine based models in which the constituents, called agents, act according to defined behavioral rules are often necessary.

Many active matter systems are embedded in an interstitial fluid [18]. In the presence of such a fluid active particles interact through hydrodynamic forces and thus can exhibit collective behaviors through hydrodynamic coupling. Examples of such collective behavior are the synchronization of cilia [98, 99]. Furthermore, active matter systems in a fluid can influence the bulk rheological properties of the fluid by changing the viscosity of the medium [100, 101] or generating large scale turbulence [102].

Other active matter systems do not rely upon physical interactions through a fluid medium, but instead rely on the chemical, tactile or visual sensation of neighboring individuals [25]. For example, bird flocking relies on the visual sensation and response of individual flyers within the group [25]. Ant trail formation instead relies on the deposition of a chemical signal (pheromones) within the environment which other ants respond to and often reinforce by depositing more pheromones.

Collective motion of organisms that interact primarily through tactile responses, such as many bacteria, are analogous to passive granular media in many ways ahutchinson2007usend lend themselves to quantitative study because they can be modeled experimentally. As an example, the collective motion of swarming *Bacilus subtilis* [92] bacteria exhibit "giant-number fluctuations", a phenomena originally described in a vibrated passive granular system [103]. Giant-number fluctuations are a phenomena in which the density fluctuations (measured as the standard deviation of density) of a group of $N$ particles increases faster than $\sqrt{N}$ (as predicted for equilibrium systems) thus leading to the "giant" fluctuations in particle density.

### 2.2.2 Flocking physics

The first physics model of flocking is that of self-propelled particles described by Viscek in 1995 [104].[†]. The particles ignore interactions with the environment and only interact with neighboring particles (defined within as those within a cutoff radius $r$). Each particle has a given velocity specifying its direction and speed. Particle interactions are such that a particle updates its orientation to the mean orientation of particles within a neighborhood defined by radius, $r$. Particle orientation is also subject to some external noise and the noise strength, $\eta$, is a tunable parameter of the simulation. It was found by Vicsek that noise

---

[†] In fact the boids implementation of self-propelled particles was originally introduced by Craig Reynolds in 1986 [105]. However this model was introduced for computer graphics purposes and was not subject to quantitative study.

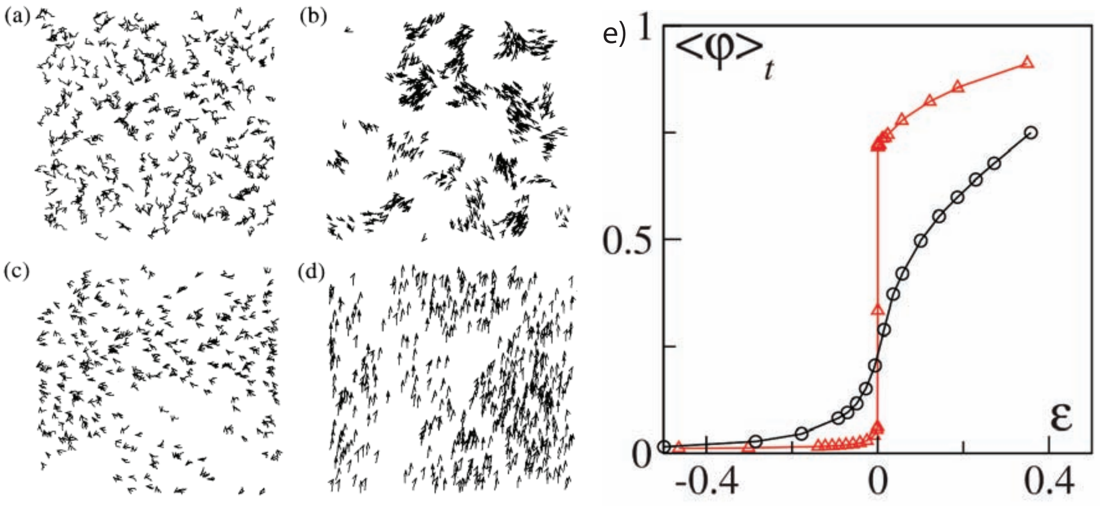

**Figure 2.16:** a-d) Examples of collective motion from the Vicsek model (From [104]). e) Orientational order parameter as a function of noise strength (from [107]).

strength, $\eta$, controls a phase transition between a disordered phase to an ordered phase of coherent flock motion (Fig. 2.16). Toner and Tu proved the existence of this ordered phase using a renormalization-group approach [106].

The Vicsek model has been modified and updated a number of times to model different update schemes and interaction rules among the flocking agents (See [108] for a review of Vicsek variations). Some of these models have been introduced specifically to account for various features observed in biological systems. One update to the Vicsek model, introduced after experimental observation of flocks of the European Starling (*Sturnus vulgaris*) [109], is the use of topological interaction rules instead of the original metric distance interaction rule [110, 109, 111]. Under topological interactions particles interact with there nearest neighbors, independent of the distance the neighbors are from them. The neighbors are determined by partitioning the space with a voronoi tesselation. The voronoi tesselation partitions a space into regions which surround each particle and whose boundaries determine the all points in that region which are nearest the interior particle. Through the voronoi tesselation nearest neighbors of the flocking particles are assigned as neighboring voronoi boundaries [111]. Thus in this scheme particle distance (i.e. metric distance) is not as important as is the location of one particle with respect to the focal particle in the flock. The topological Vicsek model exhibits a similar phase transition from disordered to ordered states. However, metric-free interactions among the active particles (or organisms) leads to more robust flocking and thus may be more advantageous for animal groups wishing to remain collected [111].

### 2.2.3 Self-organized structures

The formation of self-organized structures is a feature of many different types of animal groups. Such structures can take on one of two forms: they can be either formed from the constituent animals bodies (**self assemblages**) or they can be formed within the external environment (**externalized structures**). The processes that lead to these structures are discussed below.

#### *2.2.3.1 Self assemblages*

Self-assembled structures formed from the bodies of the constituent animals in the group are observed across a wide range of organisms from ants, bees, and snakes [112]. The most well studied self-assemblages are those found in the ants [113, 114]. Several species of ants such as fire ants (*Solenopsis invicta*) and army ants (*Eciton burchelli*) construct functional self-assemblages which serve to protect the colony (bivouacs and rafts) or to aid in the colonies mobility (bridges).

Colonies of the fire ant *Solenopsis invicta* create large floating rafts formed from interlocking limbs and body parts [113, 115, 116]. This process has been studied recently and it was shown that ant rafts grow through a diffusive mechanism in which ants wander along the surface until they are grabbed and trapped in place by an ant on the raft [113]. In this way rafts grow laterally and form wide, flat, pancake-like floating structures.

Army ants form bivouacs as they are a nomadic species and lack a central nest [117, 114]. Bivouacs provide a means of thermoregulation for the colony [114] among other protective benefits from forming this structure. Bivouacs are typically formed on the sides of rock faces, or tree trunks. The army ant bivouac has been described as a “living chain mail” [118] by biologist Nigel Franks because of the way the ants interlock and entangle limbs to to form the structure.

The entanglement of limbs and body that these structure forming ants exhibit has been

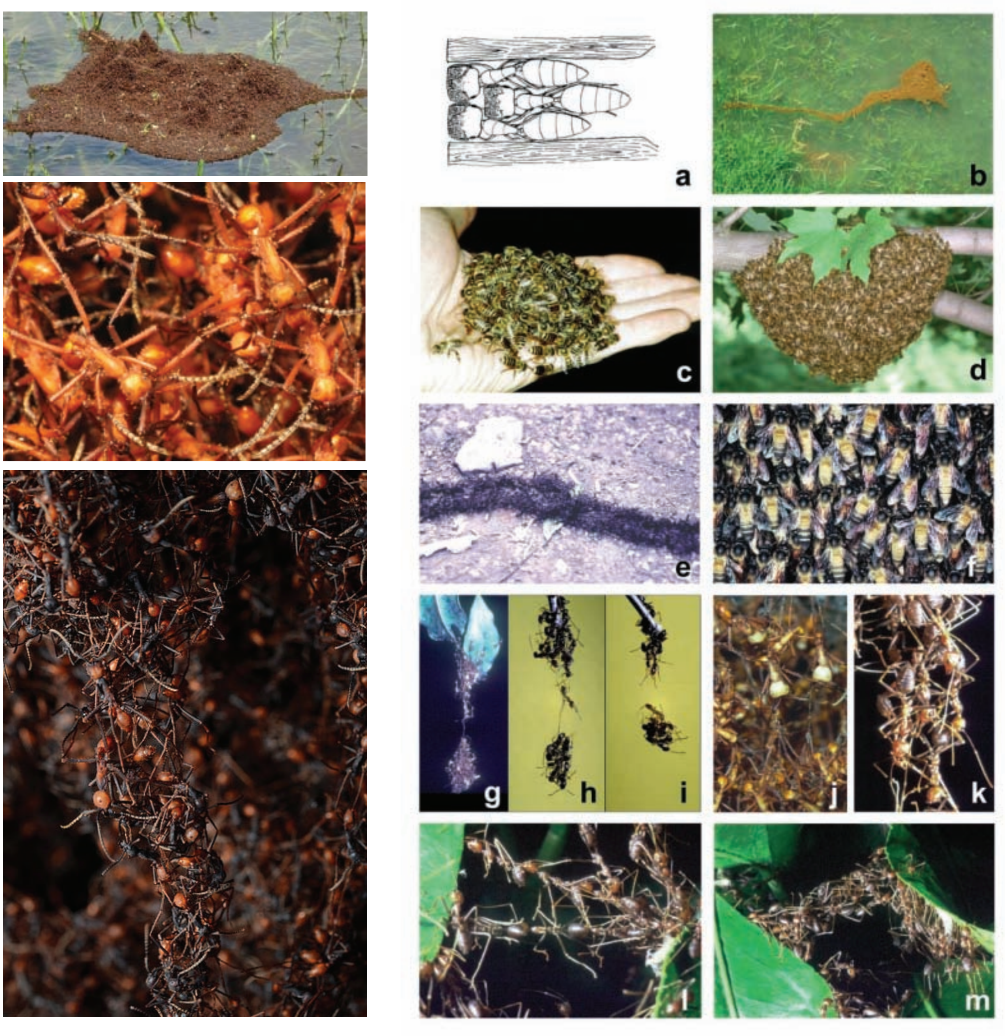

**Figure 2.17:** Examples of insect self-assemblages. In the left column we show assemblages formed by different species of ants. The top image is the raft formed by the fire ant *Solenopsis invicta*, middle and bottom are images from a bivouac of the army ant *Eciton burchelli*. The right column shows various insect assemblages formed. Reproduced from [112]

led to there interpretation as a novel active fluid [119, 120]. In experiments with the ant, *Lasius humile*, researchers directed ants to walk down a narrow wire that ended abruptly. Ants piling up at the end of the wire formed into small droplets which repeatedly fell from the end of the wire, much like a leaking faucet. This experiment is reminiscent of the classic chaotic water faucet experiment [121]. Experiment on ant droplets discovered that the inter-droplet wait times were consistent with that of the classic chaotic leaky faucet, despite the fact that this system was composed of active particles.

#### *2.2.3.2 Externalized structures*

The formation of externalized structures by animal groups is most commonly associated with the construction of a nest. Some solitary animals construct nests, however in this dissertation work we focus on organisms that act collectively to construct nests. Examples of organisms that demonstrate this collective construction behavior most often are found among the social insects: ants, bees, and termites for example [122, 123, 124]. Nests are thought to have been a crucial factor in the evolution of eusociality among animal groups, and thus their morphology and the dynamics of construction are of great interest. Furthermore nests constructed by groups of workers are particularly of interest because they arise from a self-organized process in which local interactions and environmental cues inform workers how to dig. These local interactions taking place across the nest site and among the hundreds to thousands of constituent workers leads to the self-organization of the nest and is a process called stigmergy.

Many species of ants construct subterranean nests through the excavation of soil to form cylindrical tunnels and flatter chambers [125]. These subterranean nests are constructed through the collective excavation and transportation of soil through the tunnel system. Nests can be just below the surface or in some species (*Prenolepis imparis*) can be over four meters in depth [126]. Ant nests serve to protect the colony and provide a central location to facilitate the storage of food, brood, and to participate in social interaction [127].

Measurements of the morphology of ant nests in the field necessarily destroy the nest, through pouring of a molding liquid into the nest, or physics excavation around the nest

**Figure 2.18:** Examples of externalized structures created by animal groups. From left to right: A bee hive, a plaster cast of the subterranean nest of the fire ant *Solenopsis invicta*, a termite mounds (species unkown).

[128]. In laboratory study visualizing the growth dynamics of ant nests in three-dimensional space is hindered by the opaque nature of most soils. A few recent experiments have used X-Rays to visualize to realize the tunnel network [129, 130], however in this technique one cannot visualize the actions of the individual ants. The third method to visualize tunnel growth dynamics is to force ants to dig within a thin region, quasi two-dimensional, region. In these experiments both the action of individuals and the growth of the nest can be monitored [131, 132, 133].

Another form of externalized structure is one created from soil excavated from the ground, or from excretions from the animals body [122]. Examples of these nests are the honeycomb laced hives of the Honeybee [134] or termite mounds [135]. These structures are created by a fundamentally different process than excavated nests in which material is added to the structure to form walls. Termite nests (genus *Cubitermes*)) have been studied in X-Ray computed tomography to reconstruct the inner tunnel network. A network analysis of this systems has illustrated that tunnel networks are near a percolation threshold. Thus the tunnel networks nearly span the system.

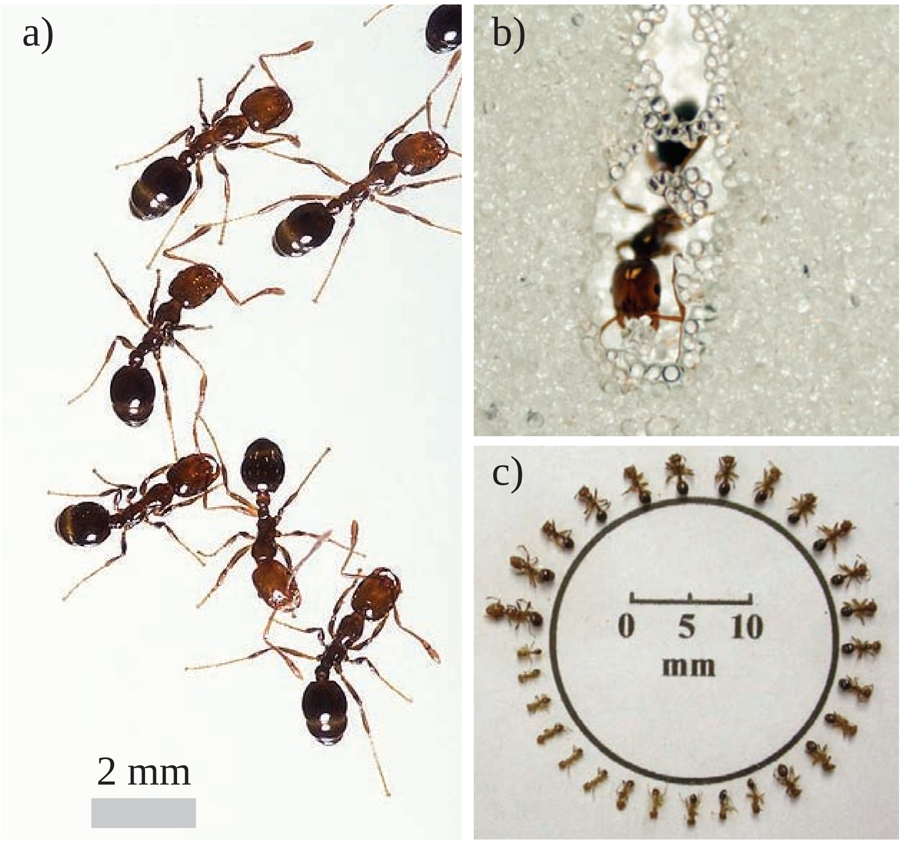

**Figure 2.19:** a) A group of fire ant workers. Image courtesy of the USDA. b) A fire ant handling soil in its mandibles c) The shape and size of fire ant workers. Image from [127]

### 2.2.4 Model organism: the fire ant

The red imported fire ant *Solenopsis invicta* Buren is an invasive species in the southern United States. Fire ants have a caste system consisting of a queen, responsible for reproduction, sterile female workers who provide the work force for the colony, and sexual males whose sole function is to mate with queens on a nuptial flight. Fire ant workers are typically 3.5 mm in body length and 0.6 mm in head width. However workers may vary in size up to three-fold (in length and width, see Fig. 2.19).

Fire ants get their name from the reddish-brown color of their bodies, and the fact that they are capable of delivering a poisonous sting when threatened. Fire ant stings are mostly harmless to humans, unless allergic, and leave a small red welt for a couple of days. Fire ant workers typically live for 6-weeks and the queen will live for typically three years [127]. Fire ants are scavengers and eat a combination of vegetable matter and foraged invertebrates.

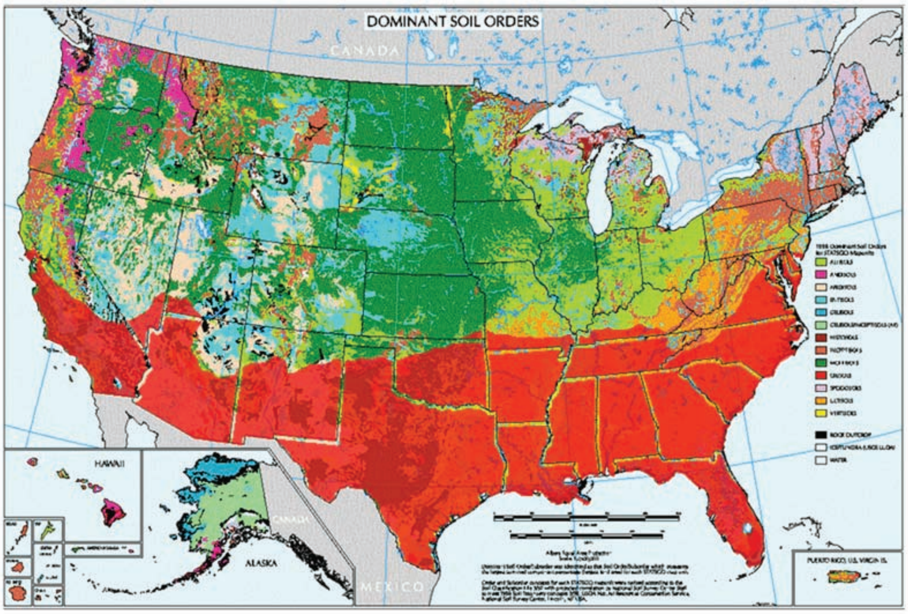

**Figure 2.20:** The invasive region of the fire ant *Solenopsis invicta* shown in red.

#### *2.2.4.1 Habitat*

Fire ants originate from the Pantanal wetlands of Argentina and Brazil, an area in which there is fierce competition for resources and survival [127]. The wetlands are subject to seasonal flooding and it was this seasonal pressure that allowed fire ants to evolve there raft formation behavior [113] as discussed in section 2.2.3.1.

Fire ants emigrated to the United States in the 1930's through Mobile, Alabama [136]. From Alabama fire ants spread across the southern United States by aid of railroads and trucks shipping agricultural materials [137]. Fire ants are found in a diversity of soil types [127, 137] from fine-powder, cohesive red clay of Georgia, to sandy soils of Florida (Fig. 2.19). Although it is known that the shape of the nest mound varies in different soils, with the sandier soils resulting in less mound volume, it is not explicitly known if soil-type limits nest construction ability.

#### *2.2.4.2 Nest structure*

Fire ant nests consist of three parts (Fig. 2.21): 1) an above surface mound 2) a vertical series of tunnels and chambers constructed directly below the mound 3) a series of horizontal

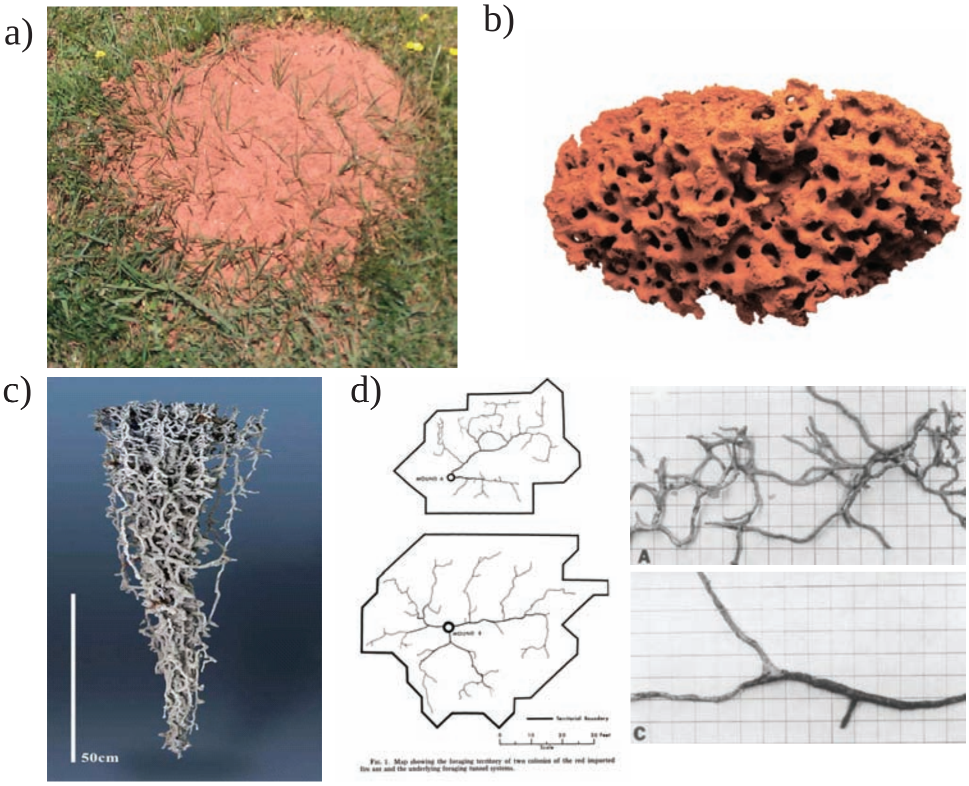

**Figure 2.21:** Three sections of the fire ant nest. a) The fire ant mound. b) A cross section of the mound showing tunnels. c) A plaster cast of the tunnels below the mound. d) A map of the horizontal tunnels

tunnels which radiate away from the central nest and are used for foraging traffic [127, 138, 139]. Tunnels within the mound are circular with a mean diameter of 0.44 mm. Tunnels below the mound range from 3 mm to 9 mm in diameter with mean diameter of 6 mm. Larger tunnels may support higher ant traffic flows. The horizontal tunnels extend laterally away from the nest and can be up to 50 m in length [138]. The diameter of the foraging tunnels ranges from to 3 and 6 mm and decreases as the tunnel gets further away from the center of the nest [140].

# CHAPTER III

# YIELD FORCE

## *3.1 Summary*

A granular material's resistance to flow, its yield force, is a function of volume fraction, $\phi$, and exhibits a transition analogous to the ductile-brittle transition displayed by metals. We study the drag force, $F_D$, on a flat plate translated from rest through a granular medium to observe yield force dynamics as a function of prepared $\phi$. We find that drag force is sensitive to $\phi$ such that $F_D$ monotonically increases with displacement for $\phi \leq \phi_c$ and for $\phi \geq \phi_c$, $F_D$ exhibits maxima. We show that $\phi_c$ corresponds to the onset of dilatancy. Quasi-2D drag experiments show that the maxima in $F_D$ for $\phi \geq \phi_c$ are associated with maximum shear strain during yield which is focused along a narrow shear band. At $\phi \leq \phi_c$ shear strain fluctuates and increases monotonically with displacement.

## *3.2 Introduction*

Dry granular materials (GM) are collections of macroscopic dissipative particles and are common in everyday life—from coffee grounds to sand. The constituents of a granular material are typically large particles (diameter $> 100$ $\mu m$) that interact through short range contact forces (friction and normal force). Because granular matter is so prevalent in industry and nature, physics studies of granular medium have many important engineering and biological applications [74, 141, 142].

Similar to fluids GM deform and flow under stress. Unlike newtonian fluids however, a granular material requires a non-zero stress to induce flow, called the yield stress. A detailed understanding of the yielding process in granular materials is of fundamental importance to understanding how animals, tools, and robots interact with soil [143].

Plate drag is a particular example of a more general class of GM interactions termed localized forcing. Localized forcing of GM consists of a localized boundary that is displaced or rotated through an extended granular media [144, 145, 71, 72, 146, 147, 148, 149, 150, 151, 152]. Understanding the force and flow response during localized forcing is complicated by the fact that the density, stress, and strain fields are spatially and temporally heterogeneous [54]. However most interactions with GM are localized and thus detailed understanding of the principles of localized forcing are needed.

Recent studies of localized forcing [54], such as horizontal drag [54], vertical penetration [153, 154, 150], or rotation [155] of a plate within granular media or impact experiments penetrator impact [156, 45] have highlighted the important role the initial volume fraction, $\phi$, of the material plays in force and flow dynamics. The sensitivity of resistance forces to initial $\phi$ is due to the compacting or dilating flow response under shear that granular media prepared at different initial $\phi$ undergo. A loosely packed GM (low $\phi$) will compact under shear and thus strengthen while a closely packed (high $\phi$) media will dilate (expand in volume) under shear weakening the media. Thus the prepared volume fraction of the granular medium in relation to $\phi_c$ determines the material response.

For quasi-static granular materials $\phi$ typically varies between the random loose pack ($\phi = 0.55$ [55]) and random close pack ($\phi = 0.64$) limits for ideal monodisperse sphere packings. In practice however GM are typically found in a smaller range of volume fractions $0.57 < \phi < 0.63$. Granular materials with initial state $\phi$ can be prepared through a combination of fluid flow and vibration [45, 157]. In this study we investigate the role of $\phi$ and in particular $\phi - \phi_c$ in the force and flow dynamics during yield of a granular media.

Here we investigate the drag force, $F_D$, on a flat submerged plate translated from rest through a granular media prepared at different $\phi$. Experiments are performed in the bulk, away from container boundaries, and additional experiments with the flat plate placed adjacent to a transparent wall were performed to visualize the granular flow below the surface.

## *3.3 Methods*

Drag measurements, see Fig. 3.1(a,c), were performed in a $27\times86\times13\,\mathrm{cm}^3$ bed of polydisperse 256±44 $\mu$m glass beads (Potters Industries; density $\rho = 2.51$ g cm$^{-3}$). Similar effects to those described here were observed in other granular materials, including heterogeneous

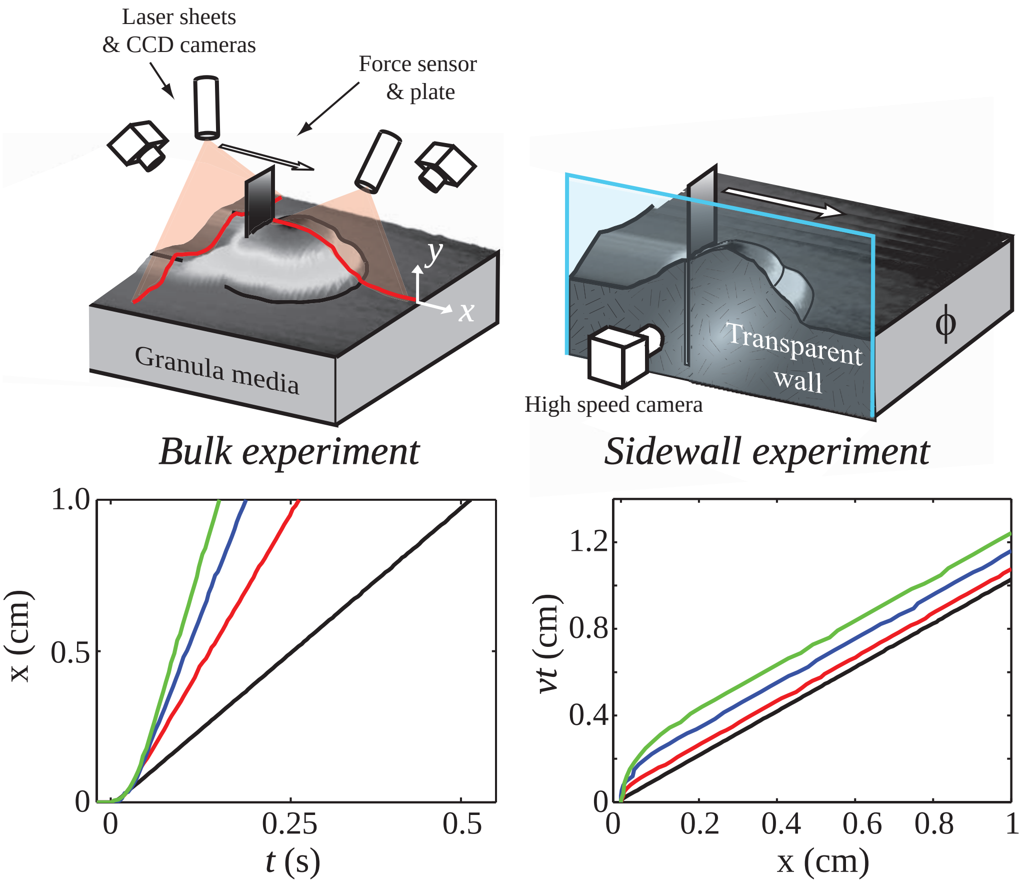

**Figure 3.1:** Drag measurements in granular media. a) Bulk experiment consists of a flat plate translated through granular media. Two laser lines and cameras measure surface deformation ahead of and behind plate. b) In side-wall experiments plate is placed against a transparent wall and high speed video is recorded. c) Displacement vs time for four speeds (2 cm/s black, 4 cm/s red, 6 cm/s blue, 8 cm/s green). d) Expected displacement (vt) and observed displacement at four speeds (2 cm/s black, 4 cm/s red, 6 cm/s blue, 8 cm/s green) illustrating that plate drag is up to speed in approximately 0.1 cm.

beach sand and poppy seeds. Air flow through the porous floor initially fluidized the medium and then a combination of air flow (below fluidization) and mechanical vibration generated the desired initial volume fraction ($0.579 < \phi < 0.619$; see Fig 3.1b). Air flow was turned off prior to testing and volume fraction determined from bed height images as $\phi = M/\rho Ah$, where $M$, $A$ and $h$ are the bed mass, area and height respectively.

A stepper motor and linear translation stage displaced a 3.9 cm wide by 0.3 cm thick steel plate submerged to a variable fixed depth $7.5 < d < 9.5$ cm over a total distance of 50 cm at a constant speed of $v = 2, 4, 6, 8\,\mathrm{cm\,s^{-1}}$. In these experiments we are only concerned with the initial 1 cm of drag, however steady state drag observation was used to characterize the dilation response of the media at different initial $\phi$. An optical encoder recorded the position of the linear translation stage and a 3-axis ATI load cell mounted between the submerged plate and translation stage measured the drag forces (sampled at 200 Hz). Using laser line profilometry, we recorded the resultant surface profile and used it to quantify the change in vertical cross sectional area, $\Delta A$, normalizing by the submerged area of the plow, $A_P =$ width × depth. Profiles were measured 35 cm from the start of drag where the profile was in a steady state [54].

We measured the time evolution of the granular surface along the direction of motion down the midplane of the plate. A laser line was used to illuminate the drag path and we placed a camera at an oblique side angle such that height changes in the granular surface corresponded to vertical motion of the laser line in the camera's image. We recorded video at 30 fps and tracked the surface height evolution in Matlab.

In separate drag experiments a flat plate at depth $5.5 < d < 6.5$ cm was positioned against a transparent wall and displaced at $v = 2\,\mathrm{cm\,s^{-1}}$ parallel to the wall to image grain flow. High speed video (250 fps) of the flow was recorded and analyzed in Matlab using image registration with a correlation time step of 0.02 s. The near-wall setup exhibited similar force fluctuations as the bulk but with approximately half the mean force. We post process our PIV velocity fields using a spatial median filter, commonly used in image processing, which reduced spurious velocity measures.

We remove a systematic variations in the force—the decrease in depth of the constant height intruder with increasing $\phi$—by defining the drag force, $F_D$, as the raw drag force multiplied by a depth correction factor $(\frac{d_{LP}}{d})^2$ normalized to the loose pack depth $d_{LP}$. Separate measurements at controlled intruder depth support this normalization technique.

## *3.4 State preparation and characterization*

Air flow and vibration of a given duration were used to prepare granular media of initial volume fraction, $\phi$ (Fig. 3.2a, error bars represent $\pm 1$ SD from 4 repetitions). Initially the granular media is air fluidized to a bubbling state to reset the granular packing. Stopping the air flow leaves the media in a loosely packed state (low $\phi$). To compact the media, mechanical vibration and air flow below the onset of fluidization is employed.

We observed that $\phi$ increased monotonically as a function of vibration duration (Fig. 3.2a). The vibration mechanism, a motor with off axis mass, required a small turn on time ($t \approx 0.5$ s), and thus $\phi$ did not vary for shake times less than this amount.

To characterize whether the initial $\phi$ is above the onset of dilatancy we used a previously described technique [54] in which we measured the cross-sectional area, $A$, of the trough left behind after drag with respect to the area of the plate $A_p$. Observing the difference in $A$ after the drag we determined whether the material compacted ($\frac{\Delta A}{A_p} < 0$) or dilated ($\frac{\Delta A}{A_p} > 0$).

In these experiments we identify the dilation transition at $\phi_c = 0.603 \pm 0.003$ (Fig. 3.2b). Furthermore we will refer to the prepared granular state as $\Delta\phi = \phi - \phi_c$ where $\Delta\phi < 0$ is a compacting GM and $\Delta\phi > 0$ is a dilating GM.

Over the four different drag speeds tested, $v = 2, 4, 6, 8$ cm s$^{-1}$, observed no significant difference in $\phi_c$. Furthermore the compaction-dilation curves, $\frac{\Delta A}{A_p}$, did not vary as a function of speed. This suggests that the average compaction-dilation response was independent of velocity for the speeds tested.

During state preparations we observed that the rate of increase in $\phi$ differed as a function of time. For $\phi$ below $\phi_c$ the change in volume fraction, $\delta\phi$, per unit packing time $\delta t$ was large while above $\phi_c$ the granular media compacted much slower. We approximate the rate of compaction with the numerical derivative $(\frac{\delta\phi}{\delta t})$ and observed that a qualitative change

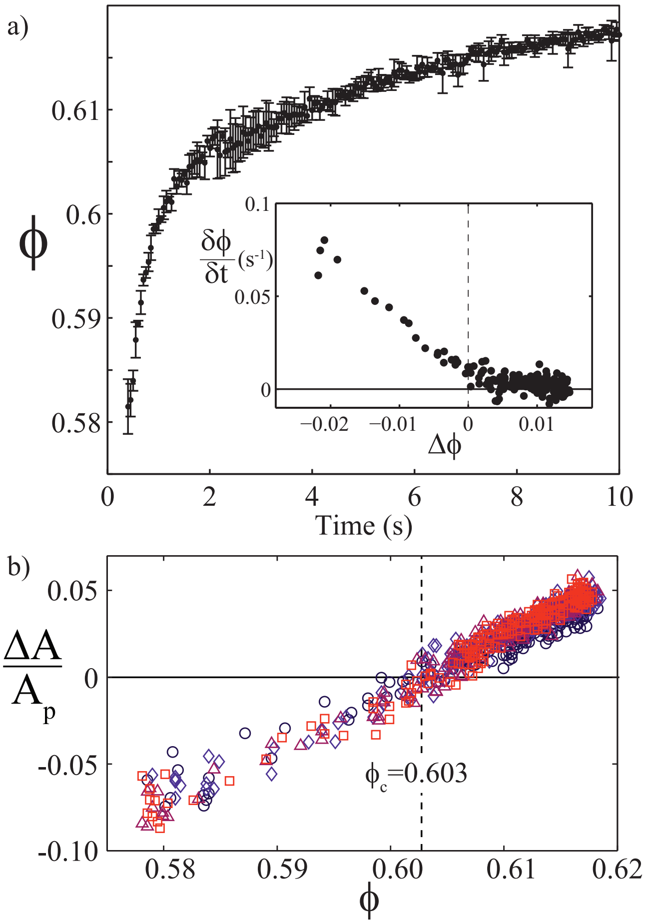

**Figure 3.2:** Compaction behavior of granular media. a) Initial $\phi$ as a function of vibration time. Error bars represent ±1 S.D. of four replicates. Inset shows numerical derivative of $\phi(t)$ as a function of $\Delta\phi$. b) Compaction-dilation response of granular media as a function of initial $\phi$.

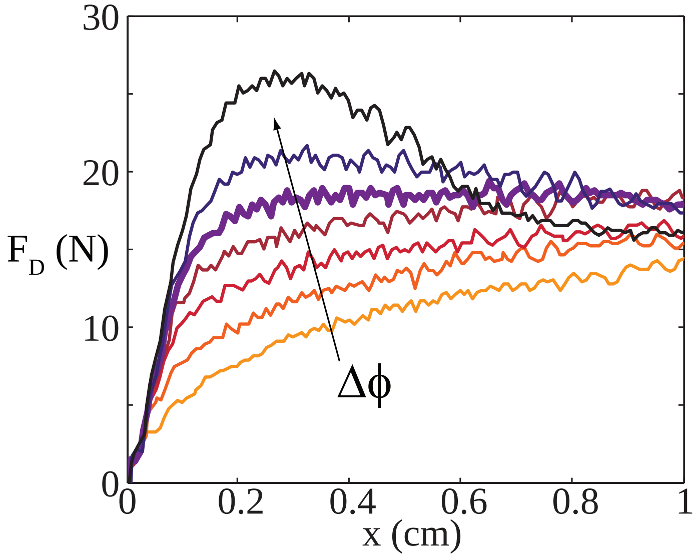

**Figure 3.3:** Yield force versus displacement at different initial $\Delta\phi$. Arrow indicates curves of increasing initial $\Delta\phi$ (in increments of $\approx 0.006$). Bold curve is near critical packing at $\Delta\phi = 0.001$

in $\frac{\delta\phi}{\Delta t}$ occurred when $\phi$ exceeded $\phi_c$ (Inset Fig. 3.2a). This suggests that the timescales associated with compaction of granular media may differ above and below the dilation transition, $\phi_c$. Although extensive research has been performed investigating compaction dynamics of granular media to our knowledge the role of the dilation transition has not been discussed (See [158] for a review).

## *3.5 Drag force*

The primary focus of this study is the yield force during drag within granular media of different initial $\Delta\phi$. The drag force, $F_D$, on a flat plate translated 1 cm was sensitive to initial $\Delta\phi$ in both magnitude and functional form (Fig. 3.3).

For $\Delta\phi < 0$, $F_D$ increased monotonically with $x$ and thus was largest at the end of the 1 cm drag. However for $\Delta\phi > 0$, $F_D$ rapidly rose to a maximum near $x_{max} = 3$ mm and subsequently decreased for the remainder of the 1 cm drag. The shape of $F_D$ differed as $\Delta\phi$ was increased, evolving smoothly between the two extremes of initial $\Delta\phi$.

The variation in $F_D$ observed for increasing $\Delta\phi$ is consistent with a ductile to brittle transition that occurs in soils of increasing packing density. In the critical state soil mechanics model it is assumed that soil, under constant shear, will either dilate or compact depending on initial $\phi$ and the instantaneous density $\phi(t)$ will approach a critical $\phi_c$. When the system evolves to this critical state no further force change is observed. For comparison we note that the drag force in media prepared near $\Delta\phi = 0$ (highlighted in bold in Fig. 3.3) is flat (unchanging with displacement) after 2 mm of drag and partitions the $F_d$ curves between compacting GM (below) and dilating GM (above) with all curves approaching a similar value at 1 cm.

We quantify the variation in $F_D$ that occurs as a function of $\Delta\phi$ by computing several metrics of the drag force (Fig. 3.4a-d). The maximum drag force, $F_{max}$, increased linearly with $\Delta\phi$ in both loose and close pack regimes however the slope of this curve exhibited a discontinuity near $\Delta\phi = 0$. The change in slope reflects the onset of the maxima in $F_D$ above $\phi_c$ (see Fig. 3.3). Similar changes in granular resistance force across a critical $\phi$ have been previously observed in penetration [154] and shear [153].

To determine at which $\Delta\phi$ the onset of a force maxima occurs we compare the maximum of $F_D$ over the 1 cm drag with $F_D$ at $x = 1$ cm. If this ratio, $\tilde{F}_{max} = \frac{F_{max}}{F_D(x=1cm)}$, is unity the drag force is monotonic and if the ratio exceeds unity a maximum exists. Figure 3.4b indicates the onset of a maxima in $F_D$ occurs at $\Delta\phi = 0$ independent of drag speed.

The drag distance at which point force is maximum, $x_{max}$, also highlights the bifurcation in force dynamics that occurs as initial $\phi$ is increased from loose to close pack (Fig. 3.4c). For $\Delta\phi < 0$, $x_{max}$ occurs near the end of the 1 cm drag because $F_D$ increases monotonically. For $\Delta\phi > 0$ however $x_{max}$ is found at $x_{max} = 0.29 \pm 0.03$ cm independent of speed. This corresponds to a drag distance of approximately 11 particle diameters.

For small initial displacements (0.1 cm) of the plate we observed that $F_D$ is roughly linear with displacement (Inset Fig. 3.4d). Thus we can measure an effective elastic stiffness of the granular material by fitting $F_D = kx$ to the drag data in this region. While $F_D$ exhibited signatures of a force and flow bifurcation when evaluated over the 1 cm displacement, for small displacements we observed that $k$ is not sensitive to the $\Delta\phi = 0$ transition.

We suspect that the lack of a bifurcation in $k$ across $\phi_c$ is because dilatancy and the resultant effects on $F_D$ are only observed when sufficient shear strain is developed. This may take tens to hundreds of grain diameters of drag to become appreciable and thus in the

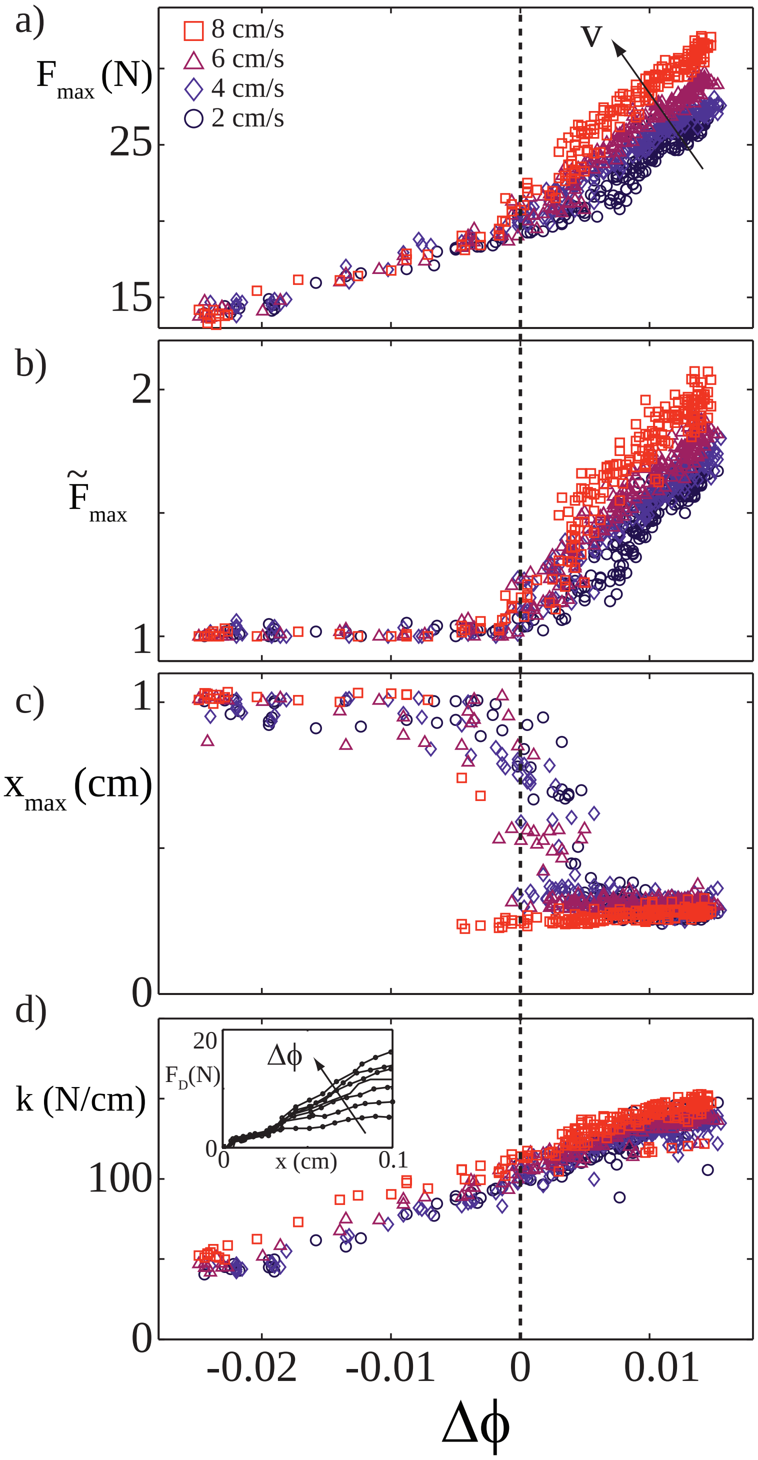

**Figure 3.4:** Yield force statistics as a function of initial $\Delta\phi$ at four separate drag speeds (See legend). a) Maximum force developed within $x = 1$ cm of plate displacement. Arrow indicates trend of increasing drag speed. b) Maximum force normalized by force on plate at $x = 1$ cm. c) Plate displacement at maximum drag force. d) Stiffness of granular media versus $\Delta\phi$. Fit line is $k = 3065x + 115$. Inset shows $F_D$ in $x = 0.1$ cm.

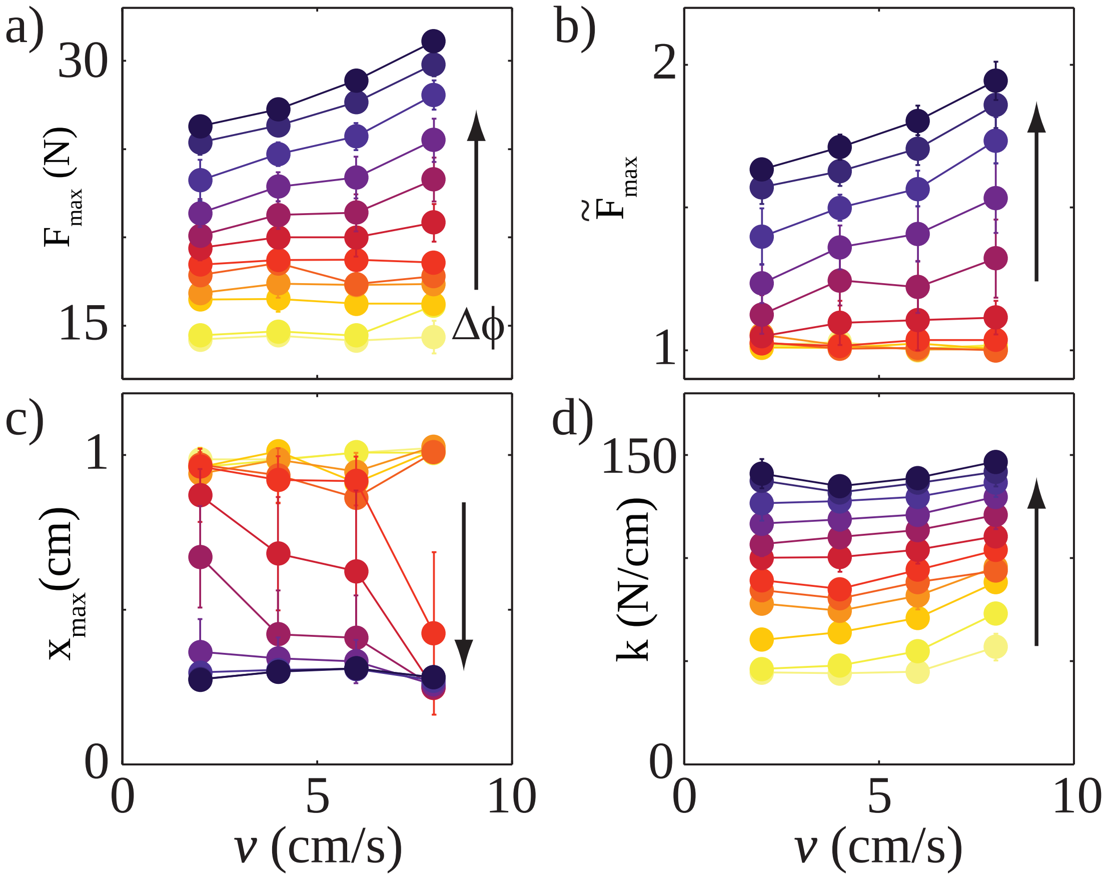

**Figure 3.5:** Velocity dependence of $F_D$ for different initial $\Delta\phi$. Color represents initial $\Delta\phi$ and arrows indicate direction of increasing $\Delta\phi$ in increments of 0.003. a) $F_{max}$ versus speed at different initial $\Delta\phi$. b) $\tilde{F}_{max}$ versus speed at different initial $\Delta\phi$. c) $x_{max}$ versus speed at different initial $\Delta\phi$. d) $k$ versus speed at different initial $\Delta\phi$.

small displacement regime we measure $k$ over it is likely that dilation-compaction dynamics do not influence the resistance force. Instead we observe that $k$ linearly increases with $\Delta\phi$. This is in qualitative agreement with recent experimental results using vane [155] and penetration geometries [153] and is likely due to a linearly increasing contact number in the packing [159].

Surprisingly we observed that $F_D$ during yield appeared to increase with velocity in the $\Delta\phi > 0$ regime while for $\Delta\phi < 0$, $F_D$ appeared to be insensitive to velocity. To quantify this functional dependence on $v$ we averaged $F_{max}$, $\tilde{F}_{max}$, $x_{max}$, and $k$ over bins of $[\phi, \phi + 0.003]$ and plot the results as a function of drag velocity (Fig. 3.5a-d).

The quantities associated with the drag force magnitude and shape, $F_{max}$ and $\tilde{F}_{max}$,

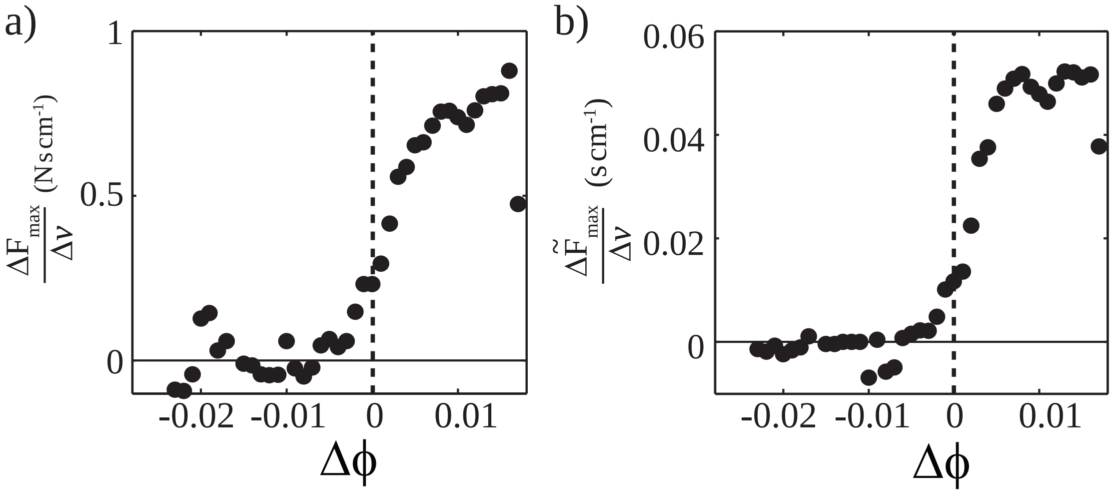

**Figure 3.6:** Velocity dependence of drag force as a function of initial $\Delta\phi$. a) Slope of linear fit to $F_{max}(v)$. b) Slope of linear fit to $\tilde{F}_{max}(v)$.

exhibited no velocity dependence at low $\Delta\phi$ and positively increased with $v$ at high $\Delta\phi$ (Fig. 3.5a,b). $x_{max}$ and $k$ however displayed more complex velocity dependence (Fig. 3.5c,d). Increasing drag speed did not influence the value of $x_{max}$ in the high and low $\Delta\phi$ regimes however it increasing speed did tend to decrease the $x_{max}$ for intermediate packings near $\Delta\phi = 0$. $k$ only slightly varied with $v$ at low $\Delta\phi$ and appeared to be insensitive to $v$ at higher packing fractions.

To determine the onset of velocity dependence in $F_D$ we measure the slope of linear fits to the force-velocity curves ($\frac{\Delta F_{max}}{\Delta v}$ and $\frac{\Delta \tilde{F}_{max}}{\Delta v}$) in Figure 3.5a,b. As a function of initial $\Delta\phi$ we observed that the onset of nonzero $\frac{\Delta F_{max}}{\Delta v}$ and $\frac{\Delta \tilde{F}_{max}}{\Delta v}$ occurred near $\Delta\phi = 0$ (Fig. 3.6a,b). This indicates that the positive dependence of the drag force on velocity during yield only occurs when the media is dilating.

The dependence of resistance force on intruder speed is surprising because slow speed intrusion or drag forces are typically found to be independent of speed [71, 153, 160]. However of these previous studies one only varied $\phi$, and the drag speeds were two orders of magnitude lower [153]. It is likely that previous experiments were performed in granular media at or below $\phi_c$ where we observe no velocity dependence of resistance forces. [161]

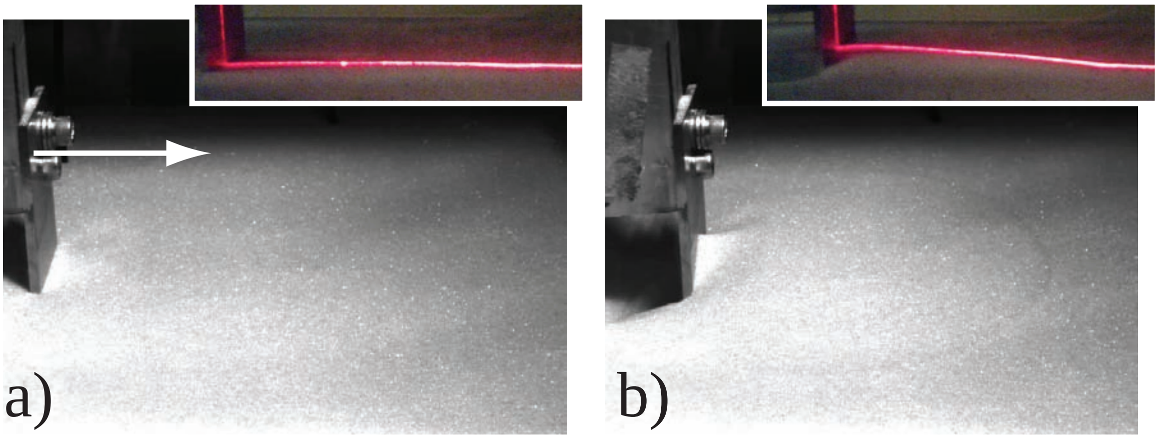

**Figure 3.7:** Oblique side view of surface deformation during yield. a) Initial position of plate. Arrow indicates direction of motion. b) Final position of plate after 1 cm drag. Inset shows surface profile measurement using laser line.

### *3.6 Surface flow*

We now turn our attention to the flow behavior of the granular media during yielding in order to understand the mechanism responsible for the variation of $F_D$ at different $\Delta\phi$. Viewed from an oblique side angle (Fig. 3.7a-b) the displaced granular material in front of the translated plate forms a hill with a cylindrical shape when viewed from above. We illuminate the granular surface during yield with a laser line and record video from a low angle side view (See inset Fig. 3.7b) to track the hill height during yield.

After yield the hill height in front of the plow was dependent upon initial $\Delta\phi$ (Fig. 3.8a). In general for increasing $\Delta\phi$ we observed that the hill height. We computed two measures of the hill shape, the maximum hill height $y_{max}$ and the total cross sectional area of the hill $A_{hill}$.

The increase in hill volume with increasing $\Delta\phi$ is a result of the transition from compaction to dilation. As can be seen in Figure 3.2b the amount of volume change that occurs in the steady-state drag is linearly increasing with $\Delta\phi$. Thus we should expect that the hill height—a measure of volume occupied by the mobile grains—should linearly increase with $\Delta\phi$.

Although we observed that hill shape was influenced by $\Delta\phi$ we did not observed a signature $\phi_c$. Thus to identify features of the bifurcation in grain dynamics that occurs at

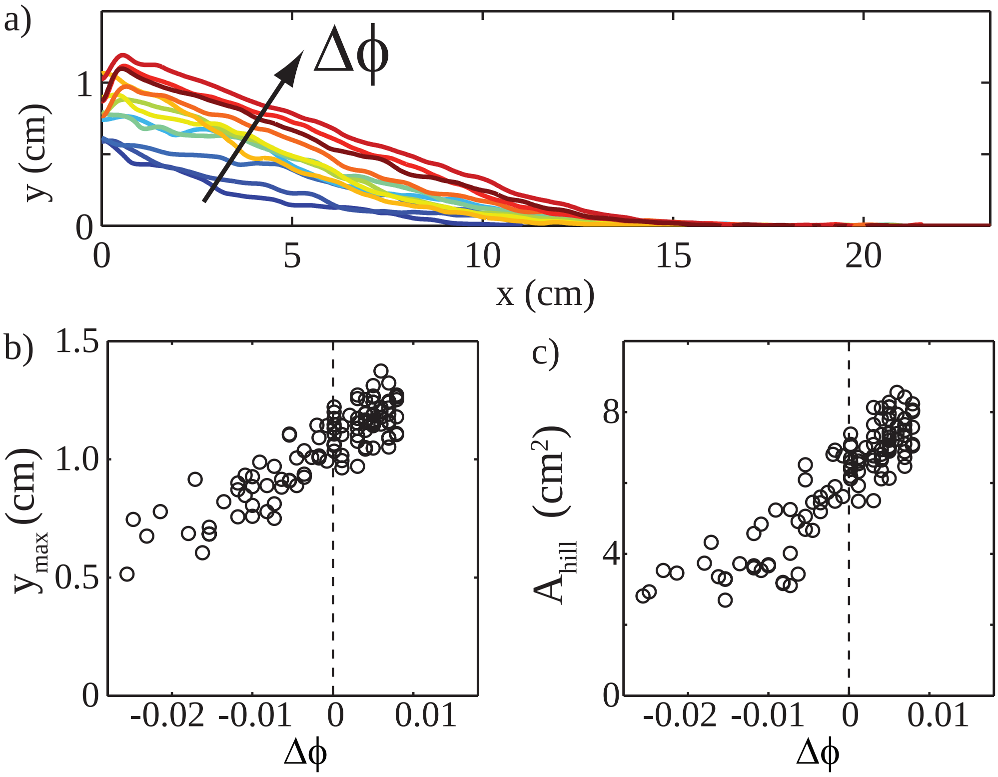

**Figure 3.8:** Statistics of surface deformation during drag. a) Surface profile after 1 cm drag measured with laser line. Arrow indicates trend for increasing initial $\Delta$. b) Maximum hill height as a function of initial $\Delta\phi$. c) Cross sectional area of hill as a function of initial $\Delta\phi$.

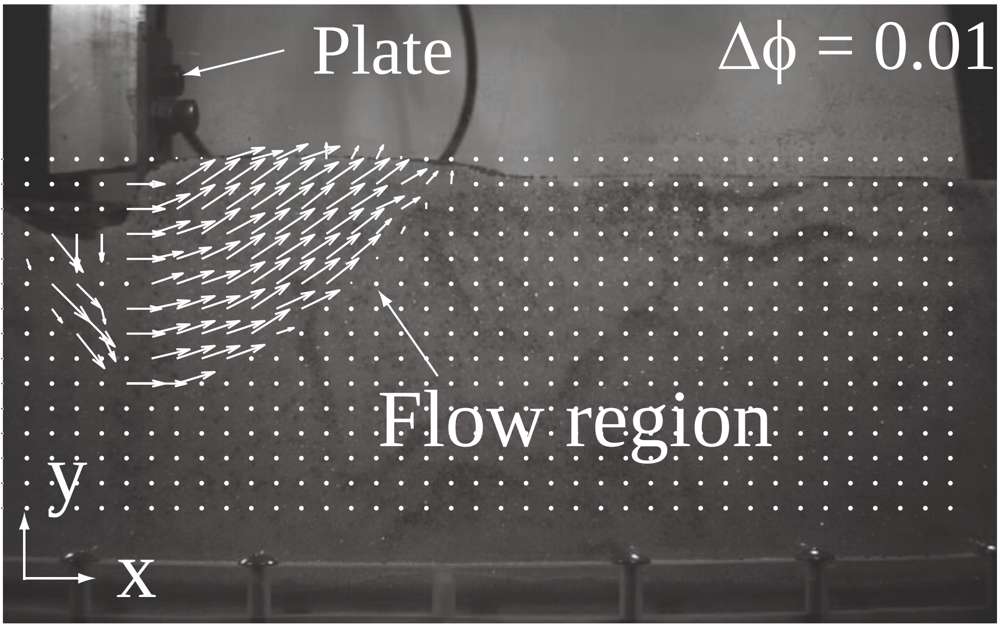

**Figure 3.9:** Side view of flow visualization experiment at $\Delta\phi = 0.01$. Velocity field from particle image velocimetry superimposed on top.

$\Delta\phi = 0$ we must look to other methods to characterize the flow response.

### *3.7 Bulk flow*

Performing plate drag experiments next to a transparent wall allowed for visualization of the granular flow in the bulk during yielding. From particle image velocimetry we determined the velocity field, $\vec{u}$, of the flowing granular media (Fig. 3.9). In general, independent of $\Delta\phi$, we observed the flow to be concentrated in a wedge shaped region directly in front of the plate (Fig. 3.9). The granular media was pushed by the plate in the positive $x$ direction and subsequently flowed in the positive $y$ direction as if up an inclined plane. This flow pattern is consistent with a coulomb wedge type failure mode of granular media and observations of similar flow patterns have been previously reported [147, 148].

A dominant dissipative mechanism in quasistatic granular flow is through shear dissipation. Thus to understand the changes in $F_D$ at different initial $\Delta\phi$ we study the shear strain present in the flow field. To determine the maximum shear strain rate of the granular flow we compute the components of the two dimensional deformation rate tensor: the normal strain rate, $e_{ii} = \frac{du_i}{di}$ $(i = x, y)$, and the average shear strain rate, $e_{xy} = \frac{1}{2}\left(\frac{du_x}{dy} + \frac{du_y}{dx}\right)$. The

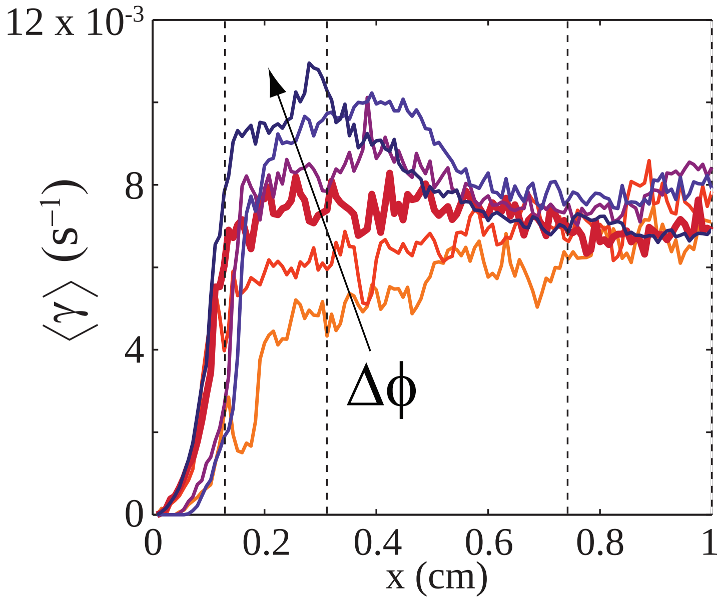

**Figure 3.10:** Spatial average of the maximal shear strain rate as a function of displacement.

maximum shear that occurs in the flowing region is then found by solving for the maximal shear strain rate field $\gamma = \sqrt{\left(\frac{e_{xx}-e_{yy}}{2}\right)^2 + e_{xy}^2}$ and its subsequent spatial average $\langle\gamma\rangle$.

The time evolution of $\langle\gamma\rangle$ during drag was sensitive to initial $\Delta\phi$ and was similar to $F_D$ in shape (Fig. 3.10). For $\Delta\phi < 0$, $\langle\gamma\rangle$ increased monotonically (neglecting rapid fluctuations) over the drag while for $\Delta\phi > 0$, $\langle\gamma\rangle$ exhibited a maximum consistent with the maximum in $F_D$ that occurs in close packed media (Fig.3.2b). Similar to $F_D$, $\langle\gamma\rangle$ a $\phi_c$ partitions $\langle\gamma\rangle$ to loose (below) and close (above) packed responses.

To compare the shear strain rate statistics with those of $F_D$ we compute the normalized maximum shear strain rate, $\langle\tilde{\gamma}\rangle = \frac{max[\langle\gamma\rangle}{\langle\gamma(1\ cm)\rangle}$ and the drag distance at which this local maximum occurs. Comparison of $\langle\tilde{\gamma}\rangle$ and $\tilde{F}_{max}$ shows that they are in very good quantitative agreement (Fig. 3.11a). Furthermore the location of the local maxima in both $\langle\tilde{\gamma}\rangle$ and $\tilde{F}_{max}$ are in good quantitative agreement indicating that when drag force is maximum the shear strain is also maximum. The signature of the bifurcation at $\Delta\phi = 0$ is clearly seen in both the flow and force measurements of Figure 3.11.

To identify the mechanisms responsible for the variation of $\langle\tilde{\gamma}\rangle$ with $\Delta\phi$ we visualize the shear strain rate field, $\gamma$, at four displacements for three separate initial $\Delta\phi$ (Fig. 3.12). For all experiments, independent of $\Delta\phi$, we observed that shear strain was concentrated

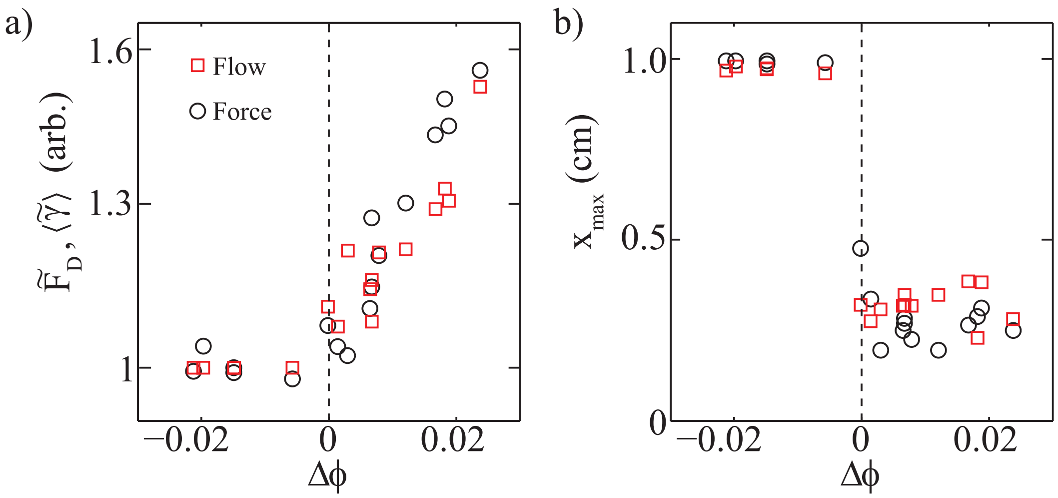

**Figure 3.11:** Comparison of yield force and shear strain statistics at different $\Delta\phi$. a) Normalized peak drag force ($\tilde{F}_D$, black circles) and average shear strain rate ($\langle\gamma\rangle$, red squares) as a function of $\Delta\phi$. b) Drag distance at maximum $F_D$ (black circles) and $\langle\gamma\rangle$ (red squares)

along in a narrow region—a shear band—which originated from the bottom of the plate and extended upwards to the surface.

Although shear bands were observed in the velocity fields of all $\Delta\phi$, the spatiotemporal dynamics and stability of these shear bands differed as a function of initial $\Delta\phi$ (Fig. 3.13). Only for $\Delta\phi > 0$ did we observe that shear bands remained localized in space (See supplementary video). At $\Delta\phi < 0$ the shape of the shear band emanating from the bottom of the plate fluctuated throughout the duration of the drag.

The spatiotemporal evolution of $\langle\tilde{\gamma}\rangle$ is best observed as a space-time graph in which the shear strain rate along a horizontal strip in front of the plate (dashed line in middle right box, Fig. 3.12a) is evolved in time. Space-time plots of $\langle\tilde{\gamma}\rangle$ in figure 3.13 illustrate the unsteady nature of the shear band at $\Delta\phi < 0$ while for $\Delta\phi > 0$ the stability onset (white arrows) and subsequent spatial localization are observed. For quantitative comparison of the magnitude of $\langle\tilde{\gamma}\rangle$ in the flowing region we plot shear strain rate profiles in front of the plate (Fig. 3.12b) evaluated after 0.8 cm of drag (white dashed line in Fig. 3.12a). Similar evolution of the shear strain rate during shear band formation of a dilating GM has been observed in MD simulation of a tri-axial test [59].

To characterize the shear band dynamics we measured the local angle of the shear band

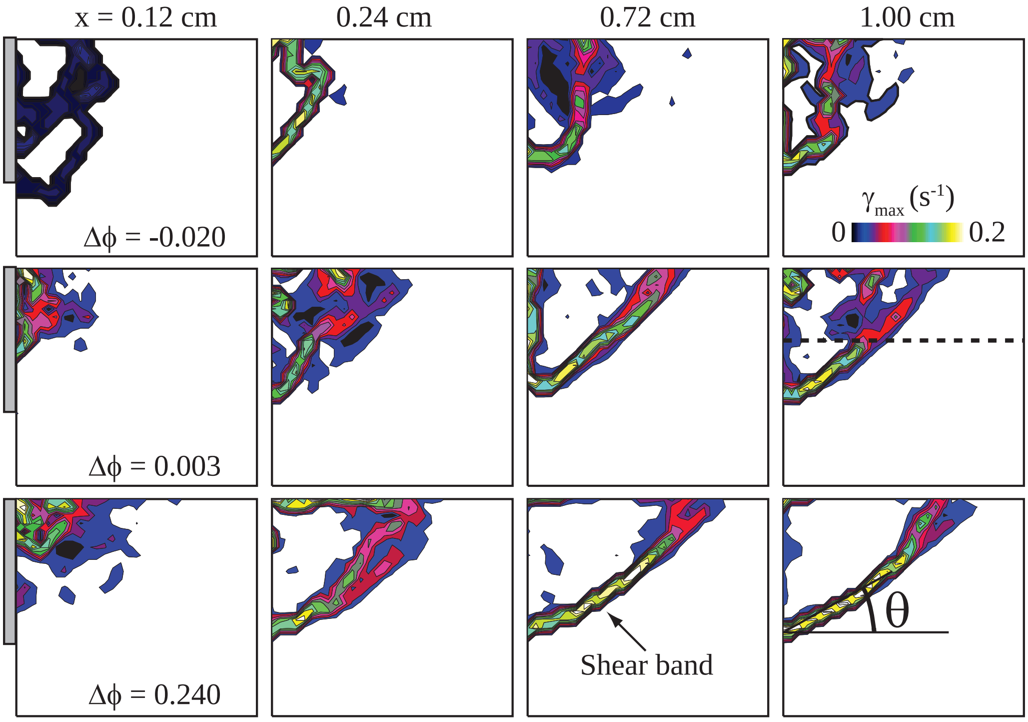

**Figure 3.12:** Maximal shear strain rate fields for three preparations (separated vertically) at four instances of displacement (horizontal). Box dimensions are 9.74×9.74 cm. Gray bar on left side of $x = 0.12$ cm fields shows plate location which is advancing to the right. Stable shear band highlighted for $\Delta\phi = 0.240$ at $x = 0.72$ cm. Shear band is oriented at angle $\theta$ from the horizontal.

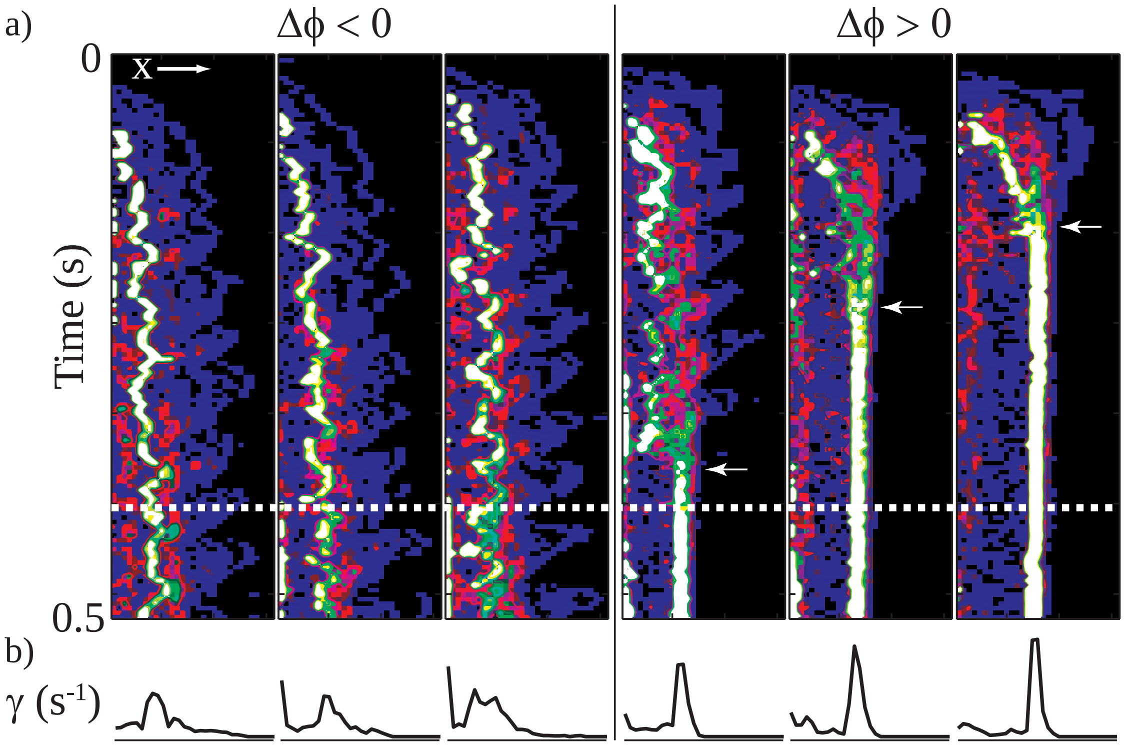

**Figure 3.13:** Spatiotemporal evolution of $\gamma_{max}$. a) Space-time plot of $\gamma_{max}$ at six initial $\Delta\phi$ (increasing from left to right). $\gamma_{max}$ is evaluated at the dashed line in middle right plot in Fig. 10. White arrows in right three plots show onset of shear band stability. b) Profile of $\gamma_{max}$ after $x = 0.8$ cm drag distance. All curves at same scale.

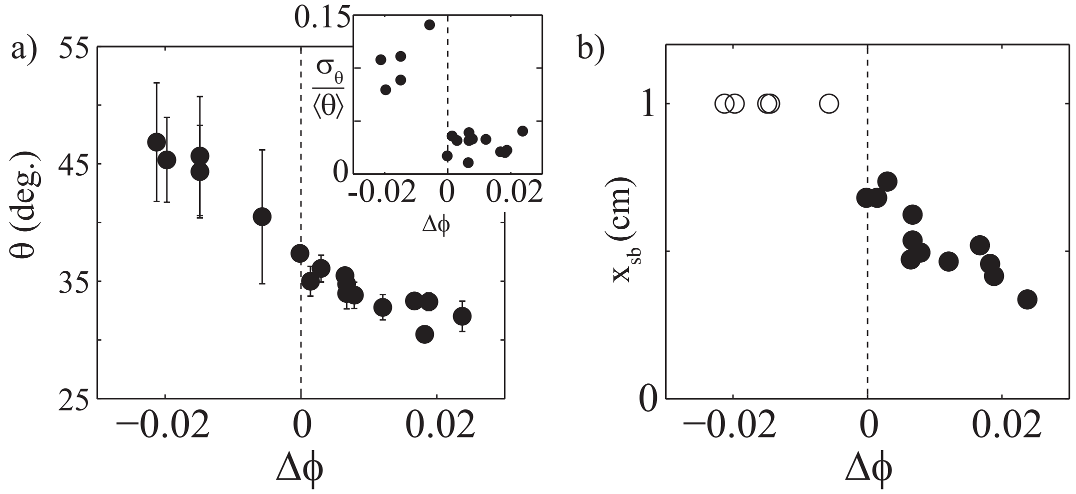

**Figure 3.14:** Shear band statistics. a) Average angle of shear band, $\theta$, over last 0.36 cm of drag as a function of $\Delta\phi$. Error bars are $\pm\sigma_\theta$ taken over last 0.36 cm of drag. Inset shows normalized fluctuation in $\theta$ over last 0.36 cm of drag as a function of $\Delta\phi$. b) Drag distance at onset of stable shear band. Open circles indicate unstable shear band at end of 1 cm displacement.

near the plate bottom, $\theta$, and the plate displacement required before the onset of shear band stability (White arrows in Fig. 3.13). The shear band angle $\theta$ (measured with respect to the horizontal) averaged over the last 0.36 cm of drag decreased roughly linearly with increasing $\Delta\phi$ (Fig. 3.14a). Furthermore as can be seen by the errorbars on $\theta$, and the inset, the temporal fluctuations in $\theta$ reduced by more than two-fold across $\phi_c$. This is another indication of shear band stability across the dilation transition.

We did not observe the formation of stable shear bands in the loose packed granular media (Open symbols, Fig. 3.14b). While in the close packed granular media we observed that the drag distance before the onset of shear band stability decreased with increasing $\Delta\phi$. This is likely due to the dilation process that weakens the sheared region and allows for the formation of the stable shear band. Likely a certain threshold of dilation must be developed before the formation of the shear band and thus as initial $\phi$ is prepared further above $\phi_c$ more dilation will occur resulting in a more rapid formation of the shear band.

The observations of the correlated maxima in force and flow during yield for $\Delta\phi > 0$ indicate that onset of granular flow in densely packed media induces a large region of shear in the bulk which because of the dilatant nature of the close packed material results in rapid failure along a shear band. In loosely packed granular flows however $F_D$ slowly increases as the material strengthens under the induced shear. This transition from hardening to weakening is well understood in the context of critical state soil mechanics [53] however to our knowledge no systematic variation of strength has been previously performed.

## *3.8 Laser speckle measurements of fast fluctuations*

We lastly look to the solid-fluid nature of the granular media near the flowing region as a function of initial $\phi$. With a CCD camera pointed towards the granular surface, we image the reflected pattern of light from a laser (spot size $\approx$3 mm) illuminating the surface 12 cm ahead of the plate's initial position. The image, called a speckle pattern [162], is the result of photon scattering in the granular media and thus small changes in grain position near the laser spot are recorded as changes in the speckle field pattern.

To characterize the solid-fluid nature of the granular media we examine the drag force and speckle pattern during 1 cm plate drag. We find that the force and speckle pattern dynamics are consistent with what he have previously observed. At loose pack $F_D$ monotonically increases and the speckle field shows an unjamming event near 0.3 cm drag followed by constant speckle fluctuation (Left side, Fig. 3.15a,b). For higher initial $\phi$ however $F_D$ exhibits a maxima and the speckle pattern identifies both a jamming and unjamming event associated with the force rise and drop in $F_D$.

The constant fluctuations in the speckle pattern that occur at loose pack indicate the granular material is constantly in a state of rearrangement. The speckle field identifies that small scale motion of the grains occurs in loose packed media even at distances far ahead of the plate where no noticeable surface motion can be viewed by eye. In closely packed material however, the jamming event that we observe associated with the force drop in $F_D$ is a result of the formation of a stable shear band. When the shear bands shown in Fig. 3.12 form, the laser spot is far enough ahead of the plate such that it is outside this flowing region. Thus the laser speckle measurement indicates that once the shear band is formed all flow outside of the wedge region ceases and the flow is totally isolated to within the plate-shear band region.

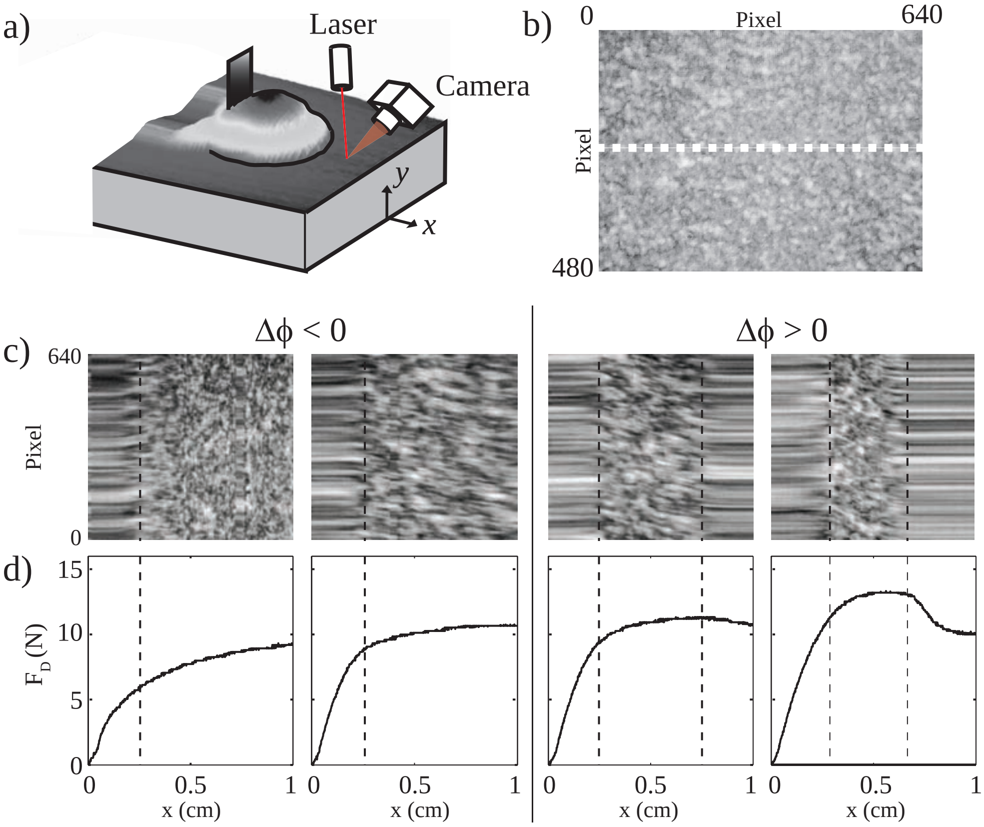

**Figure 3.15:** Laser speckle measurement of granular surface flow. a) A laser illuminates the granular surface 12 cm ahead of the plate's initial position. b) Sample image from the camera. We study the temporal evolution of the pattern along the horizontal line. c) Time evolution of the speckle pattern at four different initial $\Delta\phi$ (increasing from left to right). Dashed lines show jamming and unjamming of granular media during drag. d) $F_D$ versus displacement during speckle measurement. Dashed lines show $F_D$ during jamming/unjamming.

## *3.9 Conclusion*

In conclusion we have investigated the force and flow response of a granular material as a function of initial volume fraction $\phi$. As in a previous experiment [54] we identified the volume fraction corresponding to the onset of dilation under shear, $\phi_c$, and show that the dynamics of force and flow qualitatively and quantitatively differ across this transition. Our experiment highlight a number of nontrivial phenomena associated with granular drag.

We emphasize that the word "critical" in critical state soil mechanics was not originally meant to reflect any sense of criticality in the language of phase transitions. However several papers have suggested that the critical state of soil mechanics may be in fact be a self-organized critical state [163, 6]. Recent granular simulations of sheared granular media have shown that after the system is allowed to reach a non-equilibrium steady state it exhibits shear avalanches which have power-law distributions [164]. Thus it may be that $\phi$ is an important parameter in investigating SOC behavior in granular materials.

Lastly we wish to discuss the transition at $\phi_c$. It is currently not known what parameters $\phi_c$ depends upon in experiment. However a recent discrete element method simulation has shown that the value of $\phi_c$ is sensitive to the inter-grain friction ($\mu$) with $\phi_c \to 0.64$ as $\mu \to 0$ [59]. The approach of $\phi_c$ to the random close pack limit suggests a possible connection between jamming (which occurs at $\phi_{rcp}$ for frictionless grains). Furthermore recent experiments have highlighted the role of shear in the jamming process and suggest that the dilation transition and jamming may be related [165].

# CHAPTER IV

# STEADY-STATE DRAG

## *4.1 Summary*

We use plate drag to study the response of granular media to localized forcing as a function of volume fraction, $\phi$. A bifurcation in the force and flow occurs at the onset of dilatancy, $\phi_c$. Below $\phi_c$ rapid fluctuations in the drag force, $F_D$, are observed. Above $\phi_c$ fluctuations in $F_D$ are periodic and increase with $\phi$. Velocity field measurements indicate that the bifurcation in $F_D$ results from the formation of stable shear bands above $\phi_c$ which are created and destroyed periodically during drag. A friction-based model captures the dynamics for $\phi > \phi_c$.[*]

## *4.2 Introduction*

Granular materials fascinate because they can act like both fluids and solids [2]. Recent work has focused on the static problem of mechanical rigidity (jamming) in which the packing density $\phi$ (the ratio of solid to occupied volume [3]) is increased until grains crowd sufficiently to develop a finite yield stress [166]. Less work has explored the related process of "unjamming" [144, 167, 145, 168] where initially jammed granular ensembles flow in response to forcing and where the initial packing density plays an important role: varying $\phi$ changes the local packing structure of grains which in turn affects the flow and force dynamics of the material response.

We are interested in granular media subject to localized forcing (for instance from limbs [141, 142, 74]). In general, granular systems sheared at the boundaries evolve to a steady-state $\phi_c$ [53]: depending on initial $\phi$, the medium compacts ($\phi < \phi_c$) or dilates ($\phi > \phi_c$) as $\phi \to \phi_c$. In contrast, localized forcing, realized by an intruder translating through an initially homogeneous medium [144, 167, 145, 71] and viewed in the reference frame of the

---

[*] The following chapter was published in *Physical Review Letters* in 2010 under the title "Force and flow transition in plowed granular media"

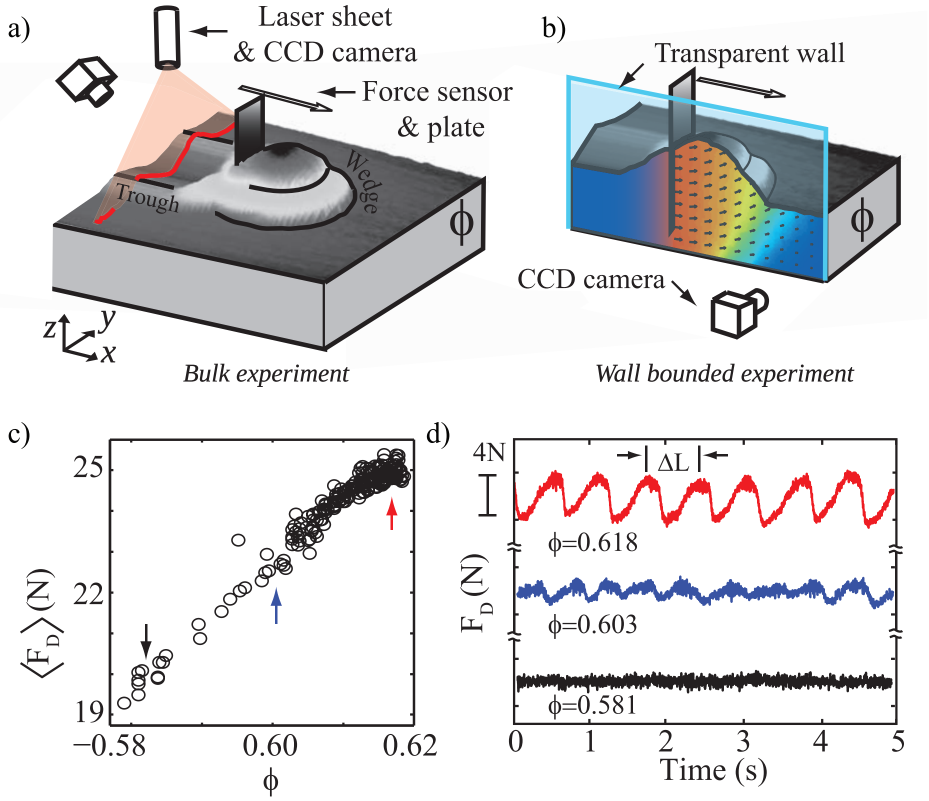

**Figure 4.1:** Experimental overview: (a) drag force, surface deformation and (b) velocity fields are measured as a function of prepared volume fraction, $\phi$. (c) Mean drag force increases linearly with $\phi$ while (d) temporal fluctuations in $F_D$ become periodic as $\phi$ is increased (arbitrary vertical shift).

intruder, drives material only in the vicinity of the intruder toward $\phi_c$ while simultaneously advecting undisturbed media into the flowing region. The result is the repeated unjamming of "fresh" material and the possibility of complex spatio-temporal dynamics in and around the zone of disturbed material surrounding the intruder.

Here we drag a flat plate through initially homogeneous granular media at prepared $\phi$ to continuously drive the system away from $\phi_c$ and measure the resulting force and flow fields. As $\phi$ increases, the onset of shear dilatancy at $\phi_c$ drives a bifurcation in force dynamics and media flow. This bifurcation is governed by a complex spatiotemporal flow response associated with the stability (instability) of shear bands nucleated by the plow above (below) $\phi_c$ and their evolution in response to plow motion. A model of shear band dynamics captures the oscillatory behavior above $\phi_c$ and suggests complex dynamics below $\phi_c$.

## *4.3 Methods*

Drag measurements, see Fig. 4.1(a,b), were performed in a $27\times86\times13\,\mathrm{cm}^3$ bed of polydisperse $256\pm44\,\mu$m glass beads (Potters Industries; density $\rho = 2.51\ \mathrm{g\,cm^{-3}}$). Similar effects to those described here were observed in other granular materials (See section 4.9), including heterogeneous beach sand and poppy seeds. Air flow through the porous floor initially fluidized the medium and then a combination of air flow (below fluidization) and mechanical vibration generated the desired initial volume fraction ($0.579< \phi <0.619$). Air flow was turned off prior to testing and volume fraction determined from bed height images as $\phi = M/\rho A h$, where $M$, $A$ and $h$ are the bed mass, area and height respectively. A stepper motor and linear translation stage displaced a 3.9 cm wide by 0.3 cm thick steel plate submerged to a variable fixed depth $7.5 < d < 9.5\,\mathrm{cm}$ over a distance of 50 cm at a constant speed of $v = 4\,\mathrm{cm\,s^{-1}}$. An optical encoder recorded the position and a 3-axis ATI load cell mounted between plate and translation stage measured the drag forces (sampled at 200 Hz). Using laser line profilometry, we recorded the resultant surface profile and used it to quantify the change in vertical cross sectional area, $\Delta A$, normalizing by the submerged area of the plow, $A_P = \text{width} \times \text{depth}$. Profiles were measured 35 cm from the start of drag where the profile was in a steady state. In separate drag experiments a flat plate at depth $5.5 < d < 6.5$ cm was positioned against a transparent wall and displaced at $v = 2\,\mathrm{cm\,s^{-1}}$ parallel to the wall to image grain flow. High speed video (250 fps) of the flow was recorded and analyzed in Matlab using image registration with a correlation time step of 0.02 s [169]. The near-wall setup exhibited similar force fluctuations as the bulk but with approximately half the mean force. We remove two systematic variations in the force — a slow increase in the baseline force during drag ($\approx 5\%$ of the mean) and the decrease in depth of the constant height intruder with increasing $\phi$— by defining the drag force, $F_D$, as the raw drag with slow drift removed (3rd order polynomial fit subtracted while preserving the mean) multiplied by a depth correction factor $(\frac{d_{LP}}{d})^2$ normalized to the loose pack depth $d_{LP}$. Separate measurements at controlled intruder depth support this normalization technique.

## *4.4 Force bifurcation*

The mean drag force increases approximately linearly with $\phi$ as expected due to increased bed density and average coordination number, see Fig. 4.1(c). A bifurcation, however, occurs in the force fluctuations: $F_D$ at lower $\phi$ exhibits small amplitude, fast, and $\phi$ independent fluctuations, while at higher $\phi$, slower, periodic, and larger amplitude oscillations in $F_D$ occur which grow in duration and magnitude as $\phi$ is increased, [Fig. 4.1(d)].

We characterize the bifurcation by measuring the standard deviation of force, $\sigma_{F_D}$, and the average plow displacement between positive slope zero crossings of the force, $\Delta L$, as a function of initial $\phi$. As $\phi$ increases we observe a sharp bifurcation in $\sigma_{F_D}$ and $\Delta L$ [Fig. 4.2(a)] at the compaction/dilation transition (i.e. $\Delta A/A_P = 0$ at $\phi_c = 0.603 \pm 0.003$), see Fig. 4.2(b). As the bifurcation is approached from below, $\sigma_{F_D}$ is small and constant; above $\phi_c$ and with increasing $\phi$, $\sigma_F$ grows linearly while $\Delta L$ increases nearly linearly For $\phi > \phi_c$, $\Delta L$ is independent of plow speed ($2 < v < 8$ cm/s), see Fig. 4.2(a) inset, revealing it as a characteristic spatial scale and implying that the temporal dynamics of $F_D$ result from granular flow mechanisms that change with $\phi$ across the dilation transition.

## *4.5 Flow bifurcation*

Direct evidence of a bifurcation in the flow is revealed by observations of the displacement of material at the surface near the plow [Fig. 4.3(a)]. Below $\phi_c$ surface deformation is smooth, and the boundary between upwardly moving grains and the undisturbed surface advances uniformly at a fixed distance ahead of the plow. At and above $\phi_c$, however, the surface flow takes the form of periodic radial upwellings of grains which give the region around the plow a stepped appearance. The generation of surface ripples is correlated with fluctuations in $F_D$ and indicates that the bifurcation in $\sigma_{F_D}$ and $\Delta L$ results from a change in grain flow dynamics.

To gain insight into the nature of the bifurcation we compare the grain velocity field at low and high $\phi$ in a vertical plane perpendicular to the displacement of the plow, see Fig. 4.3(b) and 4.9. In both cases, flow is largely confined to a wedge-shaped region with angle $\theta$ in which grains move forward and upward in advance of the plow. At both $\phi$'s a

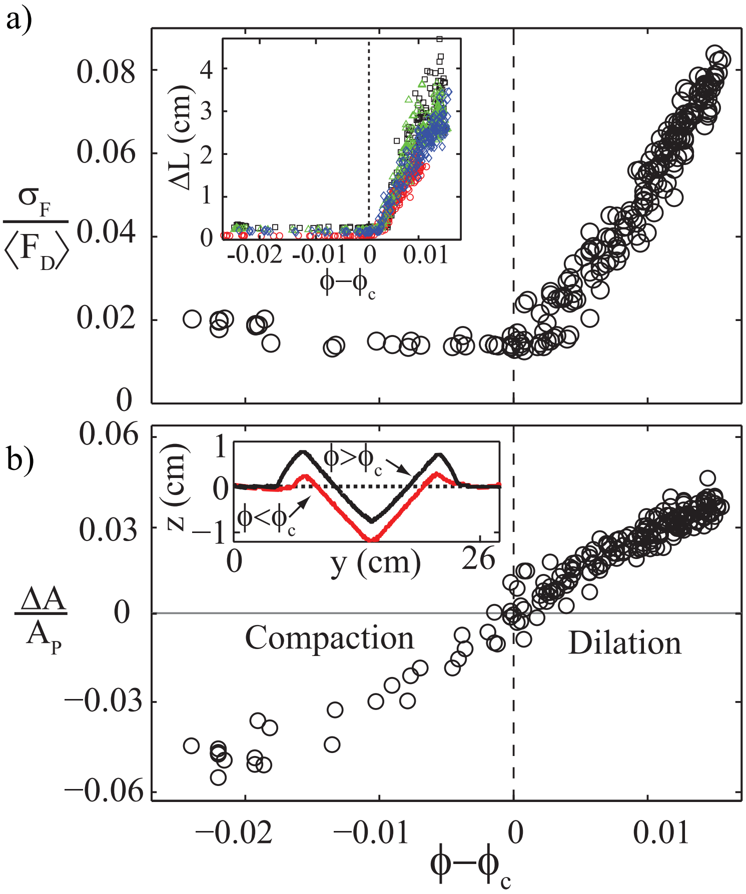

**Figure 4.2:** Bifurcation in force occurs at the onset of dilation $\phi_c = 0.603 \pm 0.003$. Small and nearly constant for low $\phi$, (a) standard deviation of $F_D$ grows linearly above $\phi_c$ while (inset) force oscillation length scale increases nearly linearly (2, 4, 6, 8 $\text{cm}\,\text{s}^{-1}$ in red circles, blue diamonds, green triangles, and black squares). (b) Compacting and dilating response of plowed granular packings vs. initial $\phi$. (Inset) Trough cross sections at high (black) and low (red) $\phi$.

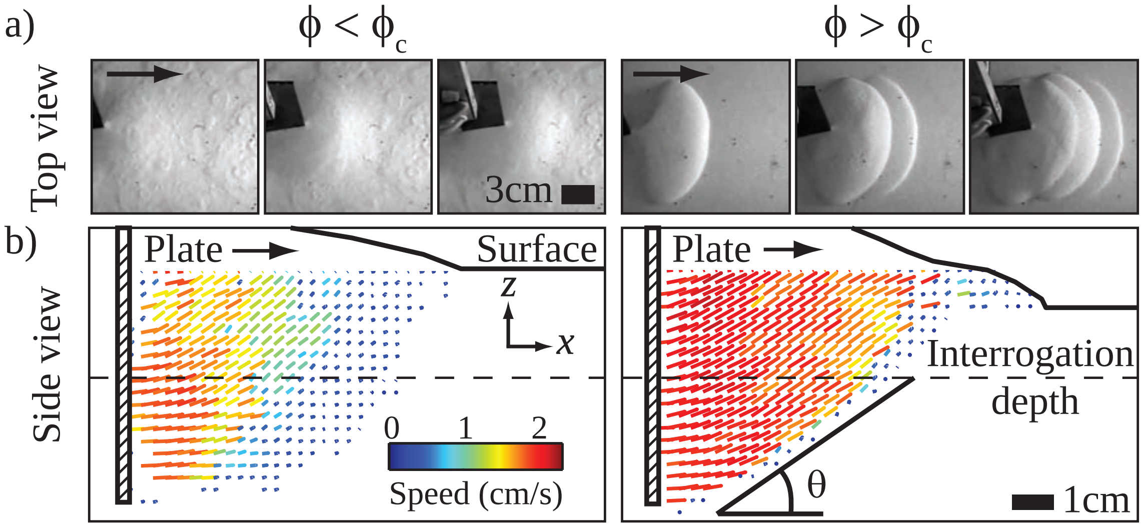

**Figure 4.3:** Surface flow and velocity fields differ below $\phi_c$ (left) and above $\phi_c$ (right). (a) Surface deformation from a submerged plate shows step like features above $\phi_c$. (b) Snapshots showing differences in velocity field structure from transparent wall experiments [Fig. 1(b)]

shear band separates the flowing wedge of grains and the effectively solidified grains outside the wedge; the lower end of the shear band terminates at the bottom of the plate while the upper end reaches the surface.

## *4.6 Temporal flow dynamics*

Despite these common features, differences in spatiotemporal evolution exist between flows at low and high $\phi$. At low $\phi$, flow is intermittent [Fig. 4.4(a)]: the horizontal extent of the flowing region, $\eta$, (measured at approximately half the intruder depth, 3.2 cm) rapidly advances and retreats as the plow moves into new material. At high $\phi$, the spatiotemporal evolution of the flowing region is periodic with $\eta$ remaining fixed for long periods of time until rapid, repeated fluctuations precede a jump forward to a new location. We quantify the pinning of this flow boundary as the fraction of time $\eta$ remains stationary ($\frac{d\eta}{dt} = 0$) during the entire drag. As $\phi$ increases $\eta$ becomes increasingly stationary indicating that the spatial shear regions are more stable. Above $\phi \approx \phi_c$, the shear band remains stationary for more than 50% of the drag duration.

Shear zone localization can be understood by the process of granular shear weakening/strengthening. Below $\phi_c$ material compacts and strengthens under shear, continually frustrating the development of fixed shear zones and forcing shear to occur along a constantly changing set of failure surfaces. Above $\phi_c$ however, material dilates and weakens under shear, causing flow to localize along a fixed plane. In a plowed system, shear localization for initial $\phi > \phi_c$ holds only shortly after shear band formation: as the plow advances into undisturbed material the localized band is forced to adjust. Using the average angle of the flow boundary, $\theta$, to characterize the orientation of the shear zone [see Fig. 4.3(b)], we find that below $\phi_c$ force and flow are largely uncorrelated while above $\phi_c$, $\theta$ and $F_D$ are strongly correlated with $F_D$ and $\theta$ increasing in concert, see examples in Fig. 4.5(a).

## 4.7 Wedge flow model

We develop a simple model based on the correlation of $F_D$ and $\theta$ to gain insight into the dependence of $F_D$ on the flow state and $\phi$. As the bottom of the shear zone is pinned to the lowest point of the plow, the flowing region is taken to be a triangular wedge of mass $m = \frac{\rho W d^2}{2 \tan\theta}$ sliding up a plane inclined at angle $\theta$. Kinetic friction between the wedge and plane, $\mu(\phi)$, is assumed to increase with $\phi$. Balancing the forces from the plow (assumed horizontal), gravity, and sliding friction, the model predicts the plowing force $F(\theta, \mu) = \frac{\rho W d^2}{2} \frac{1+\mu/\tan\theta}{1-\mu\tan\theta}$, where $W$ is the plow width [Fig. 4.5(c)]. The plowing force diverges at $\theta = 0$ (infinite block) and $\theta = \tan^{-1}\left(\mu^{-1}\right)$ and is minimum at $\theta_{min} = \tan^{-1}\left(\sqrt{\mu^2+1)} - \mu\right)$. $\theta_{min}$ decreases and $F(\theta_{min})$ increases with increasing $\mu(\phi)$.

The model predicts that an initially jammed and homogeneous material with volume fraction $\phi_0$ shears at an angle $\theta_{min}$ when the force reaches $F_{min}(\mu)$, see Fig. 4.5(b,c). For $\phi_0 > \phi_c$, shearing along the slip plane dilates and weakens the material locally, causing $\mu(\phi_0)$ to decrease to $\mu(\phi_c)$ which reduces $F_D$ and slightly increases $\theta$, see path A in Fig. 4.5(c). As the plow advances the angle of the weakened shear zone gradually increases along $F[\theta, \mu(\phi_c)]$, indicated by path B. The shear band remains fixed at the surface (causing $\theta$ to increase) instead of advancing with a constant angle because, evidently, less high $\phi$ material needs to be broken in the former case. With increasing $\theta$, the force to push the wedge $\theta_{max}$ eventually equals the force required to break the stronger material at $\phi_0 > \phi_c$, i.e. $F[\theta_{max}, \mu(\phi_c)] = F[\theta_{min}, \mu(\phi_0)]$. At this point a new shear zone forms in front of the plow, decreasing $\theta$ to

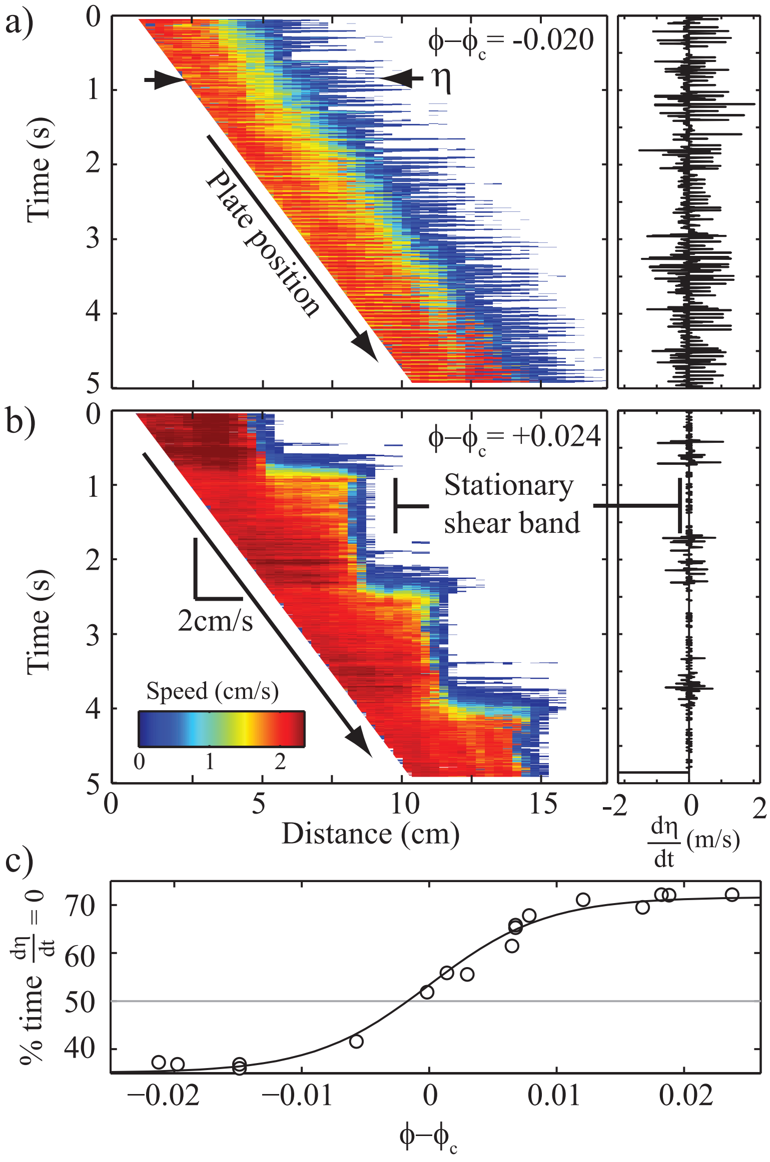

**Figure 4.4:** Temporal evolution of flow differs below and above $\phi_c$. (left) Space-time plots of flow speed along a constant depth horizontal strip show that the leading edge of the flow, $\eta$, (a) fluctuates in loose pack and (b) is stationary between shear band formation events (four shown) in close pack. (right) Time series of $\frac{d\eta}{dt}$ highlight changes in stability. (c) Percentage of time during 5 s drag that the flowing region is stationary ($\frac{d\eta}{dt} = 0$) increases with $\phi$ and is fit to $\left[1 + e^{-(\phi-\phi_c)}\right]^{-1}$.

$\theta_{min}(\phi_0)$ and the cycle repeats (path C).

The dynamics of the experimental data for $\phi > \phi_c$ are captured by the model as seen in $(\theta, F(\theta))$ space [Fig. 4.5(e)] and 4.9. Here the system evolves between two curves [$\mu = 0.65$ (blue) and $\mu = 0.78$ (red)] and the transitions between these states qualitatively match the predictions of our model. The model predicts the increase in force fluctuations with increasing $\phi$ above $\phi_c$. However for $\phi < \phi_c$ the evolution of $F_D$ with $\theta$ is more complicated because of the lack of stability of the sheared regions through shear strengthening. As we assume a feedback process exists between the flow dynamics and $F_D$, strengthening of the material during shear results in the relocation of the shear band to a weaker region in the surrounding bulk. With the continuous advection of undisturbed weaker material and the heterogeneity in $\phi$ in the previously sheared region, predicting the shear process below $\phi_c$ is more challenging.

## *4.8 Conclusion*

In summary we observe a flow and force bifurcation in localized granular drag which occurs at the onset of dilatancy. Localized forcing in granular media induces a heterogeneous $\phi$ distribution in the region of flow and represents a new way to test theories of granular flow [170, 61]. Previous studies of drag in granular media [71] were performed at slow speed to observe stick-slip fluctuations over distances on the order of a grain diameter; the effects of varying initial $\phi$ were not investigated. Our observations of a bifurcation in $\phi$ support the findings of Schröter et al. [154] who reported a transition in dynamics at $\phi = 0.598$, and our measured $\phi_c$ is similar to that reported ($\phi_c = 0.591$) in recent impact experiments [45]. It is known that $\phi_c$ is a function of the applied stresses and cohesive/frictional interactions between the grains [59, 53] so we do not place importance on the specific value here.

## *4.9 Appendix*

Here we show follow up experiments and supplementary information.

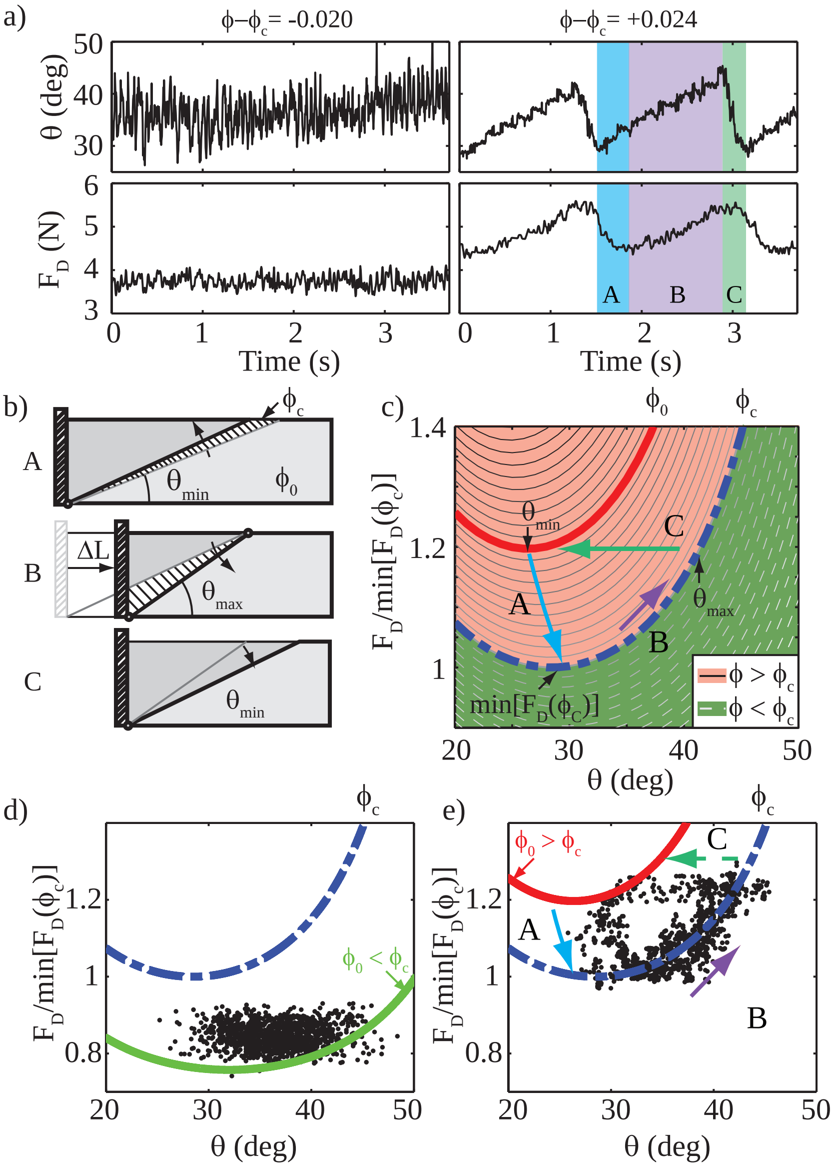

**Figure 4.5:** Force dynamics and wedge model of granular flow. (a) Wedge flow angle $\theta$ and $F_D$ are correlated above $\phi_c$. (b) Sketch of wedge flow model dynamics above $\phi_c$ with arrows indicating motion of shear band for the three phases A,B,C also shown in (a,c,e). (c) Dynamics predicted by model (arrows) showing family of $(\theta, F_D)$ curves for varying $\mu(\phi)$ and transitions between $\mu(\phi)$ curves corresponding to $\phi_0$ (solid red curve) and $\phi_c$ (dash-dot blue curve), see text. Comparison of model $(\theta, F_D)$ curves and experiment: (d) for $\phi < \phi_c$ experimental data are bounded by model curves of arbitrary $\mu < \mu(\phi_c)$; (e) for $\phi > \phi_c$ model shows good agreement with experiment.

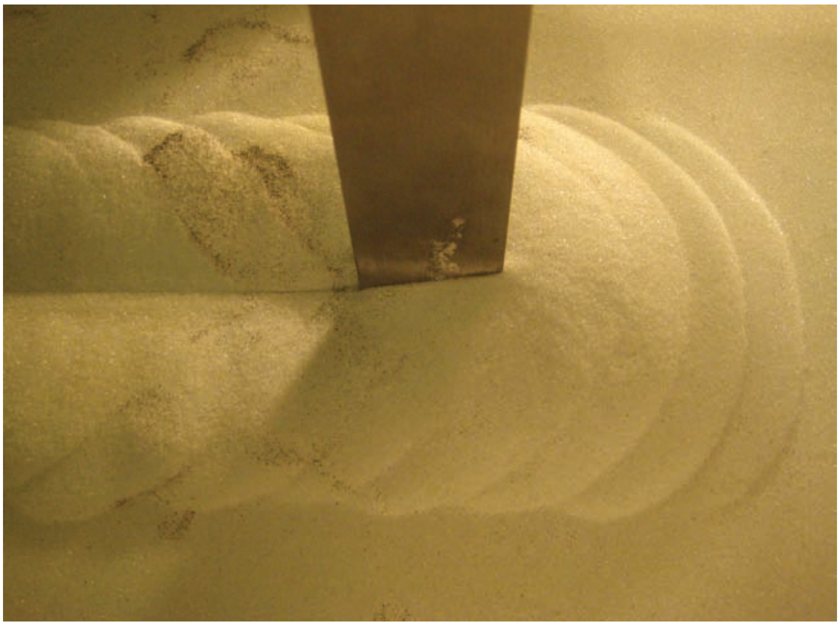

**Figure 4.6:** Shear band ripples on the surface induced from drag of an immersed plate.

### 4.9.1 Shear band ripples at the surface

In figure 4.6 we show the surface features formed from the periodic initiation of shear bands during grad at high $\phi_0$. The intruder is a flat horizontal plate submerged to a depth of depth 7 cm, with width 5 cm and height 1 cm. The submerged intruder minimally disturbs the surface granular material and allows for better observation of the shear band structures at the surface.

### 4.9.2 Force and flow bifurcation in vertical penetration

In previous experiments by Chen Li from this lab he observed similar force fluctuations in a vertical penetration experiment (Fig. 4.7). As $\phi$ was increased above $\phi_c = 0.605$ force fluctuations grow in amplitude with increasing $\phi$. This experiment was recently performed by Tapia et al. [171] in which they penetrate a rigid penetrometer vertically into a hele-shaw cell filled with brass beads (diameter$\approx$50 $\mu$m) at prepared $\phi$. The researchers find that force fluctuations grow above a critical $\phi$ and that the dynamics of these fluctuations are described by a wedge-flow model similar to the one we presented in section 4.7.

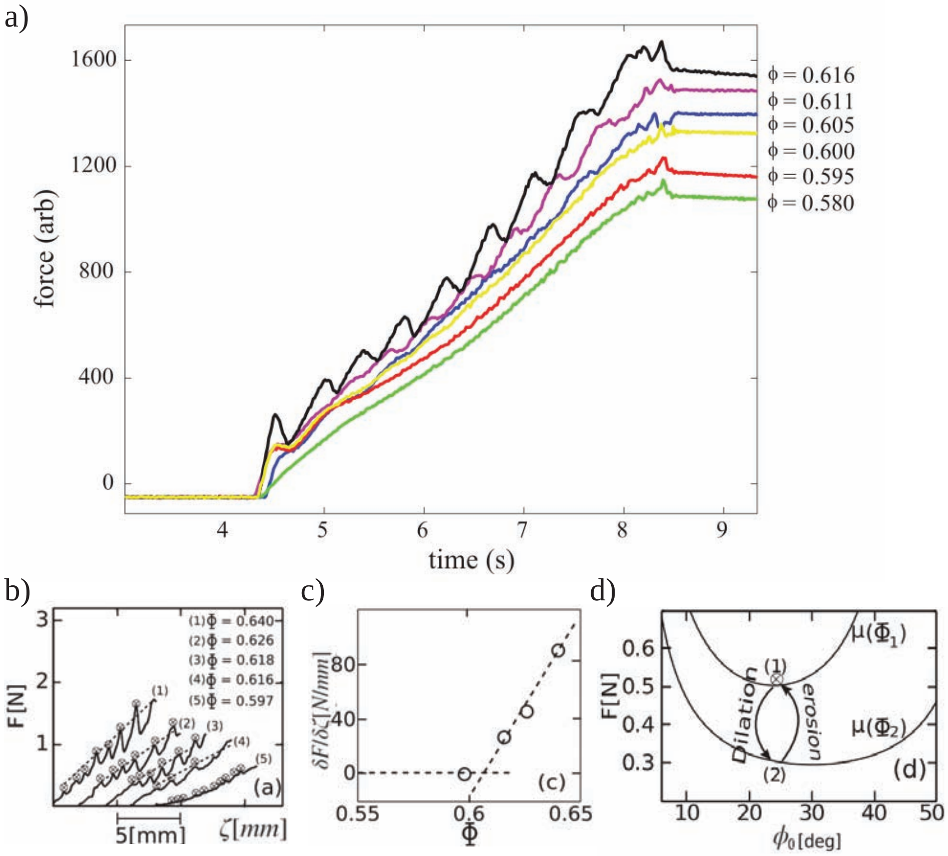

**Figure 4.7:** Force fluctuations in vertical penetration experiment. a) Data from Chen Li in the Goldman lab at Georgia Tech. Force fluctuations appear at $\phi > 0.605$ and increase in amplitude with increasing $\phi$. b-c) Results from [171] showing force fluctuations in vertical penetration (b). c) Magnitude of force fluctuations versus $\phi$ showing bifurcation. d) Model for force fluctuations similar to that of figure 4.5(e).

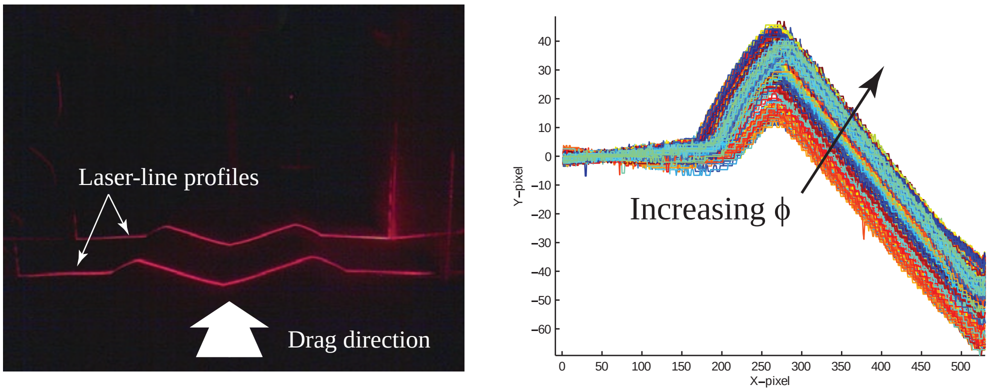

**Figure 4.8:** Laser-line profile measurements of the granular surface left after drag. a) Image of two laser lines. b) Digitized height profiles at various initial $\phi$ plotted in terms of (x,y) pixel locations in the camera image.

### 4.9.3 Surface profile measurement

We measured the surface profile of the granular material using a laser profilometry system. Two laser lines were placed such that the laser plane was vertical and perpendicular to the direction of motion of the plate (Fig. 4.8). A camera was placed behind the initial location of the drag plate and facing along the direction of drag and oriented at a low angle ($\approx 20°$ below the horizontal) towards the surface. We took images of the surface profile after each drag experiment and digitized the location of the laser lines. Using two additional cameras we captured images of the granular surface height (which varied by $\approx$1.5 cm over the range of $\phi$) to empirically determine the transfer function $y_{pixel} \rightarrow y_{surface}(cm)$.

### 4.9.4 Experiments in heterogeneous granular material

To demonstrate that this bifurcation occurs in heterogeneous granular material we performed drag experiments using natural beach sand collected from Jekyll Island, GA, USA[†]. We found that similar to spherical glass beads with a relatively tight size distribution, we observed a force and flow bifurcation in the Jekyll Island sand (Fig. 4.9). The fluctuations at high $\phi$ were similar to the glass beads in both the temporal force curve and surface flow characteristics. This indicates that the phenomena we have discovered is relatively

---

[†] This material was collected and kindly provided for use in experiments by Nicole Mazouchova

insensitive to the uniformity of the granular material.

### 4.9.5 Depth dependence on bifurcation

In additional experiments we measured the depth dependence of the plate drag bifurcation. We observed the force fluctuations versus prepared $\phi$ at four plate depths, in addition to the plate depth reported above. We find that all plate depths show signatures of the increase in fluctuations at $\phi_c$. As depth decreased to 3.18 cm we observed that the signature of the bifurcation decreased. However this is likely because drag at these depths was at the lower limit of the resolution of our force sensor.

### 4.9.6 Bifurcation insensitivity to air flow

Lastly we report results for experiments in which we applied an upwards flow of air through the granular material during the drag experiment. We prepared granular material into a high $\phi$ initial state using the method described in the previous two sections. Then, prior to initiation of the drag experiment we applied fixed, but variable voltage to the air blower to control air pressure and resultant air flow through the granular material. The influence of an upwards flow of air on drag force was to decrease $\langle F_D \rangle$ because a portion of the granular materials weight is now supported by air pressure. The decrease in effective granular weight due to air flow lowers both the gravitational component and the frictional component of force required to push a wedge up a slope.

In figure 4.11 we show results from air flow experiments at high $\phi$. We find that an increase in air flow is accompanied by a decrease in mean drag force (Fig. 4.11b). Despite the three-fold decrease in mean drag force due to air flow, we find that the $\Delta L$ only decreases by only $\approx$20%. This is consistent with our model that $\Delta L$ is independent of the density of granular material, and instead only $\mu(\phi)$ controls the angles of shear plane formation and thus $\Delta L$. Additionally we find that the peak-peak force fluctuations scale roughly linearly with $\langle F_D \rangle$ consistent with the model predictions.

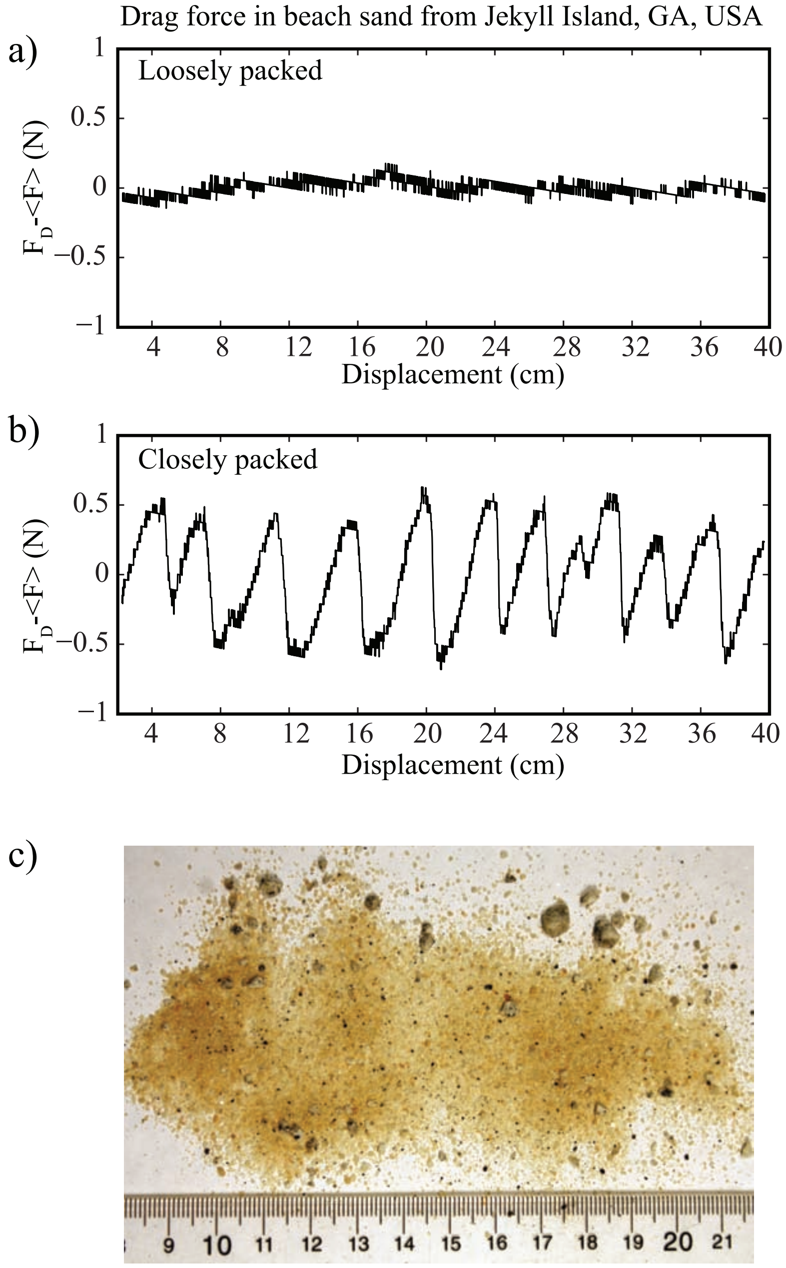

**Figure 4.9:** Drag experiments were repeated in a bed of Jekyll Island (GA) beach sand. a) Loosely packed sand exhibited smooth drag force (FD). b) FD in closely packed sand was oscillatory. The results are consistent with measurements from 250±50 mm diameter glass beads reported in the main text. c) Image of the Jekyll Island beach sand used in experiment.

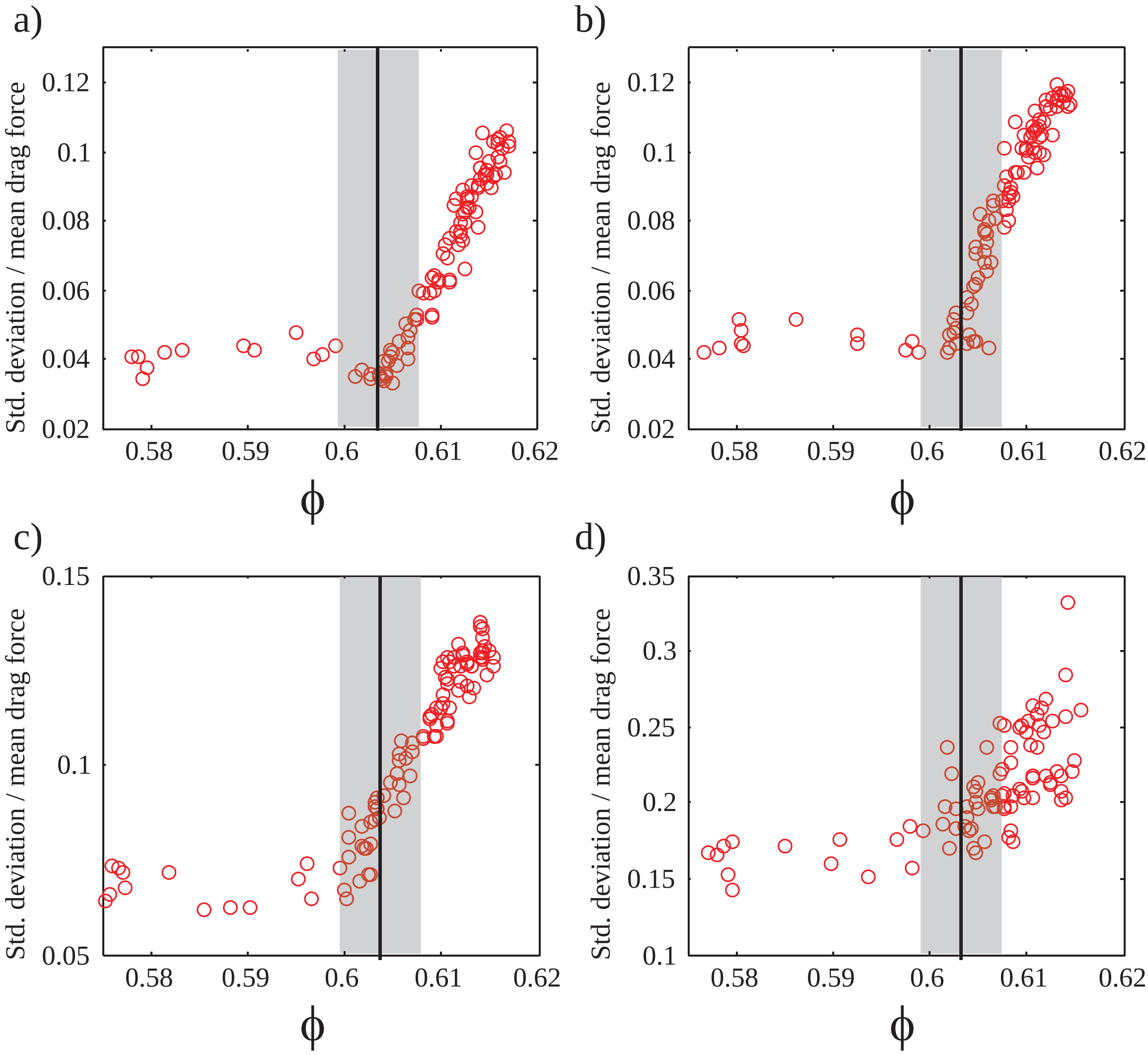

**Figure 4.10:** Depth dependence on bifurcation. Vertical black lines are $\phi_c$ and gray bar indicates uncertainty range. a) Depth = 6.99 cm. b) Depth = 5.72 cm. c) Depth = 4.45 cm. d) Depth = 3.18 cm.

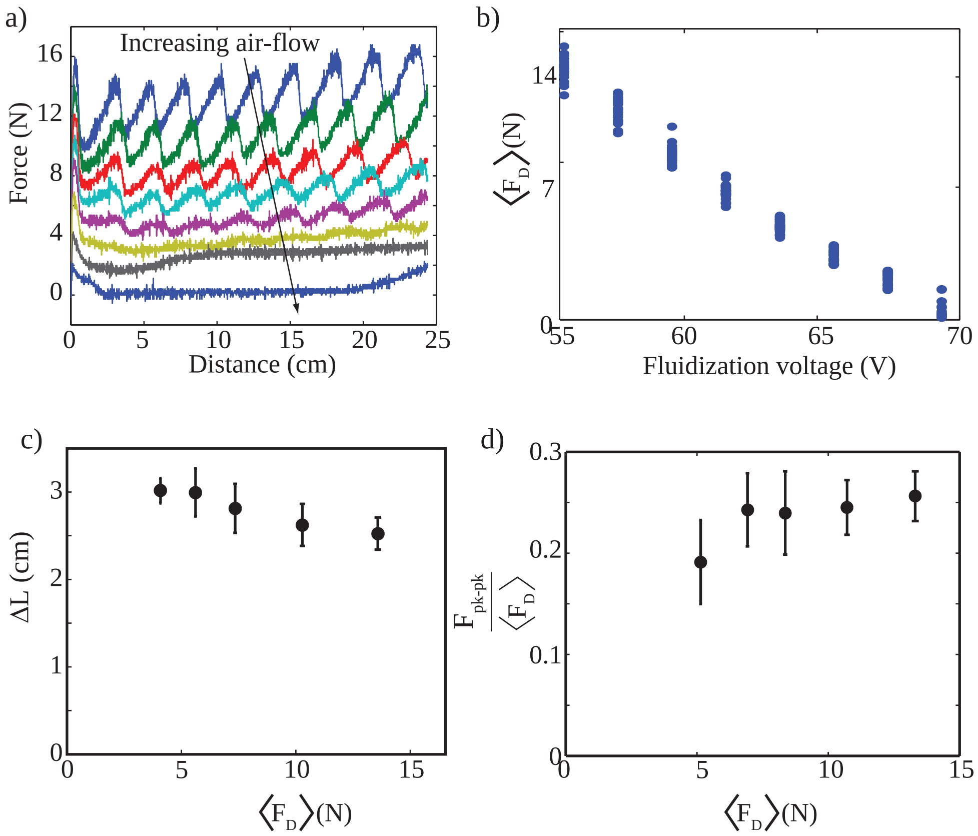

**Figure 4.11:** Effect of upward flow of air through grain pores during drag at high $\phi$. a) Raw force versus displacement plot at close pack with increasing levels of interstitial air flow through the granular material illustrated by the arrow. b) Mean drag force versus voltage of the air blower. c) Stick-slip wavelength versus average drag force. d) Normalized peak-peak force fluctuations versus mean drag force.

# CHAPTER V

# AVALANCHES

## 5.1 Summary

In this chapter we study the failure of granular material as a function of prepared volume fraction, $\phi_0$, under progressive tilting of the granular slope. Gravitational induced failure of a granular slope subjects all grains to an identical perturbation force, in contrast to experiments in which forcing occurs at the boundaries. We slowly rotate a bed of granular material from the horizontal and monitor the grain motion using high speed video. We vary the initial volume fraction to determine how $\phi_0$ influences the failure modes of the granular material. Consistent with our findings in chapters 3& 4, we observe that slope stability depends sensitively on $\phi_0$. Granular material in an initial loosely packed state, $\phi < \phi_c$ undergo intermittent strengthening—in which $\phi$ increases—prior to slope failure. The onset of strengthening occurs at an angle $\theta_0 = 7.7 \pm 1.4°$ for the loosest packing achieved ($\phi 0 = 0.588 \pm 0.013$). The maximum stability angle prior to uniform slope failure for loose packing occurred at $\theta_m = 28.5 \pm 1.0°$. As $\phi$ increased, so did both $\theta_0$ and $\theta_m$. Furthermore as $\phi$ increased $\theta_0$ approached $\theta_m$ suggesting that at high $\phi$ that uniform slope failure immediately follows the first observation of grain motion. In the case of the highest volume fractions ($\phi = 0.627 \pm 0.013$), $\theta_0 = 32.1 \pm 1.5°$ and $\theta_m = 35.9 \pm 0.7°$. We use particle image velocimetry to characterize the granular flow $[v(x, y)_x, v(x, y)_y]$, in the reference frame of the tilted slope. We find that the failure mode at $\theta_0$ differs dependent upon whether $\phi_0$ is above or below the critical state volume fraction $\phi_c$. In the case of $\phi < \phi_c$ the granular material compacts under intermittent failure events as characterized by the $v(x, y)_y$ component of the velocity field. In the case of $\phi > \phi_c$ we find that the the material dilates at initial failure.

## *5.2 Introduction*

The failure and resultant flow of a granular slope illustrates the transition between the solid-like or fluid-like state that granular materials may undergo. The spontaneous failure of a granular slope is an important process to understand for engineers that seek to avoid potentially harmful and destructive avalanches or landslides. Granular slope failure is also of interest for materials scientists because gravity induced failure is a means of global forcing in which all grains experience the same perturbing force. This is an alternative perturbation mode to that of the more commonly studied condition in which stress is applied through a movable boundary condition.

Granular materials are collections of discrete particles which interact through typically repulsive contact forces [1, 2, 3]. The packing efficiency of a granular material, measured by the initial volume fraction, $\phi_0$, may vary from loosely packed to closely packed initial configurations. $\phi_0$ is defined as the ratio of particle volume to occupied volume and for relatively monodisperse particles is typically $0.57 < \phi_0 < 0.64$. The influence of $\phi_0$ on the forces and failure modes of granular material subject to moving boundary conditions have been extensively studied (plane shear [53, 172, 58], tri-axial test [43, 59], localized forcing [54, 154]). Loosely packed granular materials (low $\phi_0$) compact when a shear strain is applied while closely packed granular material (high $\phi_0$) dilate under shear [53]. The intermediate volume fraction at which dilation onset occurs, called the critical state $\phi_c$, is important in determining the mode of failure under boundary imposed forcing [53].

The influence of $\phi_0$ in the evolution and failure of a dry granular slope under progressive loading has not been systematically studied. However, granular avalanches in the lab have been widely studied, largely because of their connection to the self-organized criticality (SOC) phenomena [173, 6]. One popular method to study granular slope failure utilizes a rotating drum to observe the periodic surface avalanches the material undergoes [170, 174] during continuous rotation. Another technique to measure the statistics of avalanche occurrence and size (important of SOC) is to slowly rain granular material atop a granular pile and observe the resultant avalanches that occur [173]. In these experimental setups however observation of $\phi_0$ dependence is only available for the first avalanche, after which the granular material and $\phi$ will evolve.

The progressive loading method, consisting of $\phi_0$ preparation followed by a slow rotation of the granular layer, is a means of observing the evolution and failure of granular material systematically prepared in initial states. The majority of progressive tilt experiments have not controlled $\phi_0$. Progressive loading experiments, all typically performed at a single prepared $\phi_0 \approx 0.60$ (the as poured state), have found that small rearrangements of the granular layer (precursors) precede the eventual surface avalanche onset [175, 176, 177, 178]. A recent study of the precursor events in progressive loading of dry granular material has reported that the intensity of these precursor events differed between two granular preparations, a densely and loosely packed initial state [178], suggesting an importance of $\phi$ on slope dynamics.

$\phi_0$ has been systematically varied in previous progressive tilt avalanche experiments with a granular material immersed in a viscous fluid (a granular suspension) [179, 178, 180]. Results from these experiments are suggestive of what we may expect in dry granular materials, increasing $\phi$ increases the angle of maximum stability. However in the presence of a dense interstitial fluid, the feedback between fluid pore pressure and the granular flow is important and alters the failure from that of the case in dry granular materials. Furthermore the volume fractions realized in suspension experiments are typically much lower than those of dry granular material, and the angle of repose for suspensions much larger.

Here we vary the prepared volume fraction of a granular media in experiment and study the pre- and post-avalanche dynamics. We find that both pre- and post-avalanche behavior is sensitive to $\phi$ and exhibit a change in stability as $\phi$ is increased above the critical state volume fraction, $\phi_c$.

## *5.3 Methods*

### 5.3.1 Rotating fluidized bed

We studied the evolution and failure of granular slopes composed of $256 \pm 44\,\mu$m diameter glass beads. The glass beads had a solid density of $\rho = 2.51$ g cm$^{-3}$. The granular material was contained in an 43 cm long$\times w$ =28 cm wide ($l \times w$) bed and was filled to a height

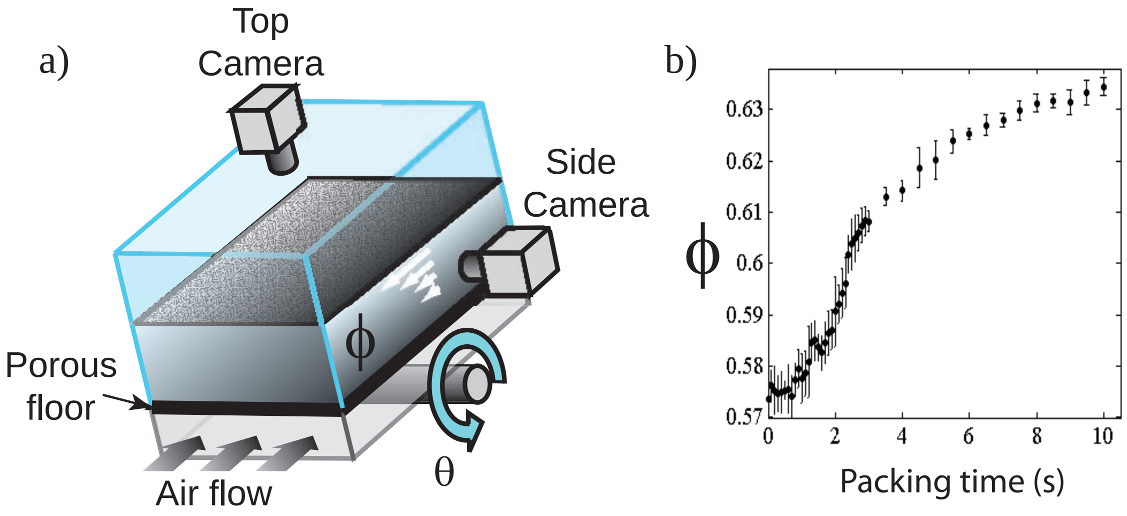

**Figure 5.1:** Experiment setup. a) Air flow through a porous floor in fluidized bed and mechanical vibration prepare granular media to desired initial $\phi$. Bed rotates about midpoint and is imaged from top and side views. b) $\phi$ vs vibration time.

which varied dependent upon $\phi_0$ between $h$ =8.24 - 9.24 cm (≈430 grain diameters). Air flow through a porous floor in the bed fluidized the granular material and a combination of flow and mechanical vibration controlled the volume fraction as a function of vibration duration. The volume fraction is defined as $\phi = \frac{\rho}{Mlwh}$ where $M$ is total grain mass. Through variation of the duration of mechanical vibration the initial $\phi_0$ was varied between $0.58 < \phi_0 < 0.63$ (Fig. 5.1b).

The granular bed rotated about a point 7 cm from one end. Rotation was controlled by a linear actuator (Firgelli motors) mounted below the bed to a rigid base and the bed at a point opposite the end of the rotation point. The instantaneous position of the linear actuator was monitored through a potentiometer in the actuator. Progressive tilting experiments consisted of the bed being rotated at speed $\omega = 2.1°/s$ from initial angle $\theta = 0°$ to a final angle of $\theta = 45°$. We did not observe any change in the avalanche failure upon increasing or decreasing the rotation speed by a factor of two.

Two sets of experiments were performed. In the first set of experiments two cameras recorded the granular motion during bed rotation. One camera mounted above the granular surface recorded surface grain motion at a rate of 30 Hz and resolution of 640×480. A second camera was mounted on the side of the bed and imaged the granular material adjacent to the transparent wall at a rate of 200 Hz and resolution of 640×480. Both cameras were fixed rigidly to the bed and thus rotated with it recording video in the rotated frame of reference. 1528 progressive tilt experiments were performed with this video capture system. In a smaller number of additional experiments (75 progressive tilt experiments) we recorded high-speed video from the side view with a high speed camera at a rate of 1000 Hz, imaging a thin vertical strip of the granular layer in the middle of the bed at resolution of 100×600. We back-lit the granular bed such that the granular surface was easily detected as an edge of high-contrast in the image. In side view we computed the velocity profiles of the granular flow using the technique of particle image velocimetry (PIV) [169].

### 5.3.2 Analysis

To monitor the evolution of the granular slope we tracked the surface profile of the granular layer in the side view as a function of rotation angle. We fit a line to the high-contrast edge of the granular surface to determine the instantaneous slope angle with respect to bed angle, $\theta$. From the linear fit we also determined the height of the bed, $h(t)$, located at the center of the observation range.

$\theta_0$ is defined as the angle of the bed at which we observe the first change in $\phi$, as measured by a change in $h$. The maximum angle of stability, $\theta_m$, is defined as the bed angle at which we observe continuous flow of duration which results in a decrease in slope angle. Lastly we measure the angle at which the avalanche comes to rest at, the angle of repose $\theta_r$. We define an avalanche as the sustained flow of granular material for over 1s in duration.

## *5.4 Effect of $\phi$ on slope stability*

Granular slope response during tilting differed as a function of $\phi_0$. In figure 5.2a we measure the average $\phi$ as a function of tilt angle, $\theta$. At low $\phi$, we observed that the slope underwent several compaction events—precursors—prior to the onset of avalanching flow. These compaction events are observed as the sudden increases in $\phi$ shown in figure 5.2a. During these compaction precursor events the granular material underwent a rapid deformation resulting in the bed height decreasing (increasing $\phi_0$). At large prepared $\phi_0$ we find that the granular slope undergoes a dilation (a decrease in $\phi$) immediately prior to avalanching flow.

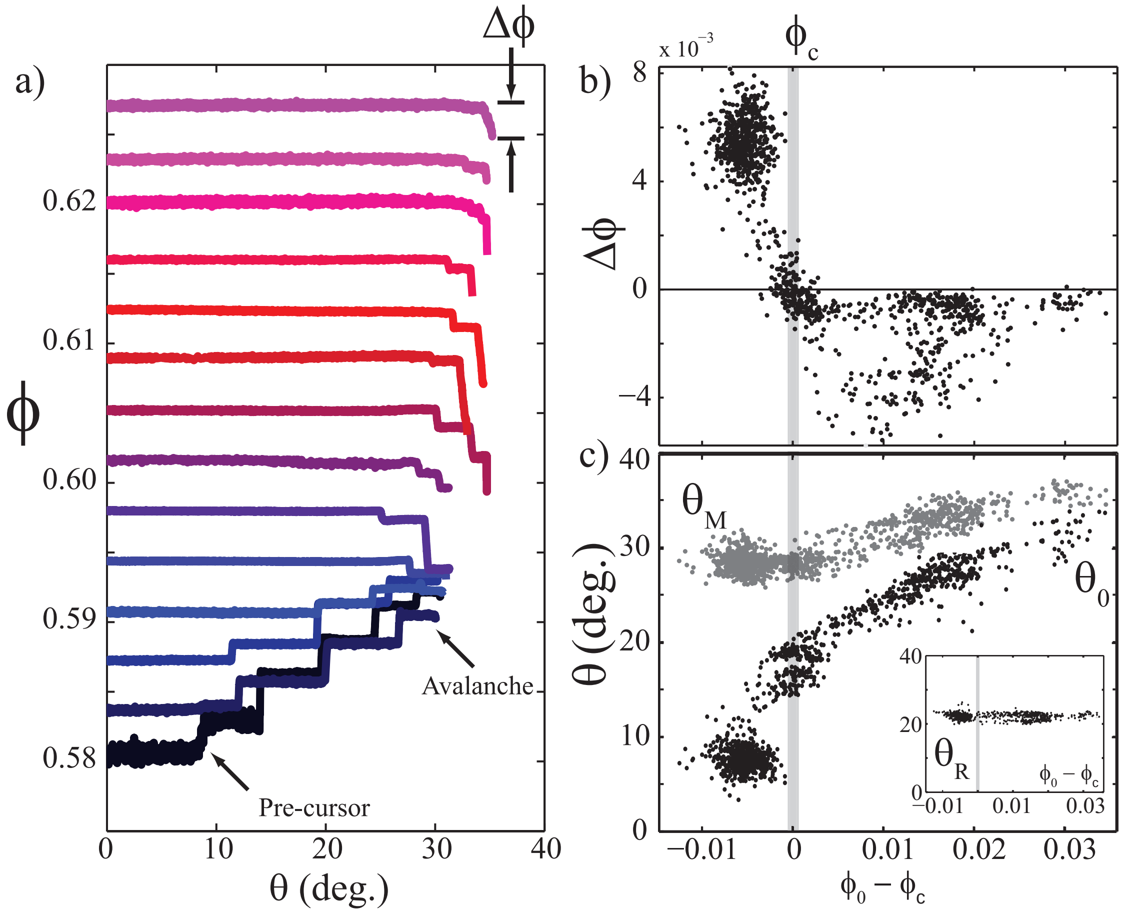

**Figure 5.2:** Avalanching dynamics. a) $\phi$ versus tilt angle, $\theta$, for thirteen experiments at different $\phi_0$. As the layer is inclined, compaction or dilation precursor events precede an avalanche. The pre-avalanche and failure dynamics are sensitive to initial $\phi$. b) Change in volume fraction $\Delta\phi$ is dependent on initial $\phi$ and changed sign at $\phi_c = 0.595 \pm 0.001$. Each point in b-c represent a single experiment. c) Initial angle of avalanche precursor, $\theta_0$, and maximum angle of stability, $\theta_m$, are sensitive to $\phi_0$. Angle of repose is insensitive to $\phi_0$ (Inset).

We measured the total change in volume fraction prior to the onset of an avalanche, $\Delta\phi = \phi_f - \phi_0$, as a function of prepared $\phi_0$. We find that at $\phi_c = 0.595 \pm 0.001$ a transition from compaction to dilation behavior occurs where $\Delta\phi = 0$ (Fig. 5.2b). The initial volume fraction at which $\Delta\phi = 0$ is the critical state volume fraction, $\phi_c$, and is the steady-state $\phi$ that granular material approaches when sheared [53].

Increasing $\phi_0$ from the minimum value observed, $\Delta\phi$ decreased from a large positive value to a large negative value as $\phi$ crossed $\phi_c$. For $\phi_0 > \phi_c$, increasing $\phi_0$ resulted in $\Delta\phi$ decreasing to a smaller yet still negative value. This indicated that the magnitude of dilation preceding an avalanche decreased with increasing $\phi$. Such a decrease in $\Delta\phi$ likely occurs because higher $\phi$ granular material experience larger internal stresses which inhibit volumetric expansion.

The bed angle at which point the first precursor occurred is defined as $\theta_0$, and the maximum angle of stability at which angle the avalanche begins at is defined as $\theta_m$. Both $\theta_0$ and $\theta_m$ were monotonically increasing functions of $\phi_0 - \phi_c$ (Fig. 5.2c). Precursors occurred at low angles for low $\phi$, with $\theta_0 = 7.7 \pm 1.4°$ in the case of $\phi_0 - \phi_c = -0.006 \pm 0.001$. As $\phi_0 - \phi_c$ increased so did $\theta_0$, and for close packing, $\phi_0 - \phi_c = -0.032 \pm 0.001$ we observed $\theta_0 = 32.1 \pm 1.5°$. However, overall $\phi_0$ did have a significant effect on the stability of the granular slope.

The bed angle at which avalanches began, $\theta_m$, was also a function of $\phi - \phi_c$ (Fig. 5.2c). Increasing $\phi_0 - \phi_c$ increased $\theta_m$ from $\theta_m = 28.5 \pm 1.0°$ to $\theta_m = 35.9 \pm 0.7°$ over the range of volume fractions observed. Although $\theta_m$ was sensitive to $\phi_0$, the difference in magnitude of $\theta_m$ over the observed $\phi_0$ was not as large as the variation observed in $\theta_0$. We expect that the decreased sensitivity of $\theta_m$ on $\phi_0$, is due to the series of precursor events that occur for $\phi < \phi_c$, which strengthened the material and increased prior to the avalanche.

The final slope angle at which the granular material came to rest at is defined as the angle of repose $\theta_r$. $\theta_r$ was independent of initial $\phi_0$ over the range of $\phi_0$ observed. The lack of dependence of $\theta_0$ on $\phi_0$ may occur because once the granular material is set in motion it will rapidly evolve to a critical state of flow, independent of it's previous state [53]. The angle of repose we observe for dry, spherical, glass beads is consistent with previous observations of $\theta_r = 22 \pm 2°$ [181]. The independence of $\theta_0$ on prepared volume fraction is further evidence that $\theta_0$ is an emergent quantity of individual grains, dependent only on the grain mechanical properties (coefficient of friction, restitution, shape, etc.) [182] and not their initial preparation.

## *5.5 Flow characteristics at* $\theta_0$

To characterize the granular flow during the precursor events at $\theta_0$ we computed the flow profile using PIV. Since precursor events consisted of a flow initiation and flow arrest, we measured the displacement field of the granular flow $[d_x(y), d_y(y)]$ along a vertically oriented line centered in the imaging region and in the reference frame of the tilted bed. The displacement field of the granular flow during the first precursor significantly differed as a function of $\phi - \phi_c$. Loose pack flow [$\phi_0 - \phi_c < 0$, see Fig. 5.3a (i)] resulted in material displacement parallel to, and down the length of the bed (positive $d_x(y)$) and a vertical displacement towards the floor of the enclosure (negative $d_y(y)$). Negative $d_y(y)$ indicates compaction of the granular material as expected for $\phi_0 - \phi_c < 0$. In the range of critical compaction, $\phi_0 - \phi_c \approx 0$ [Fig. 5.3a (ii)], $d_x(y)$ decreased compared to the loose pack, and $d_y(y)$ approached zero indicating no compaction or dilation–the definition of the granular critical state. Lastly in the dilating regime, $\phi_0 - \phi_c > 0$ [Fig. 5.3a (iii)], $d(y)_x$ decreased as $\phi$ increased and $d_y(y)$ was negative and decreasing with increasing $\phi_0$. These observations indicate that we observed a dilation transition signature in the flow profiles of granular materials. In general the vertical grain motion during a precursor is downwards (compacting) for $\phi - \phi_c < 0$ and upwards (dilating) for $\phi - \phi_c > 0$.

From the displacement profiles of the precursor flow we may now interrogate the quantitative differences in granular response in the dilating or compacting regimes. We measured the depth-averaged mean displacement of the horizontal and vertical granular flow, $\langle d_i \rangle$ $(i = x, y)$, averaged over depths 0-4.7 cm. We find that with increasing $\phi_0$, $\langle d_x \rangle$ decreased and $\langle d_y \rangle$ decreased from positive to negative and crosses zero at $\phi_c$ (Fig. 5.3b) as expected from the definition of the critical state. The difference in magnitude of $\langle d_y \rangle$ and $\langle d_x \rangle$ across $\phi_c$ shows that material at low $\phi_0$ is relatively fragile and subject to large displacements

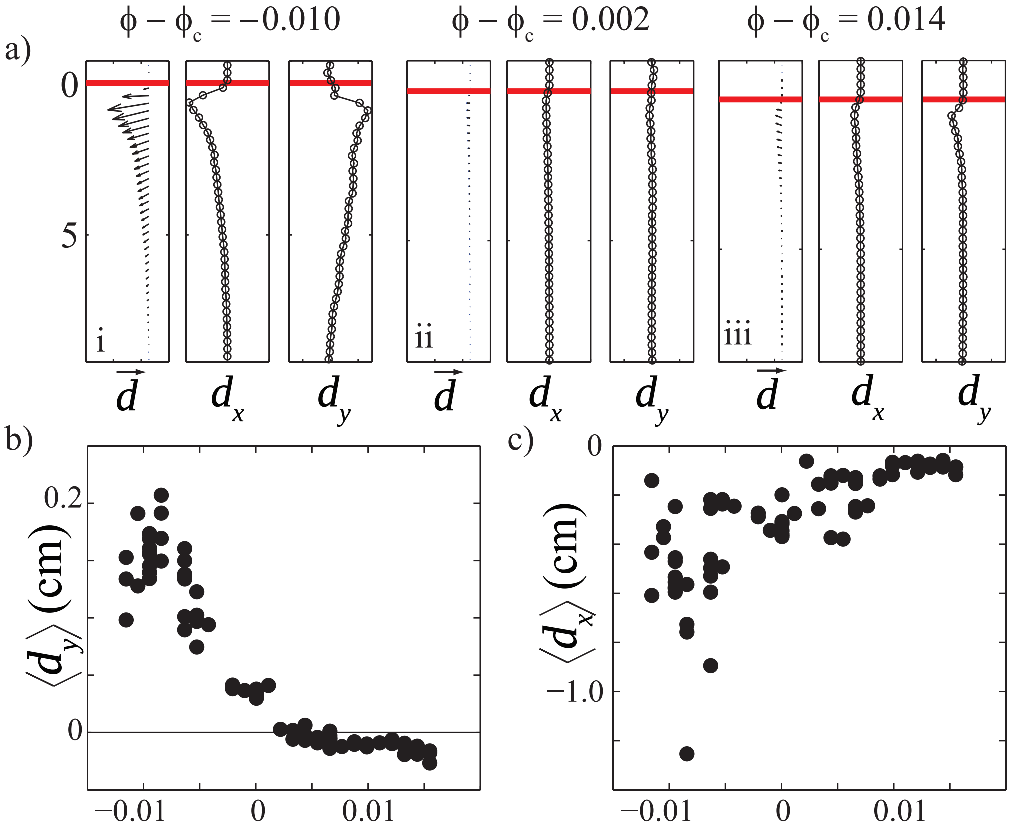

**Figure 5.3:** Profiles of granular displacement during initial failure. a) Displacement profiles of a loose (i) a critical (ii) and a close (iii) packed granular material. From left to right: vector displacement field of flow, x-displacement ($d_x$), and y-displacement ($d_y$). Red line indicates surface location. b-c) Depth averaged horizontal ($\langle d_x \rangle$) and vertical ($\langle d_y \rangle$) displacement of granular material at different prepared $\phi_0 - \phi_c$.

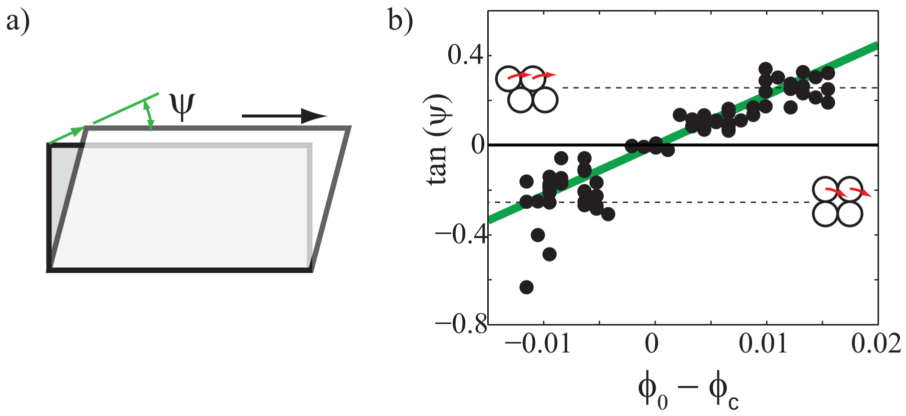

**Figure 5.4:** Tangent of the dilation, $\psi$, versus $\phi - \phi_c$. Dashed lines correspond to value for cartoons of close pack and loose pack shear drawn in figure and described in text.

when failing compared to the small displacements grains at high $\phi_0$ undergo during precursor failure (Fig. 5.3b-c).

The amount of dilation that occurs per unit shear in a granular material is measured by the dilatancy angle, $\psi$ (Fig. 5.4). In the case of our geometry, we assume translational invariance along the horizontal direction ($x$ in the frame of the rotating bed), similar to a simple-shear flow. The dilatancy angle is the angle the displacement vector of the surface deformation makes with the horizontal (Fig. 5.4a). In the case of simple-shear we may estimate the dilatancy angle as

$$\tan(\psi) = \frac{d_y}{d_x} \tag{5.1}$$

averaged over the whole depth of the flow (Fig. 5.4). We plot the $\tan(\psi)$ as a function of $\phi - \phi_c$ in figure 5.4 and we find that the dilatancy angle during precursor failure obeys the equation

$$\tan(\psi) = K(\phi - \phi_c) \tag{5.2}$$

where $K = 22.41 \pm 2.40$. Equation 5.2 was originally introduced by Roux et. al. [183] and is effectively a linearization of the function $\psi(\phi)$ about the critical state $\phi_c$.

To give perspective to the values of $\tan(\psi)$ observed in figure 5.4 we construct cartoon scenarios of dilatant and compacting flow. We imagine a 2D arrangement of diameter $D$ spheres in a square lattice (loose packing) or a hexagonal lattice (close packing). In both cases we impose a lateral displacement, $d_x$, and compute the resultant $d_y$ of the grain layer

(See cartoon insets in Fig. 5.4b). In both cases, for a lateral displacement of $d_x = \frac{D}{2}$ geometry allows us to determine that the grains displace vertically $d_y = 0.134$ in the ± direction resulting in $\tan(\psi) = \pm 0.268$ (where as in figure 5.4 (+) is dilation). The peak dilation and compaction observed in experiment are near the values of $\tan(\psi)$ predicted from the simple scenario presented above which gives some insight into the magnitude of compaction (dilation) the loose (close) pack undergoes in experiment. Larger and smaller values of $\tan(\psi)$ are likely due to the disordered nature of the granular configurations created in experiment.

We compare our results on dry granular materials with the experiments of Pailha et. al. [179] in which avalanches during progressive tilt were studied in a granular material immersed in fluid. In the experiments of Pailha et. al. [179] $K = 3.4$ and $\phi_c = 0.582$. The lower value of $\phi_c$ is explained by the contribution of the hydrostatic pressure of the fluid which reduces internal stress and thus mean pressure as predicted by equation 2.2. The fluid density in the the experiments of Pailha et. al. [179] was nearly half that of the solid density of the glass beads, thus the effective gravity in these fluid immersed experiments reduced by nearly a factor of two. A lower value of $K$ indicates that for a comparable amount of horizontal grain motion, less vertical motion is experienced in the granular suspension compared to the dry granular material. The decrease in vertical motion in the fluid-immersed experiments is likely due to the resistive influence of the pore pressure from the surrounding viscous fluid. For instance a suction pressure is generated when a fluid immersed granular material dilates, generating higher grain-grain stresses which in turn may resist further dilation, and thus lower $d_y$.

### 5.6 $\phi$ dependence of flow size

During the granular flow at $\theta_0$ we observed that the flow profile extended deeper into the granular layer than during avalanche flow at $\theta_m$. We observed this by computing image differences of successive video frames from high-speed video (1000 Hz) of the progressive tilt experiment (Fig. 5.5). In fig. 5.5 regions that are black correspond to small intensity differences between adjacent video frames at that location. White locations correspond to

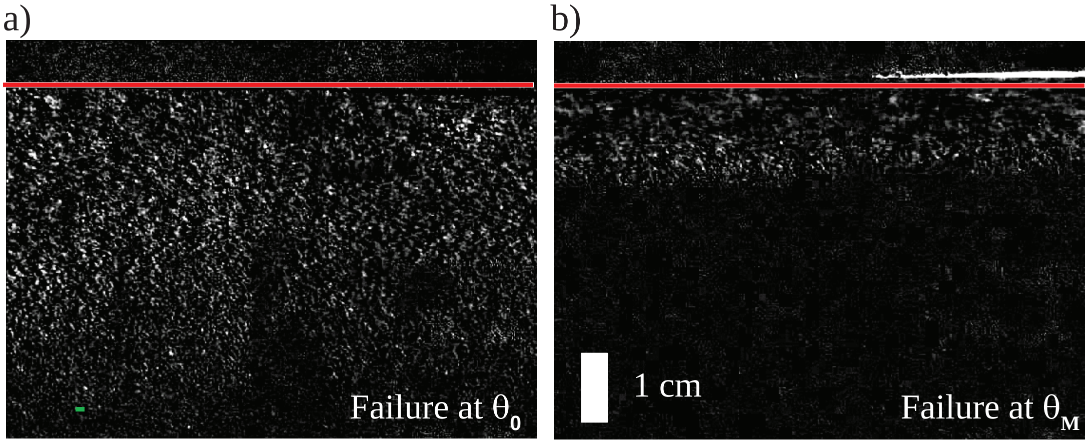

**Figure 5.5:** Difference in flow size at $\theta_0$ and $\theta_m$. a) A difference image between two adjacent video frames during a precursor failure at $\theta_0$. White corresponds to region of the image which underwent a change in light intensity due to motion of the granular material. b) A difference image of the same granular material at $\theta_m$. Avalanche flow is concentrated to a narrow band near the surface. The surface is designated by the red line.

large intensity differences. The scale of the intensity difference is arbitrary since there is always a chance that one grain gets replaced by another one in the same location between frames, resulting in a large deformation and small intensity difference.

We visualize the spatio-temporal dynamics of the avalanche process by examining the space-time evolution of the image difference magnitude in a thin vertical strip centered in the observation region. We construct space-time images by plotting image intensity at depth, $y$, and time, $t$. In figure 5.6a we show two space-time plots, one from a compacting experiment at $\phi-\phi_c < 0$ (top) and one from a dilating experiment at $\phi\phi_c > 0$ (bottom). We observe the same intermittent precursor flow at $\phi_0 < \phi_c$ prior to an avalanche as described in section 5.6 (gray region in Fig. 5.6a). As $\phi_0$ increased the angle at which the precursor flow occurred at also increased.

The space-time evolution of individual precursor events varied in shape and size across the observed $\phi - \phi_c$ experiments. In figure 5.6b-c we show two precursor events from compacting and dilating flow. In general we observed that precursor events either initiated from the surface and propagated downwards (Fig. 5.6b) or the precursor events occurred simultaneously within the layer (Fig. 5.6c). We did not observe a dependence of $\phi - \phi_c$ on this behavior. In the example we show in Fig. 5.6b the propagation speed of the event, which in this case is a compaction front, was found to be $v = 1.08$ m/s. For comparison the speed of sound propagation in granular material has been found to be 280±30 m/s [184] and the speed of sound in glass is ≈4000 m/s.

Although the precursor space-time shape did not vary as a function $\phi - \phi_c$, the magnitude of these spatio-temporal events, both in depth $D$ and duration $\Delta T$, were affected by $\phi - \phi_c$. The temporal duration of precursor event, $\Delta T$ was a non-monotonic function of $\phi - \phi_c$ and increased to a maximum near $\phi_c$. The maximum observable depth of the granular flow during failure at $\theta_0$ was defined as $D$ (Fig. 5.6). We find that $D$ was sensitive to $\phi - \phi_c$ and was approximately constant, $d = 7.94 \pm 0.60$, for $\phi < \phi_c$ and linearly decreasing, $d = -242\phi + 8.387$ for $\phi > \phi_c$. The functional difference in $D(\phi)$ as $\phi$ exceeds $\phi_c$ is another signature of a bifurcation in the granular rheology that occurs at the dilation transition.

The avalanche depth, $d = 1.13 \pm 0.44$ is significantly shallower than the precursor events as observed before in image difference (Fig. 5.5). The avalanche depth corresponds to roughly 40 grain diameters. The depth independence of the flow profile during the avalanche phase suggests that the amount of grain re-arrangement that occurs prior to the avalanche is sufficient to bring the granular material into a critical state at which point the flow is independent of $\phi_0$. This is consistent with our observation of $\theta_r$ being independent of $\phi - \phi_c$.

## *5.7 Conclusion*

In conclusion we have experimentally investigated the effect of volume fraction on the failure of a granular slope subject to progressive tilting. We find that the dynamics of slope failure are qualitatively different as a function of $\phi_0$ and can be divided into two regimes of response whether above or below $\phi_c$. For granular material prepared below $\phi_c$ the granular layer undergoes several compaction precursor events prior to the onset of sustained surface flow defined as an avalanche. The angle of compaction precursor onset in the case of the lowest $\phi_0$ occurs at $\theta_0 = 7.7 \pm 1.4°$, a value of slope failure substantially lower than what has been observed in previous avalanche experiments with "as poured" granular media in which volume fraction is not typically controlled. As $\phi$ is increased we observe an increase in $\theta_0$, which approaches the maximum angle of stability, $\theta_m$, as $\phi_0$ increases. The value of

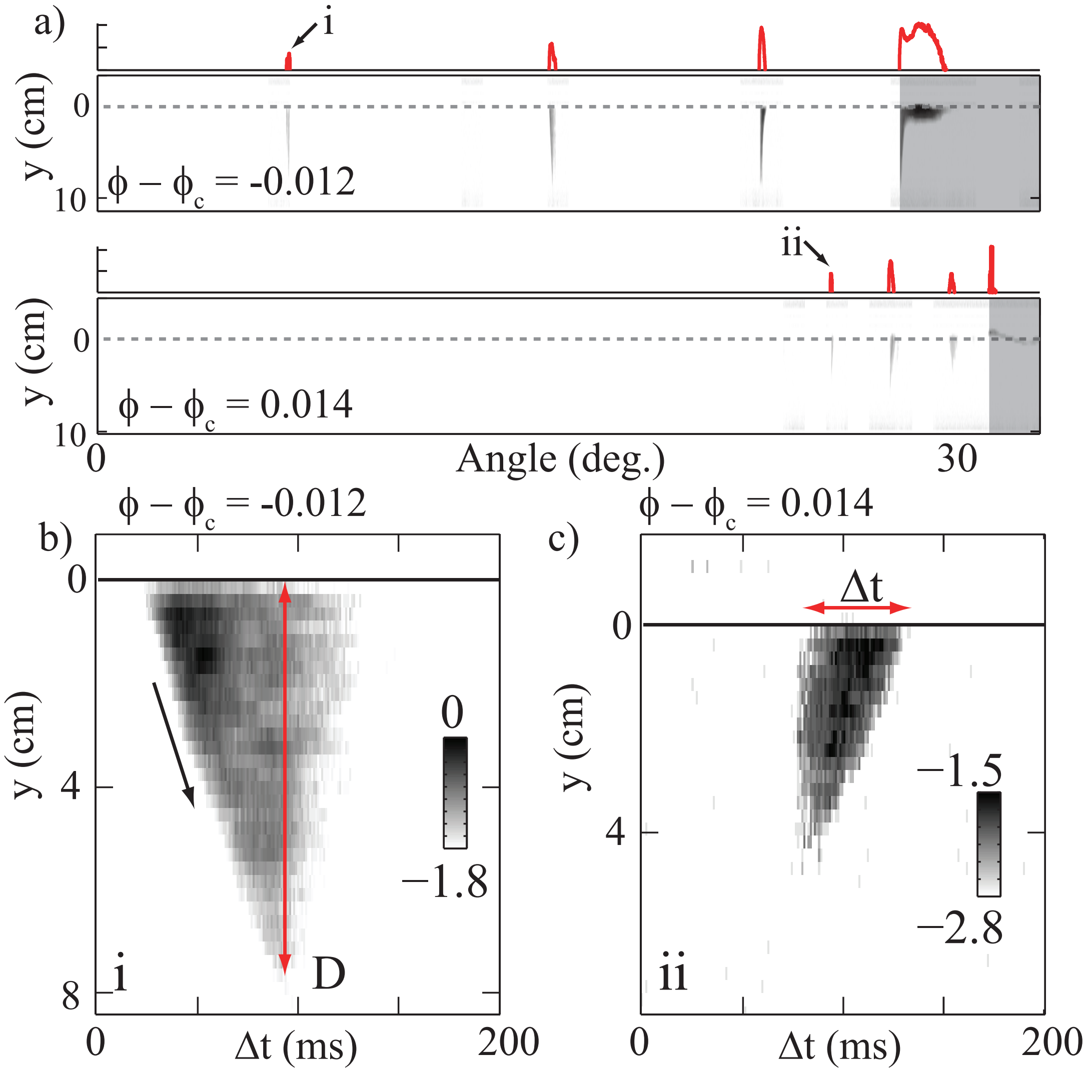

**Figure 5.6:** Space-time images of flow profile. a) Space-time profiles of granular flow generated from image differencing. Intensity plots of the flow profile are shown above the space-time plots (arbitrary units). Top plots are loose pack and show a precursor event (i) occuring at $\theta = 6.22°$. Several precursors occur prior to the initiation of a surface avalanche (gray box). Bottom plots show a close pack space-time image. A precursor event (ii) occurs at $\theta = 26°$. b) Space-time images of the precursor events at i (left) and ii (right). Flow during the loose pack precursor (left) begins at the surface and propagates vertically into the granular layer (black arrow) at speed of approximately $v = 1.08$ m/s, to a maximum depth $D$. During the close pack precursor (right) flow begins simultaneously in the layer.

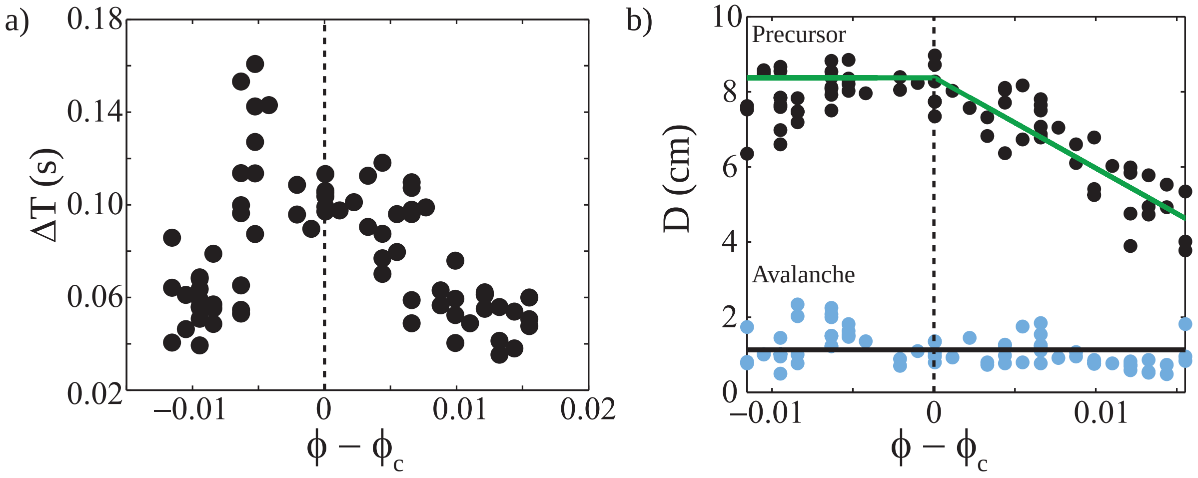

**Figure 5.7:** a)Duration of precursor events as a function of $\phi - \phi_c$. b) Depth dependence of pre-cursor and avalanche flow as a function of initial $\phi_0$. Black circles are pre-cursor flow and green line shows the functional

$\theta_m$ we observe for the critical state, $\phi_c$, is consistent with values observed for similar glass particles prepared in an "as poured" state or subject to multiple avalanches in rotating drum experiments [181]. The ability to observe the dilation transition in our experiments indicates that an incremental tilting experimental protocol may be a tractable and rapid method for measuring the $\phi_c$ of an unknown granular material. As we have shown in these experiments, and consistent with previous studies of granular material, determination of both the current state, $\phi_0$, and the critical state, $\phi_c$, are necessary to predict the failure conditions for a granular material.

# CHAPTER VI

# GEOMETRIC COHESION

## *6.1 Summary*

Many previous studies of granular materials focus on particles that are approximately spherical and are convex. Here we study the simplest concave particles, granular "u-particles". These u-particles of barb length-to-particle width ratio, $l/w$, display cohesive-like effects through mechanical particle entanglement. We study the packing and relaxation dynamics of vertical, free-standing columns formed from u-particles of fixed $l/w$ subject to sinusoidal vibration (frequency $f$, peak acceleration $\Gamma$). We vary $l/w$ to understand how particle concavity influences rheology. Increasing $l/w$ results in columns which pack to a lower volume fraction, $\phi$, with a functional form described through the use of a mean-field random contact model. Collapse dynamics are measured by monitoring column height, $h(t)$, and we find that the timescale for column collapse, $\tau$, follows the relation $\tau = f^{-1}\exp(\Delta/\Gamma)$. $\Delta$ resembles an activation energy and is maximal at intermediate $l/w = 0.394 \pm 0.045$. We perform simulation of u-particle ensembles to determine the number of mechanical entanglements as a function of $l/w$. We find that the density of entangled particles is maximum at $l/w = 0.340 \pm 0.015$, near our observed maximum in relaxation time. This optimum entanglement shape is described though through the random contact model and occurs as a competition between packing and entanglement.*

---

*This chapter has been published in *Physical Review Letters* under the title "Entangled granular media"

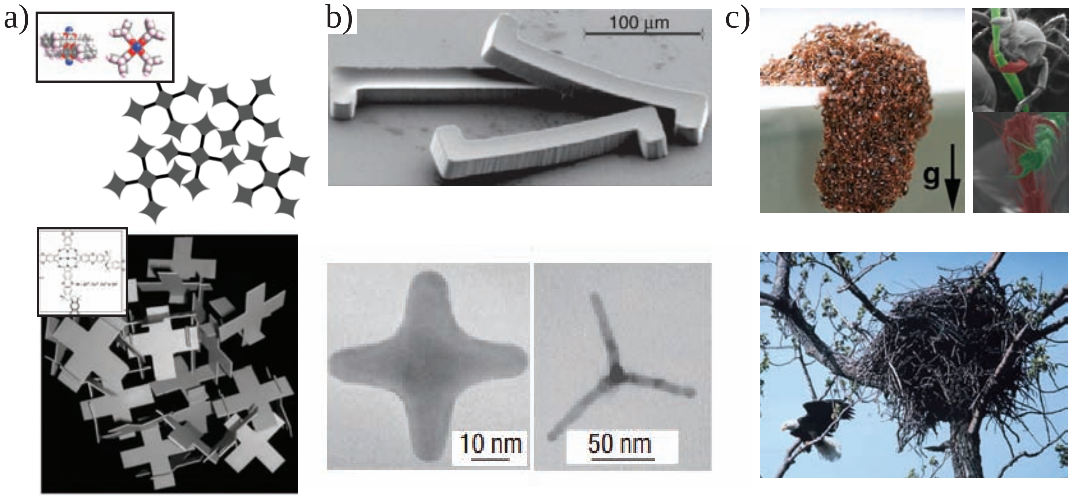

**Figure 6.1:** Concave particle assemblies from the nano- to macro-scale. a) Macromolecular assemblies of rigid oligomers (insets) interpenetrate depending on oligomer shape (top) [189] and may form into large entangled networks (bottom) [190]. b) Concave particle suspensions (top) [188] and concave colloids (bottom-left) [191] and (bottom-right) [192]. c) Concave particle assemblies found in nature, living fire ants (top) [113] and rigid branches of bald eagles nests (bottom).

## *6.2 Introduction*

Assemblies of non-spherical "particles" can be found at all scales of natural and industrial systems. Particle shape is important in determining the bulk material properties of macro-molecular, colloidal, and granular systems (See Fig. 6.1). Understanding how particle shape influences rheology is an important and open question in soft-matter physics with many potential applications in engineering and industry. Despite this fact, the majority of rheological studies on particulate systems have focused on particles of convex shape [185, 2, 56, 44], and less research has been focused on concave particles [186, 187, 188]. The fundamental difference we envision between concave and convex particle assemblies is the ability for concave particles to interpenetrate, which we call being "entangled". Mechanical entanglement of particles will alter the rheology of particle assemblies through the tensile resistance to the separation of entangled particles.

Concave particle assemblies may be found in all sizes (Fig. 6.1). The bulk packing properties and microstructure of concave particle assemblies are being exploited in the design of macro-molecules, such that the concave molecular shape hinders the ability to closely

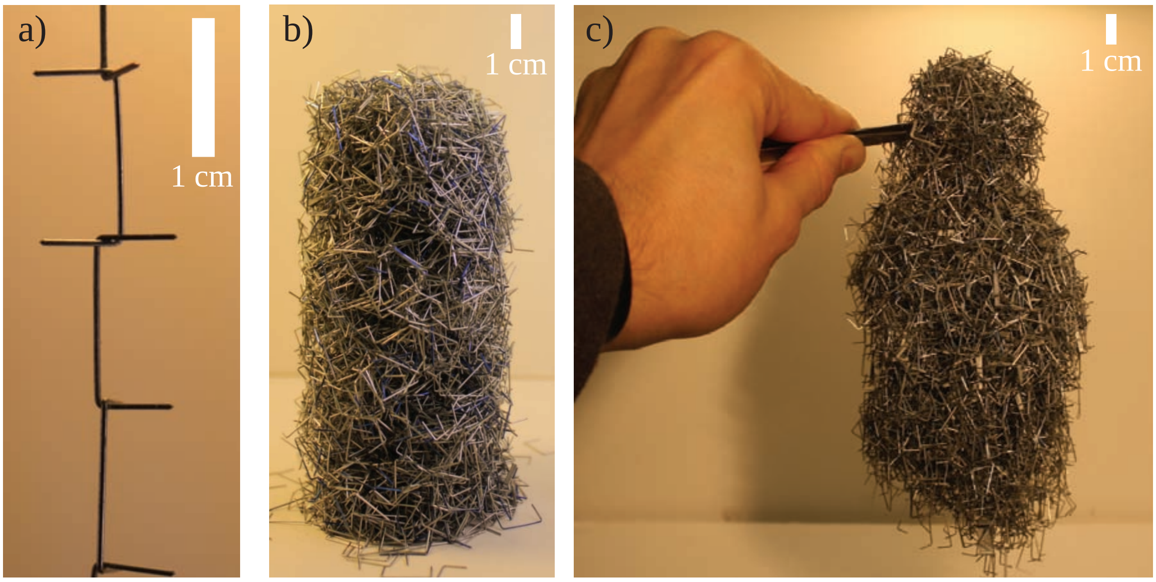

**Figure 6.2:** U-particle assemblies. a) U-particles interpenetrate to support tensile loading. b) A free-standing column of entangled u-particles. c) Grasping the tower with tweezers illustrates the tensile strength of this granular assembly.

pack and results in materials with a high micro-porosity [189, 190]. These microporous assemblies have applications ranging from nano-drug delivery systems to gas trapping. The design of concave shaped colloids and particle suspensions is currently an area of active research [191, 193]. Colloidal particles are often a starting point for the study and engineering of self-organizing, “smart” materials [194]. Granular materials, which are a frequently processed and manipulated form of matter, may also be engineered into different shapes and sizes. Recent interest in “designed” granular particles through the use of 3D printing technology has been spurred on by advancements in the application of granular jamming to robotics [195, 196].

A convenient concave particle that is found in every office is the staple (Fig. 6.2). Staples may come in many shapes and sizes and by the nature of their concave shape display the ability to interlink and form chains. Piles of staples may be formed, much like those of wet granular media, which have vertical side-walls indicating a strong cohesive effect between grains. The grain-grain cohesion is large enough such that one can lift a column of staples from the top and a majority of the pile will stay together (Fig. 6.2).

In addition to engineered systems, concave particle assemblies are found in biological

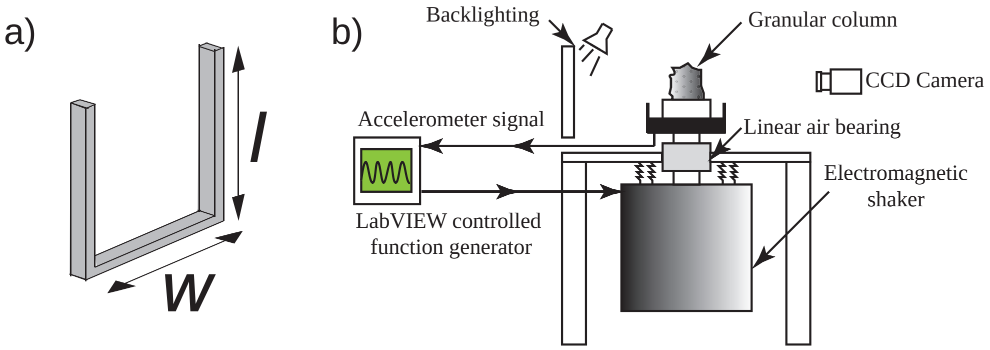

**Figure 6.3:** Relaxation dynamics of u-particle columns are studied through a mechanical vibration experiment. a) U-particle geometry. Width, $w$, is held constant and length, $l$, is varied. b) A computer controlled shaker table applies sinusoidal forcing to a granular column. A high-speed camera records column collapse from the side.

systems. The packing of actin or other protein filaments within eukaryotic cells, which drive cell motility, share many properties with granular rod packings and due to their branched nature can be considered concave [197]. The collective bridge and raft building of ants [113, 114, 112], are held together through the entanglement of ant limbs and mandibles which can be considered concave particles. Lastly, animal built structures constructed from branches and twigs such as birds nests are concave particle assemblies [198].

The goal of this work is to develop a fundamental understanding of how particle concavity influences bulk rheology which we hope will have application across the wide range of size scales at which these particles are found at.

## *6.3 Methods*

Below we describe a set of experiments to study the packing and relaxation of “u-particle” columns. We formed vertical, free-standing columns from collections of “u-particle” of varied barb length to width ratio $l/w$. By varying $l/w$ we effectively vary the concavity of the particles with $l/w = 0$ being rods with no concave region and large $l/w$ particles possessing a large amount of concavity. We study two properties of the u-particle columns: 1) the packing behavior of “u-particles” studied through measurement of $\phi$, and 2) the relaxation of columns under gravity and subject vertical vibration from the floor.

### 6.3.1 u-particles

U-particles consisted of steel staples (Duo-fast; Vernon Hills, Il.) of constant width, $w$=1.17 cm, and variable barb length, $l$ ($l/w \in [0.02, 1.125]$; Fig. 6.3a). The cross section of all particles was rectangular with thickness of 0.5 mm and width 1.27 mm which corresponded to a rod-like aspect ratio for $l/w = 0.02$ particles of $\approx 14$. We cut by hand particles of size $l/w = 0.02 \pm 0.02, 0.13 \pm 0.02, 0.15 \pm 0.03$ and $0.28 \pm 0.04$, and other particles were purchased at that size.

### 6.3.2 Column formation

Collections of monodisperse particles with fixed $l/w$ were formed into free standing cylindrical columns with column diameter, $d$=4.4 cm or $d$=5.6 cm, and height, $h_0 = 3$ cm. Columns were prepared by pouring particles into the cylindrical container followed by a 20 s sinusoidal vibration of the base at a frequency, $f = 30\ Hz$, and peak acceleration, $\Gamma = 2$ (in units of gravitational acceleration $g$). We confirmed that steady state volume fraction was reached through our preparation protocol in separate experiments conducted over a 60 s time period. Columns occupied a volume $V = \pi h (d/2)^2$, and the volume fraction was calculated as $\phi = \frac{M}{\rho_{st} V}$ where $M$ is total particle mass and $\rho_{st} = 7.85\ g/\text{cm}^3$ is the density of steel.

### 6.3.3 Column vibration

Sinusoidal oscillation was generated by an electromagnetic shaker (VTS; Aurora, OH; Fig. 6.3b). The shaker piston was attached to a linear, square-shaft, air bearing which insured that the motion was primarily vertical. The shaker was mounted to a thick aluminum plate through a collection of springs. This mounting system reduced vibration coupling which would occur if the shaker was mounted to the ground. Vibration experiments were performed at a frequency of $f = 30 Hz$ and variable peak acceleration $\Gamma \in [1.2, 2.5]$ (in units of gravitational acceleration $g$). The shaker was controlled by LabVIEW and a Tecron 7550 power amplifier. Acceleration of the vibration table was measured by an accelerometer embedded in the vibration table (PCB Piezotronics; Depew, New York).

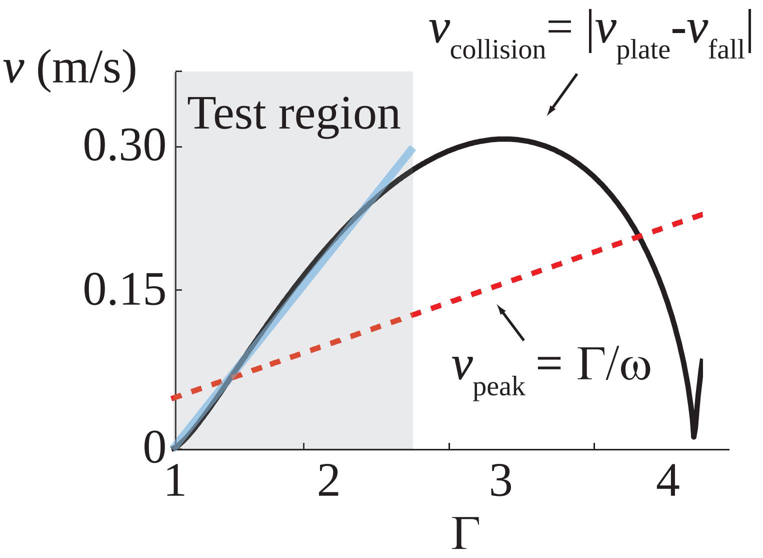

**Figure 6.4:** Difference in speed between oscillating plate and free-falling column as a function of Γ. Collision speed has non-monotonic dependence on Γ. However within the experimental range of Γ chosen here (Gray shaded area) the relationship between collision speed and Γ is approximately linear.

The effective "heating" in the granular pile is induced by the pile being thrown up into the air and then under free-fall colliding with the oscillating plate. Here we describe how this collision velocity varies as a function of Γ. From previous study of elastic and inelastic balls interacting with an oscillated floor, we know that the speed of collision between the plate and free-falling ball is non-monotonic in Γ. To use Γ as an appropriate measure of "heating", we want to only oscillate in the range where the collision velocity is monotonic, and ideally linear, with Γ. To do this we solve for the collision velocity between the plate and ball for our chosen vibration frequency, $f$, shown in Fig. 6.4. From this, we choose Γ to be below a maximum of $2.75g$, which within this range the collision velocity is monotonic and approximately linear in Γ.

Column collapse was monitored using a high speed camera (Point-Grey; Richmond, BC, Canada). Image capture was triggered externally by a function generator controlled by LabVIEW such that images were captured at a constant phase of the oscillation cycle, and at frequencies of $f$, $f/2$, and $f/4$. Images were analyzed in Matlab. Columns appeared black on a white background and thus we extracted the foreground column using an image threshold. We then dilated the foreground region to insure that the column was a singly connected region and finally measured the centroid height, $h(t)$, of the column and the projected 2D area $A(t)$.

## *6.4 Results and discussion*

### 6.4.1 Packing experiments

Particles were rained into the cylinder and came to rest in an initial volume fraction $\phi_0$ which was dependent on particle packing (Fig. 6.5). Applying vibration for 60s resulted in a steady-state final volume fraction, $\phi_f$, which reached steady-state within approximately 20 seconds. As can be seen in Figure 6.5b, $\phi_0$ and $\phi_f$, decreased with increasing $l/w$. Compaction, defined as $\chi = \frac{\phi_f - \phi_0}{\phi_0}$, linearly increased with $l/w$ and was fit by the function $\chi = 0.23(l/w) + 0.12$ ($R^2 = 0.65$). Larger $l/w$ particles likely exhibit a higher amount of compaction because their long barbs cause them to jam in lower $\phi_0$ initial states, while their large internal volume also allows them to pack to high $\phi_f$.

For a comparison with similar experiments, the value of $\phi_f = 0.28 \pm 0.01$ we observed for $l/w = 0.02$ particles is close to the range, $\phi_f = 0.28 - 0.34$, observed in cylindrical rod packs with comparable aspect ratio (length/thickness $\approx 14$) [199, 82, 83, 87]. The variance in cylinder rod values is due to difference in preparation method. The lower value observed in our $l/w = 0.02$ particles is likely due to the fact that our particle have a rectangular cross-section while the values we compare to are from cylindrical cross-section rods.

The final volume fraction, $\phi_f$, decreased monotonically with increasing $l/w$. This is consistent with what is observed in rod packing studies in which increasing the length (aspect ratio) of rods decreases the volume fraction [199, 82, 83, 87]. For long rods the volume fraction scales inversely with rod-length, and this behavior is described through a statistical model of particle packing called the random contact model which we describe in section 3. One way to qualitatively understand this decrease in $\phi_f$ with increasing $l/w$ is that larger $l/w$ particles have larger internal volumes and thus pack less efficiently.

### 6.4.2 Collapse experiments

After we formed cylinders of packed u-particles in the packing experiment, we removed the confining container which left the column free-standing. During removal of the confining

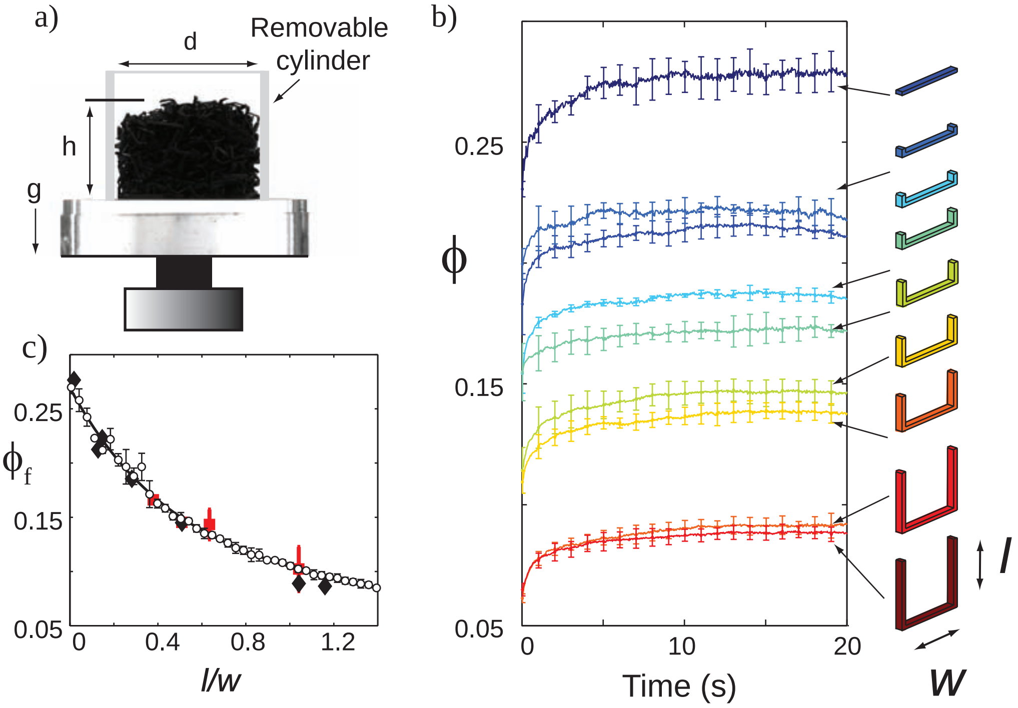

**Figure 6.5:** Formation and packing of u-particle columns. a) Experimental setup to form free-standing u-particle columns. Particles were packed within a containing cylinder of diameter d = 4.4 cm or d = 5.6 cm which was removed after the packing protocol. b) $\phi(t)$ during column preparation for various u-particle assemblies. c) Final packing fraction, $\phi_f$, as a function of particle geometry in experiment (column diameter d = 4.4 cm diamonds and d = 5.6 cm squares) and simulation (white circles). Line is theory prediction from the random contact model.

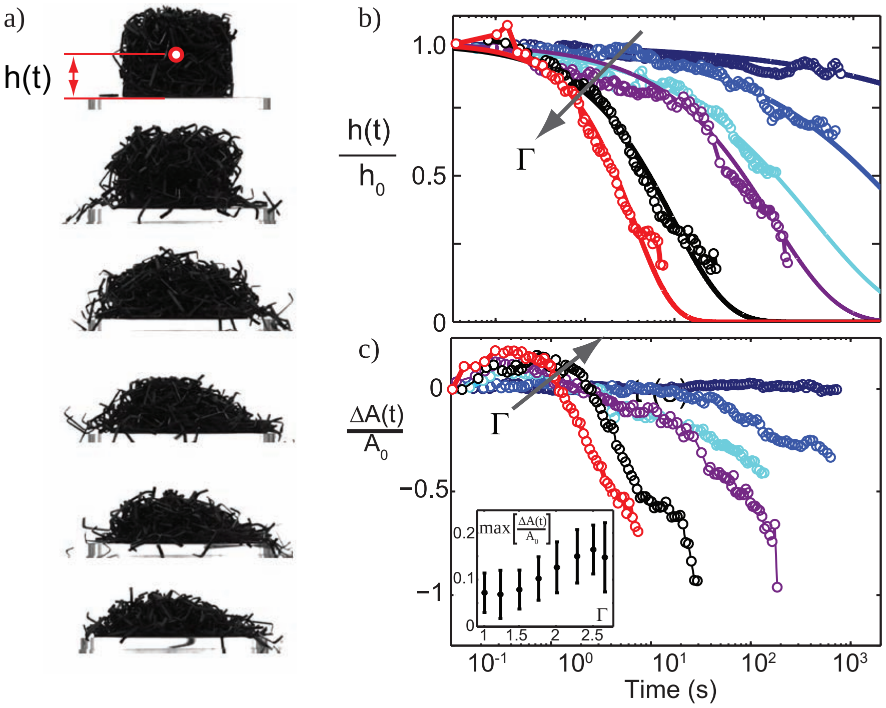

**Figure 6.6:** Column collapse dynamics. a) The normalized centroid height, $h(t)/h_0$ (red dot) of the column during collapse. Vibration parameters are $\Gamma = 2$, $f = 30$Hz, and images are separated by 90 oscillation periods. b) Relaxation of $h(t)/h_0$ as a function of time is shown for $l/w = 0.379$ for $\Gamma = 1.23, 1.48, 1.70, 1.96, 2.20, 2.53$ respectively (arrow denotes increasing $\Gamma$). Fit lines are stretched exponentials with equation given in the text. c) Change in projected area of the column, $\frac{\Delta A(t)}{A_0}$, as a function of time. $\Gamma$ corresponds to values in (b) with arrow denoting direction of increasing $\Gamma$. Inset shows the peak area increase, $\max[\frac{\Delta A(t)}{A_0}]$, as a function of $\Gamma$ averaged over all $l/w$ (error bars are std. deviation).

cylinder the $l/w = 0.02$ particles were marginally stable with partial column collapse occurring approximately 50% of the time, similar to the results reported in [88]. Spontaneous collapse of the $l/w > 0.02$ columns was rarely observed. To explore the dynamical stability of u-particle columns we next subjected them to vertical vibration from the base and observed column collapse.

We applied sinusoidal vibration to the base of the free-standing column and observed the collapse process from a lateral view with our camera (Fig. 6.6a). We characterized collapse dynamics by monitoring the centroid height, $h(t)$, and cross-sectional area $A(t)$, of the column (Fig. 6.6b). The collapse dynamics of $h(t)$ were well described by a phenomenological stretched exponential fit function $\frac{h(t)}{h_0} = e^{[-(\frac{t}{\tau})^{\beta}]}$. The parameter $\tau$ is the characteristic collapse time and $\beta$ is the stretching parameter [200]. Consistent with previous studies [201, 202] $\beta$ was in the range of 0.5 - 1 and decreased slightly as $\Gamma$ increased but was independent of particle geometry. The stretched exponential function is frequently applied to the description of relaxation dynamics of disordered systems [200].

For fixed $l/w$, we found that the collapse time of the column found from the stretched exponential, $\tau$, decreased with increasing $\Gamma$. This supports our intuition that larger perturbations cause a more rapid collapse of the column. Furthermore, the logarithm of $\tau$ increased linearly with $1/\Gamma$ (Fig. 6.7a) and $\tau$ was fit by an exponential $\tau = f^{-1}e^{\Delta/\Gamma}$ with $\Delta$ as the single fit parameter ($f = 30Hz$).

The exponential fit is indicative of an Arrhenius-like process observed in the relaxation of activated systems. The Arrhenius process describes the escape probability of a thermally or mechanically activated particle from a potential well of depth $\Delta$. In thermal systems the escape time is proportional to one over the Boltzmann factor $\exp(-\frac{E}{kT})$ where $E$ is the activation energy required to overcome the potential barrier. In our system thermal effects are negligible, and instead mechanical excitation plays the role of a thermal energy like source ($\Gamma$ analogous to $kT$) and $\Delta$ is analogous to an energy barrier resulting from particle entanglement.

The second quantity we measured during column collapse was the change in projected cross-sectional area, $\frac{\Delta A(t)}{\Delta T}$ of the column. The cross-sectional area displayed an initial increase during the first second of vibration indicating that prior to collapse and particle shedding from the column, the structure initially expands (dilates). The amount of dilation that occurred during collapse, $\max[\frac{\Delta A(t)}{\Delta T}]$, was an increasing function of $\Gamma$ for all experiments (See inset Fig. 6.6b).

The stretched exponential fit (Fig. 6.6) suggests that the column collapse process may be qualitatively similar across varied $\Gamma$ with only the timescale changing. However the variation in column dilation during collapse suggests that the internal particle processes leading to collapse may differ as a function of $\Gamma$. At small $\Gamma$ we hypothesize that frictional contacts are mobilized through vibration and thus particles can relax through a sliding process while collisions are not important. At higher $\Gamma$ we observe that particles appear

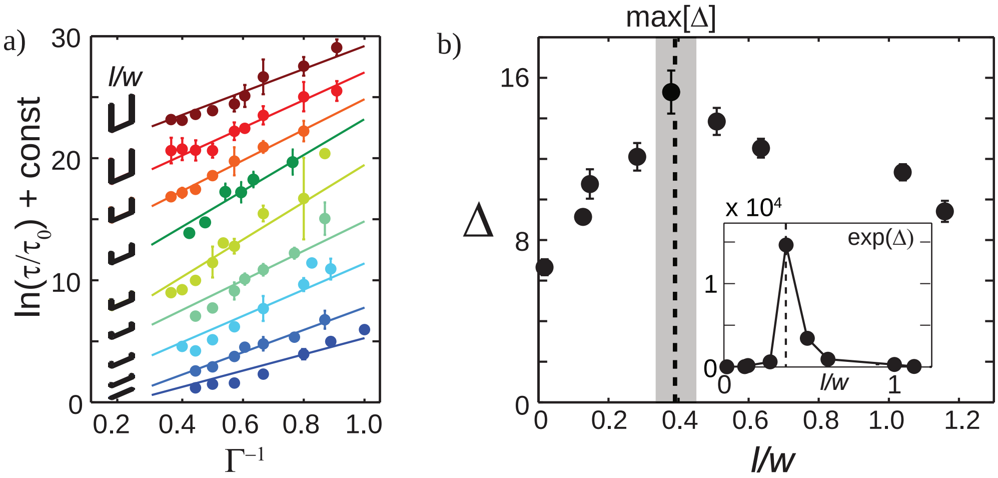

**Figure 6.7:** Time-scale of collapse process. a) The logarithm of the relaxation time versus inverse acceleration with exponential fit lines $\tau = f^{-1}e^{\Delta/\Gamma}$ ($\tau_0 = 1$ s). Curves are offset vertically for clarity. Error bars are standard deviation of 4 or greater replicates. b) $\Delta$ as a function of $l/w$. Dashed line indicates estimated maximum of $\Delta$ (see [16]). Error bars represent 95% confidence interval of the best fit lines from (a).

highly mobilized and often collide with each other which likely leads to the dilation we observe during the initial collapse process. Thus we hypothesize that in different regimes of $\Gamma$ the particle scale dynamics of collapse may differ, however the macroscale collapse time is well described by the stretched exponential.

Column collapse occurred through the separation of entangled particles during vibration. We therefore expected that the hindrance of motion due to particle entanglement—and thus $\Delta$—would increase monotonically with the size of the concave region and thus particle length. Instead we found that $\Delta$ was a non-monotonic function of $l/w$ (Fig. 6.7) with $\Delta$ reaching a maximum value at intermediate $l/w = 0.394 \pm 0.045$ [†]. $\Delta$ appears in an exponential and thus the relaxation time for fixed $\Gamma$ displays a surprising sensitivity to variation of particle shape (Inset Fig. 6.7b). We posit that the maximum in $\Delta$ is related to the statistics of particle entanglement within the bulk, and we next study entanglement propensity in theory and simulation.

---

[†] We estimate the maximum and standard deviation of $l/w$ in experiment using a weighted average of points near the peak

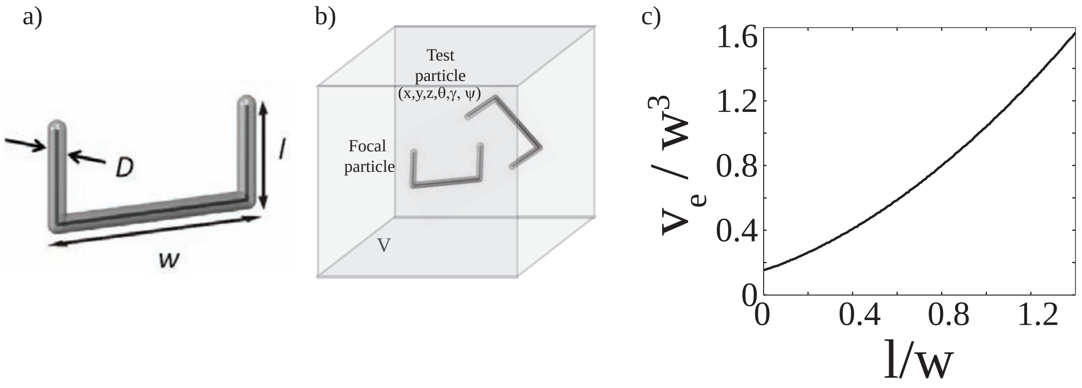

**Figure 6.8:** Overview of simulation. a) Three sphero-cylinders form a u-particle in computer simulation with dimensions given in the text. b) We compute the excluded volume of u-particles through a monte-carlo simulation measuring the probability for two randomly placed particles to overlap within a large volume V. c) Excluded volume of u-particles as a function of $l/w$.

## *6.5 Simulation*

In this section we describe the theoretical modeling of u-particle packing and stability as a function of particle shape. We discuss excluded volume which plays an important role in particle ensembles in which only steric interactions are important, such as our macro-scale granular particles. Next we introduce the random contact model proposed for colloidal rods. We apply this model to our u-particle system and show that we find good agreement between the model and our experimental results. We lastly generate u-particle ensembles in computer simulation and investigate the statistical packing properties of particle arrangements. We show that particles at intermediate $l/w$ display maximum particle entanglement. We discuss implications this maximum in particle entanglement has on bulk rheology as measured in experiment.

### 6.5.1 Random contact model of rods

The random contact model was originally proposed to describe the packing of straight, rod-shaped, colloids [82]. This model relates the bulk volume fraction, $\phi$, of the ensemble to the particle volume, $V_p$, and excluded volume, $V_e$, of the constituent particles. The random contact model assumes only that particles are homogeneously distributed in space and has been shown to work well for rod-shaped particles over a large range of aspect ratios

[82, 199, 82, 83]. Below we will derive the random contact model and explain how it is used in the calculation of "u-particle" packing statistics.

The particle's excluded volume is defined as the volume of space one particle excludes from another, averaged over all possible particle-particle configurations (Fig. 6.8). Another definition of $V_e$ is in relation to the probability of finding a two particles in contact within a larger volume, $V$. This can be represented as

$$V_e = pV \tag{6.1}$$

where $p$ is the contact probability. A simple example to consider is that of a spherical particle of radius $r$. A spherical particle excludes a volume $V_e = \frac{4}{3}\pi(2r)^3$ from another identical particle. Thus there is a volume of space, $V_e$, which particles cannot be placed in without overlapping the original particle. This again is indicative of the probabilistic nature of excluded volume since the probability to randomly place a sphere in a position overlapping the original sphere is $p = \frac{V_e}{V}$.

The relationship between volume fraction and $V_e$ follows as such. For a volume of space, $V$ with $N$ particles of volume $V_p$, the solid volume occupied by the particles is $V_o = NV_p$. The volume fraction is defined as $\phi = \frac{V_o}{V}$ which using equation 6.1 we can rewrite as $\phi = pN\frac{V_p}{V_e}$. We interpret $pN$ as the average number of contacts per particle within the packing, $C$, and arrive at the random contact equation [‡]

$$\phi = C\frac{V_p}{V_e} \tag{6.2}$$

The random contact model describes the bulk packing of homogenously distributed particles in free space, with particle properties $v_p$ and $v_e$ and average contact number $C$. This model has been tested in experiment and simulation with rod-shaped objects at the microscopic and macroscopic scale [199, 82, 83, 87] and surprisingly all experiments have found a similar contact number $C \approx 10$. We note that this model is applicable for particles

---

[‡] We note that in the original text of Philipse [82] the random contact model is introduced with the prefactor $2\langle c\rangle$ instead of $C$. In this case $\langle c\rangle$ is the ratio of total number of contacts by number of particles and multiplying this value by two gives, $C$ the average number of contacts per particle. We will use this form of the equation in the text and when comparing to studies using the alternate version we convert reported values of $\langle c\rangle$ to $C$.

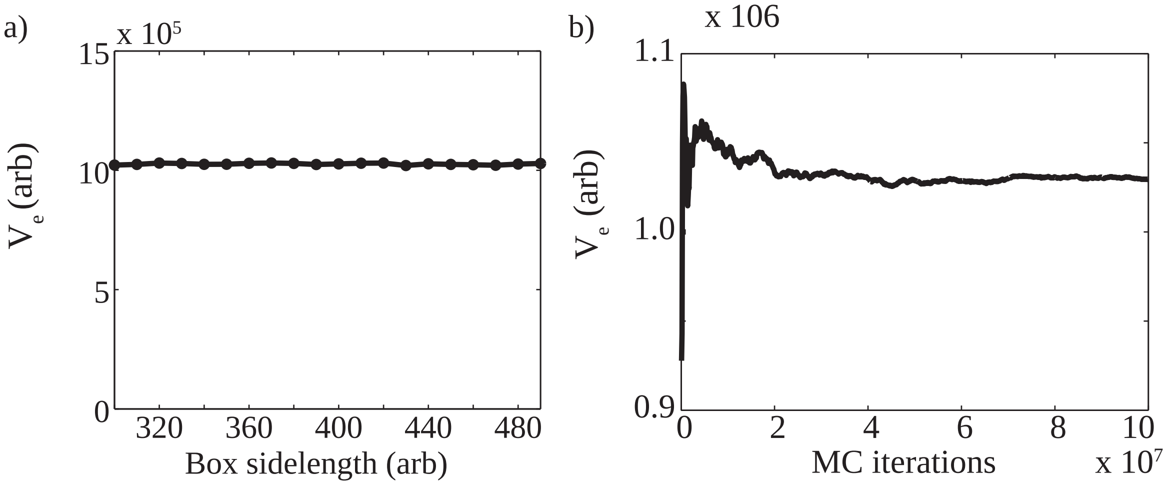

**Figure 6.9:** Convergence of numerical computation of $v_e$. a) Convergence as a function of bounding-box size b) Convergence as a function of monte-carlo iterations.

that pack with spatially uncorrelated contact points. Applying this model to spheres fails because contact points between particles are always spatially correlated (by definition a distance $D/2$ from the particle location).

We compute $V_e$ numerically for u-particles in a monte-carlo simulation by using the probabilistic definition of excluded volume. We form u-particles from a combination of three sphero-cylinders oriented at right angles with each other to form a u-particle. U-particle dimensions are normalized by the sphero-cylinder cross-sectional diameter, $D$. The width of the base sphero-cylinder is fixed at 14D and the barb lengths are varied from 0 to 16D, consistent with the u-particles used in experiment. In simulation we randomly place test-particles within a large volume, $V$, with respect to a focal particle fixed at the center. For each iteration of the computation, we choose a random location $(x, y, z)$ and random orientation (defined by the Euler angles of the particle, $\theta, \gamma, \psi$) to place the test particle at. We then check whether the test particle overlaps with the focal particle at this location-orientation combination. to determine the overlap of two u-particles we must simply compute the pairwise minimum distance between each particles constituent sphero-cylinders. If any of these 9 pair-wise distances are less than the sphero-cylinder diameter, $D$, the particles overlap. To detect if particles overlap we compute the minimum distance

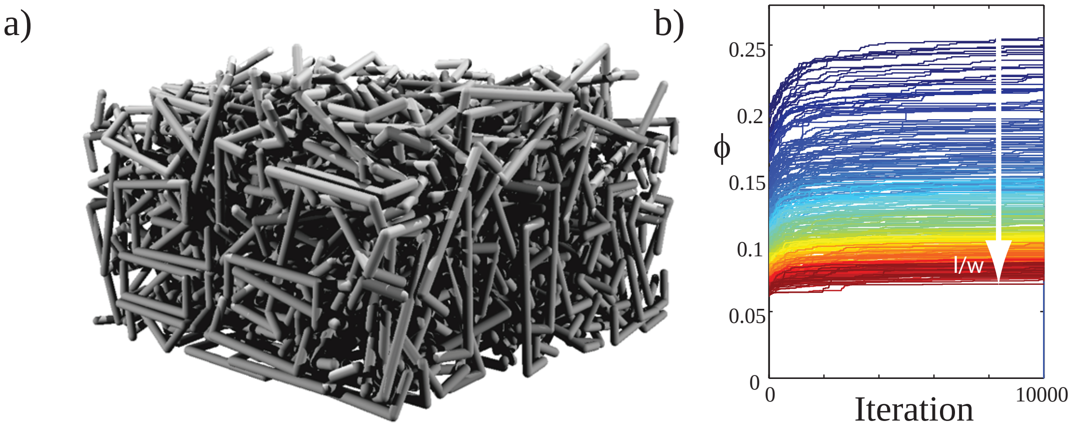

**Figure 6.10:** Computer simulated u-particle ensembles. a) A computer generated ensemble of u-particles of l/w = 0.35. b) Volume fraction of particle ensembles as a function of simulation iteration. Particle ensembles are packed together in a monte-carlo simulation until the volume fraction reaches steady-state. Particle $l/w$ is varied from 0-1.4 with increasing $l/w$ indicated by arrow.

between two line-segments along the centers of the sphero-cylinders. We compute the distance between line-segments using an algorithm originally developed for computer graphics [203] §. If particles are found to overlap we increment a counter $N_o$. After $N$ iterations of this algorithm, the fraction $\frac{N_c}{N} \rightarrow p$ and thus our calculation converges on the excluded volume $V_e = V\frac{N_c}{N}$ (Fig. 6.9).

We fit a polynomial to $V_e$ and find that $V_e = 0.460(l/w)^2 + 0.530(l/w) + 0.148$ (in units of $W^3$, see Fig. 6.8). We approximate the particle volume as $V_p = \pi W(D/2)^2 + 2\pi L(D/2)^2 + \frac{4}{3}\pi(D/2)^3$. Comparison of the measured volume fraction from experiments and the prediction from the random contact model show that the model is in good agreement with the data when using a contact number $C = 9$. This value of $C$ is close to the values reported for rod-packings of $C = 8.4 - 10.8$ which depends on preparation [82, 83, 199], which is surprising given the difference in particle shape between rods and u-particles. Having verified that the random contact model works for u-particles we may proceed with the calculation of packing statistics for u-particle ensembles.

---

[§] We have uploaded a Matlab implementation of this algorithm to http://www.mathworks.com/matlabcentral/fileexchange/32487-shortest-distance-between-two-line-segments

### 6.5.2 Packing simulations

We study the packing of u-particles in a computer simulation to identify properties of the particle entanglement within the pile. Particle packings are generated through a monte-carlo simulation. We do not perform molecular dynamics in these simulations, instead we solely enforce the condition that particle configurations which result in an overlap are not allowed. From these packings we study the statistics of u-particle entanglement.

To generate u-particle packings we used an exhaustive packing algorithm to generate close packings of non-overlapping particles. Packing proceeded in two steps: In the first step particles were placed at random position and orientation inside a cubic volume of cross sectional area ($52 \times 52D^2$) such that the particles did not overlap. If a newly placed particle resulted in an overlap this particle was removed and a new position was randomly selected. If after 10,000 iterations a suitable particle location was not found the algorithm proceeded to step two. In the second step particles in the volume were selected at random and displaced downwards a small random direction and distance $\frac{D}{10}$. If the new location of the particle resulted in particle overlap the particle was returned to the original location and a new particle chosen. The algorithm was halted after the center of mass height of the ensemble appeared to reach steady-state. The volume fraction of the simulated packings was determined by measuring the average height of the pile and multiplying it by the areal-dimension to obtain the occupied volume and then dividing this by the total volume of particles. A sample packing simulation and packing dynamics are shown in Figure 6.9. In simulation particles gradually approach a steady-state volume fraction which is consistent with the experimental data (Fig. 6.5c).

We hypothesized that particle entanglement within the column would influence the relaxation time during vertical vibration. Thus we expected that the maximum in $\Delta$ should correspond to a maximum in the density of particle entanglements. In simulation we defined two particles as entangled when the center line of one particle intersected the internal plane of the neighboring particle (Inset Fig. 6.6a). We measured the number of entanglements per particle, $N$, for each particle in simulation. The probability distribution function, $P(N)$, was sensitive to $l/w$ (Fig. 6.6a) with mean value $\langle N \rangle$ increasing monotonically with $l/w$

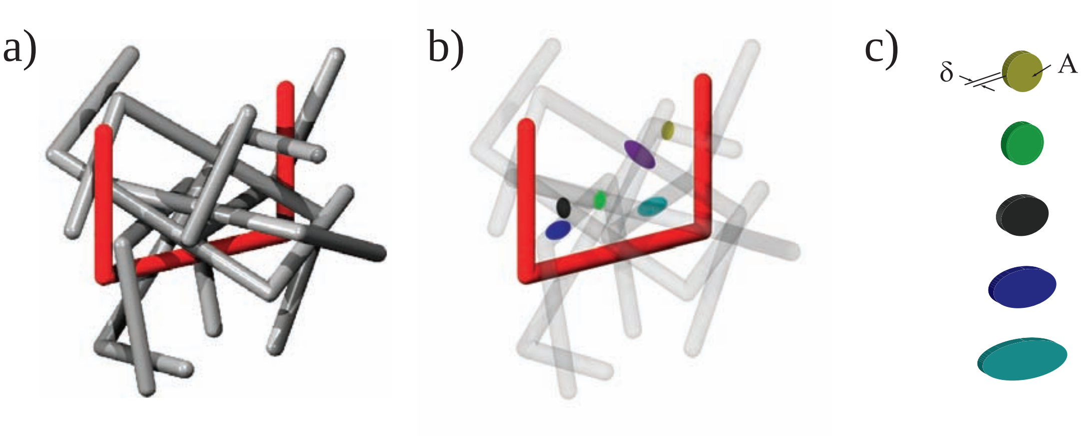

**Figure 6.11:** Entanglement counting in simulation. a) A rendering of entangled particles within the ensemble. b) To predict the number of entanglements within the packing we consider the infinitesimally thin volume of space within the focal particles (red) concave region. The intersection of entangled particles with this plane forms thin ellipses. c) The cross-sectional area of the intersection region can vary from a circle of diameter D to an ellipse with minor axis D/2.

(Fig. 6.6b). The increase was sub-linear indicating that $\langle N \rangle$ grew slower than that of the particle's convex area $(l-D)(w-2D)$.

The scaling of $\langle N \rangle$ with $l/w$ can be determined by considering the solid volume occupied by the entangled particles in the focal particles convex region (the convex area with infinitesimal thickness $\delta$). Assuming a homogeneous packing the solid volume in this region is $V_{ent} = \phi_f (l-D)(w-2D)\,\delta$. Since each entangled particle contributes only a portion to $V_{ent}$ in the shape of an ellipse of thickness $\delta$, on average $V_{ent} = \alpha \langle N \rangle \pi \delta \frac{D^2}{4}$ where $\alpha > 1$ accounts for the non-planar crossings (Fig. 6.12c). Solving the above relations yields

$$\langle N \rangle = \frac{4C}{\alpha} \left( \frac{V_p (l-D)(w-2D)}{\pi V_e D^2} \right) \tag{6.3}$$

With single fit parameter, $\alpha = 2.648 \pm 0.108$, we find excellent agreement between the predicted number of entanglements per particle and those measured in simulation (Fig. 6.12b).

The spatial density of particle entanglements is $\rho_{ent} = \langle N \rangle \rho$ where $\rho = \frac{C}{V_e}$ is the number density of particles (Fig. 6.12b). Substitution for $\langle N \rangle$ yields

$$\rho_{ent} = \frac{4C^2}{\pi \alpha} \left( \frac{V_p (l-D)(w-2D)}{V_e^2 D^2} \right) \tag{6.4}$$

and again the simulation and theory are in good agreement (Fig. 6.12c) using the previously determined fit parameters $C$ and $\alpha$. Furthermore the experimental maximum max[$\Delta$] at

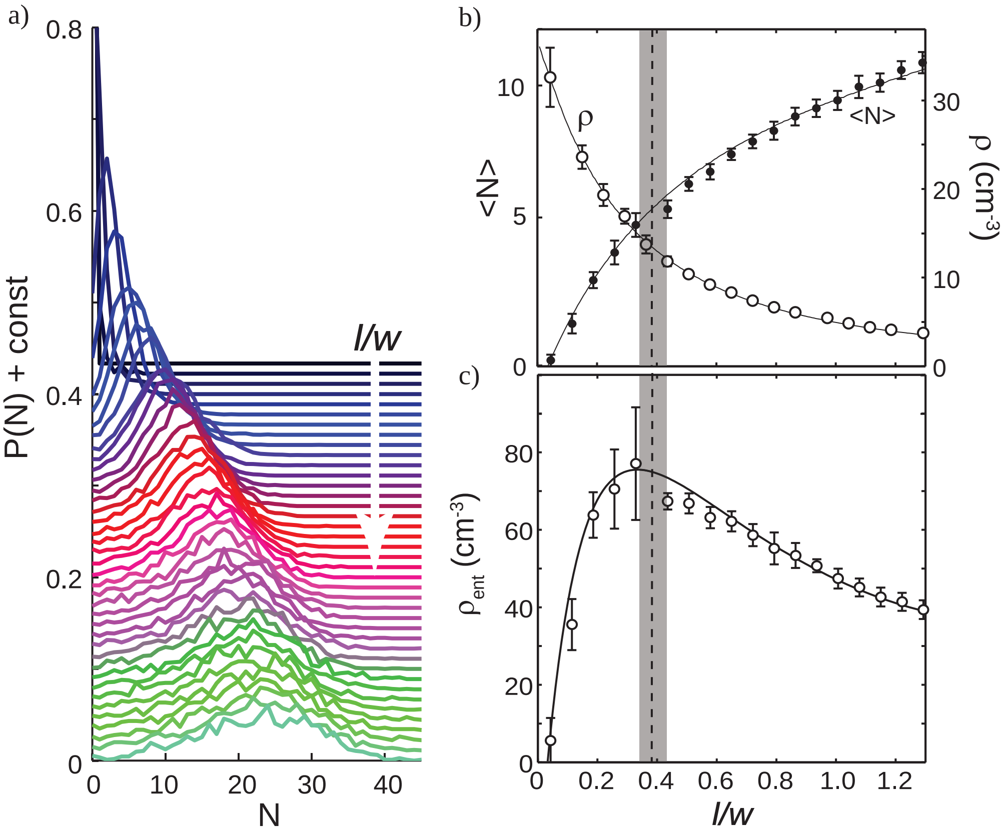

**Figure 6.12:** Statistics of particle entanglement in simulation. a) The probability distribution of entanglement number, $N$, as a function of $l/w$. Curves are shifted vertically for clarity; $l/w = 0$ at top and increases in increments of 0.036 down. Inset: red particle containing 6 entangled neighbors. b) Mean values for $N$ and $\rho$ measured in simulation (circles) and the theoretical fit (black line). c) Density of entanglements as a function of $l/w$ and the theoretical fit (black line). Vertical dashed line and gray bar correspond to the mean and standard deviation of the estimated maximum of $\Delta$ from experiment.

$l/w = 0.394 \pm 0.045$ is close to the value obtained in simulation and theory of $l/w = 0.340 \pm 0.015$ suggesting that the large relaxation times for the intermediate u-particle columns is due to the large density of mechanical entanglements.

## 6.6 Conclusion

Similar to rod-like particles [199, 82, 83, 87], columns formed from u-particles are stabilized through the inhibition of particle rotation and translation among the entangled particles. The addition of the transverse ends which form concave u-particles leads to mechanical entanglement and increases column stability. However the increase in entanglement with increasing length is offset by the decrease in particle packing density. These two trends conspire to generate a maximum in the density of mechanical entanglements in collections of non-convex particles of intermediate $l/w$–thus columns of these particles most strongly resist separation.

Vibro-fluidization has been previously used to study the relaxation of dry granular materials under gravity [68, 204, 69]. However this method has not been applied to characterizing the strength of cohesive GM. We envision that vibration-relaxation experiments like those reported here will be useful to explore rheological properties of fluid or electrostatic mediated cohesive GM. Although granular materials in the natural world often posses some interstitial fluids, there is still much to be learned about cohesive granular materials.

Macroscale model-systems like those described here and elsewhere [205, 206] are useful tools to explore how particle shape influences ensemble rheology. Future study of the particle-scale dynamics of non-convex particles may provide further insight into the rheology of entangled or crowded particulate systems. For instance, model systems may have application to better understand the particle scale dynamics of anomalous diffusion within the crowded cellular environment [207, 208, 209, 210]. Because, particles found in nature are often non-spherical [44] we hope that experiments like those described here will advance the experimental and computational tools we have to study non-spherical or even non-convex particulate systems.

The random contact model utilized to explain the optimum geometry for entanglement of u-shaped particles assumes only uncorrelated particle contacts within the bulk. Thus we expect the results to apply to rigid non-convex particulate systems of all scales. A recent study of suspension rheology found that convex particles of differing shape collapsed to a viscosity-stress master curve while concave particle did not collapse to this curve; this difference was attributed to particle entanglement effects [188]. At the micro-scale, polymers with rigid pendants oriented perpendicular to the polymer chain increase internal molecular free volume and hinder polymer motion which significantly affects rheology similar to geometric entanglement [211]. At the macroscale strain-stiffening of model polymers is associated with entanglement [205]. Even organisms can benefit from geometric entanglement. For example the fire ant *Solenopsis invicta* and the army ant *Eciton burchelli* create waterproof rafts and shelters–which have been described as akin to living chain mail [118]–through the interlocking and entanglement of limbs and mandibles [113, 112].

# CHAPTER VII

# FIRE ANT WORKER SIZE EFFECTS ON TUNNEL CONSTRUCTION

## *7.1 Summary*

We now focus on an active granular system, collections of the fire ant *Solenopsis invicta*. Social insects such as fire ants work together to complete tasks, however different individuals within a colony may vary in task proficiency. We investigated if fire ant worker body size influenced the ability to construct tunnels-a key component of subterranean nests. We monitored excavation by worker groups in a substrate of small wetted glass particles in two-dimensional arenas. Morphological and network features of the tunnel system were measured. Total tunnel area did not differ significantly between groups of large and small workers, although the tunnel area of control sized workers was significantly larger than that of large workers. Moreover, large workers created wider but shorter tunnels, with slower growth rate of tunnel number. However, edge-vertex scaling and degree distribution of the tunnel network were similar across all treatments. In all cases, the amount of excavated material was correlated with the number of active workers. Our study reveals that morphological features of excavated tunnels show modest variation when constructed by workers of varying sizes, but topological features associated with the tunnel network are conserved. These results suggest that important behavioral aspects of tunnel construction-and thus nest building-are similar among morphologically distinct members of fire ant societies. [*]

---

[*] This chapter has been published in *Journal of the Royal Society Interface*, 2012 entitled "Effects of worker size on the dynamics of fire ant tunnel construction"

## *7.2 Introduction*

The remarkable success of social organisms is due in part to their ability to share and divide colony level tasks among individuals [125]. For example, most social insects (ants, social bees, social wasps, and termites) cooperate to construct nests [212]. Social insect nests are thought to have been critical to the evolution of sociality [213]. Nests serve to protect the colony from predation and exposure to the elements, while providing a location with homeostatic features [214] for rearing the young and safely storing food [123, 122, 125]. In addition to providing protection from the elements and predators, the architecture of the nest organizes the colony and influences the frequency and type of social interactions that occur. These interactions facilitate information transfer and worker recruitment and are important to the colony's daily function [131, 215, 216, 127, 217]. Thus the efficient construction and maintenance of a nest is fundamental to the success of social insects.

Many ants construct subterranean nests which consist of underground tunnels and chambers formed through the excavation of soil [125]. Nests are often initiated by newly mated queens [218, 125] and are later cared for by the worker population. Nest construction and repair is an essential task that colonies must face throughout their life. For instance ant species that remain in the same nest must continuously expand to accommodate colony growth while ants that relocate periodically must construct entirely new nests [219, 220, 125, 221, 222].

The basic mechanics of tunnel construction are similar among ant species (Sudd, 1969): workers loosen a soil pellet from the tunnel face with their forelimbs and mandibles and then carry the pellet in their mandibles to the surface where it is deposited in a pile (see Fig. 7.1). Groups of ants that collectively excavate ultimately form a network of interconnected tunnels and chambers [131, 126] that is thought to facilitate traffic flow, food and brood storage, and gas and temperature regulation [123, 122, 125]. The formation of this tunnel network is a self-organized process in which workers operate according to excavation rules which may differ across species or even across worker caste [131, 223, 224, 126, 217, 225].

The excavation behaviors of social insects and the dynamics of tunnel network formation have been studied extensively through laboratory experiment [131, 226, 129, 227, 228, 229,

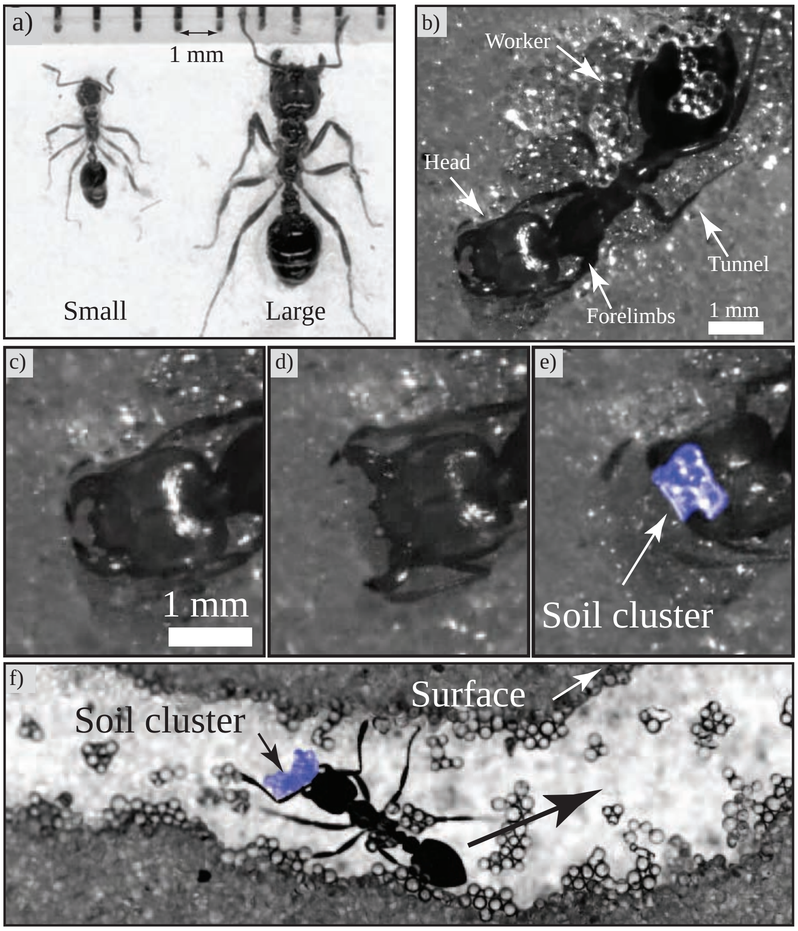

**Figure 7.1:** *S. invicta* workers digging tunnels. a) Comparison of size difference between small and large workers. b) Ventral view of a tunneling worker. c-e) The mechanics of tunnel excavation involve loosening, carrying, and transporting substrate (0.25±0.04mm diameter wetted glass particles) from the tunnel face to the surface (see supplementary material for videos). Excavated material is loosened and manipulated using the mandibles (particle cluster rendered blue in image to improve visibility). f) Excavated material is held in the mandibles and carried to the surface.

230]. Environmental factors such as soil granularity and cohesiveness influence the morphology and orientation of tunnels [226, 129, 231] while the excavation dynamics (digging rate, network growth rate) are a function of group size [132, 227] and worker age [217].

Morphological features of the ant could also play a role in digging proficiency and thus the ability to construct a nest. For example, worker body size is an important trait that affects colony function and is believed to be under evolutionary selective pressures. Moreover, variation in body size (polymorphism) in social insects can influence the likelihood and effectiveness of performing certain colony tasks such as the rearing of brood or foraging for food [232, 233, 234, 235, 236]. Since mandible width correlates with body size [237] and since tunnel excavation involves use of mandibles to loosen and carry soil to the surface, a natural hypothesis is that body size should correlate with digging proficiency. However, the relationship of ant size and tunneling performance has not been investigated.

The red imported fire ant (*Solenopsis invicta*) is an excellent species to examine the role of worker size on tunnel construction. First, worker size in *S. invicta* is influenced by genetic and environmental factors [238, 239, 139], and workers display considerable variation in size. For example worker head width varies continuously over a nearly three-fold range (Fig. 7.1a). Second, the large subterranean nests constructed by *S. invicta* can house hundreds to hundreds of thousands of colony members and are among the most complex structures made by ants [126]. Fire ant nests have a characteristic structure which can be divided into three components: (1) a surface mound densely filled with tunnels, (2) subsurface tunnels directly below the mound that extend downwards up to 1.5 m deep and connect to larger horizontal chambers, and (3) shallow (1-10 cm deep) foraging tunnels which radiate horizontally away from the mound and can be upwards of 50 m in total length [139, 240, 127, 140]. Finally, *S. invicta* is an invasive species and thus in addition to constructing nests in their native range of the Amazon basin of South America *S. invicta* build nests within the diverse array of soil types found in the Southern United States (like clay, dry and wet sand) [127].

In this paper, we investigate the role of worker body size on tunnel excavation in *S. invicta*. We visualize tunnel network growth and ant digging behavior by teams of *S.*

*invicta* workers of varying body size in quasi two-dimensional (2D) digging arenas, similar to those previously used in studies of ant tunnel construction [226, 227, 229]. Based on the expectation that increased mandible size allows ants to carry larger loads (See [236] and data in section 7.6.2), we hypothesize that larger ants should outperform smaller ants during tunnel excavation. Through morphological and topological analysis of the growing tunnel network we show that workers of all size exhibit similar digging proficiency and we show quantitatively how worker size influences (i) the rate of tunnel growth (ii) the morphology of excavated tunnels (iii) and the topology of the interconnected tunnel network.

## *7.3 Methods*

### 7.3.1 Ant husbandry

Five mature *S. invicta* colonies (colonies A-E) were collected during the summer and fall of 2008 and 2009 from roadsides outside of Atlanta, GA, USA. Colony members were separated from the soil in the laboratory using the water drip method [241]. Colonies were then housed in plastic bins that contained an enclosed nest area made from petri dishes and an open foraging arena. Colonies were provided ad libitum water and insects as food.[†]

Digging experiments were carried out with three treatments of worker size: small workers, large workers, and control workers. Large and small workers from each colony were isolated using a sieving process in which ants migrated downward from a light source through a series of sieves with decreasing mesh size. Small workers were collected from the bottom sieve (bounding mesh size $< 0.71$mm) and large workers were collected from the top sieve (bounding mesh size $> 1$ mm). Control workers, which represented a random sample of workers from the focal colony, were collected from the remaining worker groups, having gone through the same sieving process as the large and small worker treatments. The body size distribution of mature *S. invicta* colonies is skewed such that a majority of the colony are smaller workers [127] and thus the control groups were comprised of a relatively large number of small workers with a few larger workers.

Approximately 150 workers of a given size class were then separated using the wet mass

---

[†] These experiments were performed in conjunction with co-authors Nicole Mazouchova and Mateo Garcia.

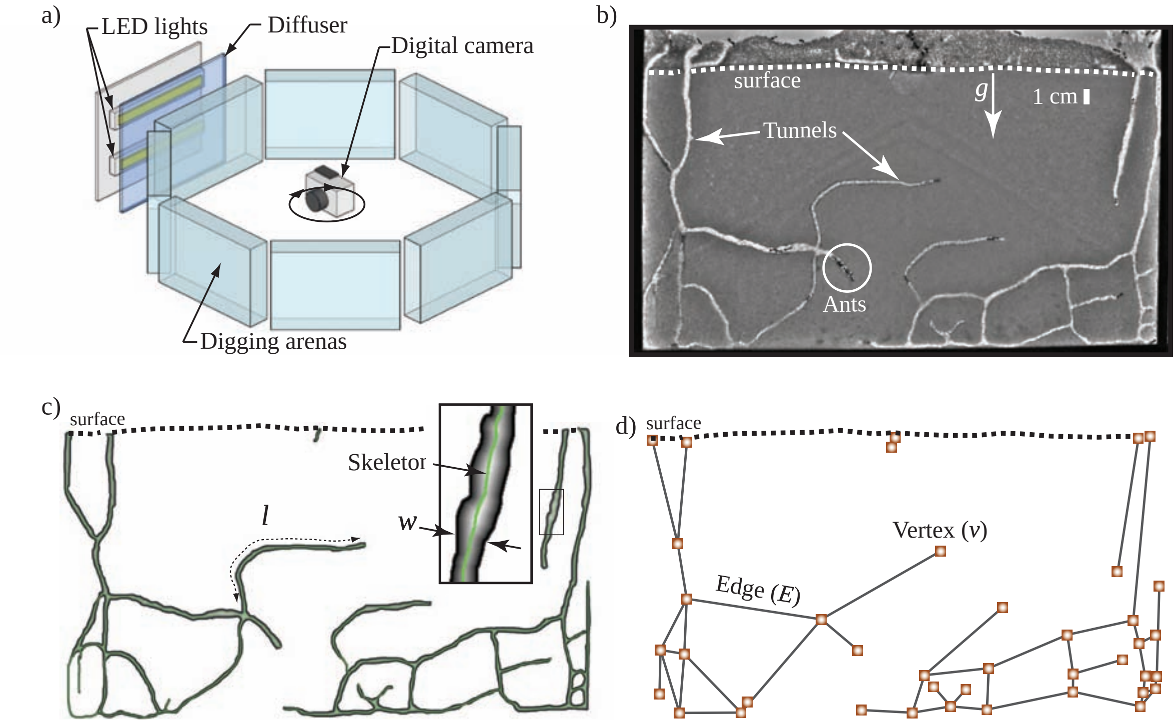

**Figure 7.2:** Overview of the experimental setup and digging arena. a) Time lapse images were collected from eight arenas simultaneously using a rotating camera. b) Quasi-two dimensional digging arenas were filled with a substrate of wetted 0.25 mm diameter glass particles. Tunnels extend downward vertically from the surface and branch subsurface forming a connected network of paths. Excavated material was deposited by the ants in a loosely packed pile on the surface. c) Tunnel networks were represented as binary image masks. d) The network representation considered tunnels as edges and the branch and end points as vertices.

of 25 individuals from each treatment as a gauge of the relationship between worker mass and worker number (wet mass of 25 individuals: small 14.56±1.53 mg, large 56.73±9.34 mg, control 29.34±9.18 mg). Groups of ants were momentarily sedated by placing the confinement chamber atop an ice bath for 30 seconds after which they were transferred to the digging arena. As in previous digging experiments, queen and brood were not present during experiments [227, 228, 229, 230, 231]. Brood items were explicitly excluded because large and small *S. invicta* workers display different behaviors in their presence [127].

Digging trials were conducted on groups of workers drawn from five colonies (A - E). Each trial spanned three days. Eight digging trials (an octet) were prepared on a single date. Octets always included a combination of large, small, and control worker groups from a given colony. Colonies A, B, C were used to supply worker groups for octets on two or more occasions while worker groups from colonies D and E were each used in only a single octet. Between the varied treatments and test dates, 71 digging trials were performed in total with a breakdown of 23 large worker treatments (A=5, B=5, C=8, D=3, E=3), 23 small worker treatments (A=6, B=5, C=8, D=2, E=2), and 25 control treatments (A=5, B=6, C=8, D=3, E=3).

### 7.3.2 Digging arenas

We studied excavation in the laboratory so that we could isolate and test for the effects of ant size on tunneling proficiency. As in other studies, quasi-2D digging arenas were used to enable visualization of ant behavior and tunnel growth simultaneously [133, 132, 226, 227, 228, 229, 230, 231]. Arenas were created from two pieces of glass separated by a steel spacer, forming a 27 × 34 × 0.3 cm digging chamber (Fig. 7.2). Similar to previous studies [226, 129, 230], we used approximately spherical, wetted 0.25 mm diameter glass grains as a digging substrate. The arenas were initially filled with dry grains to a height of approximately 20 cm, leaving a 9 cm gap at the top of the arena. Grains were then wetted with 100 mL of water which was allowed to drain through the digging arena (and out a porous bottom) prior to the introduction of the ants. Water is important for the stability of tunnels [226], and it is known that expansion of *S. invicta* nests in nature typically occurs after rainfall [127]. The substrate was not intended to mimic the natural soils of the *S. invicta* habitat, which vary widely in water content and particle size distribution. Instead, the media was chosen to control the digging substrate properties (cohesiveness, granularity) and produce reproducible excavation conditions among replicate experiments. We note, however, that this substrate is similar in particle size and wetness to sandy soils in which fire ant nests in nature can be found [127]. Eight digging arenas arranged on an octagonal frame with a digital camera in the center were simultaneously used during experiments (see Fig. 7.2). Digging experiments were performed in a darkened room. The camera was pointed at each arena in turn by a stepper motor controlled by LabVIEW. Images of the arenas were captured every 5 minutes, illuminating a backlight momentarily behind each arena prior to image capture.

### 7.3.3 Analysis

Tunnel images from 12 hour increments were used to create a black-and-white image mask of the tunnels in Adobe Photoshop (Fig. 7.2). Image masks were imported into Matlab and tunnel morphology and network topology was measured (see appendix for details). Morphological measurements included total projected tunnel area, A, total path length of tunnels, L, and tunnel width W. Furthermore the path length of tunnel segments between branch points, l, was recorded. Network measurements included the number of edges, E, and vertices, v, (Fig. 7.2) along with the degree of each vertex, k, defined as the number of edges coming together at the focal vertex.

All statistics were performed using JMP (SAS software; Cary, NC) or Matlab (Mathworks; Natick, MA). Statistical tests for differences among treatments were computed using an ANOVA considering treatment as a fixed effect, colony as a random effect, and date (octet) nested within colony as a random effect. Tukey's HSD was used to determine differences among treatments. We used linear and non-linear regression to determine fit parameters where necessary. We used ANCOVA to test if linear slopes differed among treatments and ANOVA to test for differences in y-intercepts. We used the method of [242] to estimate non-linear regression fit parameters. All results are presented as the least squares mean ± the standard error of the measurement.

## *7.4 Results*

Upon introduction into the arena, workers in all *S. invicta* treatments began digging within 2-4 hours. We estimated that only 20-30% of the workers in the groups participated in the digging process at any one time; the remaining workers aggregated on the arena wall above the digging substrate. Tunnels were initiated at the surface and extended downwards for all treatments. Observations of fire ant workers at the tunnel face indicate that ants excavated and manipulated the digging substrate using their mandibles as well as their forelimbs (Fig. 7.1) as has been described for many other ants [243]. After approximately 24 hours lateral tunnel branches were created off the main tunnels. As the lateral tunnels grew in length they often recombined with previously created tunnels forming new tunnel junctions and paths through the network. Tunnels were excavated through the successive trips of workers from the tunnel face to the surface and the excavated material was deposited in large piles on the surface.

### 7.4.1 Tunnel area, length, and width

We characterized the shape and size of the tunnel networks created by different treatments. The total size of the tunnel network was measured by the two-dimensional projected area. Since tunnel networks can grow in size through both the widening and lengthening of tunnels we also measured the length and width of tunnel segments. The final area after 72 hours, A, significantly differed among size treatments (Fig. 7.3 and Table 7.4.1; $F_{2,60} = 5.34$, p = 0.007). There was no significant difference in A between large and small (p = 0.344) and control and small (p = 0.168) workers; however the control groups produced larger tunnel networks than the large treatments (p = 0.005). Worker size had a significant effect on the final length of tunnels, L (Table 7.4.1; $F_{2,60} = 13.520$, p ¡ 0.0001). The tunnels of the large treatments were significantly shorter in total tunnel length compared to the small (p = 0.010) and control group (p ¡ 0.0001) treatments. However the total tunnel length between the small and control treatments was not significantly different (p = 0.095).

The growth rate in the first 12 hours was significantly influenced by treatment (Fig. 7.3;

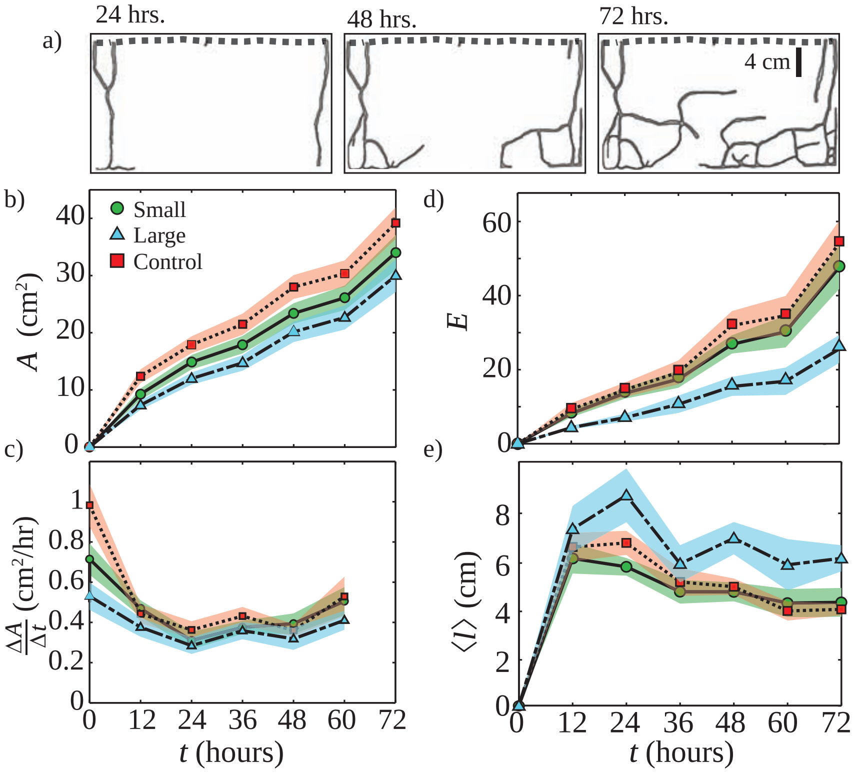

**Figure 7.3:** Digging dynamics in quasi two-dimensional *S. invicta* arenas. a) Image masks showing tunnel network growth as a function of time. b) Tunnel area versus time for small, control, and large ants (green circles, red squares, and blue triangles respectively) . Shaded areas are ± S.E. c) Digging rate ($\Delta A/\Delta t$) versus time. d) The number of edges in the tunnel network increased in time. e) The mean path length, $< l >$, between vertices in the network decreased in time after 72 hours.

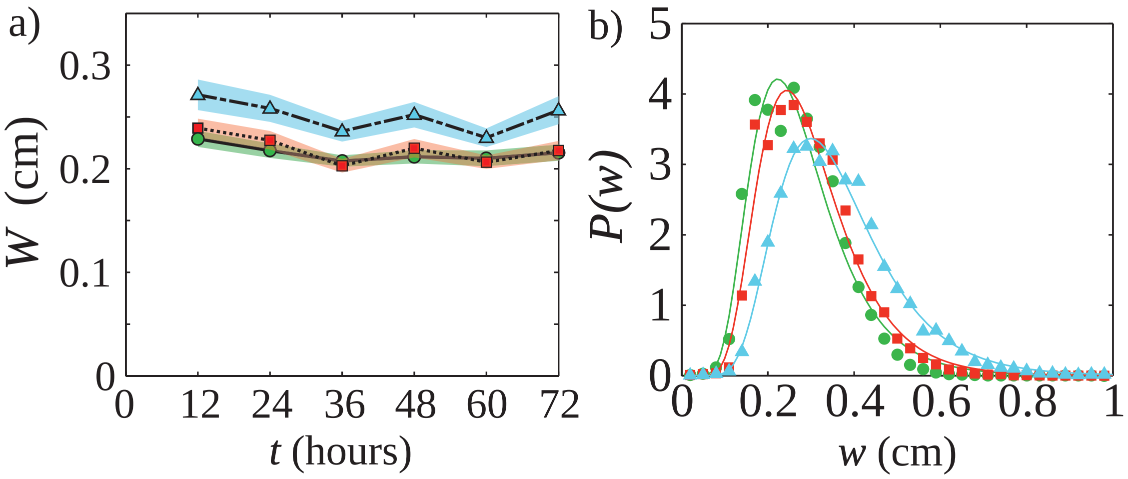

**Figure 7.4:** Tunnel width. a) The mean width, W, of the tunnels vs time for small, control and large ants (green circles, red squares, and blue triangles respectively). Shaded areas are ± S.E. b) The probability distribution of local tunnel width, $P(w)$, is fit by a log-normal function (described in the text) with parameters given in Table 7.4.1.

$F_{2,60} = 8.336$, p = 0.0006). The control group outperformed the large workers (p = 0.0004) but the difference in initial growth rate between the control and small worker groups was not significant (p = 0.078). Furthermore the difference in initial digging rate between the large and small worker groups was not significant (p = 0.161). For all treatments, the average tunnel width, W, was approximately constant in time indicating that tunnels grew in size primarily through lengthening and not widening (Fig. 7.4). Tunnel width was significantly affected by worker size (Fig. 7.5; $F_{2,60} = 16.167$, p¡0.0001) and groups of large workers created the widest tunnels, which were significantly wider than both the control (p=0.0002) and small treatment (p¡0.0001) tunnels. The small worker and control groups created tunnels which were not significantly different in width (p=0.522). The probability distribution of the local width, w, evaluated along the center of tunnels was fit by a log-normal function, $P(w) = \frac{1}{\sqrt{2\pi} w\sigma} \exp(-\frac{(ln(w)-\mu)^2}{2\sigma^2})$, for all treatments where and are fit parameters (Fig. 7.4b; $R^2 > 0.98$ for all treatment fits; See Table 7.4.1 for $\mu$ and $\sigma$.

### 7.4.2 Tunnel network properties

We measured the network topology to understand how the connectivity of the tunnel networks varied among worker treatments. Junctions where tunnels terminated or came together are called vertices and the tunnel sections that connected these vertices are called edges [244]. The analysis included counting the number of edges and vertices and examining the functional relationship between the two. We also counted the number of edges emanating from a vertex; this is defined as the vertex degree. Lastly the path length $l$, is defined as the distance an ant must walk to traverse an edge.

The number of edges in the network, $E$, grew throughout each test (Fig. 7.3). In the final network E was significantly affected by treatment ($F_{2,60} = 11.001$, p ¡ 0.0001). Although $E$ in the small and control treatments did not differ significantly (p = 0.436), $E$ for the large treatment was significantly less than $E$ for both small (p = 0.005) and control treatments (p ¡ 0.0001). The relationship between the total number of vertices and total number of edges composing the network was linear, $E = \beta v$, with slope $\beta$ independent of treatment (See Fig. 7.5a; ANCOVA parameters for slope difference, $F_{2,70} = 0.356$, p = 0.702).

**Table 7.1:** Mean (±s.d.) values of *S. invicta* tunnel network structure, topology and activity among three treatments composed of groups of small, large and control workers after 72 h of digging. Area is the total excavated area. Length is the total length of tunnels and width is the mean tunnel width. The probability distribution function of the tunnel widths was fitted by a log-normal function, where $w$ is the local tunnel width and $\mu$ and $\sigma$ are fit parameters. The tunnel network consisted of edges representing tunnels and vertices representing tunnel junctions. A connected component is a self-contained network in which all vertices are accessible from the other. The number of surface entrances and connected components did not differ among treatments. $N_{12h}$ is the number of subsurface ants at 12 h and $\langle N \rangle$ is the average number of subsurface diggers over the duration of the test.

| | Treatment | small | large | control |
|---|---|---|---|---|
| | replicates | 23 | 24 | 24 |
| *Spatial* | Area (cm$^2$) | 34.03±14.75 | 29.99±13.72 | 39.18±13.84 |
| | Length (cm) | 159.17±61.73 | 119.17±51.07 | 186.04±70.28 |
| | Width (cm) | 0.22±0.04 | 0.26±0.07 | 0.22±0.05 |
| | $\mu$ (Log-normal fit param.) | -1.35±0.05 | -1.07±0.03 | -1.27±0.05 |
| | $\sigma$ (Log-normal fit param.) | 0.40±0.06 | 0.37±0.02 | 0.38±0.04 |
| | Mode$[P(width)]$(cm) | 0.22 | 0.3 | 0.24 |
| *Network* | Vertices | 50.70±34.54 | 25.65±19.20 | 61.44±39.76 |
| | Edges | 49.78±31.03 | 27.83±17.61 | 58.72±34.98 |
| | Connected components | 5.13±3.40 | 4.70±2.65 | 5.24±3.72 |
| | Surface entrances | 7.13±4.32 | 5.91±3.30 | 7.56±4.55 |
| *Activity* | $N_{12h}$ | 5.00±4.72 | 4.52±3.38 | 9.76±7.30 |
| | $\langle N \rangle$ | 8.46±6.49 | 7.01±4.59 | 10.96±6.74 |

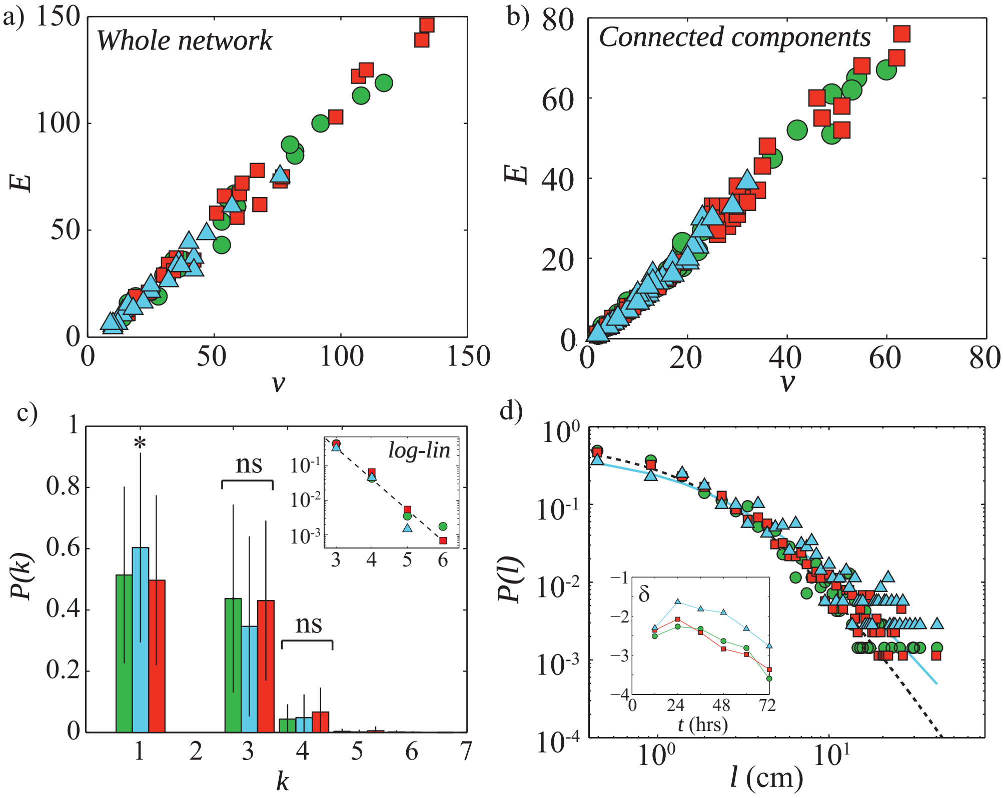

**Figure 7.5:** Tunnel network properties. a) edge to vertex relationship for small, control, and large treatments (green circles, red squares, and blue triangles, respectively) were linear for the entire network b) edge-vertex relationship of individual connected components. c) Distribution of vertex degree. The $*$ symbol denotes statically significant effect of treatment and n.s. indicates no treatment effect. d) The probability distribution of path lengths was fit by an extended power law, (see text). Small and control treatment fits are given by the black dashed line and the large treatment fit is given by the blue line. The inset shows the time dependence of the extended power law exponent $\delta$.

Tunnel networks were often composed of several connected components-each of which were independently connected sections of the tunnel network that did not merge below the surface (See Fig. 7.2 for example). The edge to vertex relationship for the connected components was linear with slope independent of treatment and slightly larger compared to that of the entire network ($\beta = 1.13 \pm 0.01$; ANCOVA parameters for slope difference, $F_{1,351} = 0.003$, p = 0.957). Treatment did not significantly affect the size of the largest connected component, measured as the number of edges in the connected component normalized by the total number of edges (Fig. 7.5; $F_{2,60} = 1.194$, p = 0.312). The largest connected component with respect to the total network size was on average, $v_{conn}/v = 0.56 \pm 0.21$, with a value of 1 representing a completely connected network and a value near 0 representing many unconnected components.

The vertex degree probability distribution, P(k), significantly differed among the three treatments for the k = 1 vertices only (Fig. 7.5; $F_{2,60} = 9.565$, p = 0.0002). Vertices with k = 1 comprised tunnel ends and surface entrances. Networks created by large worker groups were composed of slightly more degree 1 vertices compared to the small (p = 0.005) and the control (p = 0.0003) treatments. Differences between treatments for k ¿ 1 were not significant (k = 3, $F_{2,60} = 0.521$, p = 0.597; k = 4, $F_{2,60} = 1.167$, p = 0.319). The tail of the degree distribution was linear on a semi-log axis for all three treatments indicating a possible exponential decay of P(k) at large k (inset Fig. 7.5). Furthermore, the number of surface vertices (entrances) did not significantly differ between treatments (Table 7.4.1; $F_{2,60} = 1.134$, p = 0.328).

The probability distribution of path lengths was fit by an extended power law function, $P(l) = Q(l + l_0)^{\delta}$, for all treatments (Fig. 7.5). The constant was constrained $Q = -(\delta + 1)(l_0)^{\delta+1}$ due to the normalization condition of the probability distribution. The fit parameters for $P(l)$ between the control and small worker treatments did not differ significantly (small vs. pooled, $F_{48,44} = 0.659$, p = 0.920; control vs pooled, F46,46 = 1.577, p = 0.063). However the large worker treatment did significantly differ from the pooled small-control data ($_{F54,92}$ = 2.469, p ¡ 0.0001). The fit exponent, $\delta$ represents the probability to find longer tunnels in the network and a decrease in corresponds to a decrease in this probability (Fig. 7.5). Thus, over time, all tunnel networks experienced a "shortening" effect in which the path length between vertices decreased. This was also observed in the mean path length (Fig. 7.3) which decreased over time.

We compared $P(l)$ for the small and control networks at 48 hours and the large networks at 72 hours and found that they did not significantly differ (small vs. pooled, $F_{103,43} = 1.414$, p = 0.101; control v pooled, $F_{99,47} = 1.058$, p = 0.423; large vs. pooled, $F_{94,52} = 0.843$, p = 0.766). Thus the exponent $\delta(t)$ is similar in shape for all treatments but the large worker treatments lag behind the smaller and control worker treatments in time by roughly 12-24 hours. A similar time lag of the large treatment network was also observed in the number of edges (Fig. 7.3) and tunnel length. This indicates that topological features of large treatment networks were similar to the other treatments but grew at a slower rate.

### 7.4.3 Subsurface workers during digging trials

We measured the number of workers below the surface in the captured images at 12 hour increments during tunnel excavation (Fig. 7.6). The number of workers subsurface after 12 hours differed significantly among the treatments ($F_{2,60}$ = 12.6195, p ¡ 0.0001). The control treatments outnumbered the small (p = 0.0002) and large (p = 0.0002) treatments in quantity of subsurface workers ($F_{2,60}$ = 12.6195, p ¡ 0.0001). However the number of subsurface workers did not differ significantly between large and small treatments (p = 0.9996). In contrast, after 72 hours of digging, the number of ants subsurface was not significantly different among treatments ($F_{2,60}$ = 2.4576, p ¡ 0.0942). Linear regression indicated that the number of subsurface ants increased over time for all treatments (small: $R^2 = 0.07$, N = 138, test against zero slope, $F_{1,136} = 9.768$, p = 0.002; control: $R^2 = 0.03$, N = 150, test against zero slope, $F_{1,148} = 4.77$, p = 0.03; large: $R^2 = 0.15$, N = 138, test against zero slope, $F_{1,136} = 24.16$, p ¡ 0.0001).

To determine how worker activity affected digging performance we computed the mean number of subsurface workers $\langle N \rangle$ (over the three day tests). The mean number of workers subsurface during the digging tests was linearly correlated with the final tunnel area, $A = \alpha \langle N \rangle$ , ($\alpha = 3.62$ cm$^2$, $R^2 = 0.3$) with independent of treatment (ANCOVA test for

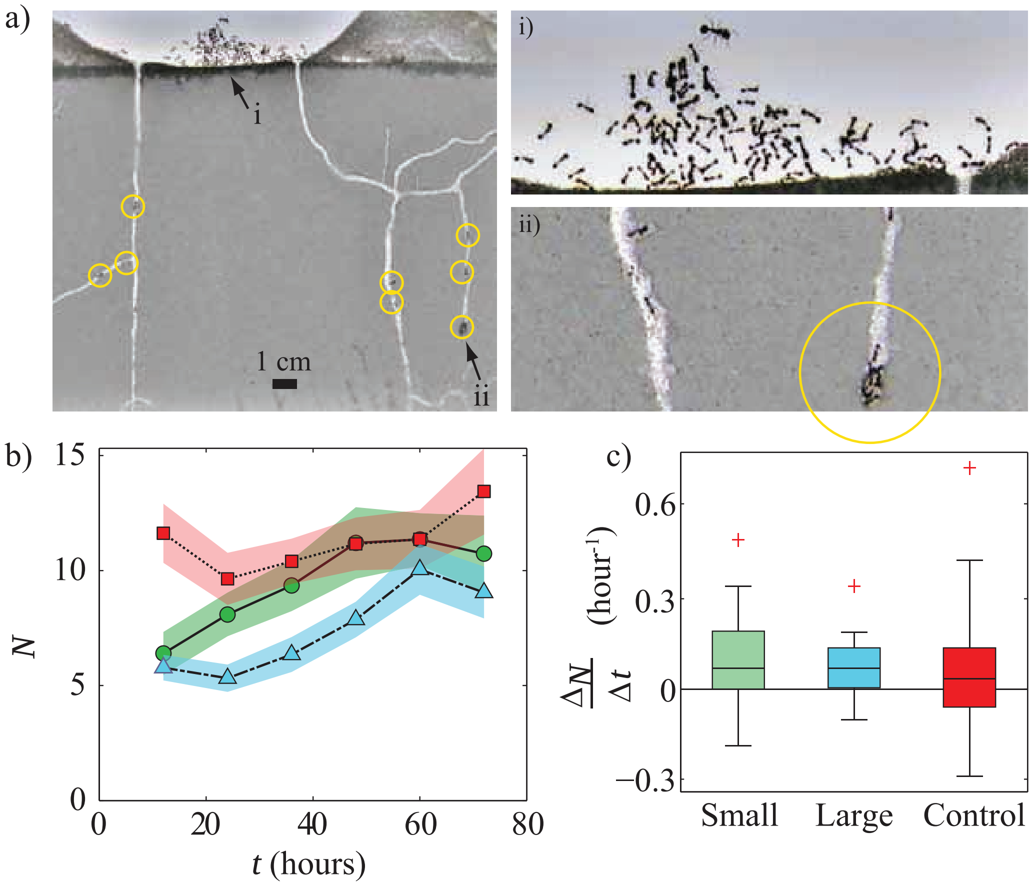

**Figure 7.6:** Worker activity during tunnel construction. a) Workers in an arena were typically found either (i) clustered together above the surface of the digging substrate or (ii) subsurface engaged in digging activities. Shaded areas are ± S.E. b) The number of ants subsurface (N) as a function of time. c) The mean time rate of change of N for the three treatments.

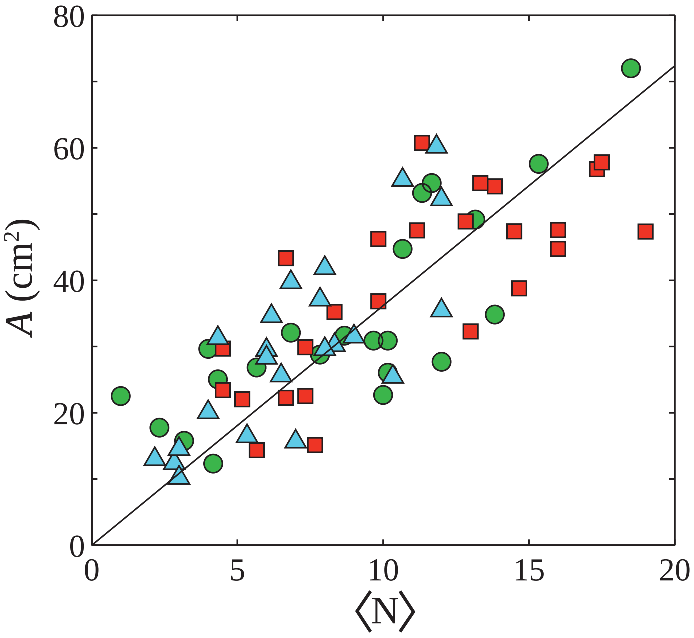

**Figure 7.7:** Tunnel area vs subsurface workers. Tunnel area after 72 hours was positively correlated with the time average number of ants ¡N¿ found subsurface over the same period $[A = \alpha\langle N\rangle;\ \alpha = 3.62]$. The slope, $\alpha$ did not differ among the three treatments. Small, control, and large treatments are represented by the green circles, red squares, and blue triangles respectively.

difference in slope among treatments; $F_{2,64} = 1.210$, p = 0.305), see Fig. 7.7.

## *7.5 Discussion*

Our results indicate that despite a factor of three in body size (four-fold difference in mass), excavation rate was insensitive to fire ant size. However, the control treatments (containing a mixture of approximately 70% small and 30% large ants) significantly outperformed the large treatments. We now discuss the morphological, topological, and behavioral differences exhibited by the three treatments during tunneling trials.

### 7.5.1 Tunnel area, length, and width

Groups of large and small workers excavated tunnel networks which did not differ significantly in total tunnel area (Fig. 7.3). This indicates that worker size does not have an effect on digging proficiency and *S. invicta* workers of all sizes are capable of excavating or repairing tunnels. This lack of difference in the areal rate of tunnel growth between the large and small workers is surprising given the differences in body size. In addition to larger mandible width in larger ants, a scaling argument that considers both metabolic energy consumption [245] and stride frequency versus body mass predicts that the average walking speed of an ant increases as (body mass)$^{1/4}$ [246]. Experiments across 24 ant species are consistent with this scaling. Thus, although larger *S. invicta* workers might walk faster and carry larger loads, the observation that their digging performance is comparable to that of small workers suggests that behavioral factors in addition to body size are likely important in determining excavation rate.

We observed slight morphological differences in tunnel shape between the large and small treatments. Larger workers built wider and, thus, shorter tunnels compared to small workers. The tunnel width however was only 20% wider in the tunnels of the large workers compared to the small and control treatments (Fig. 7.4). This was also surprising given that the head width of large workers is approximately three times that of the small and control treatments.

Control groups significantly outperformed large worker treatments from the same colony, excavating tunnels of approximately 35% greater final area. The proximate cause of this difference was that the initial growth rate of the control treatments was nearly twice that of the large treatments and thus control treatments took an early lead in tunnel growth and maintained it for the duration of the experiment (Fig. 7.3). After 24 hours the digging rate was similar among all treatments. We posit that the high initial digging rate of the control treatments was due to the large number of digging ants observed in the initial 12 hours (Fig. 7.6). It is noteworthy that tunnel shape did not significantly differ between the control and small treatments. This may be due to the fact that natural body size distribution of *S. invicta* colonies is skewed such that smaller workers of head width less than 0.75 mm account for 70% of the colony [247, 236].

### 7.5.2 Worker activity

The final tunnel area and length were positively correlated with the number of ants observed below the surface over the duration of the experiment (Fig. 7.7). The slope of the best fit line to this data was independent of treatment. These observations suggest an explanation for the variance in final tunnel area-larger tunnel networks were created when more workers participated in the digging process. Such a relationship has also been observed in a field study [217]. The independence of slope also indicates that individual ants excavate at approximately the same rate. From the best fit slope, we estimated that the upper limit digging rate for a single *S. invicta* worker was 0.05 $\text{cm}^2$/hr independent of worker size. For comparison, the worker excavation rate we observed for *S. invicta* workers was similar to those observed for other ant species in similar laboratory experiment (*Messor sancta* 0.024 $\text{cm}^2$/hr [131], *Lasius niger* 0.027 $\text{cm}^2$/hr [230]) and field study (*Pogonomyrmex badius* 0.0156 $\text{cm}^2$/hr [217]). We note that our estimate is an upper bound of the digging rate because we were likely underestimating the number of digging workers in our measurement.

It is unclear why relatively few ants (20%-30%) participated in excavation in our experiments. A previous study of laboratory colonies of *S. invicta* reported that workers were only active for 10 out of every 30 minutes [248]. However traffic and overcrowding at the tunneling site may also be important in determining the number of workers that participate in digging. Studies of worker flow on foraging trails [249, 250, 251] and within artificial nests have shown that traffic dynamics are important in organizing worker movement [41] and determining tunnel size and branch locations [252, 253]. Furthermore the diameter of foraging tunnels in *S. invicta* nests in nature decrease in size away from the nest, which may reflect a decrease in worker traffic at these distances [140]. Thus the constraints imposed by locomotion within confined and crowded environments including traffic and multi-ant interactions could be important in ant nest construction and warrant future study.

### 7.5.3 Tunnel network topology

Several topological properties such as the edge to vertex ratio and degree distribution of the tunnel networks did not depend on worker size. The number of edges increased linearly with number of vertices with a slope slightly greater than 1 for both the whole network and the connected components. In a previous study of tunnel networks of the ant *Messor sancta*, the edge-vertex relationship followed a power-law ($E \propto V^{1.31}$) [133]. We hypothesize that the difference in edge-vertex relationship between M. sancta and *S. invicta* is a reflection of the different excavation rules individual ants follow during tunnel construction.

The network topology of all three treatments was similar when rate effects were removed. The rate of tunnel lengthening of the large treatments lagged behind that of the small and controls groups and after 72 hours the large worker networks contained approximately the number of edges as in the small and control worker networks 12-24 hour earlier. This slower growth rate of the larger worker tunnels resulted in slower overall network edge-vertex growth in the large treatment networks and when this time delay was accounted for, the differences in the edge number and path length distribution, $P(l)$ vanished among the three treatments. It is likely that large workers exhibited this time lag because of a slower initial worker recruitment leading to slower tunnel growth. The invariance of the tunnel networks among the three treatments when properly rescaled by the different tunnel growth rates suggests universal excavation behaviors among fire ant workers of all sizes.

### 7.5.4 Conclusion

Our study revealed that *S. invicta* workers of all body sizes constructed subsurface tunnel networks with comparable spatial and topological features. The distribution functions characterizing the tunnel morphology were similar across treatments, and the topological network measures were conserved across worker size as well. The control group created the largest, most complex nests, largely a result of more rapid initial digging. Thus our results provide support to the hypothesis of adaptive demography such that the worker size distribution of a colony is tuned to optimize ”success”, of which tunnel construction is a critical aspect. In our system the natural (control) distribution of worker sizes within nests was most effective at undertaking tunneling behavior, and the behavioral programs directing tunnel construction are similar across workers of different sizes. We also found that a large percentage of the worker population was inactive at any time during digging experiments. Consequently, nest size was regulated by the fraction of workers in the group that participated in digging.

While our study focused on digging in a controlled substrate composed of slightly wet particles, we note that fire ants are found in a diverse array of terrains and soil types and it is known that the nest properties are dependent upon the soil properties [127]. For instance, in fire ant nests in nature, the above surface nest mounds created from cohesive soils like clay are substantially larger than mounds created from sandy soils [127]. It is likely that the soil properties determine the stability and size of these structures; for instance the cohesive soils are held together through interparticle capillary forces or van der Waals forces and thus stick together strongly [226]. Such observations indicate that future study is required to elucidate the factors important to tunnel excavation in varied soil types.

Finally, the division of labor among worker groups in social insect colonies is a complex process, and understanding the behavioral rules that govern task allocation is important to understanding the biology of social insects. The division of labor and problem solving abilities of social insects has already led to significant technological advances such as ant colony optimization algorithms [254]. Therefore detailed understanding of the tunnel navigation and cooperative excavation abilities by social insects may provide principles for the development of autonomous subterranean robot teams. Such autonomous systems could work together to excavate or navigate in subterranean environments like those found in disaster sites or after earthquakes. The development of robotic excavators may shed light on the important constraints of cooperative tunnel excavation and thus provide further information about the challenges that tunneling ants must overcome.

## *7.6 Appendix*

### 7.6.1 Details of experimental apparatus

In figure 7.8 we show an image of the interior of the octoganal structure which holds the digging arenas. The structure consisted of four main components: (1) A digital camera was mounted in the center of the octagon. (2) A stepper motor controlled the rotational orientation of the camera and could be rotated 360°. (3) Quasi two-dimensional digging arenas were placed on the faces of the octagon shape and mounted to the structure with C-clamps. (4) Rows of LED lights were mounted behind the digging arenas and they were turned on and off using a relay controlled by the parallel port output from a computer.

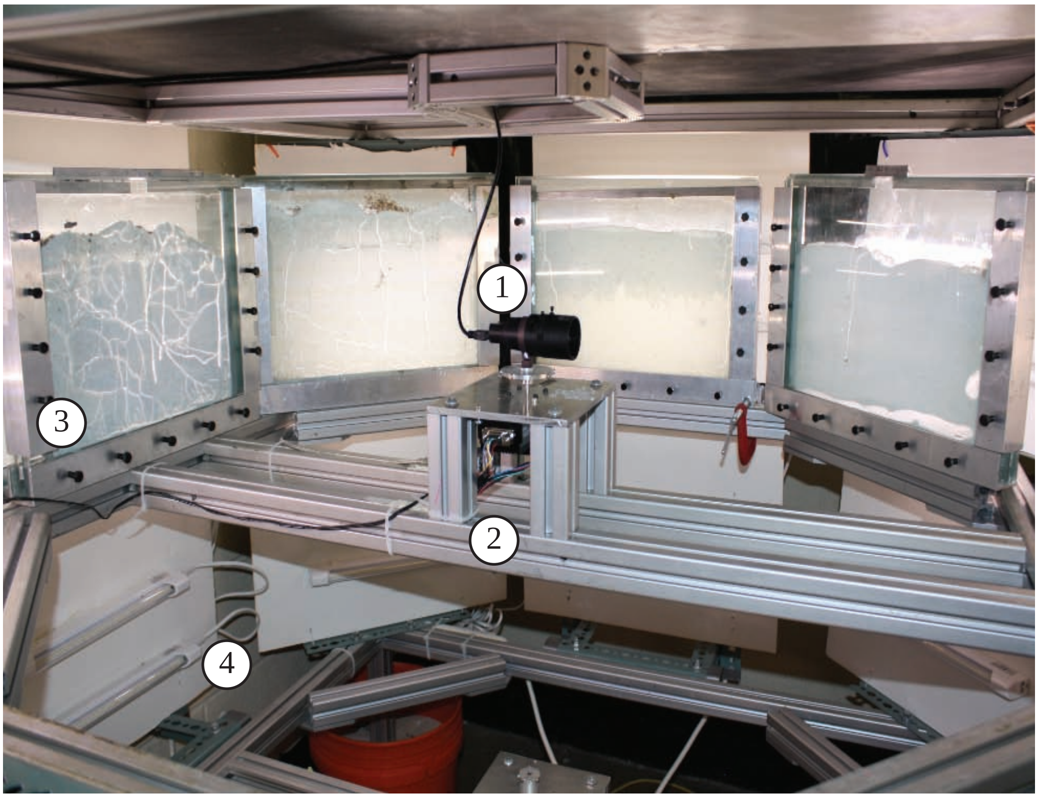

**Figure 7.8:** Image of the inside of the octoganal mounting structure for monitoring ant tunnel construction.

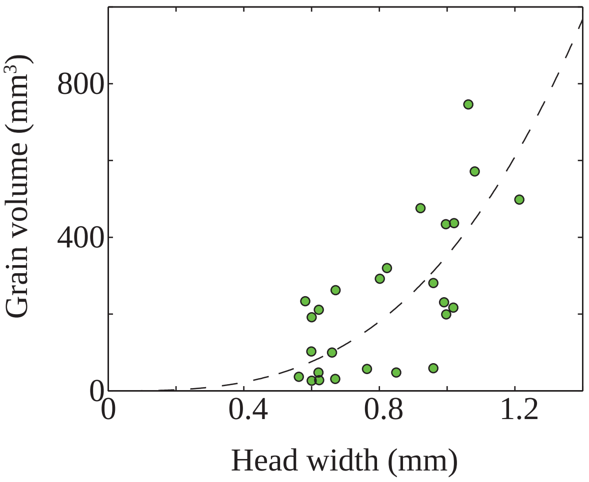

**Figure 7.9:** Soil pellet size as a function of ant head width. Data reproduced from [236]. Dashed line is a fit to the equation $V = mw^3$ where $w$ is head-width.

### 7.6.2 Previous evidence of ant size effect in carrying capacity

In a previous study E.O. Wilson monitored fire ant workers removing gravel pellets from the entrance of their nest and studied the relationship between pellet mass and ant head width [236]. To relate volume of particle carried with the ant head width we have have re-plotted this data as pellet volume versus ant head-width (Fig. 7.9) assuming a constant density of gravel as 3 g/cm$^3$. We find that the data follows a cubic relationship between head-width ($w$) and volume, $V = mw^3$.

If we assume particles are spherical this implies a linear relationship for head-width and particle cross-sectional dimension,

$$\frac{4}{3}\pi R^3 = mw^3 \tag{7.1}$$

$$R = \left(\frac{3m}{4\pi}\right)^{1/3} w \tag{7.2}$$

Thus this evidence suggests for solid particles, larger workers carry larger loads determined by their mandible width. It is not clear if this relationship holds when the loads to be carried are amorphous and deformable, as is the case for wetted soil pellets.

### 7.6.3 Example tunnel networks

In figure 7.10 we show final tunnel networks from different digging experiments among the three treatments.

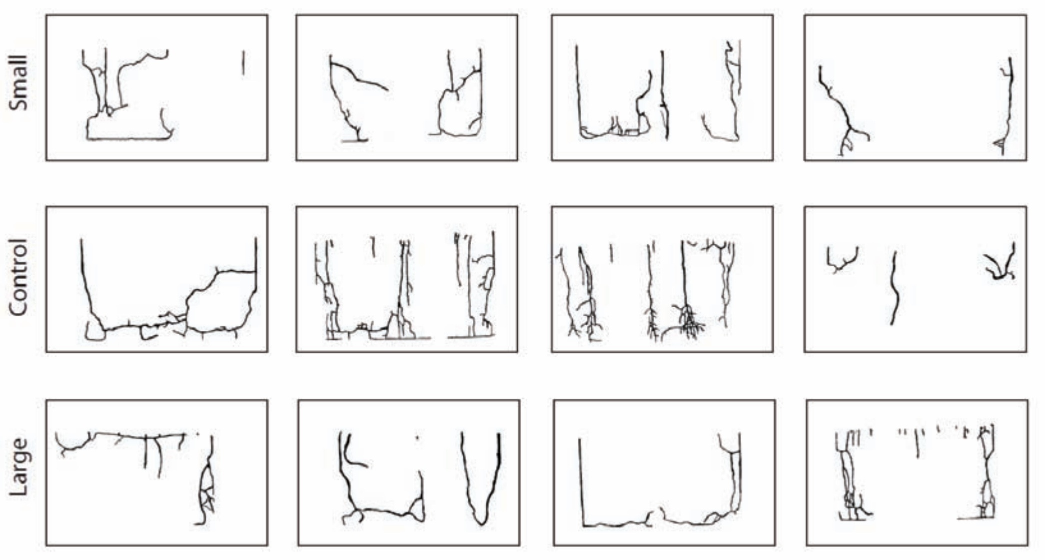

**Figure 7.10:** Examples of tunnel networks from different replicates and treatments. Horizonal rows are replicates from treatment labeled on the left.

# CHAPTER VIII

# LOCOMOTION IN TUNNELS

## *8.1 Summary*

Movement emerges from effective interactions of a locomotor with its environment. Principles of biological terrestrial locomotion have been discovered on unconfined vertical and horizontal substrates and have inspired high-performing robots. However a diversity of organisms construct, inhabit, and move within confined spaces. Such animals are faced with locomotor challenges including limited limb range of motion, crowding, and visual sensory deprivation. Little is known how these organisms accomplish their locomotor tasks, and such environments challenge human-made devices. Here we study the confined locomotion of the fire ant *Solenopsis invicta* which constructs subterranean tunnel networks (nests). Laboratory experiments reveal that ants construct tunnels with diameter, D, comparable to body length, $L = 0.35 \pm 0.05$ cm. Ants achieve rapid locomotion within these environments; their tunnels allow for effective limb, body, and antennae interaction with walls which facilitates rapid slip-recovery. To examine the limits of slip-recovery in artificial tunnels we perform perturbations consisting of rapid downward accelerations, which induce falls. Below a critical tunnel diameter, $D_s = 1.31 \pm 0.02$ L, falls are always arrested through rapid deployment of appendages and antennae which engage with tunnel walls to jam the falls. $D_s$ is comparable to the size of incipient nest tunnels ($D = 1.06 \pm 0.23$ L) supporting our hypothesis that fire ants engineer their environment to simplify their control task when moving through the nest, likely without need for rapid nervous system control. We predict that such a strategy could allow swarming robot teams to construct and move within confined, crowded environments. [*]

---

[*] This chapter is reproduced from the manuscript "Climbing, falling, and jamming in subterranean ant locomotion" which is currently in review in *PNAS*

## *8.2 Introduction*

Terrestrial animals and increasingly robots move in a diversity of environments, including running across flat landscapes [255], swimming in sand [74], climbing vertical surfaces [256], and squirming through cracks [257]. Much progress in discovery of locomotor principles has been made by simplifying the environment into relatively featureless, flat and unconfined spaces [258]. Recent appreciation of the importance of mechanics in the interaction with the environment has helped understand how stable and robust movement emerges as a result of appropriately tuned dynamics of foot-ground interaction [259, 260]. For example rapid perturbations to locomotion may be corrected by so-called "preflexes" [261] in which mechanical design of the limb and appropriate kinematics enable rapid recovery from perturbation [262, 263, 264]. The incorporation of these principles into the design of robotic devices has led to advances in robotic, legged, locomotors [265]. However when robots operate in more complex environments than planar landscapes mobility tends to be limited [266]. Thus understanding how organisms can accomplish spectacular locomotor feats and why robots often fail requires understanding of locomotor-environment interactions [142].

Many subterranean-dwelling organisms live and move within confined spaces in their environments [267, 268]. The morphology [269, 126] energetic costs [270, 271, 272, 273], and genetic basis [274, 275] for creating subterranean burrows and nests, which are examples of the "extended phenotype"[276], have been studied across a diversity of organisms. However, the constraints on locomotion of individuals and groups inhabiting these environments are largely unexplored. Rapid locomotion within the confines of a subterranean nest is essential for inhabitants to escape or respond to predators [267, 277], evacuate during flooding [278], or transport resources and information effectively. However lack of vision [267, 268, 279], limited limb mobility [267], and excessive crowding among individuals [280] would seemingly challenge efforts at rapid locomotion within confined environments. Thus we seek to understand how such environments influence the mobility and stability of animals moving within them.

Ants are excellent organisms with which to study confined locomotion. Many ant species construct large underground nests through the excavation of soil [125]. Nest shape and size-in addition to ant shape and size-varies widely across species but typically consists of vertical tunnels that interconnect larger chambers used for food storage and brood rearing [126, 125]. A majority of an ant colony worker's life is spent below the surface within the nest-tending to brood or performing routine nest maintenance-and only near the end of life do worker ants forage above surface [125, 281, 282, 127]. The evolutionary pressure of subterranean life has led to several adaptations among ants such as partial or complete loss of vision in some species [283, 284] and long-range acoustic [285, 286, 287] and chemical communication systems [283, 288, 289]. However, almost nothing is known about how ants move through their confined nest environments.

We hypothesize that ants have developed strategies and adaptations for rapid movement within nests, particularly during crucial times such as nest reconstruction or evacuation. A species that frequently must contend with evacuation and reconstruction of their nest is the red imported fire ant (*Solenopsis invicta*). Fire ants originate from the Pantanal wetlands in South America, which are subject to seasonal rains and flooding [127]. Fire ant colonies construct large and relatively complex subterranean nests [127] which can be up to 2 m deep and contain greater than 50 m in length of tunnels [138]. As an invasive species in the Southern United States fire ants have demonstrated their proficiency at constructing nests within a wide range of soil conditions [127]. Construction of such large nests demands the ability to move repeatedly and stably within the nest confines while transporting soil.

In this paper we seek to identify principles of locomotion within confined environments which challenge animals with an entirely different set of locomotive constraints than in above-ground study. We investigate the effects of subterranean confinement (tunnel diameter) on the mobility and stability of a subterranean organism: the fire ant (*Solenopsis invicta*). We show that climbing in confined environments is a robust mode of high-speed locomotion, in which slips, falls, and frequent collisions with the environment do not necessarily prevent high-speed ascent and descent. We also demonstrate an unusual behavioral response of fire ants when dislodged from the tunnel wall-the use of antennae as limb-like appendages to arrest and jam falls. Overall, we find that stable locomotion within subterranean environments is a function of the local tunnel morphology within which the organisms move.

## *8.3 Methods and apparatus*

### 8.3.1 Ant collection and care

The *S. invicta* colonies were collected during the spring of 2012 from roadsides outside of Atlanta, GA. Nests were excavated and transported to the laboratory and ants were separated from the soil using the water drip method [290]. Colonies were housed in open plastic bins in a temperature controlled room with 12 hour on, 12 hour off lighting. Colonies were provided ad libitum water and insect larvae as food.

### 8.3.2 Digging experiments

The digging arenas were placed on a rotating stage controlled by a stepper motor (Lin Engineering) which was located 76 cm from a 110 kVp, 3 mA X-ray source. An image intensifier was located 103 cm from the source and a Phantom v210 camera (Vision Research) was used to visualize the X-ray images. Samples images were taken at angular increments of 0.9 degrees. We chose tunnels that were not adjacent to a wall (Fig. 8.1) and extracted the tunnel shape using the Chan-Vese active contours method [291]. Tunnel properties were measured using the Matlab image morphology toolbox. We computed the distance transform of the tunnel shape using the Matlab command *bwdist* and considered the maximum value of the distance transform as the effective tunnel diameter.

### 8.3.3 X-Ray CT digging experiment

Groups of fire ant workers were challenged to dig tunnels in the laboratory. 8.2 cm diameter cylindrical containers (Fig. 8.1) were filled to a depth of 12 cm with a dry granular material of particle size 250 ± 50 $\mu m$ (Jaygo Inc., Dragonite Soda Lime Glass beads, #5210). Arenas were first fully immersed in water to saturate the soil and then allowed to drain for 1 hour. Wet soil is known to induce digging in natural fire ant nests [127]. Workers were introduced into the arena and were allowed to dig for 24 hours with a constant light source maintained above to stimulate digging. We evaluated tunnel the tunnel cross-section shape at various depths among 10 separate digging trials, each containing multiple tunnels, which resulted

**Figure 8.1:** Overview of the X-Ray CT digging trials. a) Digging arena consisted of a circular plastic, or aluminum container of diameters 8.2 or 3.8 cm, filled to a height of approximately 12-15 cm with a simulated soil of monodisperse 50, 210, or 810 $\mu$m diameter, wetted, glass beads. b) A horizontal cross-section from X-Ray CT reconstruction at a depth of 6.8 cm from the surface. Top and bottom arrow indicate two tunnels not adjacent to arena wall. Four other tunnels are present but against the tunnel wall. c) Cross-section of the top (left) and bottom (right) tunnels from (b) with extracted tunnel shape from active contours method shown as green (left) and purple (right) lines.

in 2,262 observations of tunnel diameter.

In a second set of nest construction experiments we $^{\dagger}$ varied soil moisture content and particle size. We used collections of glass beads of diameter 50 $\mu$m, 210 $\mu$m, or 595 $\mu$m which were mixed with water and prepared at moisture contents of 1,3,5,10,15, and 20% (measured by mass). Supplementary Table 1 summarizes particle size distribution. Digging substrate was placed in a 3.8 cm diameter digging arena filled to a height of 14.5 cm. A 1 cm diameter plastic tube inserted into the center of the surface constrained the workers to initiate digging away from walls. We generated uniform compaction of the moistened media by sieving the wetted granular material through a mesh grid with 1 mm grid spacing using VTS 500 single vibrator system. Groups of 100 workers were introduced into the digging arenas and we evaluated tunnel shape in CT scans at 10, 15, and 20 hours. Eight separate colonies were tested at each particle size and moisture content combination resulting in 185 excavation experiments. We measured tunnel depth and cross-sectional shape at a depth of half the tunnel depth. We tested for the effect of particle size, water content, and the

---

[†] These experiments were performed by Daria Monaenkova. Daria and I both analyzed the data using the analysis code I wrote.

interaction (particle size)×(water content) using an analysis of variance in which colony and test date were treated as random effects.

### 8.3.4 Climbing experiments

#### *8.3.4.1 Arena experiments*

Quasi two-dimensional arenas, $27 \times 34 \times 0.3$ cm in size, were filled with the same wetted granular material as described in Digging experiment 1 were prepared to allow for ant visualization during locomotion (See [290] for details). A group of 150 ants excavated in the simulated soil for 48 hours. We observed tunnel locomotion using a macro lens and a Phantom v210 camera, capturing video at 500 Hz. We encouraged high speed ascent and descent through ant-created tunnels by triggering an alarm response among the workers in which we exhaled gently into the nest entrance at the top surface.

#### *8.3.4.2 Glass tunnel climbing experiments*

We used a simulated-nest environment to study ant climbing in smooth glass tunnels in which we could view the interaction of all limbs and antennae with the climbing substrate (See Fig. 8.2). An enclosed, light-proof box which contained a wetted porous floor (plaster of paris) served as a nest, and housed 150-300 worker ants during the course of an experiment. The simulated-nest was connected to a foraging arena through a series of nine vertical observation tunnels ranging in inner diameter from 0.1 - 0.9 cm in increments of 0.1 cm. Tunnels were 10.7 cm long and we observed a 9.6 cm length of them. Tunnels were illuminated by LED lights for visualization with a high-speed camera. Ad libitum water and food were provided in the foraging arena which encouraged worker traffic to and from the nest. A heat lamp was placed over the foraging arena to create a temperature gradient between the “above-surface” foraging arena and the ”subterranean” simulated-nest. The simulated-nest and foraging arena setup encouraged ants to freely traffic within the tunnels and allowed us to observe tunnel climbing while performing a natural, unperturbed behavior.

Ant climbing posture was computed in Matlab in which we isolated the ant body from the stationary background using an active contours algorithm [127]. We computed the vertically oriented bounding box of the ant-profile with the horizontal dimension of this box representing $x_{span}$. Climbing ants could be found at any angular location along the tunnel wall and thus we removed all runs in which ants were visualized from the lateral sides. Furthermore in measuring horizontal limb span we only included ant-postures in which the body axis measured from gaster to head deviated from the vertical by less than 10°. This resulted in 483,525 observations of climbing posture.

#### *8.3.4.3 Glass tunnel perturbation experiments*

To observe the falling response of ants within tunnels we performed a perturbation experiment. Glass tunnels were mounted to a vertical air piston maintained at 551 kPa and controlled through a computer. The piston's motion stopped upon impact with the mounting plate and vertical motion halted in less than 2.5 ms. We calculated that the final downward speed of the tunnels prior to impact was 0.66 m/s which suggests that ants were subject to a mechanical perturbation of 26.9 g upon stopping.

Activation of the air piston was controlled by a computer program which monitored motion in the upper portion of the tunnel region. When an ant was detected entering this region a relay was activated which controlled a high-speed solenoid that engaged the air piston. Simultaneously a trigger signal was sent to an AOS high speed camera which captured 2 second perturbation-response videos at 1024x1280, 400 fps and 500 $\mu$s exposure time. Analysis of perturbation experiments was performed using Matlab image analysis tools. Users determined fall-distance, ant-length, ant-orientation, fall-time, and fall code (successful arrest, no arrest, no fall) from the perturbation-response videos. We observed 2,268 perturbation-response experiments among worker ants from five of the six host colonies (B - F).

## *8.4 Results and discussion*

### 8.4.1 The shape and form of excavated fire-ant tunnels

To examine the interaction of fire ants with the tunnels that they constructed, we first measured the size and shape of nest tunnels excavated by fire ant workers (body length L = 0.35 ± 0.05, N = 2,611 measurements) in three-dimensions in a laboratory experiment using

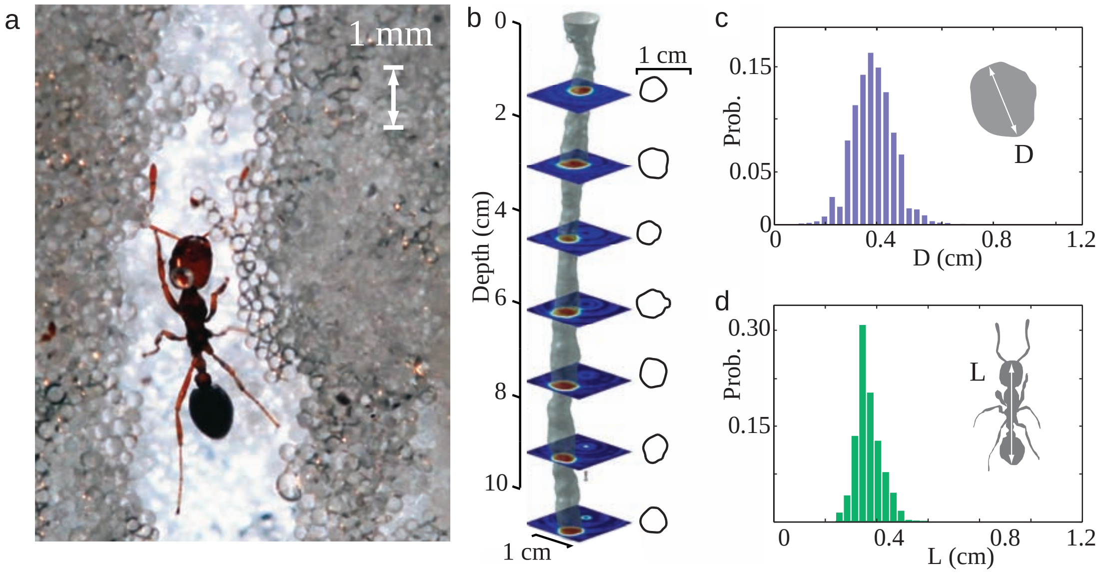

**Figure 8.2:** Fire ants create and move through subterranean tunnels. a) Image shows fire ant worker climbing within an ant-constructed tunnel against a clear glass pane. b) X-ray CT scan reconstruction of a fire ant tunnel segment. b) Distribution of tunnel cross-sectional diameter, D. c) Distribution of ant body length, L, (measured from tip of head to tail of gaster) in laboratory climbing experiments.

an X-ray computed tomography (CT) system (See figure 8.2 and section 8.6.1). We allowed isolated fire ant workers to excavate tunnels within an 8 cm diameter, and 12 cm deep, volume of laboratory soil over the course of 20 hours. The tunnels were roughly circular in cross section (Fig. 1b and SI) and that the effective cross sectional diameter within the tunnels was, D = 0.37 ± 0.08 cm (N = 2,262 observations from 10 experiments).

To determine if soil-substrate had an effect on tunnel shape and size, we repeated this experiment using different substrate combinations of particle diameter (50, 210, 800 $\mu$m) and soil moisture content (1, 3, 5, 10, 15, 18, 20% by mass)[‡]. We challenged worker groups from 8 separate colonies to tunnel in each substrate combination and collected 168 separate X-Ray CT tunnel excavation observations. We found a significant effect of both particle diameter ($F_{2,136} = 10.48, p < 0.0001$) and soil moisture content (${}_{F}6, 136 = 5.38, p < 0.0001$) on excavated tunnel depth indicating that substrate had a strong effect on digging proficiency

---

[‡] These experiments were performed by Daria Monaenkova. Daria and I both analyzed the data using the analysis code I wrote.

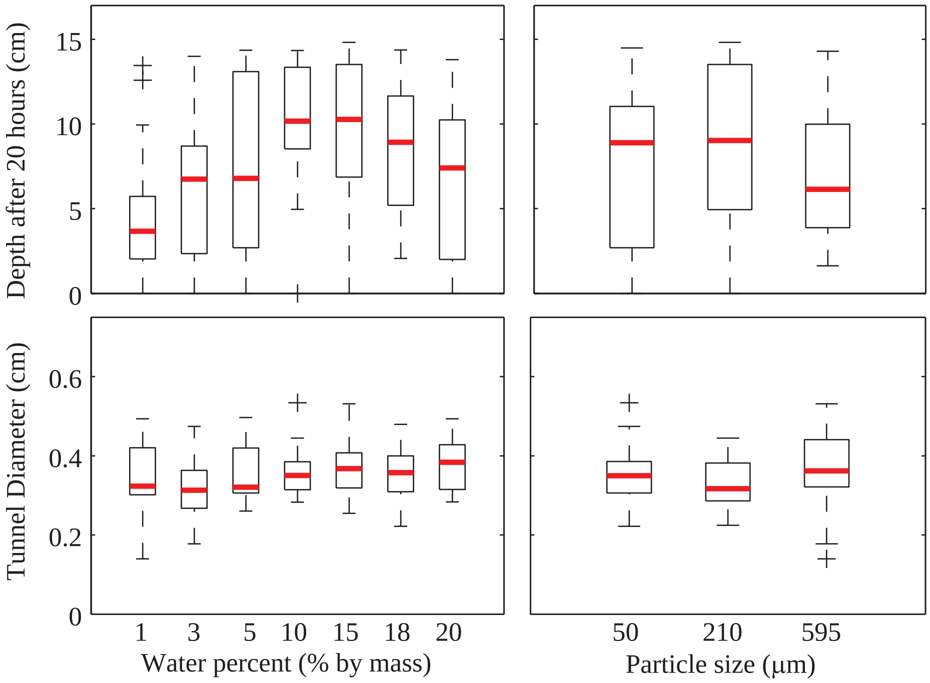

**Figure 8.3:** Tunnel morphology as a function of particle size (left column) and water percent (right column). Box-plots of maximum tunnel depth after 20 hours are plotted along the top row and box-plots of tunnel diameter are plotted along the bottom row. We find that particle diameter and water percent statistically affected tunnel depth, but did not statistically affect tunnel diameter.

(Fig. 8.3. However we found no significant effect of soil moisture ($F_{6,106} = 1.06, p = 0.39$), particle diameter ($F_{2,106} = 1.56, p = 0.21$), or the interaction of moisture and particle size ($F_{12,106} = 1.47, p = 0.15$), on the tunnel diameter (see Supplementary Material). Tunnels constructed in laboratory X-ray CT were similar in diameter to tunnels found in natural fire ant nest mounds (0.44 cm; [139]), nest entranceways (0.3-0.4 cm,[138]), and incipient nests (0.31 ± 0.01 cm; [292]), although tunnels deeper within the nest may be larger in size (0.6 ± 0.3; [139]), due to higher traffic flow in these locations [139, 140]. Nevertheless, our results demonstrate that fire ants show a relatively fixed behavioral program by building tunnels of approximately the same diameter in a variety of conditions. This suggests that the diameter of the tunnel could be important in fire ant locomotion.

### 8.4.2 Tunnel size effects on the biomechanics of confined-climbing

To investigate the biomechanics of locomotion within tunnels, we monitored fire ants climbing within ant-constructed tunnels (Fig. 8.2) and smooth cylindrical glass tubes (Fig. 8.4). We tracked the position of ascending and descending ants freely trafficking between a foraging arena and nest through glass tubes of diameters, D = 0.1 - 0.9 cm (in increments of 0.1 cm). We will refer to these glass tubes as "glass tunnels". In the glass tunnels, ants rapidly ascended ($1.98 \pm 0.75 Ls^{-1}$, N = 1621 ants) and descended ($2.28 \pm 0.70 Ls^{-1}$, N = 990 ants). The kinematic relationship between stride-frequency and speed (Fig. 8.4) was fit by the function $v = ax^2 + bx$ for both the ascending ($a = 0.039 \pm 0.003 Ls^{-1}; b = 0.41 \pm 0.01 L$) and descending ($a = -0.018 \pm 0.005 Ls^{-1}; b = -0.49 \pm 0.02 L$) climbs. The speed-frequency relationship of ascent did not significantly differ among the ant-constructed tunnels and the glass tunnels of diameters, $D = 0.3 - 0.4mm$ (comparable to that of the self-constructed tunnels; $F_{2,361} = 1.8150, p = 0.1643$). We did however, find a small but significant difference in functional form of the speed-frequency relationship during descent ($F_{2,252} = 113.9, p < 0.001$). To test maximal performance within ant-constructed tunnels we induced an alarm response among the colony by exhaling into the tunnel entrance. Within ant-constructed tunnels ants rapidly descended ($6.9 \pm 2.1 Ls^{-1}$; N = 21) and ascended ($4.1 \pm 1.8 Ls^{-1}$; N = 45) at speeds greater than observed in the glass tunnels and surprisingly were able to move at

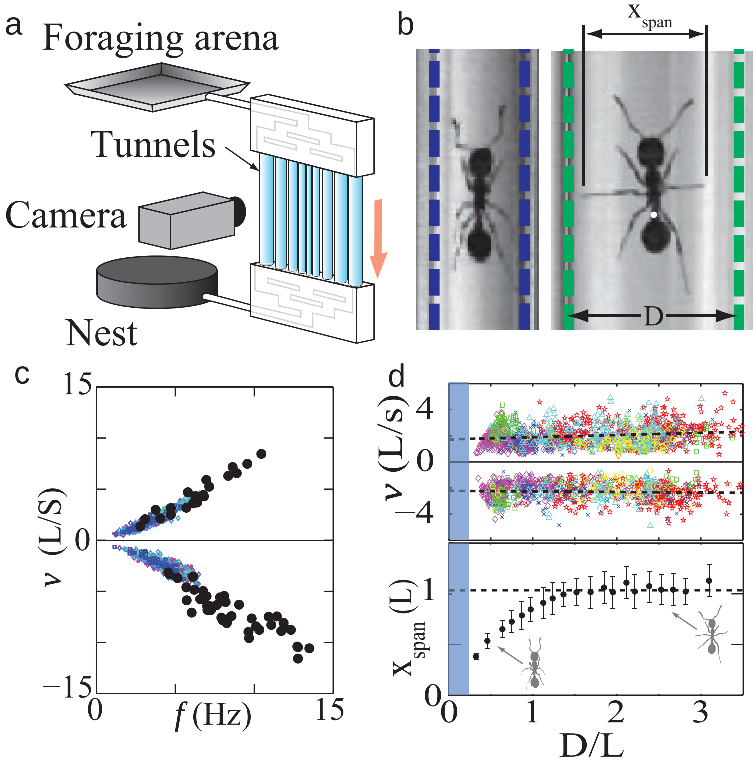

**Figure 8.4:** Climbing posture and antennae use in glass tunnels. a) Schematic of climbing biomechanics experiment. b) Posture of ascending ant in a 6 mm diameter tunnel (left; in normalized units $D = 1.36$ L) and in a 2 mm diameter tunnel (right; $D = 0.60$ L). Left image shows posture variable, $x_{span}$, measured in experiment. Circle and white line indicate distance from touch-down location of limb to petiole. c) Stride frequency and speed relationship for glass tunnels (colored points) and ant-created tunnels (filled black circles). d) Top: Speed versus D/L. Color indicates colony. Dashed lines are linear fits described in the text. Blue box indicates the minimum predicted tunnel diameter an ant could fit in. Bottom: Lateral limb-span (mean ± s.d.) as a function of normalized tunnel diameter. Dashed line indicates constant limb-span of $x_{span} = 1.04 \pm 0.14$ L independent of tunnel diameter.

speeds greater than 9 L $s^{-1}$ within the confined, simulated nest environment.

Over the range of tunnel sizes, tunnel diameter had a weak but significant effect on ascending speed (Top Fig. 8.4) as a function of D/L ($v = m(D/L) + b$; F-test for non-zero slope, $p < 0.001; m = 0.17{\pm}0.04L^2D^{-1}s^{-1}, b = 1.73{\pm}0.07Ls^{-1}$). During descent in tunnels, D/L did not have a significant effect on speed (F-test for non-zero slope, p = 0.10). We thus hypothesized that the minimum tunnel diameter through which an ant can move is slightly larger than the animal's head width. Fire ant head width is $0.24 \pm 0.01L$ [237] and this sets the lower limit of the range of observable D/L values (Shaded blue box Fig. 8.4). Both ascending and descending speeds near this lower limit ($D/L < 0.5$) appeared to sharply decrease (Top Fig. 8.4) suggesting that only in the case of extreme confinement would we observe a strong effect of tunnel diameter on ascending or descending velocity. Overall, this suggests that ants move at a near constant upward and downward speed, over a wide range of tunnel sizes, while freely trafficking within the nest.

Tunnel diameter had a significant influence on the ant's climbing posture (Bottom Fig. 8.4). Ants exhibited one of two stereotyped climbing postures: 1) within glass tunnels of $D > L$, ants adopted a sprawled posture in which mid-limbs were extended laterally away from the body (Fig. 8.4) and 2) within glass tunnels of $D < L$, mid-limbs were bent and pointed posteriorly (Fig. 8.4). We determined the critical tunnel diameter at which this postural transition occurs at by fitting the function

$$x_{span} = \begin{cases} k\frac{D}{L} & \text{if} D < D_c \\ c & \text{if} D > D_c \end{cases} \tag{8.1}$$

We determined that in glass tunnels of diameter above Dc = 1.03 ± 0.01 L the lateral limb-span, $x_{span}$, was independent of tunnel size (R2 ¡ 0.001) with mean value of $x_{span}$, determined from fit parameter c = 1.04 ± 0.14 L (Fig. 8.4). In glass tunnels of diameter less than Dc, limb posture was altered by tunnel confinement and xspan subsequently decreased (Fig. 8.4). For comparison to ant-created tunnels, excavated tunnel diameter was $D = 1.06 \pm 0.23L$. Thus ants modify their limb position depending on tunnel size, but maintain approximately the same rate of ascent and descent despite these modifications. Furthermore ants climbing within tunnels they construct are capable of utilizing their spread-limb posture

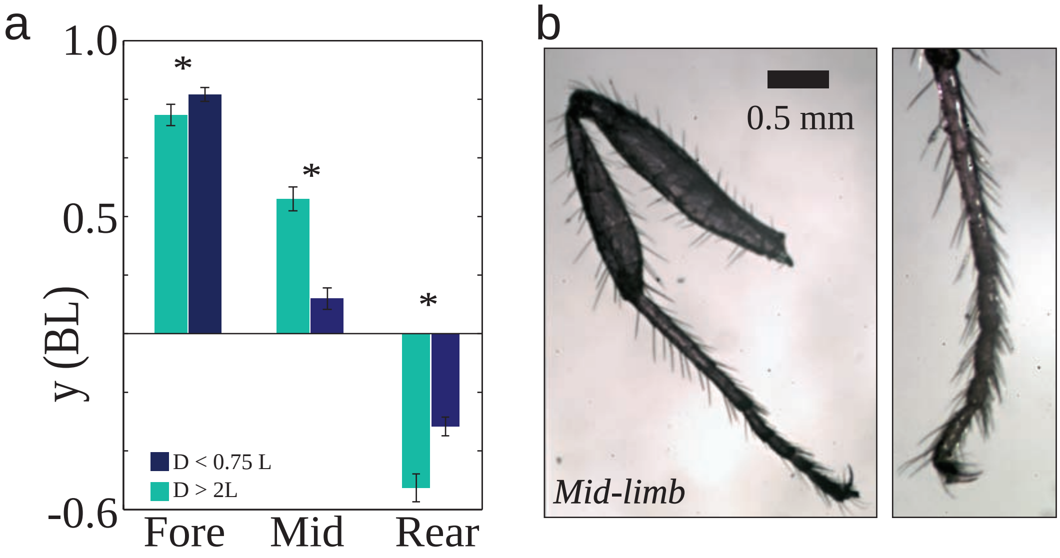

**Figure 8.5:** Anterior extreme position (AEP) of the fore-, mid-, and rear-limb and limb morphology. a) AEP from climbs in large and small tunnels in the fore-aft direction measured with respect to the ant petiole (White dot in Fig. 8.4b). b) Mid-limb morphology showing tarsal claws and spiny hairs along the length of the limb.

which may have implications for locomotor stability.

The alteration of the mid-limb posture in smaller tunnels suggests that a transition occurs in the direction of locomotor force production by the mid-limb. In the sprawled posture, mid-limb tarsi contact-forces pulled towards the body and the tarsal hooks and adhesive pads are likely engaged. In contrast, when the limb is in the compact posture, the limb pushed down and away from the body to generate forward thrust. In the compact posture, to generate thrust force, it is likely that the rows of 50-350 $\mu$m long spiny hairs along the limb (Fig. 8.5) are utilized to engage asperities in the climbing substrate and allow the limb to push. Such multifunctional limb design has been previously shown to aid in rapid locomotion on horizontal substrates through the engagement of spiny limb hairs with rough surfaces [293]. This suggests that the mid-limb changes its motion and function depending on tunnel diameter.

### 8.4.3 Slip recovery through rapid jamming

Fire ants possess a pair of elbowed antennae capable of a wide range of articulated motion about the head (Fig. 8.6). Antennae are primarily considered sensory organs used for

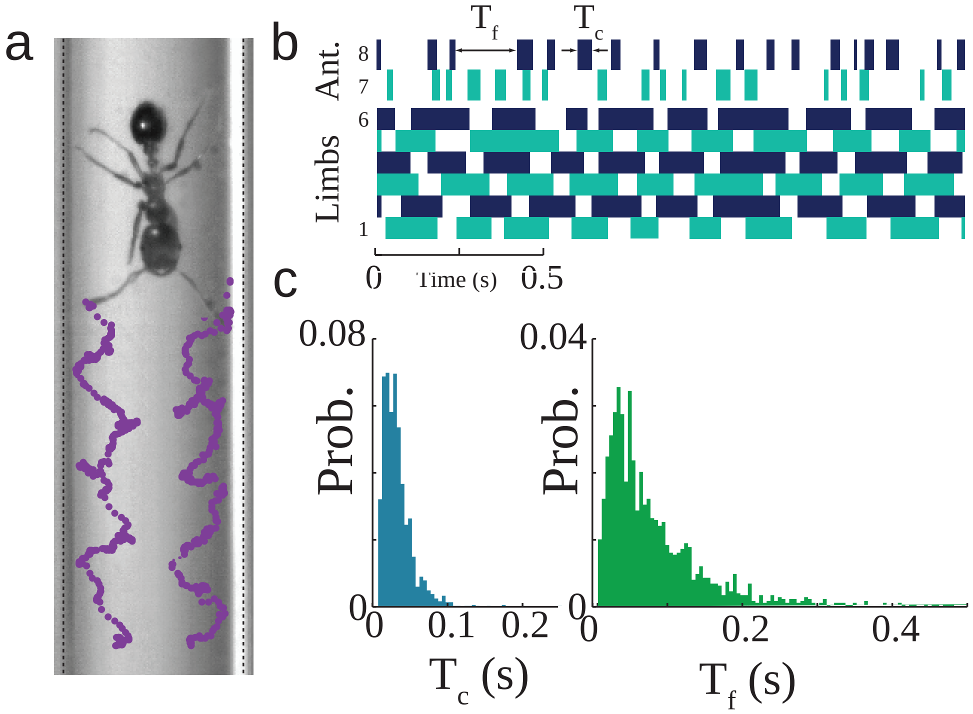

**Figure 8.6:** Antennae use in confined locomotion. a) Image of ant descending in a tunnel with tracked position of antennae tips shown in purple. $D = 3mm$. b) Stepping and antennae contact diagram for a vertical descent in a tunnel. Light and dark blue highlight limbs that form alternating tripods during locomotion. Time of antennal contact, $T_c$, and time free, $T_f$, are highlighted. c) Probability distribution for both $T_c$ and $T_f$.

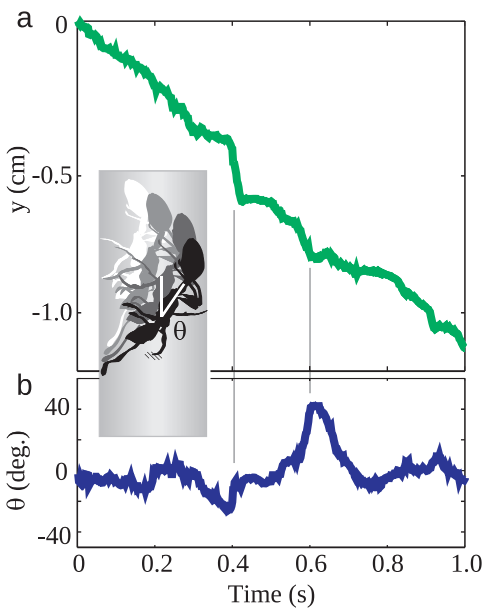

**Figure 8.7:** Kinematics and perturbation-recovery during tunnel climbing. a) Vertical position of ant while descending. b) Body angle ($\theta$) with respect to tunnel axis descending climb. Two slip-recovery events are highlighted by vertical gray lines. During slip events antennae and limbs are jammed against the wall and the body pitches into the tunnel face (illustration).

tactile, chemical, and acoustic sensation [125]. While ascending and descending, ants rapidly placed antennae in contact with the tunnel walls (Fig. 8.6). In the glass tunnels, antennae-wall contact time was $T_c = 29 \pm 23ms$ (Fig. 8.6; N = 1840 contacts from 54 climbs) during head-first descent. The time between contacts was $T_f = 82 \pm 81ms$ (Fig. 8.6). The rapid and repeated antennae-wall contact is important for sensing the subterranean environment. However observations of ants slipping within glass and natural tunnels led us to hypothesize that these sensory appendages could also have important biomechanical functions for climbing in confined spaces.

During high-speed ascent and descent, ants exhibited slips that were rapidly corrected for by placing antennae and limbs against the tunnel surface (See Fig. 8.7). Ants rapidly arrested short downward slips (in which the instantaneous downward velocity exceeded 1.5 cm s-1) within $82 \pm 21ms$ (N = 456 slips among 54 individuals) within glass tunnels. During head-first slips, antennae were placed against the tunnel wall prior to arrest in 92% of the observed slips (422 antennae contacts out of 456 slips). Excluding slips in which antennae began in contact with the wall, the time between slip onset and antennae-wall contact was $32 \pm 22ms$ (N = 265). The observations indicate that antennae are rapidly and readily used for slip-correction when climbing in confined space. In the case of larger slips, the antennae deformations also suggest that antennae provide significant mechanical support to the falling ant. These observations illustrate that antennae are more multi-functional than previously thought, and play a significant role in locomotion stability when climbing in tunnels. Morphological adaptations to subterranean life are well documented[294]; here we have observed for the first time that fire ant antennae-which are evolved from ancestral arthropod limbs [295]-retain partial functionality as locomotion appendages. Antennae can act effectively like 7th and 8th limbs to arrest falls.

Rapid fall arrest while bracing antennae against a tunnel wall relies on the ability to quickly jam limbs and body against opposing locations along the tunnel wall. Thus we hypothesized that the ability to rapidly arrest slips through body-jamming would be sensitive to tunnel diameter. To test this hypothesis we subjected ants climbing within glass tunnels to perturbations consisting of a rapid downward translation of the tunnels (Fig. 8.4). High speed perturbation-response experiments challenge the fastest neural response times, and thus help to determine the role of body kinematics and morphology in rapid locomotion stabilization [262, 264, 296, 297]. Glass tunnels were mounted to a vertical air piston maintained controlled through a computer. The piston translated the tunnels downwards 0.5 cm at which point the motion was stopped in less than 2.5 ms upon impact with the mounting plate. The final downward speed of the tunnels prior to impact was estimated to be 0.66 m/s which suggest that ants were subject to a mechanical perturbation of $\approx$ 27g upon stopping.

We found that 52% (1092 falls out of 2584 perturbations) of the perturbation experiments did not lead to ants being displaced from the tunnel wall (Fig. 8.8). This indicates that the fire ant tarsi and adhesive footpads are robust to substantial perturbations, consistent with other measurements of the ant's adhesive strength [298, 299]. However, displacement did occur in 48% of experiments, and the outcome of perturbations was strongly influenced by the interaction of ant tunnel size.

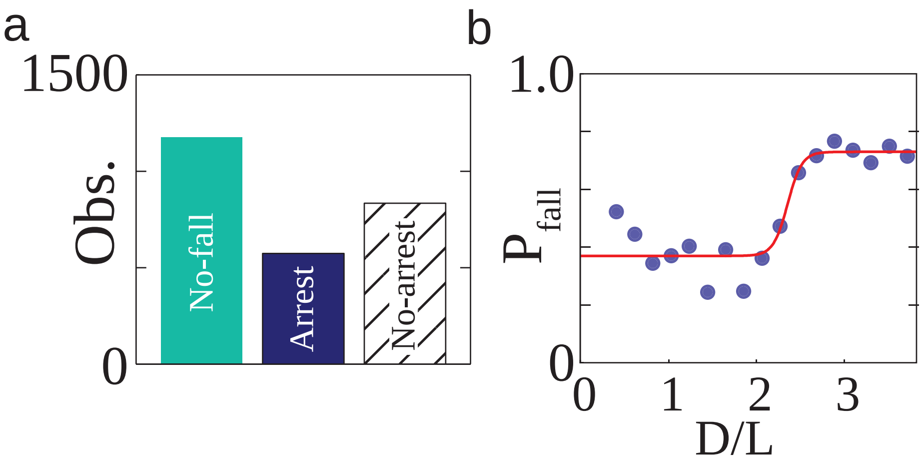

**Figure 8.8:** a) Number of observations from perturbation experiments. b) Probability to fall during a perturbation experiment as a function of D/L. Red line is logistic fit described in text.

We found that tunnel diameter, with respect to ant body length, had a significant effect on the probability to fall during a perturbation experiment, with smaller tunnels aiding in the ants perturbation resistance (Fig. 8.8). The probability to fall during a perturbation doubled from 36% when $D < 2.28L$, to 73% when $D > 2.28L$. The high resistance to perturbation in tunnels of D ¡ 2.28 L was likely due to the ability of fire ants to robustly engage surfaces. When climbing vertical planar surfaces, animals have to contend with gravity which, because the center of mass is offset from the climbing surface, generates an overturning moment on the animal which must be overcome. In contrast, when climbing in small tunnels, ants may be able to minimize torque induced gravity on the body by placing limbs laterally against walls and thus keeping the center of mass in the same vertical plane as limb contact points.

Ants perturbed from the tunnel wall either arrested their fall within a vertical distance y, or fell to the tunnel bottom (Fig. 8.10). Arrest distance, y, increased with increasing tunnel size normalized by bodylength, D/L (Fig. 8.9). The upper envelope of y (dashed line in Fig. 8.9) increased linearly with a slope 6.7 ± 0.7 cm ($R^2 = 0.95$). This relationship can be understood through a kinematic argument: to arrest falls ants extend limbs and antennae towards tunnel walls which are a further distance away within larger tunnels, and result in longer fall distances (Fig. 8.9).

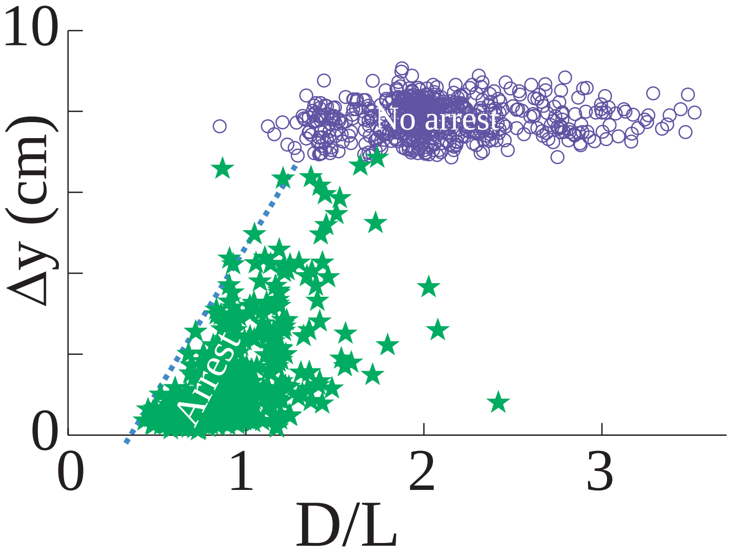

**Figure 8.9:** Correlation between tunnel morphology D/L and fall distance. Fall distance, y, as a function of D/L. Purple circles indicate no arrest while green stars indicate arrest.

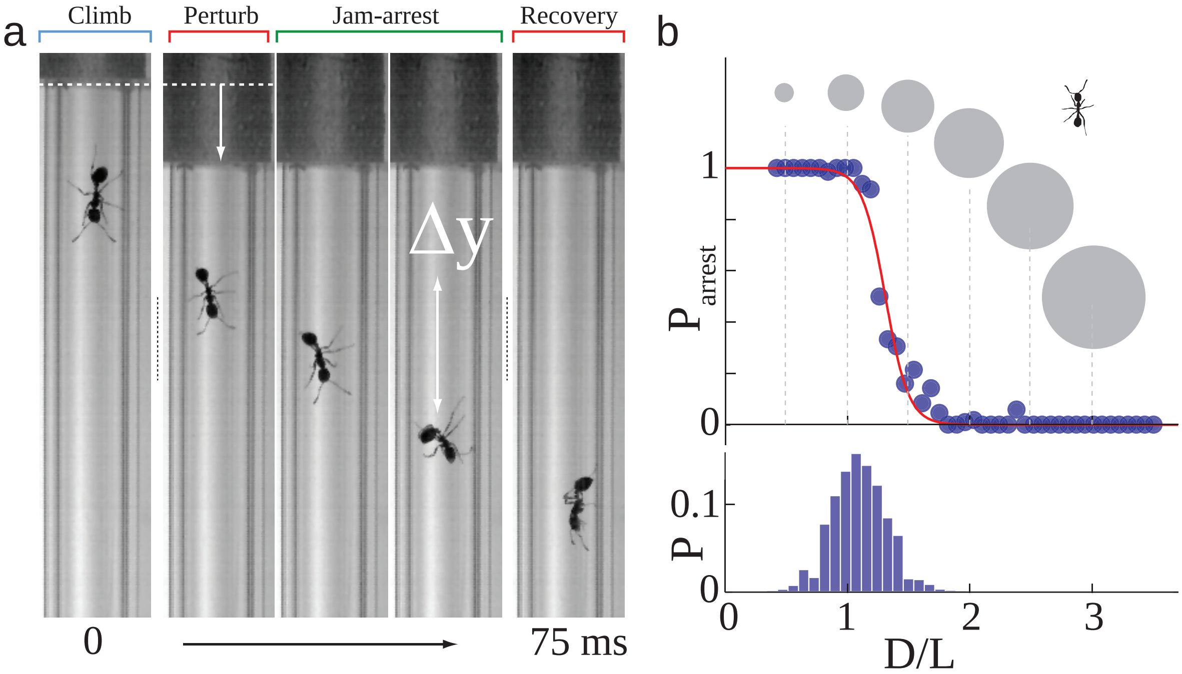

**Figure 8.10:** Climbing perturbation experiment. a) Image sequence of perturbation and recovery. Left image is immediately prior to perturbation. Middle images show recovery which took place over 75 ms ($\Delta T = 30$ ms for middle three frames). Ant continued descending after perturbation recovery (Right image). b) (Top) Probability to arrest falls, $P_{arrest}$, versus D/L. Line is logistic fit described in text. Gray circles are tunnel diameter drawn to correct scale of ant illustration. (Bottom) Probability distribution of tunnel diameter in units of ant bodylength (L) for excavated tunnels (Data reproduced from Fig. 8.2).

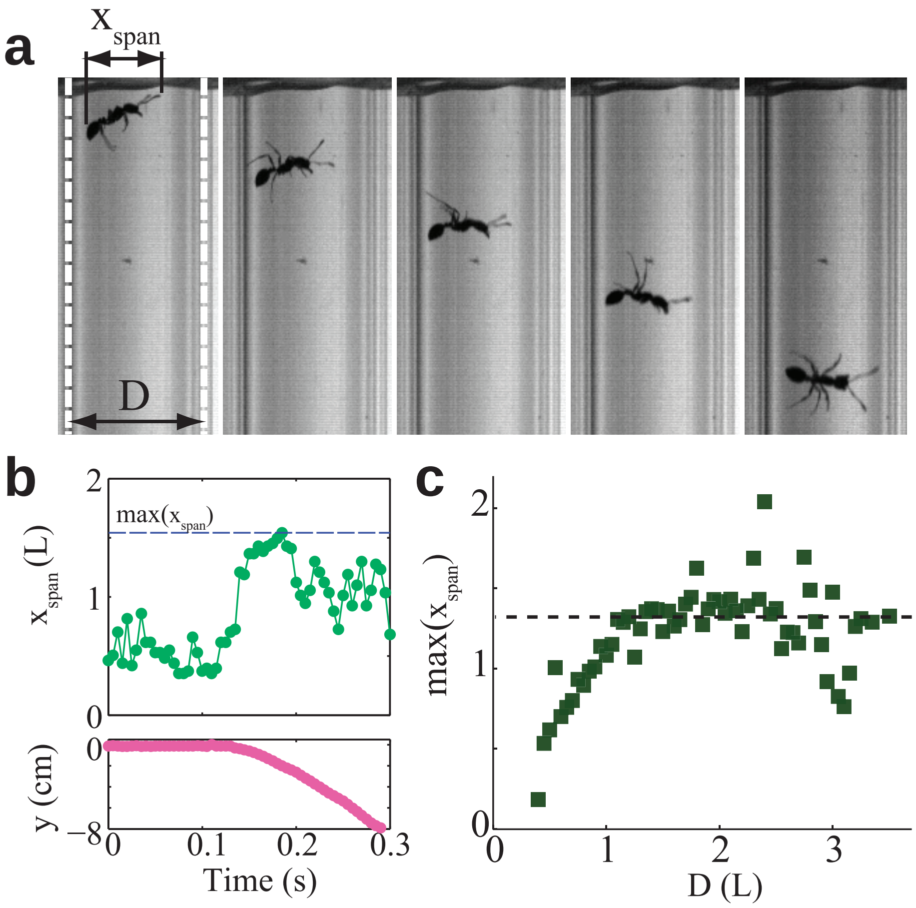

**Figure 8.11:** Falling posture and arrest probability. a) Five images from a perturbed fall. Images are separated by 10 ms. During perturbed falls we measured the total horizontal span of limbs, antennae, and body, called $x_{span}$. b) $x_{span}$ and vertical position, y, plotted versus time. Perturbation occurs at 0.1 s and vertical descent is accompanied by an increase in xspan. c) Maximum lateral limb-span [max($x_{span}$)] exhibited during fall as function of D(L). Limb-span is constant above $D > 1.3$ L with max($x_{span}$) $= 1.33 \pm 0.22$ L (dashed line shown).

The probability to arrest a fall, $p_{arrest}$, within a tunnel of size D/L decreased from 1 to 0 as D/L increased. We fit $p_{arrest}$ to a logistic function, $p_{arrest} = \frac{1}{1+\exp(\frac{D_s-D}{L})}$ (Fig. 8.10) and found the cutoff tunnel diameter, $D_s = 1.31 \pm 0.02$ L ( = -10.54 ± 1.76), at which arrest probability decreased to below 50%. Within ant-constructed tunnels (of mean diameter 1.06 L; Bottom Fig. 8.10) we predict that 93% of falls will be arrested. This demonstrates that ants display a high degree of climbing stability within tunnels of equal size to those they create (1.06 L); however an increase in tunnel diameter by 50% reduced arrest probability to less than 5%.

We hypothesized that tunnel diameter would limit the ability to recover from falls through a, "jam-arrest" mechanism, within tunnels. Thus we expected that, $D_s$, was governed by morphological limitations of ant limb use. We measured the lateral limb-span, $x_{span}$, for free-falling ants (Fig. 8.11 and found that ants extended limbs maximally to a width of $\max(x_{span}) = 1.33 \pm 0.22L$ independent of tunnel size when $D > 1.3L$. This measurement is consistent with the typical mid-limb span of fire ants 1.31 ± 0.09 L reported in the literature (See (45)) and suggests ants are extending limbs as much as possible to re-engage the tunnel wall while falling. In tunnels whose diameter exceeded the physical reach of the ants, $D > 1.3L$, ants were largely unable to engage walls and the arrest probability decreased substantially in tunnels above this diameter.

We return to the digging experiments in which groups of ants constructed tunnels to understand how constructed tunnel size relates to stability in confined spaces. The average diameter of tunnel created by ants across all excavation experiments was found to be D = 1.06 ± 0.23 L. Thus we find that fire ants construct tunnels which facilitate rapid locomotion through the enablement of slip-recovery by antennae and limb jamming, without hindering limb kinematics. Many other factors are likely important in the determination of the equilibrium nest tunnel size-such as traffic, food transportation requirements, ventilation. However during incipient nest construction, such as after a flood, we expect that speed of locomotion and subsequently excavation is important to survival.

## 8.5 Conclusions

We have shown here that fire ants inhabit and construct tunnels of a size which enable climbing stability and slip recovery. The ability for organisms to offload locomotion control to their environmental structures represents a new paradigm and a novel example of the integration of the organism's extended phenotype. Fire ants achieve rapid motion within their nest through the use of multi-functional limbs and antennae to effectively engage surfaces within their constructed environment. The functionality of antennae as load-bearing, locomotor appendages is a surprising result, one which highlights the importance of studying locomotion within the context of the organism's natural environment.

We propose that the construction of control surfaces suited to the locomotors body size and limb kinematics reduces locomotion control requirements within subterranean environments and may be a general feature of robust control within organism-engineered substrates such as tunnels, trails, or burrows. A universal scaling of burrow cross-sectional area with body-length[269]-sampled across a wide array of organisms varying by over six orders of magnitude by mass-gives evidence of the commonalities of locomotor constraints among subterranean animals. Thus the robust locomotor control strategies for subterranean environments we describe here for fire ants may extend to a diversity of animals. We also expect that our biological discoveries will provide inspiration for and simplify control in swarming robotic devices that will have to move within confined environments such as search and rescue zones. In addition, we speculate that future robot teams could enhance survival in harsh terrestrial and extraterrestrial environments though collective construction of appropriately engineered nests.

## *8.6 Appendix*

### 8.6.1 X-Ray computed tomography

#### *8.6.1.1 Overview*

These experiment use x-ray imaging and computed tomography (CT) volume reconstruction to visualize the three-dimensional growth of ant nests in time. X-ray CT scanning equipment is now standard in medical diagnosis and research and thus there is a wealth of literature and information available. X-ray imaging equipment is becoming increasingly inexpensive and thus more accessible to experimentalists.

#### *8.6.1.2 X-Ray image collection*

In this study we utilized a fluoroscopy x-ray system. This system was configured in a cone-beam CT geometry in which x-ray photons are emitted from the source (treated as a point source) and pass through the sample and terminating on the face of a two-dimensional image intensifier. X-Ray computed tomography (CT) requires three components: an x-ray source, an x-ray imager, and a means of rotating the sample with respect to the imager. In some cases, primarily in medical use, the the x-ray source and imaging equipment are rotated around the sample. In medical and laboratory x-ray applications, x-ray photons are generated through Bremsstrahlung in which electrons are accelerated towards a (typically) tungsten target where they are rapidly decelerated by the proton heavy nucleus of the tungsten. Two parameters are important in x-ray generation by this means: the current and the electric potential. The number of electrons being decelerated, and thus the photon intensity of the x-ray beam, is controlled by the current measured in milli-amps (mA). The speed of the electrons as they reach the tungsten target, controlled by the electric potential of the accelerator, determines the energy spectrum of the resultant x-ray beam. The potential is measured in peak kilovoltage (kVp) and can range from 10 - 120 kVp.

On the other side of the sample is the imaging system, the image intensifier (IIT) and high-speed Phantom v210 camera. The image intensifier converts x-ray photons to visible light photons which are imaged by the high-speed camera. The camera uses a 12-bit analog-digital converter to generate 12-bit pixel depth grayscale images. Since 12-bit pixel depth is not a standard format we up-convert to 16-bit lossless video and images for our data capture.

In the center of the CT system is a stepper motor which controls a rotation stage capable of continuous rotation. The stepper motor is connected to the sample mount through a 20:1 planetary gearbox which eliminates any backlash and vibration which would have been introduced through the stepper. The stepper motor rotates the sample at a rate of 72°/s (1 rotation every 5 seconds) and we record video at 80 Hz resulting in 400 images per rotation and an angular resolution of 0.9°. Rotation and frame rates were carefully chosen such that every images from multiple rotations are exactly shifted by 400 images in the video and thus we can average over several rotations to reduce noise. We collect videos of 10 rotations and average each of the 400 angular locations with the 10 replicate images from that rotational position.

X-ray's interact with matter in a variety of ways, including absorption and scattering, but in general a sample of thickness $l$ will attenuate an x-ray beam given by the Beer-Lambert law

$$I_{out} = I_{in} \exp(-\frac{l}{\lambda}) \tag{8.2}$$

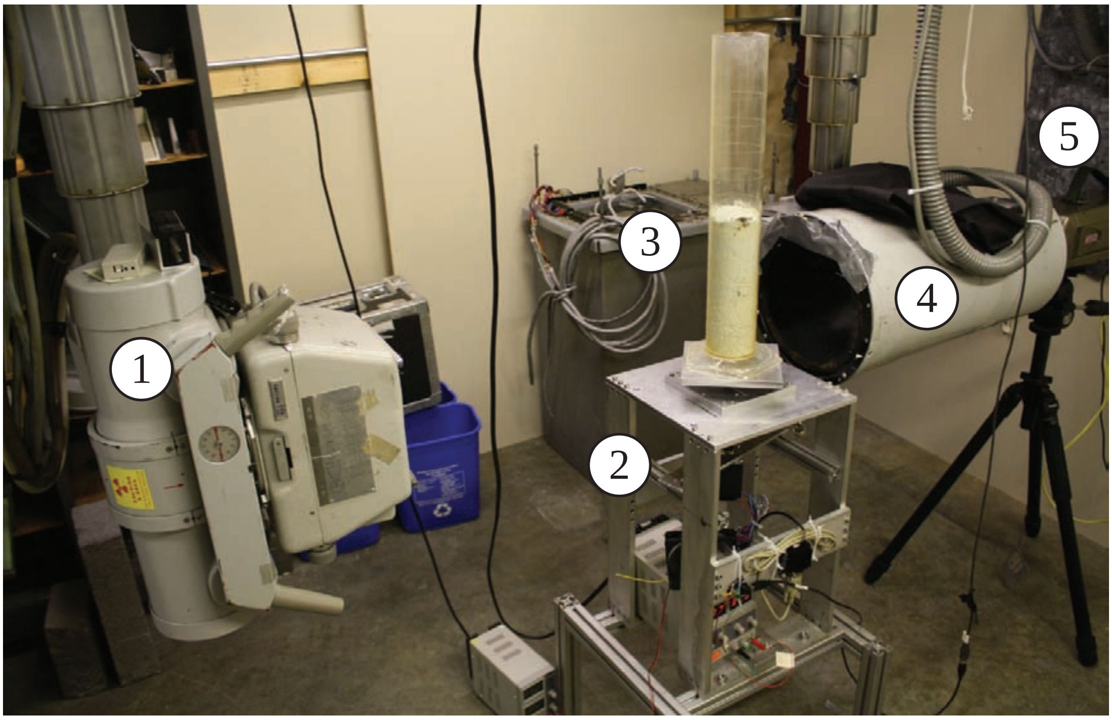

**Figure 8.12:** X-Ray computed tomography apparatus. (1) X-Ray source with collimator. Beam is directed to the right in the image. (2) Stepper motor controlled rotation stage. (3) Ant nest on top of rotating stage. (4) Image intensifier. (5) Phantom v210 camera.

where $\lambda$ is the attenuation coefficient of the material. In figure 8.13 we show the attenuation profile for a rectangular plastic container filled with glass beads. The absorption contribution from the plastic walls of the container were found to be negligible compared to the attenuation from the glass beads. From this data we find that the dry 250 $\mu$m glass beads in an "as poured" state have an attenuation coefficient of $\lambda = 2.80$ cm. The inset shows that at large absorption distance we measure an x-ray intensity larger than what is predicted from equation 8.2. This is due to the noise floor of the imaging system (image intensifier and camera) often called dark current. The dark current value we measure is 0.46% the peak intensity observable.

A major challenge in successful x-ray imaging of samples with large thickness is the ability to resolve features in the center interior, where the cross section is thickest, while not over-saturating the boundaries where the sample is often thinner. To resolve this issue we implement a beam-shaping filter called a wedge filter which preemptively attenuates regions of the beam which are focused on thinner sections of the sample (Fig. 8.14). The

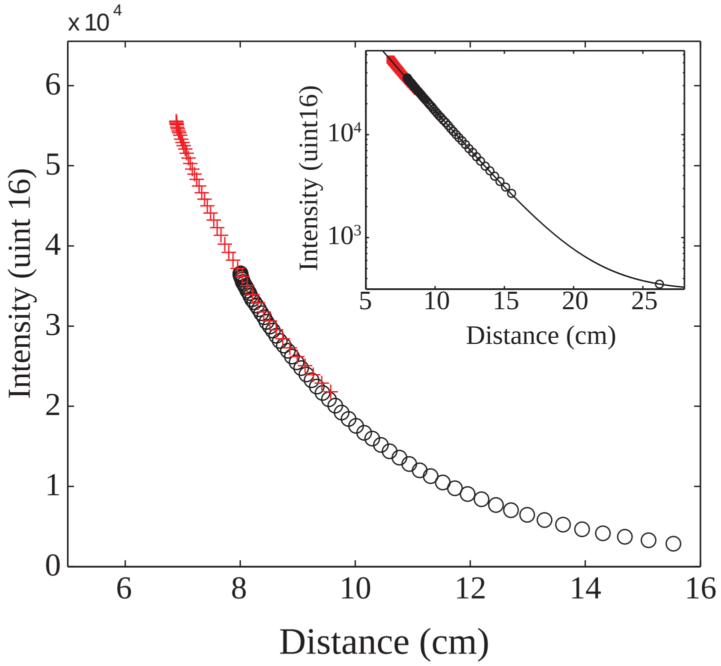

**Figure 8.13:** Plot of average intensity of x-ray beam after absorption by glass beads and plastic wall as a function of absorption distance. Inset shows semi-log plot with fit $a\exp(x\frac{d}{\lambda}) + c$ (a = 597,627, b = 2.80 cm, c = 302).

wedge filter decreases the incident x-ray intensity at the edges of the circular sample while allowing a higher incident x-ray intensity at sample center. To ensure the wedge filter does not interfere with CT reconstruction we take an image of the beam profile before placing the sample in the system so that we can divide out the spatial structure of the beam in post-processing. Additionally we measure the output intensity of the x-ray source by measuring the image intensity in an unobstructed fiducial region of the wedge filter (Green box in Fig. 8.14c).

Variation of the potential and current alters the beam intensity (Fig. 8.15). Changing the current changes the beam intensity linearly since current directly controls the number of x-ray photons produced. The electric potential (kVp) of the x-ray source influences the beam intensity non-linearly (Fig. 8.15). The non-linear effect of kVp on beam intensity is likely due to the non-linear dependence of a samples attenuation coefficient on x-ray photon energy.

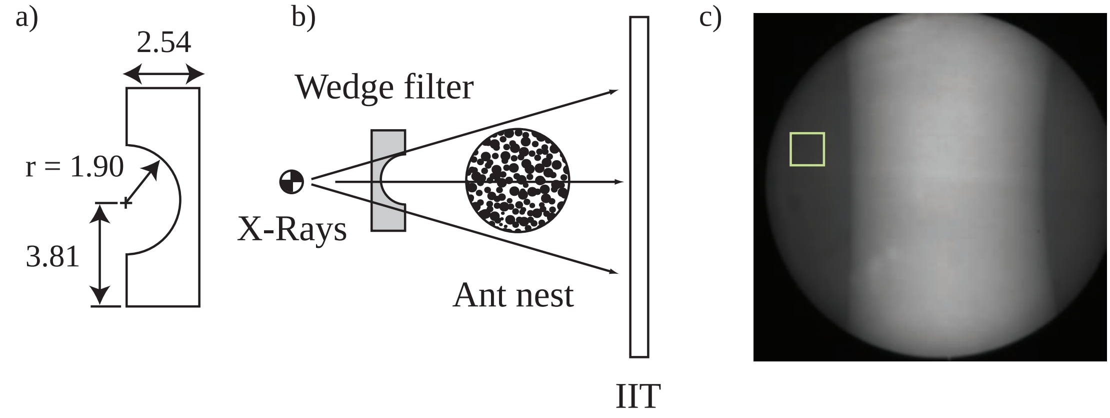

**Figure 8.14:** a) Schematic of the wedge filter. Dimensions are in cm. Material is Aluminum. Filter extends 7.62 cm into the plane. b) Wedge filter setup for beam shaping. Wedge filter preferentially reduces X-Ray intensity in regions where absorption length in the sample is low. IIT is image intensifier. c) Image of the beam shape from a wedge filter. Wedge filter is oriented vertically. Black circular region is image intensifier boundary.

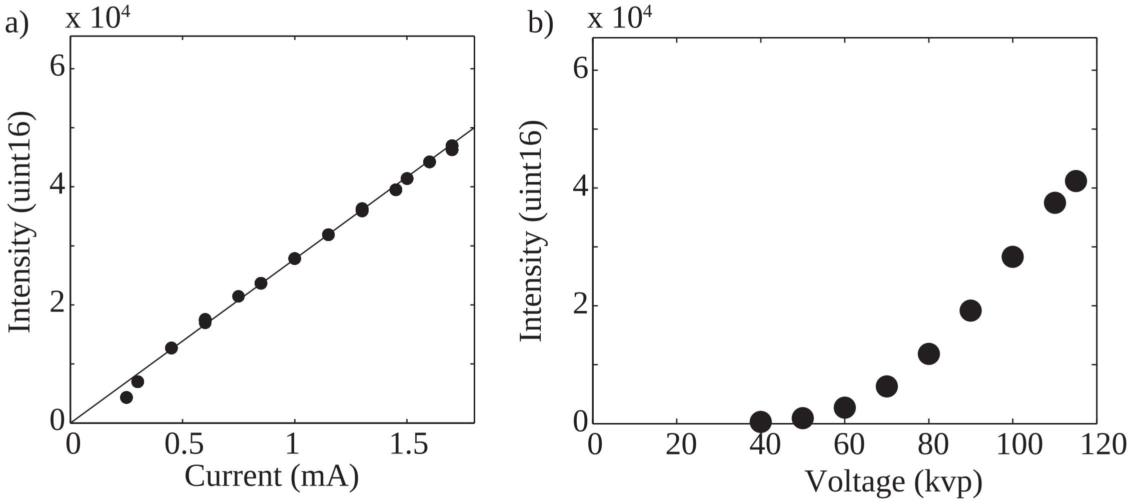

**Figure 8.15:** a) Effect of X-Ray source current on peak X-Ray intensity at image intensifier for fixed X-Ray source potential. Line is $y = 2.77 \times 10^4 I$ where $I$ is source current. b) Effect of X-Ray source electric field potential on peak intensity at fixed current.

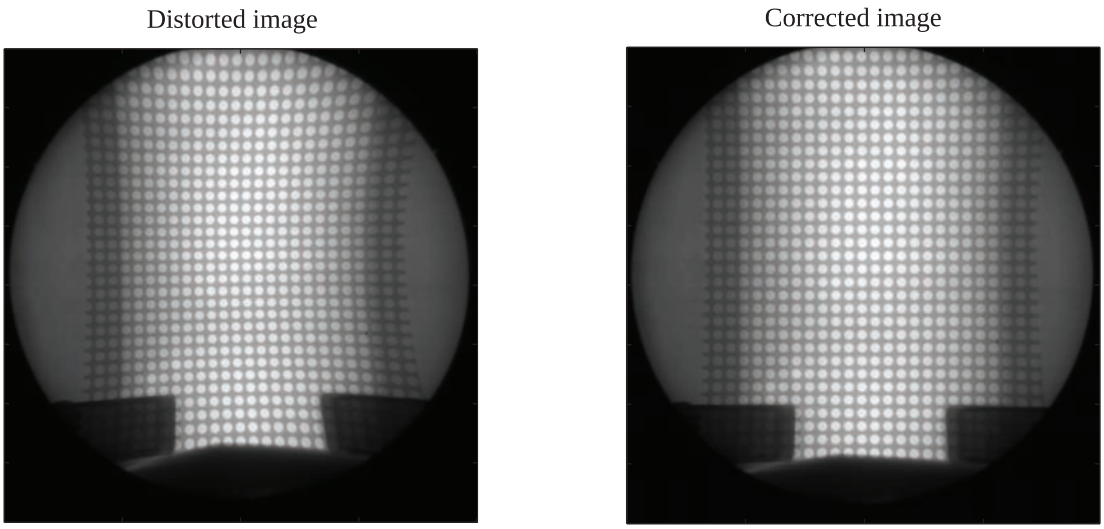

**Figure 8.16:** Correction of image distortion in image intensifier. Left is raw image of a square grid showing image distortion. Right is image distortion corrected through a spatial transform in Matlab.

#### *8.6.1.3 X-Ray image processing & reconstruction*

*Preprocessing*—In the collection of an x-ray CT we record a video of ten rotations of the sample at 400 images per rotation, resulting in a video with 4000 frames. At first we average over the ten replicate images at each of the 400 angular increments resulting in a single image for each rotational position. We then normalize each image by the scalar intensity of the fiducial region (see Fig. 8.14c). Next images are divided by the background image which removes the spatial structure from the beam intensity profile that is introduced by the wedge filter. Lastly we remove spatial distortion in the imaging system with a spatial mapping from a predetermined calibration image (Fig. 8.16).

At this stage images are ready for CT processing. We use an open source Matlab implementation of the popular Feldkamp-Davis-Kress (FDK) cone beam algorithm [300] called Oscar [301]. The FDK algorithm is an iterative solver which computes the density field (called a back-projection in CT terminology) of the sample being imaged. The details of the FDK algorithm are beyond the scope of this section but can be found in any radiological imaging textbook.

*Post-processing*—The x-ray computed tomography method produces data in the form of a three-dimensional matrix in which each matrix element represents the attenuation

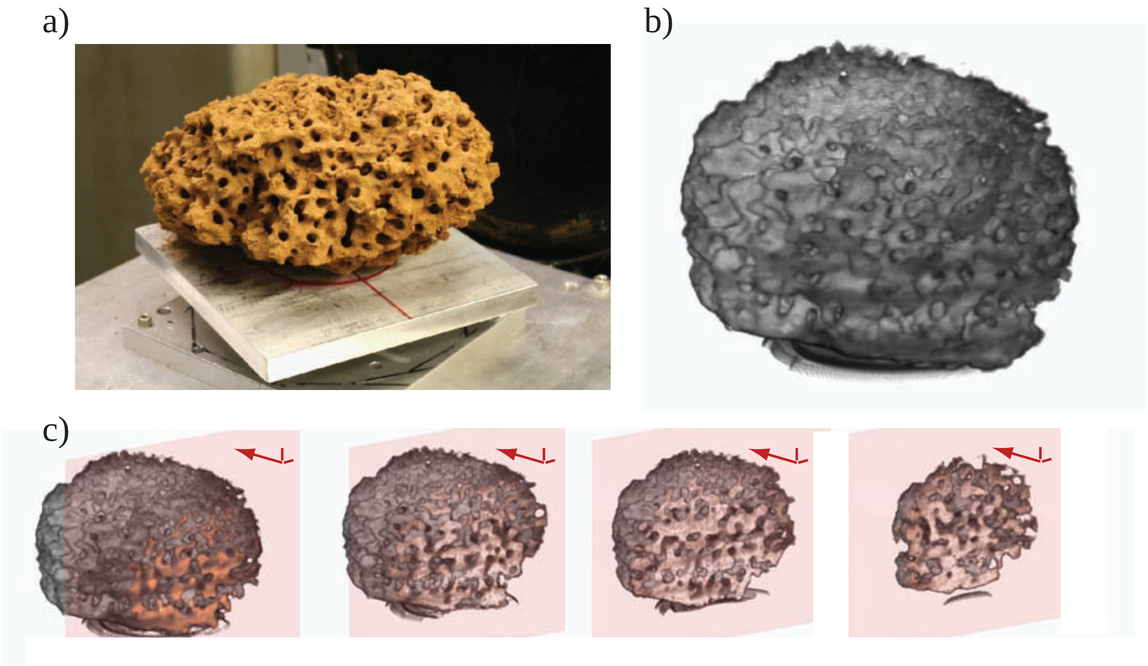

**Figure 8.17:** Example output of x-ray CT. a) A fire ant nest mound section. b) the CT reconstruction of the nest mound. c) Cutting away sections of the CT reconstruction shows the interior structure of the nest mound.

coefficient of the material at that location. An element of this three dimensional matrix is a voxel and in our system we have a voxel dimension of 0.25 mm. For an example of the input and output of this system we show a CT of the surface mound of a fire ant nest in figure 8.17.

Once we have computed the back-projection from the CT reconstruction we may measure any quantities we like. In the case of this experiment we are interested in tunnel cross-sectional shape. We determined the cross-sectional shape of tunnels using an active contours algorithm [291]. This works by taking an initial perimeter around the tunnel cross-section and minimizing some energy functional based off of an elastic bending energy of the perimeter and an interaction of the perimeter with the energy landscape of the image. This method produced reliable tunnel masks which accurately fit many different tunnel shapes and sizes as determined by eye (Fig. 8.18a).

We characterized tunnel shape using two methods (Fig. 8.18: 1) fitting an ellipse to the tunnel cross-section at different depths and 2) computing the distance transform of tunnel

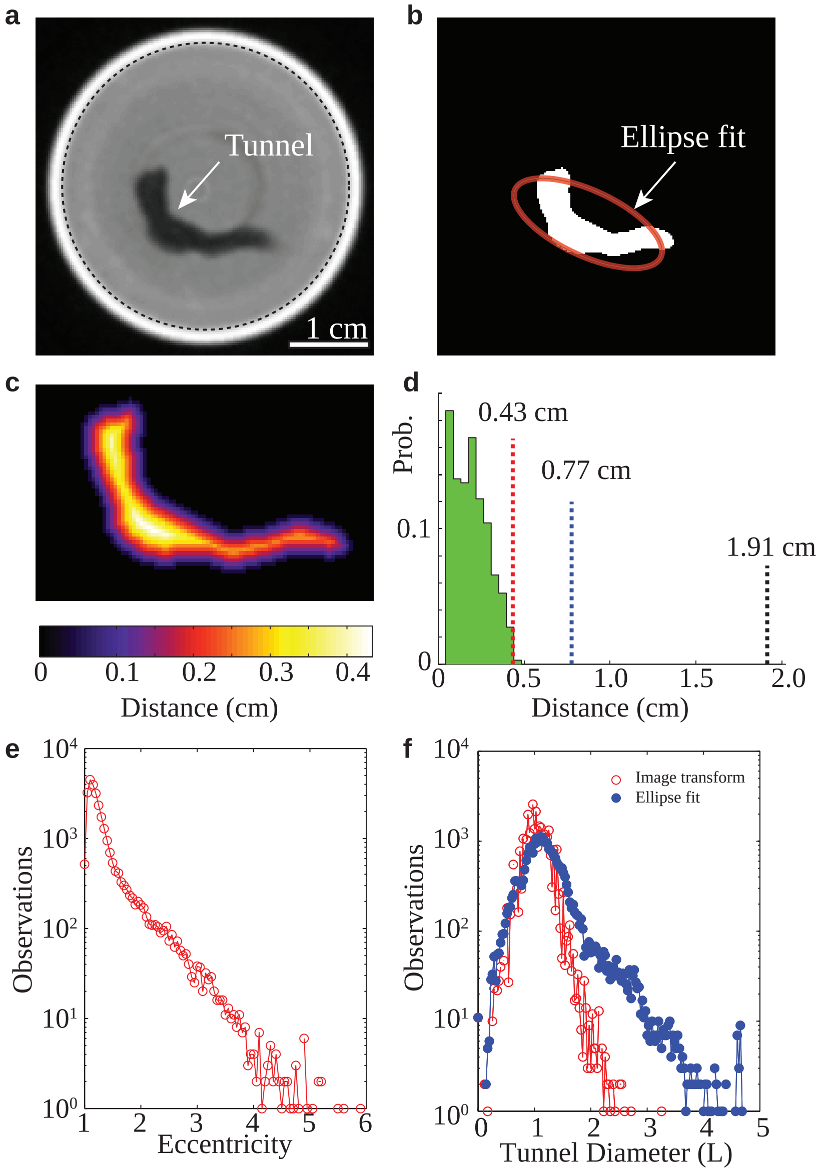

**Figure 8.18:** Tunnel morphology analysis from X-Ray CT data. a) Tunneling experiment in a 3.8 cm outer diameter tube. Inner wall of digging arena shown as dashed line. An oblong shaped tunnel is highlighted in the center of the arena. b) Elliptical fit of tunnel shape. c) Euclidean distance image metric of tunnel shape. Color represents minimum distance of each pixel location to tunnel wall. d) Comparison of ellipse and image distance transform measures. Histogram of distance metric evaluated at all points in tunnel mask (green). Vertical dashed black line is major axis length from elliptical fit, dashed blue line is minor axis, and red line is maximum distance measured from distance transform. e) Distribution of eccentricity defined as major axis divided by minor axis from fitted ellipse fits. f) Distribution of tunnel diameter measured from distance transform and ellipse fit.

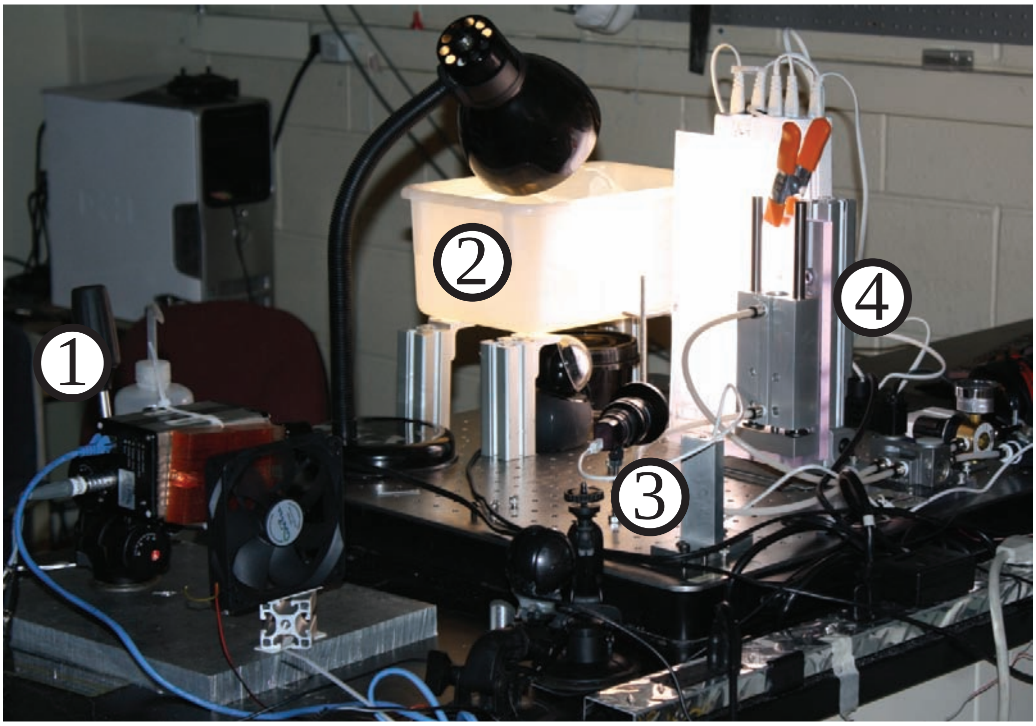

**Figure 8.19:** Perturbation apparatus setup. 1) High speed camera. 2) Foraging arena and light proof nest below. 3) Pneumatic translation stage. 4) USB camera used for motion detection.

image mask, and multiplying the maximum by a factor of two. The distance transform of the image measures the nearest Euclidean distance to a tunnel wall at every pixel-location within the tunnel mask. Taking the maximum value of the distance transform for a given tunnel cross-section in effect estimates the "worst-case scenario" location for an ant to fall in that tunnel because that location is furthest away from tunnel surfaces. Since we are focused on locomotion stability we use the maximum of the distance transform as the metric for local-tunnel size and further refer to this as tunnel Diameter in the text.

### 8.6.2 Perturbation apparatus

To perform perturbation experiments on freely climbing ants we used a setup as shown in Fig. 8.19 and described briefly in section 8.3.4.3. Here we will describe the experimental setup further. The Perturbation apparatus consisted of the four main components shown in Fig. 8.19.

A high speed camera with internal memory recorded video of perturbation events and

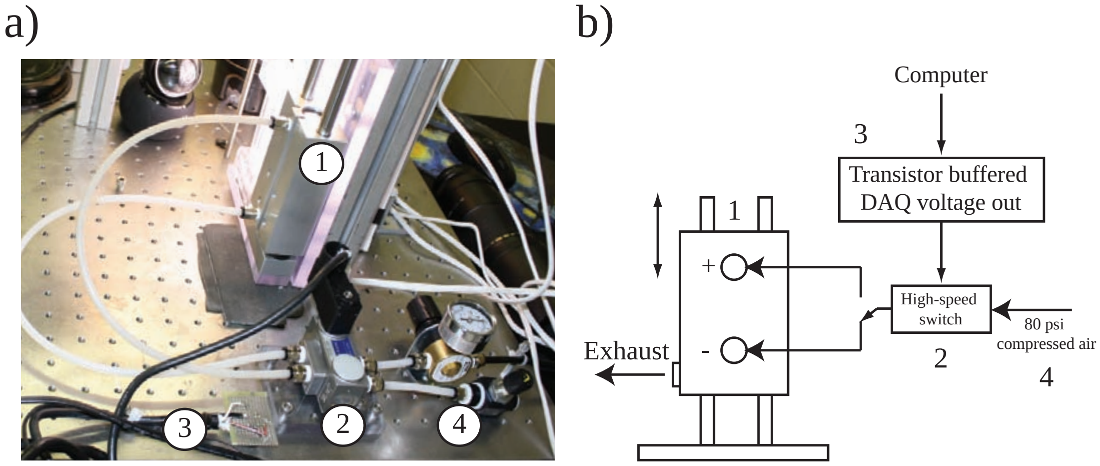

**Figure 8.20:** Perturbation apparatus setup. 1) Pneumatic air piston. 2) High speed solenoid and compressed air switching port. 3) Transistor circuit to power solenoid switch. 4) Pressure regulator feeding compressed air into pneumatic air piston.

was triggered to record 2 s of video at a rate of 500 Hz, to begin 500 ms prior to initiation of the perturbation (Fig. 8.19(1)). The camera was controlled through a custom C++ program written using the vendors software development kit. Ants freely trafficked between an above surface foraging arena which consisted of a plastic bin with a chemical coating, fluon, surrounding the walls so that ants could not escape (Fig. 8.19(2)). Ants accessed the above surface arena through a series of tunnels as described in 8.3.4.3 which in turn were connected to a closed tupperware dish which was spray painted black to block light. The black dish simulated a darkened nest environment. A bright light was placed over the foraging arena to create a light and temperature gradient between the simulated “surface” and “nest” environments. A second camera controlled over USB monitored the vertical tunnels continuously to determine when ants crossed a region of interest at the top of the tunnels (Fig. 8.19(3)). A LabVIEW program repeatedly computed the difference between two adjacent images in time captured by the USB camera and when the difference in pixel intensity exceeded a threshold in the region of interest, signifying the entrance of an ant into that location, a signal was sent to a voltage output on a USB digital signal acquisition card (DAQ). The vertical tunnels were mounted to a pneumatic air piston maintained at 80 psi and which would displace a distance of 0.5 cm in ≈15 ms (Fig. 8.19(4)).

The pneumatic air piston (Fig. 8.20(1)) was controlled by a compressed air switch which toggled the output of compressed air to one of two possible outputs (Fig. 8.20(2)). A high speed solenoid toggled the switch from its default state through an applied voltage to solenoid (Fig. 8.20(2)). The solenoid was controlled by a DAQ voltage out which was connected to the base of a transistor connected to a 12V power supply.

# CHAPTER IX

# TRAFFIC IN TUNNELS

## *9.1 Summary*

Fire ant colonies create extensive underground networks of foraging tunnels which serve to protect foraging workers from predation and exposure. Foraging tunnel networks can reach upwards of 50 meters in length and thus take a considerable energetic investment from the colony to create. Surveys of the shape of these foraging tunnels indicate that the diameter of the tunnel decreases as the tunnel distance from nest site increases. It is thought that this decrease in diameter is due to a smaller amount of worker traffic at the points further away from the nest in analogy to fluid flow in river networks. In this study we examine the traffic dynamics of fire ant workers freely walking between a nest and a foraging arena in the laboratory. Ants are presented with a tunnel 11 cm long tunnel of constant cross sectional diameter (varied per experiment from 2,3,4,6 mm) in which we monitor the traffic with a high speed camera. We study the traffic flow of workers as a function of tunnel size to determine how tunnel size influences the statistics of ant traffic. We find that in tunnels of 3,4,6 mm in diameter, the spatial and temporal correlations of ant position within the tunnel look similar and we observe slowing down of the traffic dynamics with increasing number of ants in the tunnel. In the smallest tunnel, 2 mm in diameter, we observe that relaxation times of the traffic flow are much more sensitive to number of ants within the tunnel and indicate the formation of large traffic jams not seen in the larger tunnels. We show that the formation of these jams is associated with the inability of worker ants to pass each other in this tunnel.

## *9.2 Introduction*

Fire ants build complex nests through the excavation of soil [127]. The central nest region extends vertically into the soil and contains flat, pancake-like chambers in which food and brood are stored. Radiating off of the central nest is a network of horizontal tunnels which serve as foraging tunnels (See fig. 2.21 in section 2.2.4.2 [138, 140]). The purpose of foraging tunnels is to provide fire ant workers protection from predation and exposure as they forage. Foraging typically incurs the highest mortality among ant workers and thus foraging tunnels can be seen as an evolved strategy to minimize worker mortality [127]. In this chapter we investigate traffic phenomena in laboratory foraging tunnels.

The study of traffic has a long history in physics research (See [302, 303] for reviews). Traffic phenomena is a transport process and in the simplest case can be viewed as a situation in which particles move along a single direction and interact with each other by the simple fact that they cannot overlap (i.e. they exclude volume). This case of uni-directional traffic in which particles exclude volume has been studied extensively in computation and numerics and is called the asymmetric simple exclusion process (ASEP [302]). This process has also been observed in biological systems as well, in the case of uni-directional ant traffic along trails [304, 305] and in the traffic of motor proteins along microtubules [306]. See [307] for a comprehensive review of traffic in biological systems.

The size and shape of foraging tunnel cross-sections created by fire ants varies as a function of the tunnel distance from the central mound [140]. This decrease in tunnel size is matched by a decrease in the density of foraging workers within the tunnel as the distance from the central nest increases [140]. Thus a natural hypothesis is that the cross-sectional size of foraging tunnels is optimized to the carrying capacity of the foraging traffic of ants at that location. Traffic within a confined environment is different from previous observations of ant traffic in which ants were monitored on unconfined trails [308, 249], or along paths in which there were several choices of trail [280]. In confined traffic within tunnels we expect that the excluded volume of ants will be important in governing the dynamics in different situations of ant density within the tunnel. In this chapter we perform a laboratory experiment to study traffic phenomena in simulated foraging tunnels. We use concepts from inert granular systems to study the traffic patterns and find that tunnel diameter has a strong effect on the dynamics of ant mobility within tunnels.

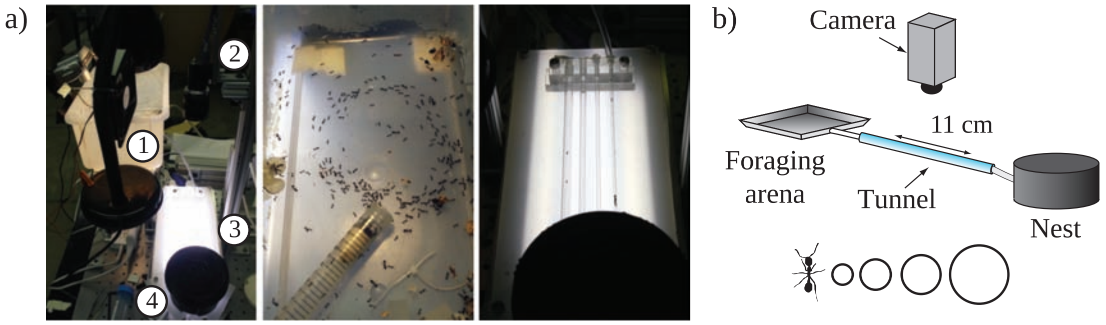

**Figure 9.1:** Traffic experiment apparatus. a) Left image shows the traffic experiment. (1) Foraging arena, (2) Camera, (3) foraging tunnel, (4) nest. Middle image shows above surface foraging arena. Right image shows Foraging tunnels. b) Schematic of the experiment and tunnel size compared to ant body size.

## *9.3 Apparatus and analysis*

Here we investigate the traffic dynamics of groups of fire ant workers in a laboratory experiment. We monitor free-flow, unperturbed, traffic between a simulated nest and an open foraging arena (Fig. 9.1). Groups of 500-2000 worker ants were collected from their host colonies and placed in the foraging arena to begin the experiment. Care was taken to remove queens, male sexuals, and brood from the worker group. We provided ants with a test tube filled with water and blocked with a cotton ball in an open foraging arena that was illuminated with a heat lamp. The foraging arena was connected through a single glass tunnel to an enclosed, light-proof, tupperware container which served as a nest. Within the nest we placed a porous plaster of paris floor which was wetted. The glass foraging tunnel was 11 cm in length and varied in diameter between $[2, 3, 4, 6]$ mm. Only one tunnel was in place for an experiment. For reference the typical body length of a worker fire ant is $\approx 3.5$ mm and in figure 9.1c we show the tunnels drawn to scale with respect to an ant.

Data collection consisted of recording video sequences of traffic within a tunnel. We used a high-speed, high-resolution camera to collect images of tunnel traffic captured at a rate of 100 Hz, and resolution of $100\times1328$ pixels where 1 cm = 120 pixels. Video sequences of 40 s in duration were stored in computer memory and then saved to a hard disk using the lossless lagarith video compressor. After the collection of each video, we performed pre-processing in Matlab in which we constructed the space-time image and measured ant density during each frame in the sequence. Once pre-processing was finished we saved a data file associated with the video and then repeated the capture process.

The space-time image, $\rho(x,t)$, is measure of the number of ants at horizontal location $x$ and time $t$ within the tunnel. $\rho(x,t)$ was constructed by first calculating a background image for the video sequence. The background image was calculated by determining the median value of each $(x,y)$ pixel location taken across 100 images from the sequence. We divided each frame of the video by the background image to get a normalized image in which a pixel value of 1 represents no change from background, and pixel value of 0 is a dark object that was not in the background image. We chose this segmentation method because ants are naturally represented as black pixels. We thresholded the background normalized video frame with a threshold level of 0.75, retaining all pixels in the image with intensity below this value. Lastly we summed the thresholded image over the y-direction which resulted in a single row of the space time image in which the value of $\rho(x,t)$ represents the density of ants at that horizontal position, $x$, and time $t$, within the tunnel.

Figure 9.2 shows an example of a space-time image from a 40 s duration video sequence of ant traffic. Using space-time images we are able to examine locomotion of individual, and collections of many ants in close proximity, without the concerns of particle tracking in which occlusions may result in tracking error. Conceptually we envision ant traffic as a 1-D transport process in which the space-time image, $\rho(x,t)$, represents the instantaneous cross-section of ants at location $x$ and time $t$ within the sequence.

Since ants will continuously forage we continuously monitored traffic-flow and captured 10,514 videos of traffic flow among worker groups. These videos are drawn from 25 separate test dates over which tunnel diameter was varied (2,3,4,6 mm). Five worker groups drawn from separate host colonies were monitored in the experiment. In this chapter we have included all experimental observations of tunnel traffic, including observations in which inactive ants are stationary within the tunnels.

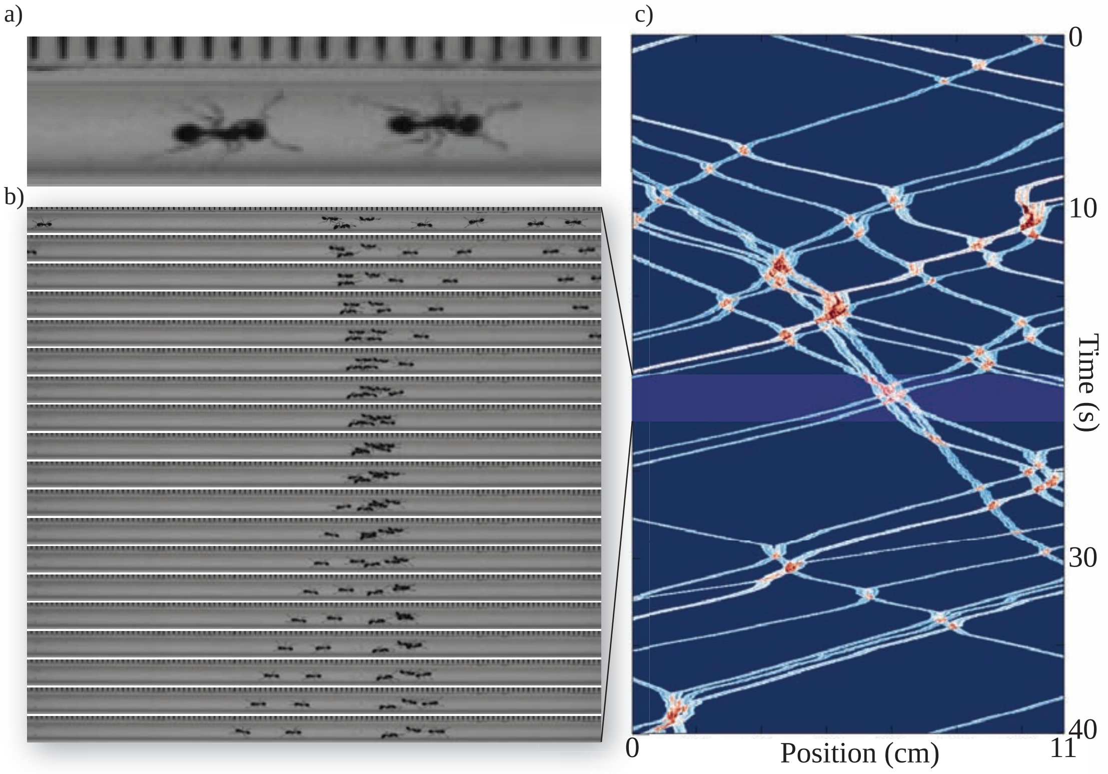

**Figure 9.2:** Video and space-time analysis of ant-traffic. a) Close up image of two ants within a 3 mm diameter tunnel. b) Image sequence of ants moving bi-directionally within the tunnel. In the middle of the tunnel three ants come from the left and two from the right to cross paths and interact, after which they pass each other and proceed in the same direction. Images are separated by 14 ms. c) Space-time representation of the ant traffic within the tunnel. Image sequence is taken from the highlighted section in the middle of the space-time plot.

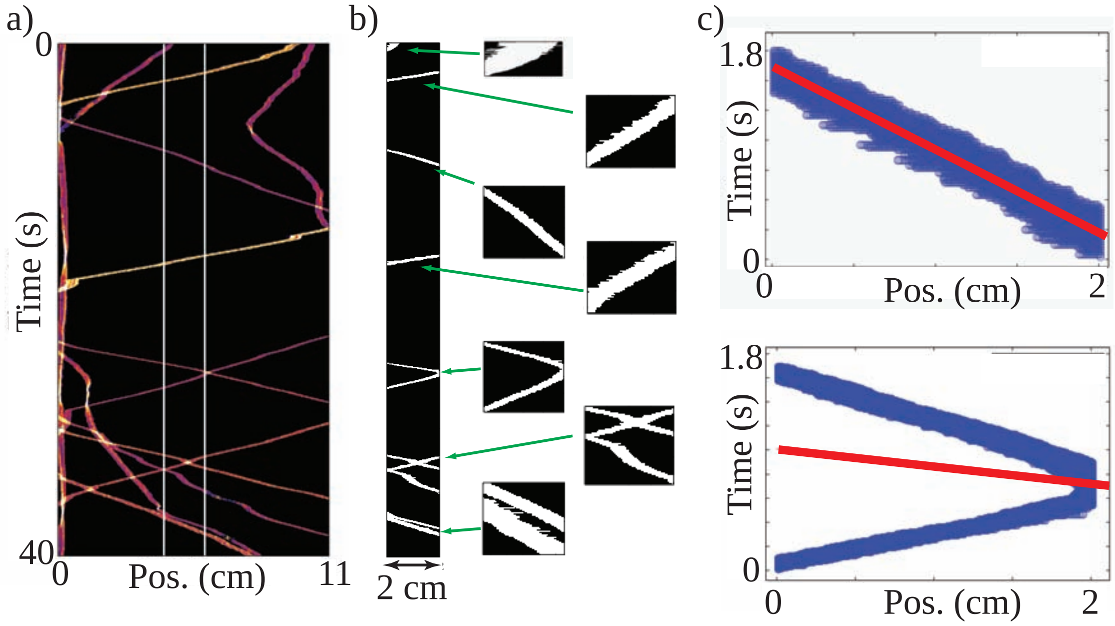

**Figure 9.3:** Analysis of ant free speed in tunnels. a) Space-time diagram of ant traffic. b) Extracted 2 cm wide and 40 s long image from the space-time diagram. Single and collective ant trajectories are shown on the right with arrows pointing to their location in the space-time image. c) Lines fitted to a single ant trajectory (above) and multiple ant trajectories (below). Goodness of fit determines whether trajectory is from a single ant (top) or multiple ants that interact (bottom).

## *9.4 Effect of tunnel size on single ant locomotion*

We begin our study of tunnel size-effects on traffic by investigating how tunnel size influenced the free-flow speed of individual ants. Understanding the effect of tunnel size on free-flow ant speed, independent of collective effects, is important for determining a baseline mobility. To study the free-flow speed of individual ants we use single-ant trajectories in the space-time images (Fig. 9.3). We find all ant trajectories within the middle 2 cm of the tunnel (Fig. 9.3a,b) by isolating the connected components in this central image region. We fit lines to the connected components and set a criteria for single-ant trajectories such that the $R^2 > 0.9$ from the linear fit. In figure 9.3c we show two examples of this line fitting, one for a single-ant trajectory (Fig. 9.3c top), and one in which two ants merged (Fig. 9.3c bottom). We reject the merged trajectories by the poor linear fit. Ant speed, $v$, is the inverse slope computed from the linear fit.

To determine if tunnel size influenced ant limb use or stepping pattern we found three

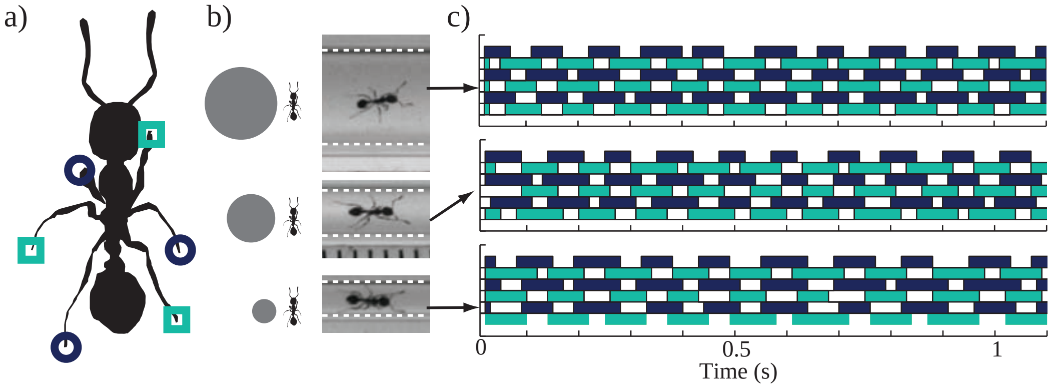

**Figure 9.4:** Ant stepping pattern in three different tunnels. a) Schematic of the alternating tripod stepping pattern. Opposing limb tripods are shown by circles and squares respectively. b) Images of worker ants in three different tunnel sizes (top 6 mm, middle 4 mm, bottom 2 mm). c) Stepping pattern for locomotion. Colored regions correspond to limbs in contact with the ground. In order from top to bottom: left-fore, left-mid, left-rear, right-fore, right-mid, right-rear.

instances in which ants traveled at similar velocity (within ≈10%) and measured their stepping pattern (Fig. 9.4). Six-legged, hexapod, insects like ants often step with an alternating tripod gait during forward locomotion [259]. This means that alternating pairs of fore and rear limb on one side are in contact while the mid-limb on the opposing side is in contact (See diagram in Fig. 9.4a). We observe that ants utilized an alternating tripod gait in the largest and smallest tunnel size as seen in figure 9.4c. The invariance of gait as a function of tunnel size supports previous observations from section 8.4.2 that tunnel size has only small influences on locomotion.

In figure 9.5a we show the probability distribution function of single ant walking speeds in the four different tunnels. We find that there was no significant effect of tunnel size on ant walking speed (two-way ANOVA with colony as a random effect, $F_{3,45436} = 4.74$, $p = 0.0831$). Single ant free speed was found to be $v = 1.90 \pm 0.58$ mm/s (45,444 observations). Our observation of the single ant free-flow speed within tunnels is very similar to the free-flow speed of single fire ants running across a horizontal planar substrate, $v = 1.96 \pm 0.64$ cm/s, which was observed fire ants foraging in nature [140]. The observation of Tschinkel [140] was made in a field setting in which fire ants were exhibiting their natural foraging behavior and thus gives evidence that the locomotory behavior observed in simulated foraging within

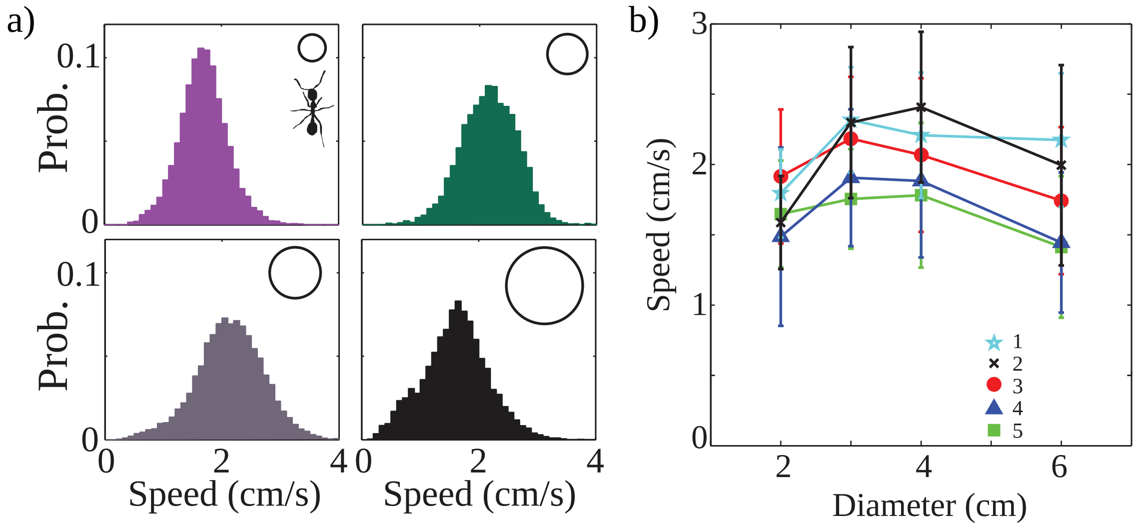

**Figure 9.5:** Analysis of single ant speed in tunnels. a) Probability distribution functions for ant speed in different diameter tunnels. 2 mm (upper left), 3 mm (upper right), 4 mm (bottom left), and 6 mm (bottom right) tunnels. Inset circles represent tunnel cross-section and are drawn to scale with ant in upper-left plot. b) Mean±standard deviation of single ant speed as a function of tunnel diameter for the five colonies in experiment.

our experiment is similar to that of fire ant behavior in nature.

Although it appears in figure 9.5a that there is a slight increase in speed for the 3 & 4 mm diameter tunnels, this effect is explained by the variance in ant speed among the separate colony experiments (removing colony from the ANOVA resulted in tunnel size having a strong significance on speed). This can be seen in figure 9.5b in which we show the mean±standard deviation values for single ant speed in different tunnel diameters among the five colonies.

Thus in summary we find that tunnel size has no significant effect on the free speed of ants locomoting between the nest and foraging site. Furthermore the limb-use patterns appear the same across the different tunnel sizes. Subsequent differences that we will later observe in the locomotion of collections of ants within different tunnel diameters will thus be due to the collective effects of locomotion in confined spaces.

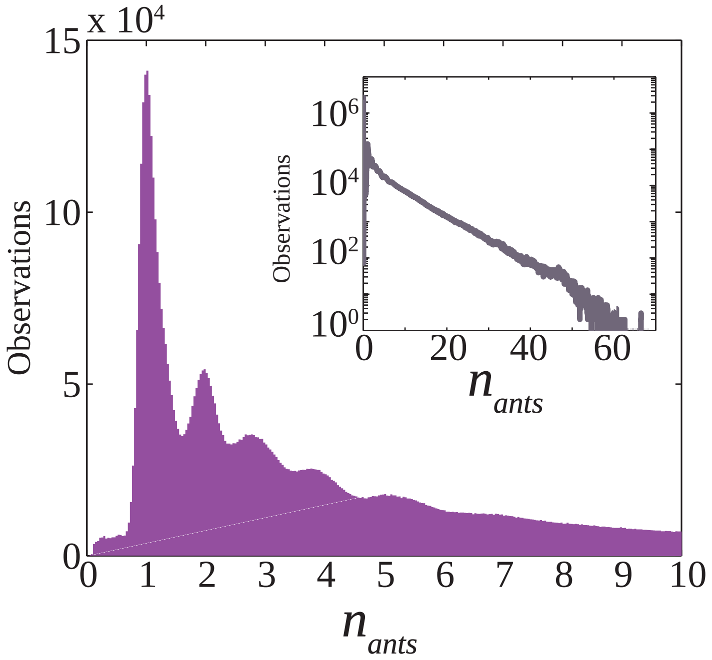

**Figure 9.6:** Histogram of ant-tunnel density across all experiments. Inset shows y-axis on a logarithm scale and illustrates the exponential decay of the histogram.

## *9.5 Spatio-temporal dynamics of ant traffic*

### 9.5.1 Spatial statistics of traffic flow

We define the ant-tunnel density at time $t$ as $n_{ants}(t) = \frac{1}{C}\sum_x \rho(x,t)$ where $\sum_x$ is the sum over entire length of the tunnel, and $C$ is a normalization constant which sets $n_{ants}(t) = 1$ when one ant is in the tunnel ($C = 58$, determined by visual inspection). A histogram of observations of $n_{ants}$ across all experiments illustrates that the majority of tunnel observations corresponded to a single ant within the tunnel (Fig. 9.6) . The broadening of the peaks of the histogram are due to the variance in ant size within the experimental colonies. The probability to observe increasingly larger numbers of ants within the tunnel decays exponentially (inset Fig. 9.6). This suggests that the entry and exit of ants into the tunnels may be approximated by a random, Poisson process (we discuss this point further in section 9.5.3).

### 9.5.2 Spatial correlation of traffic flow

To explore how the spatial arrangement of ants within the tunnel varies as a function of density and tunnel size, we compute the spatial autocorrelation of ant configurations when $n$ ants are present in the tunnel. We define the spatial autocorrelation as $g_n(l) = \langle \rho(x,t)\rho(x+l,t)\rangle$ with lag distance $l$. The brackets, $\langle \cdot \rangle$ represent an ensemble average over observations in which $n_{ants}(t)$ is within $\pm 2$ ants of the focal $n$. We normalize $g_n(l)$ such that $g_n(0) = 1$ and $g(\infty) = 0$.

We interpret this auto-correlation function as a measure of the probability to find ants within a distance $l$ of each other along the length of the tunnel. In figure 9.7a we show a space-time image from a 4 mm tunnel experiment and in (b) of this figure we show the instantaneous ant density along the length of the tunnel. The spatial autocorrelation effectively measures how much the the density overlaps itself as we shift the curve to the right. This is often called the density overlap function and in this case is the spatial density overlap function. For a lag distance $l = 0$ there is 100% overlap ($g_n(0) = 1$) while for increased lag distance the overlap of the curve with itself decreases and so does the autocorrelation function. In figure 9.7c we show the normalized spatial autocorrelation for the function in (b) in addition to other replicates at comparable ant density.

We find that both tunnel diameter and number of ants affect the shape of $g_n(l)$ (Fig. 9.8a). In general, for small $n_{ants}$ the spatial autocorrelations were similar in shape across all tunnels. However, the decay of $g_n(l)$ from unity to zero occurred over a longer lengthscale as the number of ants in the tunnel increased. This effect matches our intuition: as more ants are found in the tunnel, there is a higher probability to find aggregations of ants in turn resulting in a larger spatial correlation of ants along the tunnel (higher $g_n(l)$). To quantify the decay of $g_n(l)$ we fit functions of the form $g_n(l) = \exp\left[\left(-\frac{l}{\lambda}\right)^{\beta}\right]$ where $\lambda$ is a characteristic decay distance of the autocorrelation function and $\beta$ is a stretching parameter (see section 6.4.2).

In figure 9.8b we show how $\beta$ and $\lambda$ vary as a function of $n_{ants}$ for the four different tunnel diameters. We find that $\lambda$ increases linearly with $n_{ants}$ for all tunnel diameters. $\beta$ decreases from a value of 1.5 for small $n_{ants}$ to near 1 for higher ant densities. The

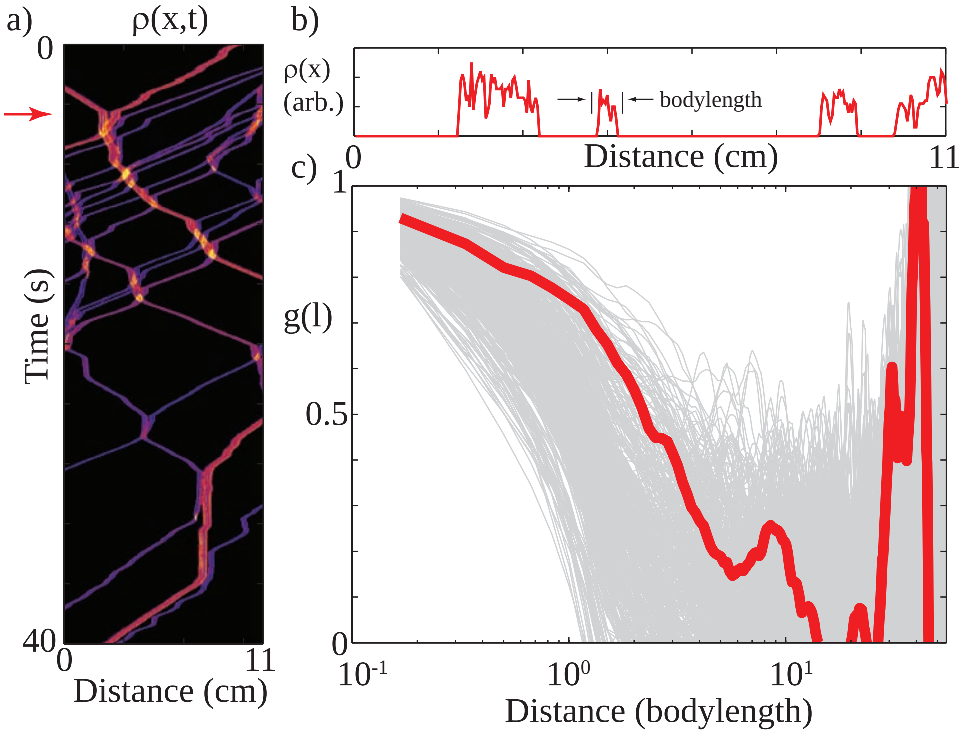

**Figure 9.7:** Spatial density overlap correlation function statistics. a) Space-time image, $\rho(x,t)$ of a 40 s traffic interval in a 4 mm tunnel. b) Instantaneous ant density within the tunnel at time indicated by the red arrow in (a). The two arrows indicate the length of a single ant within the tunnel. c) We show in bold red the spatial autocorrelation, $g_n(l)$, for the configuration of ants within the tunnel shown in (b). Gray curves are from other replicate observations which had similar $n$.

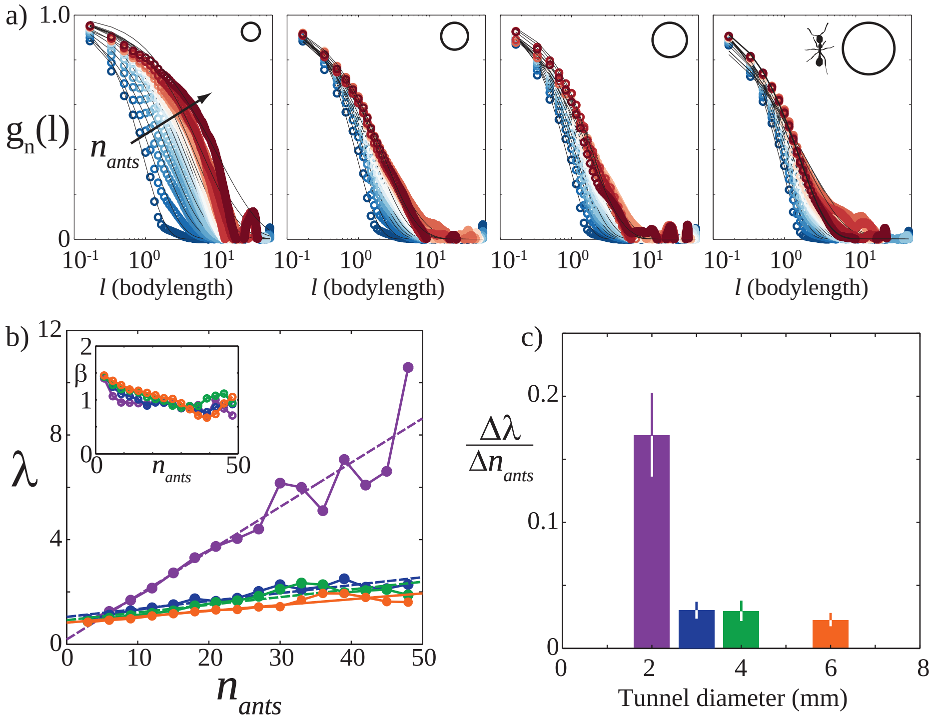

**Figure 9.8:** Spatial density overlap correlation functions for different tunnel diameters. a) The function $g_n(l)$ for different tunnel diameters (2,3,4,6 mm from left to right) and different number of ants (increasing $n_{ants}$ indicated by arrow in left figure). b) Decay constant of the spatial autocorrelation as a function of $n_{ants}$ in different tunnel diameters (2 mm purple, 3 mm blue, 4 mm green, 6 mm orange). Lines represent linear fits. c) Slope of the linear fits in (b) as a function of tunnel diameter.

sensitivity of $\lambda$ to ant density is measured by the slope the linear fits in figure 9.8. The 2 mm diameter tunnel had a significantly steeper slope than the other tunnels indicating a larger probability to find aggregations of ants within the 2 mm tunnel than in the the others (Fig. 9.8c).

Thus in observations of the static configurations of ants within the tunnel we find that there is little difference in the correlation functions for tunnels 3,4,6 mm respectively. However within the 2 mm tunnels the spatial autocorrelation decays over a significantly longer lengthscale for increasing ant number, possibly signifying a qualitative shift in the traffic dynamics in this tunnel. To determine how traffic dynamics differ among the tunnels we must now examine how traffic patterns vary in time.

### 9.5.3 Temporal statistics of traffic flow

We begin our analysis of the temporal statistics of traffic flow by focusing on a point along the length of the tunnel and counting the time between ant crossings at that location, the wait-time, and the duration of time ants occupy that location, the occupancy-time. This is analogous to traffic flow measurements performed on municipal roadways in which a pneumatic sensor counts the duration of, and time between car-crossings [309]. In figure 9.9 we show measurements of $\rho(x_j, t)$ for three fixed locations, $x_j$, as a function of time. From $\rho(x_j, t)$ we measure the wait-time and occupancy-time for ant crossings at that location (See Fig. 9.9). In our experiment we measure the occupancy-times, and wait-times, at every position along the length of the tunnel. We first discuss the distribution of wait-times observed in the experiment.

In figure 9.10 we show the probability distribution of wait-times for different experiments (represented by different color) in the four different tunnels. We find that wait-time distributions for all experiments across all tunnels were exponential thus signifying that ant entry and exit within the tunnel occurs randomly. The different slopes of the curves represents different levels of activity of the colony in different experiments. In experiments in which the traffic appeared to be most active, the decay of the wait-times function is well approximated by $\exp(t/8\ s)$ with a time constant of 8 s (red line in figure 9.10). In figure 9.6

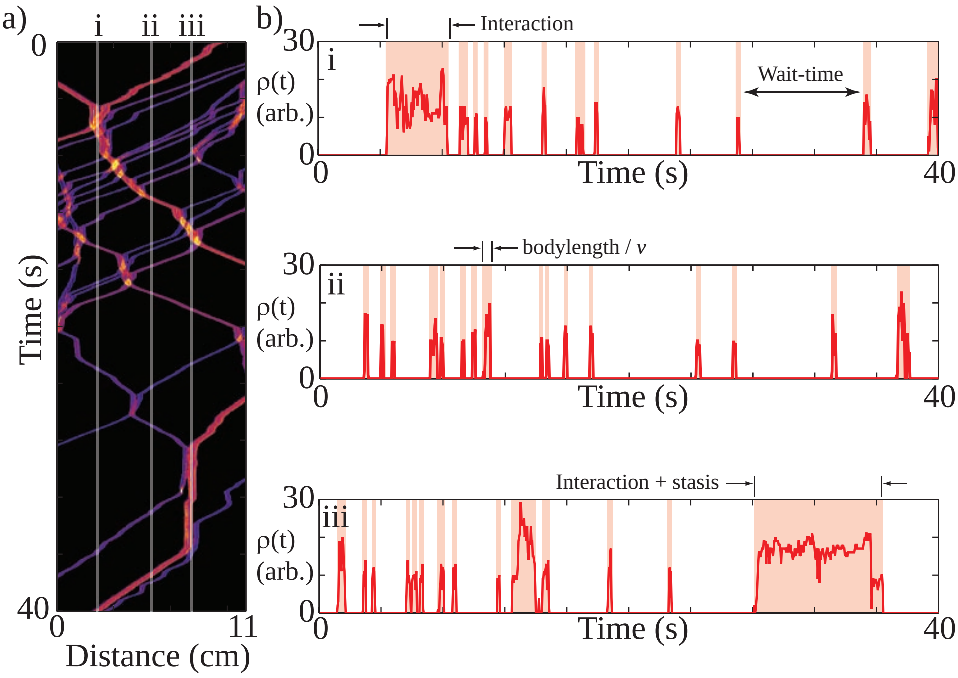

**Figure 9.9:** Temporal statistics measured from space-time images. a) Space-time image showing three representative cases of traffic flow at that point in space (i-iii). b) Here we show the value of $\rho(x,t)$ for three fixed positions along the tunnel length as a function of time. Shaded region shows occupation duration. In position (i) we show a case in which the first occupation of the observed tunnel segment corresponds to the interaction of two ants (see space-time image). Subsequent occupations correspond to crossings of individual, mobile ants. In position (ii) we observe no ant-interactions, only short-time occupations of the observed tunnel segment which correspond to mobile ants crossing the segment. In tunnel position (iii) we highlight a tunnel-occupation which corresponds to an ant-ant interaction, followed by one ant remaining in the same position for several seconds prior to moving again.

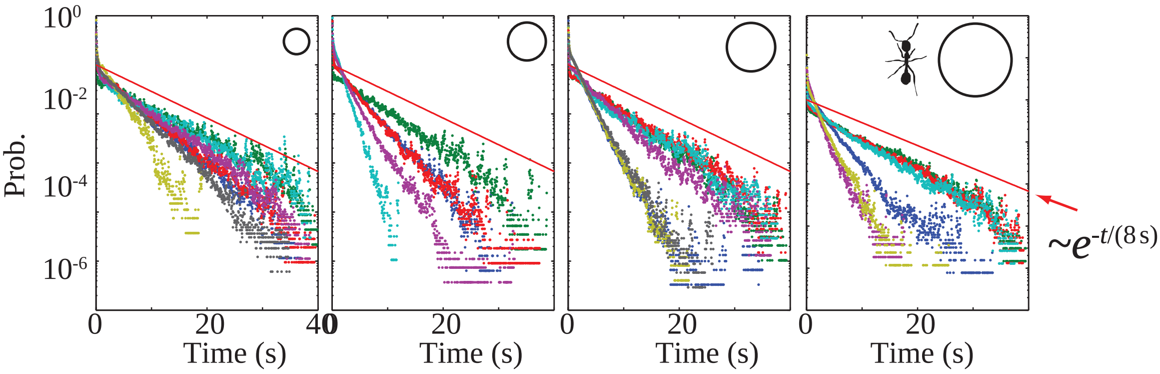

**Figure 9.10:** Probability distribution of the time-duration between ant crossings within a tunnel. Tunnel diameters from left to right: 2, 3, 4, 6 mm. Different color curves represent different experiments. Red curve shows an exponential curve with decay constant of 8 s to guide the eye.

we saw an exponential decay in tunnel density which suggests that ant entry and exit may be treated as a Poisson process. The exponential probability distribution of wait-times for an ant to cross an arbitrary location within the tunnel (Fig. 9.10) further supports evidence that ant entry and exit to the tunnel occur randomly and thus are described by poisson statistics in which the wait time between events is exponential.

The duration of time that an ant occupies a specific location, $x$, within the tunnel is called the occupancy time (Fig. 9.9). We show in figure 9.11 the distribution of occupancy-times among the separate experiments across the four tunnels. As shown in figure 9.9 the distribution of occupancy-time reflects several different behaviors ants exhibit within the tunnel, namely: locomotion, interaction, inactivity. Inactivity may seem like an inefficient feature of foraging tunnel traffic, however in natural foraging tunnels platoons of fire ants remain stationed at locations within the tunnel so that they may be rapidly recruited to food sources when discovered [140]. Thus inactive ants within our laboratory tunnels may be reserve foragers waiting to be recruited. Freely moving ants contribute the most to the occupancy-time distribution as indicated by the peak at $t = \frac{bodylength}{v} = \frac{0.35cm}{1.9cm/s} \approx 0.18$ s (See insets Fig. 9.11). The distribution of occupancy-times varied across experiments, yet all exhibit power-law behavior in the tail of the distribution with an exponent of approximately $-3$.

The non-exponential nature of the occupancy-time probability distribution function is

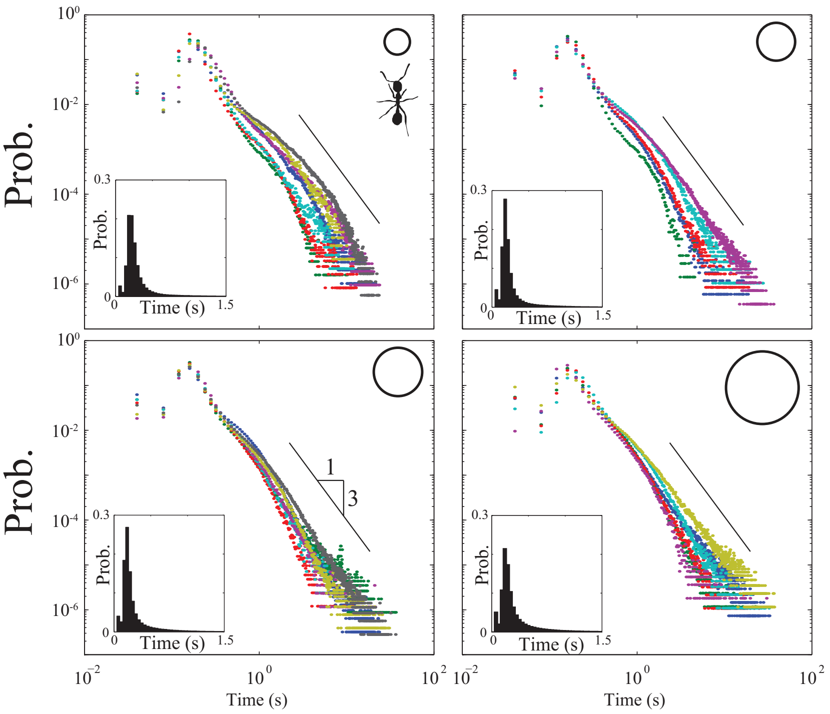

**Figure 9.11:** Distribution of tunnel occupation durations. Tunnel size is denoted by drawing in upper right hand corner. Inset shows linear-linear histogram of the peak.

of interest because all other observations of temporal statistics within the tunnel system suggest that traffic flow is random, and thus we should expect exponential distributions. However we observe non-exponential distributions of the occupancy time, suggesting a non-poisson process which governs the time over which ants stay fixed in place within the tunnel. Here we introduce a simple model of ant traffic flow within tunnels which illustrates how the inclusion of a social-component to ant-interaction rules gives rise to a power-law distribution in occupancy time.

In experimental observation ants move bi-directionally through the tunnel and stop only upon encountering another ant (we ignore inactive ants, or ants that perform u-turns within the tunnel in this simulation). Thus we may model the traffic of ants within the tunnel using simple ant "agents" which walk at a constant speed until coming in contact with another agent, at which point they pause for a certain delay time, after which they resume moving again (See Fig. 9.12). Ants are defined to have length, $L = 0.35$ cm, and move along a one-dimensional tunnel in the left or right direction with speed $v_i$ (where $i$ is the $i^{th}$

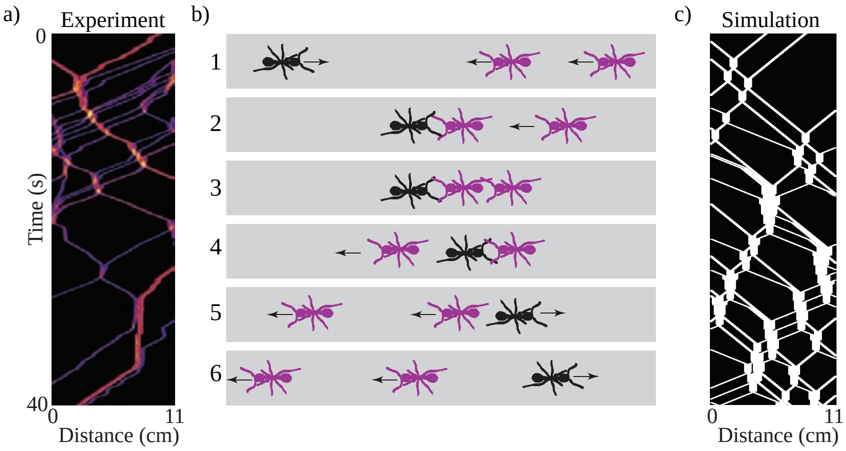

**Figure 9.12:** Overview of simulation of ant traffic. a) Space-time image from experiment. b) Ants enter the tunnel from left (black) and right (purple). When two ant encounter each other they pause (2), this can lead to multi-ant jams (3). After ants have paused for time $T = T_0 + \kappa\rho$ (see text for details), they move past each other and continue along until another collision occurs (4). c) Space-time image from simulation of traffic flow.

and) which is randomly drawn from a gaussian distribution with mean and variance equal to the free-speed observations from section 9.4. When the center-center distance between two ants becomes less than $L$, ants remain stationary for a time duration $T = T_0 + \kappa\rho$ where $T_0$ is a constant lag-time, and $\kappa\rho$ is a local density dependent lag-time. $\rho$ is the number of ants within a distance $\pm 2L$ of the collision location, and $\kappa$ is a constant which governs the social-interaction time. After time $T$ has passed, the two ants that collided swap places and proceed again along the tunnel at their original speed $v_i$ (see Fig .9.12b (4)). We simulate this traffic model along a tunnel of length 10 cm and for time durations comparable to those of the experiment (40 s) to generate space-time observations, $\rho(x, t)$, of the simulated traffic flow (Fig. 9.12). Lastly, in the simulation we allow ants to enter at random with a characteristic entrance rate comparable to that of the experimental observation.

We vary both the offset time, $T_0$, and the social factor, $\kappa$, in simulation. We find that when $\kappa = 0$ we observe occupancy-time distributions which are exponential with a time constant that increases as $T_0$ increases (See left panel of Fig. 9.13 and inset). Thus, constant $T_0$, with $\kappa = 0$ generates poisson occupancy-time statistics contradictory to what we observe in experiment. The poisson statistics of the occupancy-time probability distribution for $\kappa = 0$ are a result of the random nature of ant encounters within the tunnel as imposed by

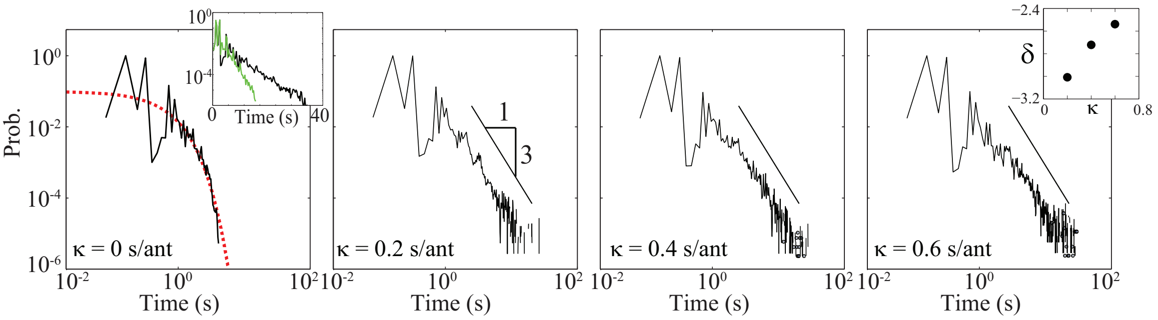

**Figure 9.13:** Occupancy-time distributions from simulation for $T_0 = 0.2s$ and various values of $\kappa$. $\kappa$ increases from left to right. In the case of $\kappa = 0$ (left) we fit an exponential to the probability distribution, $Aexp(-\frac{t}{t_0})$, with $A = 0.1$ and $t_0 = 0.5$ s (red dashed curve in left plot). Exponential time constant for $\kappa = 0$ increases with increasing $T_0$ as shown in inset with $T_0 = 0.2$ (green) and $T_0 = 0.5$ (black). In the three plots on the right with $\kappa \neq 0$ we show a power-law curve, $At^{\delta}$, with exponent $\delta = -3$. Inset in right plot shows $\delta$ versus $\kappa$ from power-law fits to the distribution tail.

the random entry of ants in simulation (matching observation from experiment).

By including a non-zero $\kappa$ term in the model for lag-time we find that the occupancy-time probability distribution transitions to a power-law distribution (Fig. 9.13). Thus the inclusion of the local-density dependent aggregation term, $\kappa$, results in a feedback in the traffic flow in which ants in high-density situations pause for a longer time, leading to traffic jams that persist for a longer duration than expected from a null model of ant-interactions. We find that the power-law probability distribution exponents generated in the simulation are consistent with those observed in experiment. Social-cohesion models of animal encounters are typical in models of flocking and swarming animals ([24] and section 2.2.2). The study of traffic flow in a simple model of collective ant motion presented in this section has illustrated how non-poisson temporal dynamics in traffic flow may arise from a simple social cohesion-process in ant-encounter behaviors.

### 9.5.4 Temporal correlations of traffic flow

Similar to the spatial autocorrelation function in the previous section, we now seek to compute the temporal correlation function for traffic flow. We seek to quantify the mobility of ants in the tunnels as a function of tunnel diameter and instantaneous density. The temporal correlation function is a sensitive measurement of mobility that has been used

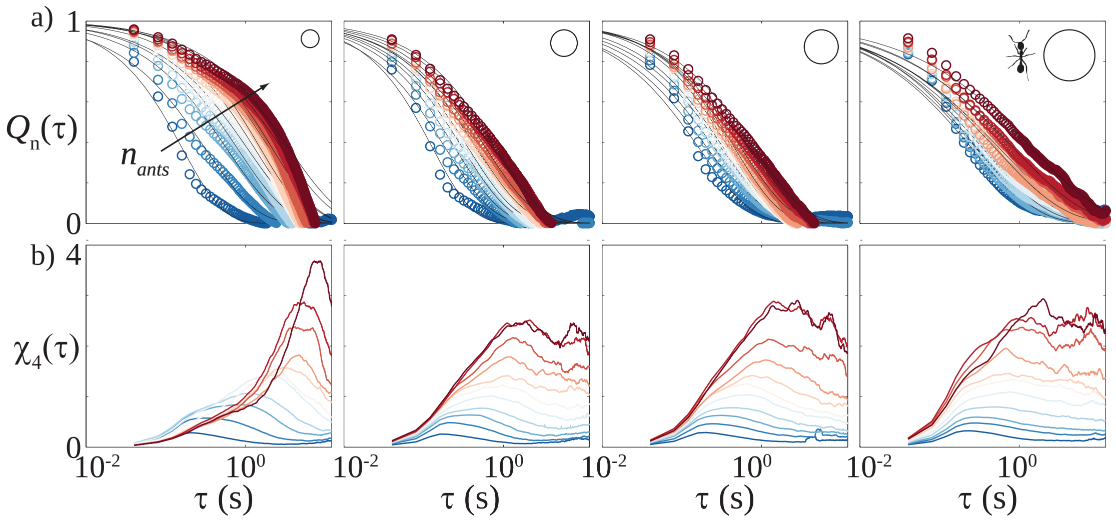

**Figure 9.14:** Temporal correlation function and susceptibility as a function of ant density within the four different tunnels (2,3,4,6 mm from left to right respectively). a) Temporal correlation function, $Q_n(\tau)$, as function of lag time $\tau$. Curves of increasing ant-density within the tunnel increase from left to right (as shown by arrow in top left). b) Susceptibility of the temporal correlation function, $\chi_4$, versus lag time $\tau$. Peaks of $\chi_4(\tau)$ correspond to characteristic relaxation times of the systems.

extensively in passive soft matter studies [310]. As an example of the use of the temporal correlation function, in general for a single ant of bodylength $L$ moving at constant speed $v$, the correlation will decay to 0 within a time $\frac{L}{v}$. If the correlation function does not decay to 0 within this time period, this signifies a possible reduced mobility of the ants within the tunnel and thus the likely presence of traffic jams.

We define the temporal correlation function as $Q_n(\tau) = \langle \rho(x,t)\rho(x,t+\tau) \rangle$ where the brackets represent the same ensemble average as described in the previous section. We show curves of $Q_n(\tau)$ for increasing number of ants in the tunnel in the four separate tunnels experimentally tested (Fig. 9.14). Characteristic jam times can be extracted from $Q_n(\tau)$ by computing the dynamic susceptibility, $\chi_4(\tau) = n_{ants}\left[\langle Q_n(\tau)^2\rangle - \langle Q_n(\tau)\rangle^2\right]$. $\chi_4(\tau)$ was originally developed for passive, soft-matter systems such as colloids [311], glass forming liquids [312], and granular materials [313] and is a measure of the timescale associated with the decay of correlated regions in time (in our case traffic jams). See [310] for a review of $\chi_4$ in various soft matter systems.

$\chi_4$ is most easily understood as a measure which is proportional to the variance of $Q_n(\tau)$

within the ensemble of constant $n$. For zero time delay there is a 100% correspondence in the the temporal signal of ant density within the tunnel (i.e. $Q_n(0) = 1$), and thus the variance of $Q_n(0)$ is zero ($\chi_4(0)$). At large lag times, there is 0% correspondence between the original ant configuration and the current configuration ($Q_n(\infty) = 0$) and correspondingly the variance is zero ($\chi_4(0)$). However at some intermediate lag time, $\tau^*$, some ant jams will persist and give a high value of $Q_n(\tau^*)$ and some ant jams will have separated and give a low value of $Q_n(\tau^*)$. Thus at this intermediate time $\tau^*$ the variance in $Q_n(\tau^*)$, and thus by definition $\chi_4(\tau^*)$, will be maximum. The time-scale at which point $\chi_4$ is maximum is known as the characteristic relaxation time, $\tau^*$, of correlated regions of ants within the tunnel. In our system these regions are stationary traffic jams.

In figure 9.14a we show plots of $Q_n(\tau)$ and $\chi_4(\tau)$ for various conditions of ant density and tunnel diameter. We observe that increasing $n_{ants}$ increases the decay time of the temporal correlation function. However, as with the spatial correlation function of section 9.5.2 the effect is most prevalent in the 2 mm diameter tunnel. In figure 9.14b we show $\chi_4(\tau)$ which for all values of $n_{ants}$ shows a peak at different lag times, $\tau^*$.

To check the validity of our interpretation of $\tau^*$, which we have defined as a measure of the characteristic time-scale that an ant density will spend at a location in space. we examine $\tau^*$ in the dilute limit (low $n_{ants}$). When there are very few ants within the tunnel we expect that there will be no interaction among the ants (assuming they are distributed randomly) and thus the characteristic decay time should be $\tau^* = \frac{L}{v}$ where $L$ is bodylength and $v$ the free-speed. From our previous observations, tunnel size does not have a significant effect on $v$, and thus we predict that $\tau^*$ in the dilute limit will be independent of tunnel diameter. From our previous observations of free speed ($v = 1.90 \pm 0.58$ cm/s) and ant bodylength ($L = 0.35 \pm 0.05$), we predict that $\tau^* = 0.18 \pm 0.06$. Experimentally we find that for $n = 3$, $\tau^*$ varies between 0.22-0.27 among the different tunnel sizes and is independent of tunnel diameter. The agreement between our expected and mesured $\tau^*$ confirms our hypothesis that $\tau^*$ is a signature of the decay time of spatial-correlations within the tunnel over time.

We plot $\tau^*$ versus the number of ants within the tunnel for the four different tunnels in

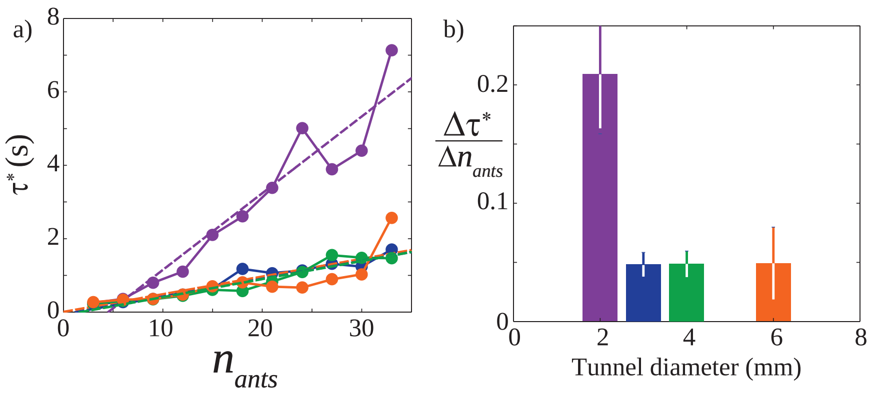

**Figure 9.15:** Sensitivity of relaxation time to tunnel size and ant density. a) $\tau^*$ versus number of ants in the tunnel for the four tunnel diameters. b) Slope of the linear fits from (a) as a function of tunnel diameter.

figure 9.15. Similar to the sensitivity of spatial correlations to $n_{ants}$ and tunnel diameter (see section 9.5.2), tunnels of 3,4,6 mm diameter display weak sensitivity of $\tau^*$ to $n_{ants}$ compared to the case of the 2 mm tunnel in which $\tau^*$ is substantially more sensitive to number of ants. We interpret the steep slope, defined as $\frac{\Delta\tau^*}{n_{ants}}$ (Fig. 9.15b), as a measure of the prevalence to form jams within the tunnel. We observe the similar dependence of $\tau^*$ on $n_{ants}$ for the 3,4,6 mm diameter tunnels which suggests that the sensitivity to jam formation within these tunnels is identical and low compared to the 2 mm tunnel.

Thus we have shown, in agreement with the spatial statistics of ant traffic, that ants in a 2 mm tunnel exhibit a sensitive slowing down of the traffic dynamics as the density of workers in the tunnel increases. Traffic dynamics also slow down in the larger tunnels with increasing ant number, however the effect is not as significant. Furthermore we find that the traffic dynamics in the 3, 4, and 6 mm tunnel are quantitatively similar suggesting that ants are able to mitigate high traffic levels in these tunnels independence of confinement effects.

## *9.6 Catastrophic jams*

To understand the sensitivity of the $\tau^*$ within the 2 mm tunnel we evaluated the traffic flow within this tunnel at conditions of high traffic. In figure 9.16 we compare instances of similar $n_{ants}$ among the 2 mm and 6 mm tunnels. We see that in the 2 mm tunnel a large jam forms in the center of the space-time image and continues to grow in size as more ants merge (figure 9.16a). Observation of the video for this situation indicates that this jam forms because the tunnel diameter is small enough such that ants are no longer able to pass each other (see images in figure 9.16a). Thus ants pile up in the center until eventually one group advances forwards and the other backwards until they exit the tunnel. These catastrophic jams are only observed in the 2 mm tunnels and this likely explains the acute sensitivity of the relaxation time to ant number in the 2 mm tunnel.

For comparison in figure 9.16b we show a similar density of ants within a 6 mm tunnel. We see that ants are able to negotiate the high traffic conditions by moving around each other. We do not observe the formation of large catastrophic jams in tunnels above 2 mm in size and this is likely because in tunnels of this size ants can effectively move around each other.

## *9.7 Conclusion*

In conclusion we have studied the individual and collective mobility of ants within confined tunnel environments that simulate the natural foraging tunnels fire ants construct in nature. We have employed statistical methods derived from the study of jamming in granular and colloidal soft-matter systems to elucidate the characteristic temporal and spatial scales associated with ant traffic jams that may occur in subterranean tunnels. We have shown that traffic dynamics within confined tunnel environments are relatively insensitive to tunnel size when the tunnel diameter is equal to 3 mm or greater. This is in the range of observed tunnel diameters constructed in natural nests [138, 140, 139] and lab studies (chapter 8). The remarkable ability of individual ants, and ant collectives, to maintain mobility within the tunnel environment across a wide range of tunnel cross-sections (3-6 mm diameter) beckons for further study to determine the interaction rules and traffic laws in this confined environment.

We expect that the occurrence of catastrophic jams has significant disadvantages to the mobility and transport of food items and brood along foraging tunnels and nest tunnels. In our observation of ant tunneling we observed that less than 5% of tunnel diameters were

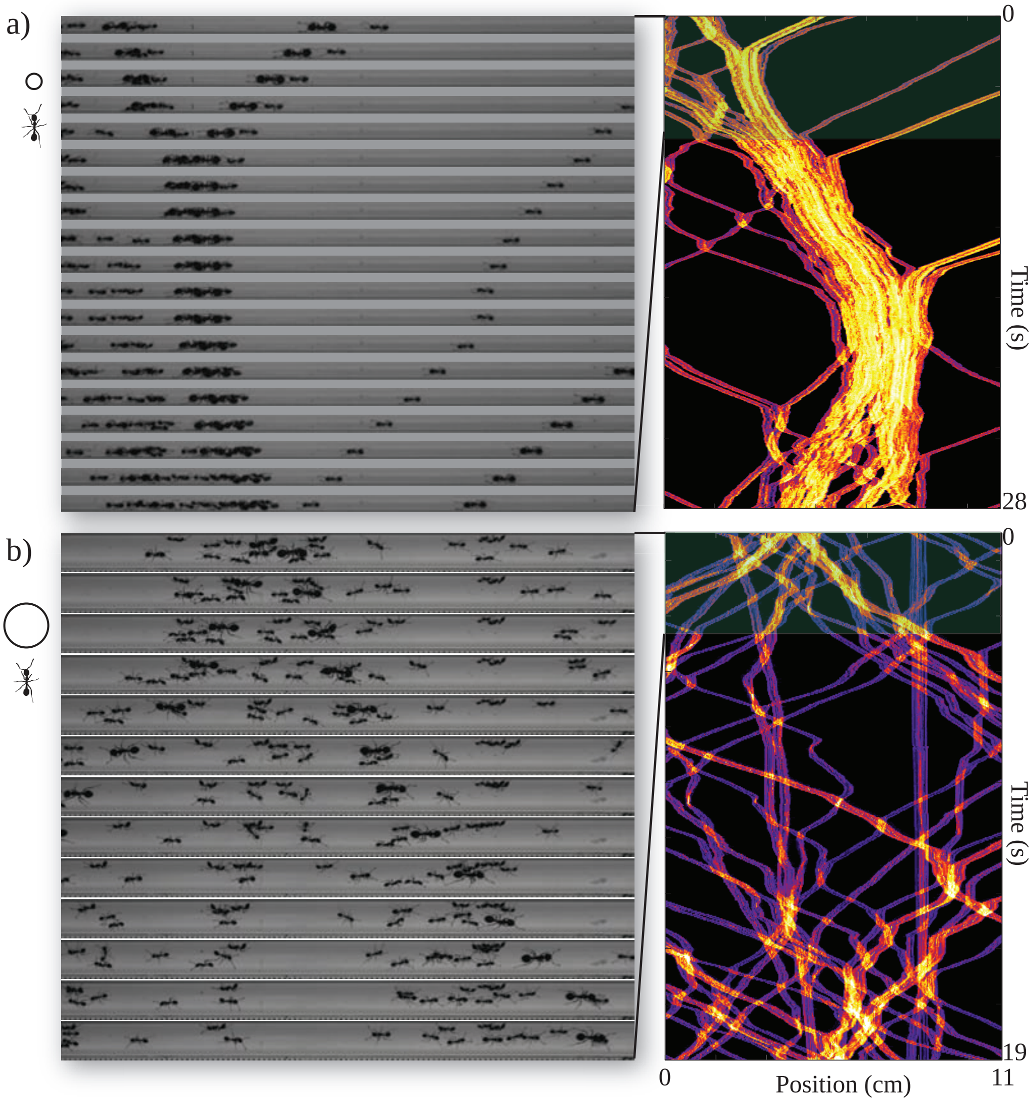

**Figure 9.16:** Comparison of similar density situations in 2 mm (top) and 6 mm (bottom) tunnels. Left side shows image snapshots of the ant positions along the tunnel (separated by 0.4 s). Right shows space-time image of traffic flow. a) In 2 mm tunnels we observe that ants have difficulty passing each other rapidly and thus large spatio-temporal jams can form. These jams persist for a long time period as the ants struggle to get past each other. b) In similar density conditions in 6 mm tunnels ants have little trouble negotiating the crowded environment.

smaller than 2 mm in diameter. Thus we can understand the lower bound to the tunnel diameters observed in x-ray CT as a function of collective mobility of workers within the tunnel. Tunnel construction involves several trade-offs, in general smaller tunnels are more rapidly constructed because they require less material excavation, yet making the tunnel too small introduces significant time costs because of the high cost of traffic jams.

# CHAPTER X

# CONCLUSION

## *10.1 Conclusion*

### 10.1.1 General remarks

In this dissertation I have described a program of study to identify features of collective motion of active and passive granular materials. The principle property of **matter with granularity** is that "grains" fill space and interact through local contact forces. Thus when a granular material, either active or passive, is set in motion the flow dynamics are dominated by the local interactions of constituent grains. Flowing grains must move and rearrange to accommodate the motion of their neighbors and this leads to the rich suite of granular phenomena observed.

In chapters 3-5 we reported physics studies of passive granular materials which show that the failure modes of granular material are sensitive to the initial volume fraction, $\phi_0$. The formation of shear bands has been well known from previous granular materials studies, however the stability and evolution of these shear bands under perturbation was previously un-studied. Our studies of shear band formation and evolution in granular materials highlight the importance of knowing and understanding the dilation transition (at $\phi_c$) for the prediction and modeling of granular failure modes. Follow up studies, inspired by chapted 4, have since been performed by other granular materials researchers. Two papers report similar dynamics in vertical penetration of granular materials [171, 150], one of which extends the model presented in chapter 4.7 to the case of penetration experiments [171].

Avalanches in granular materials have been of interest for many practical reasons. However the sensitivity of avalanche dynamics to $\phi$ have been largely unexplored. We reported in chapter 5 that granular slope stability is very sensitive to $\phi_c$ and exhibits a similar bifurcation in flow response as $\phi$ increases above $\phi_c$. By understanding the slope stability limits as a function of $\phi$ we may be able to future predict the flow response and perturbation sensitivity of granular slopes to be traversed by vehicles or robots.

Stationary-state studies of granular materials are not sufficient to understand the complex force and flow dynamics that occur when for instance a runners foot impacts a sandy ground. The evolution of previously undisturbed granular material, subject to a localized perturbation, is an area of research that is gaining in importance as it highlights features of granular rheology we still don't understand and has practical implications. The importance of initial $\phi$, Reynolds dilatancy, and the granular critical state are highlighted by such localized intruder experiments. Furthermore developing an understanding of how initial $\phi$ controls failure modes under local forcing will aid in the development of control strategies for legged locomotors on granular terrains.

Inspired by the self-assemblages observed among two different species of ants, in chapter 6 we reported the first study of the stability of piles of non-convex granular materials. Non-spherical, and in particular non-convex particles are found at all scales of particulate systems (colloids to grains) and advances in colloidal synthesis are pushing the development non-convex colloids. However ways in which these non-convex particles configure and entangle was previously unknown. Through experiment on a model convex "u-particle" we discovered an unexpected result, that particles of intermediate concavity resisted perturbation for the longest time duration. Thus particles of intermediate concavity effectively display the strongest "cohesion". The cohesion we observe among u-particles is not due to electrostatic charging or moisture and instead is mediated only by shape, and is the result of steric interactions among mechanically entangled particles. Thus we have discovered a new mode of granular cohesion in which cohesion interactions can be finely tuned by particle shape.

In chapters 7-9 we turned our attention to an active particulate system—colonies of the fire ant *Solenopsis invicta.* Active granular systems exhibit similar dynamics as passive granular systems, such as collective jams of ant flow or mechanically jamming in tunnels. We performed a series of experiments with fire ant colonies to understand the principles of collective construction of, and motion within subterranean tunnels.

In chapter 7 we presented experiments to study the role of ant body size in tunnel construction. The worker distribution within a mature fire ant colony is skewed such that most of the workers are smaller (headwith$\approx$0.6 mm) while a smaller percentage of workers are up to 3× larger (headwidth$\approx$ 1.2 mm). An open question in the study of social insects is if there is a functional significance to this worker polymorphism. In our studies we explicitly tested the hypothesis that larger workers within a population will construct tunnels at a faster rate than smaller workers. In digging experiments among workers of differing body size, we found surprisingly that worker size did not have a significant influence on the speed of tunnel construction. The lack of specialization among workers of different body size in digging performance illustrates that fire ant colonies are robust to perturbations of colony demography which is likely an important feature in the tumultuous environment of the Amazon.

In chapters 8-9 we reported results from studying the jamming of individuals and groups of ants within tunnels. We show in chapter 8 that jamming within a tunnel has important beneficial effects on the locomotion of individual ants. When fire ants construct tunnels of an appropriate size, approximately 1.3 times there body length, they are able to rapidly arrest slips when climbing vertically. This rapid arrest due to animal-environment interaction suggests that locomotion control can be embedded in the environment through suitable tunnel construction. Such environmentally endowed stability could explain how ants are capable of high-speed locomotion in their pitch black nest.

Lastly, in chapter 9 we studied how jamming can hinder the locomotion of many organisms when they collectively aggregate within a confined tunnel. The traffic of ants within tunnels is an example of an excluded volume transport process in which only a finite number of ants may pass each other at a given time because of the tunnel size. We find that ants display spatio-temporal dynamics which are largely insensitive to tunnel size when tunnel diameter is equal to or greater than 3 mm. In 2 mm tunnels ants display large catastrophic jams in which immobile groups of ants jam together within the tunnel. These results will allow us to understand the shape and form of fire ant foraging tunnels in nature and suggest that ants are actively engineering their tunnels to mediate traffic flow. This study along with providing insight into the fire-ant social biology will help in understand how collective groups of robots navigate and coordinate in confined spaces, such as during search and rescue operations.

### 10.1.2 Future directions

#### *10.1.2.1 Passive granular materials*

The importance of the dilation transition at $\phi_c$ on granular dynamics—force production or material flow—has been greatly under-appreciated in physics based granular studies. The majority of physics studies on granular materials study the phenomena of interest at one particular $\phi$. However we have shown that the flow response of granular materials is sensitive to $\phi - \phi_c$ and can display qualitatively different behavior in the different regimes of loose ($\phi - \phi_c < 0$) and close pack ($\phi - \phi_c > 0$). Thus we advocate that a broader understanding of granular materials must be developed through future study of force and flow evolution across the spectrum of $\phi$.

An exciting and nascent field of granular research is the application of granular materials to soft robots. Soft robotics works off the dilation principle that a sheared, closely packed, granular material must expand in volume. For application to soft robotics the volume expansion of a closely packed granular material is inhibited by placing it in a latex bag under vacuum. When an object is sheared across the latex surface this force is resisted by the granular material. Thus objects can be picked up through friction.

One goal for soft-robotics is thus to design a granular material with a predefined rheology for some functional application in a soft robot. However to the relationship between particle shape and rheology cannot be directly inferred. For instance our study of the packing and stability of non-convex particles explored how a simple change in particle shape can influence the granular rheology in a non-trivial way. Thus a future goal of granular materials research will be to develop a dictionary of particle shape influences on the relaxation and stability mechanisms of granular material.

#### *10.1.2.2 Active granular materials*

In this dissertation we explored the role of worker size on tunnel construction among groups of fire ants. We showed that the final nest size grew linearly with the number of workers we observed participating in the digging process. On average only 20% of the workers participated in the digging process indicating that a large number of workers remain inactive while the others construct the nest. This leads to the question of whether the workers of this digging minority are fixed throughout the experiment, or if workers from the sedentary population take turns digging? We envision future experiments on tunnel construction will employ means of ant identification among the population so as to whether the population of digging works is fixed or flexible. Such experiments may use ant painting, adhered barcodes, or adhered radio-frequency id tags (RFID), to identify ant workers.

The study of nest construction among larger colonies (with queen and brood), digging in larger three-dimensional arenas will be of great interest. The studies reported here focused on somewhat limited digging environments, quasi two-dimensional arenas or smaller three-dimensional arenas. However a goal of future research would be to observe the time evolution of nest (and colony) growth from the first tunnel created by a newly mated queen. Furthermore through the use of low-density hollow micro-spheres as digging substrate and an iodine laced water supply it may be possible to observe the realtime motion of workers below the surface in a three-dimensional geometry. The simultaneous observation of nest growth and worker location in an unconfined, three-dimensional setting, is a goal of such future study.

# REFERENCES

[1] H. M. Jaeger and Sidney R. Nagel. Physics of the granular state. *Science*, 255: 1523–1531, 1992.

[2] H. M. Jaeger, S. R. Nagel, and R. P. Behringer. Granular solids, liquids, and gases. *Reviews of Modern Physics*, 68(4):1259–1273, 1996.

[3] R.M. Nedderman. *Statics and kinematics of granular materials.* Cambridge University Press, 1992. 352 pp.

[4] Jacques Duran. *Sands, powders, and grains: An introduction to the physics of granular materials.* Springer Verlag, 2000.

[5] Pierre-Gilles de Gennes. Granular matter: a tentative view. *Reviews of modern physics*, 71(2):374–382, 1999.

[6] Per Bak, Chao Tang, Kurt Wiesenfeld, et al. Self-organized criticality. *Physical Review A*, 38(1):364–374, 1988.

[7] Henrik Jeldtoft Jensen. *Self-organized criticality: emergent complex behavior in physical and biological systems*, volume 10. Cambridge university press, 1998.

[8] Fergal Dalton, David Corcoran, et al. Self-organized criticality in a sheared granular stick-slip system. *Physicsal Review E*, 63(6):61312–61312, 2001.

[9] Per Bak. How nature works: the science of self-organized criticality. 1999.

[10] Paul B Umbanhowar, Francisco Melo, and Harry L Swinney. Localized excitations in a vertically vibrated granular layer. *Nature*, 382(6594):793–796, 1996.

[11] Igor S Aranson and Lev S Tsimring. Patterns and collective behavior in granular media: Theoretical concepts. *Reviews of modern physics*, 78(2):641, 2006.

[12] Daniel I Goldman, MD Shattuck, Harry L Swinney, and Gemunu H Gunaratne. Emergence of order in an oscillated granular layer. *Physica A: Statistical Mechanics and its Applications*, 306:180–188, 2002.

[13] John R De Bruyn, C Bizon, MD Shattuck, D Goldman, JB Swift, and Harry L Swinney. Continuum-type stability balloon in oscillated granular layers. *Physicsal Review Letters*, 81(7):1421–1424, 1998.

[14] Alain Barrat, Jorge Kurchan, Vittorio Loreto, and Mauro Sellitto. Edwards measures: A thermodynamic construction for dense granular media and glasses. *Physical Review E*, 63(5):051301, 2001.

[15] Antonio Coniglio, Annalisa Fierro, Hans J Herrmann, and Mario Nicodemi. *Unifying Concepts in Granular Media and Glasses: From the Statistical Mechanics of Granular Media to the Theory of Jamming.* Elsevier Science, 2004.

[16] Corey S OHern, Leonardo E Silbert, Andrea J Liu, and Sidney R Nagel. Jamming at zero temperature and zero applied stress: the epitome of disorder. *Physical Review E*, 68(1):011306, 2003.

[17] Corey S O'Hern, Stephen A Langer, Andrea J Liu, and Sidney R Nagel. Force distributions near jamming and glass transitions. *Physicsal Review Letters*, 86(1): 111–114, 2001.

[18] MC Marchetti, J.F. Joanny, S. Ramaswamy, TB Liverpool, J. Prost, M. Rao, and R.A. Simha. Soft active matter. *arXiv preprint arXiv:1207.2929*, 2012.

[19] Claudio Castellano, Santo Fortunato, and Vittorio Loreto. Statistical physics of social dynamics. *Reviews of modern physics*, 81(2):591, 2009.

[20] Frank Schweitzer. *Brownian agents and active particles: collective dynamics in the natural and social sciences.* Springer, 2007.

[21] Pawel Romanczuk, Markus Bär, Werner Ebeling, Benjamin Lindner, and Lutz Schimansky-Geier. Active brownian particles. *The European Physical Journal-Special Topics*, 202(1):1–162, 2012.

[22] Claire Detrain and Jean-Louis Deneubourg. Self-organized structures in a superorganism: do ants behave like molecules? *Physics of Life Reviews*, 3(3):162–187, 2006.

[23] Yael Katz, Kolbjørn Tunstrøm, Christos C Ioannou, Cristián Huepe, and Iain D Couzin. Inferring the structure and dynamics of interactions in schooling fish. *Proceedings of the National Academy of Sciences*, 108(46):18720–18725, 2011.

[24] Tamás Vicsek and Anna Zafeiris. Collective motion. *Physics Reports*, 2012.

[25] David JT Sumpter. The principles of collective animal behaviour. *Philosophical Transactions of the Royal Society B: Biological Sciences*, 361(1465):5–22, 2006.

[26] Marco Dorigo, Mauro Birattari, and Thomas Stutzle. Ant colony optimization. *Computational Intelligence Magazine, IEEE*, 1(4):28–39, 2006.

[27] Erol Şahin. Swarm robotics: From sources of inspiration to domains of application. *Swarm Robotics*, pages 10–20, 2005.

[28] Gerardo Beni. From swarm intelligence to swarm robotics. *Swarm Robotics*, pages 1–9, 2005.

[29] E. Altshuler, O. Ramos, Y. Nunez, J. Fernández, AJ Batista-Leyva, and C. Noda. Symmetry breaking in escaping ants. *The American Naturalist*, 166(6):643–649, 2005.

[30] D. Helbing, I. Farkas, and T. Vicsek. Simulating dynamical features of escape panic. *Nature*, 407(6803):487–490, 2000.

[31] M. Moussaïd, D. Helbing, and G. Theraulaz. How simple rules determine pedestrian behavior and crowd disasters. *Proceedings of the National Academy of Sciences*, 108 (17):6884–6888, 2011.

[32] Armin Seyfried, Oliver Passon, Bernhard Steffen, Maik Boltes, Tobias Rupprecht, and Wolfram Klingsch. New insights into pedestrian flow through bottlenecks. *Transportation Science*, 43(3):395–406, 2009.

[33] Richard D Peacock, Erica D Kuligowski, and Jason D Averill. *Pedestrian and evacuation dynamics*. Springer, 2011.

[34] Norris R Johnson. Panic at" the who concert stampede": An empirical assessment. *Social Problems*, pages 362–373, 1987.

[35] J. Tang and RP Behringer. How granular materials jam in a hopper. *Chaos: An Interdisciplinary Journal of Nonlinear Science*, 21(4):041107–041107, 2011.

[36] Kiwing To, Pik-Yin Lai, and HK Pak. Jamming of granular flow in a two-dimensional hopper. *Physicsal Review Letters*, 86(1):71–74, 2001.

[37] I. Zuriguel, A. Janda, A. Garcimartín, C. Lozano, R. Arévalo, and D. Maza. Silo clogging reduction by the presence of an obstacle. *Physicsal Review Letters*, 107(27): 278001, 2011.

[38] F. Alonso-Marroquin, SI Azeezullah, SA Galindo-Torres, and LM Olsen-Kettle. Bottlenecks in granular flow: When does an obstacle increase the flow rate in an hourglass? *Physical Review E*, 85(2):020301, 2012.

[39] Shie-Chen Yang and Shu-San Hsiau. The simulation and experimental study of granular materials discharged from a silo with the placement of inserts. *Powder Technology*, 120(3):244–255, 2001.

[40] GA Frank and CO Dorso. Room evacuation in the presence of an obstacle. *Physica A: Statistical Mechanics and its Applications*, 390(11):2135–2145, 2011.

[41] M. Burd, N. Shiwakoti, M. Sarvi, and G. Rose. Nest architecture and traffic flow: large potential effects from small structural features. *Ecological Entomology*, 35(4): 464–468, 2010.

[42] LB Wang, JD Frost, and JS Lai. Three-dimensional digital representation of granular material microstructure from x-ray tomography imaging. *Journal of Computing in Civil Engineering*, 18(1):28–35, 2003.

[43] M Oda and H Kazama. Microstructure of shear bands and its relation to the mechanisms of dilatancy and failure of dense granular soils. *Geotechnique*, 48(4):465–481, 1998.

[44] Gye-Chun Cho, Jake Dodds, and J Carlos Santamarina. Particle shape effects on packing density, stiffness, and strength: natural and crushed sands. *Journal of Geotechnical and Geoenvironmental Engineering*, 132(5):591–602, 2006.

[45] Paul Umbanhowar and Daniel I Goldman. Granular impact and the critical packing state. *Physical Review E*, 82(1):010301, 2010.

[46] ME Cates, JP Wittmer, J-P Bouchaud, and Ph Claudin. Jamming, force chains, and fragile matter. *Physicsal Review Letters*, 81(9):1841–1844, 1998.

[47] Trushant S Majmudar and Robert P Behringer. Contact force measurements and stress-induced anisotropy in granular materials. *Nature*, 435(7045):1079–1082, 2005.

[48] Eirik G Flekkøy and Knut Jørgen Måløy. Continuum description of granular flows: Simulation and experiment. *Physical Review E*, 57(6):6962, 1998.

[49] Igor S Aranson and Lev S Tsimring. Continuum description of avalanches in granular media. *Physical Review E*, 64(2):020301, 2001.

[50] Dennis C Rapaport. *The art of molecular dynamics simulation.* Cambridge university press, 2004.

[51] P Philippe and D Bideau. Compaction dynamics of a granular medium under vertical tapping. *EPL (Europhysics Letters)*, 60(5):677, 2007.

[52] James B Knight, Christopher G Fandrich, Chun Ning Lau, Heinrich M Jaeger, and Sidney R Nagel. Density relaxation in a vibrated granular material. *Physical Review E*, 51(5):3957, 1995.

[53] Andrew Noel Schofield and Peter Wroth. Critical state soil mechanics. 1968.

[54] Nick Gravish, Paul B Umbanhowar, and Daniel I Goldman. Force and flow transition in plowed granular media. *Physicsal Review Letters*, 105(12):128301, 2010.

[55] Melissa Jerkins, Matthias Schröter, Harry L Swinney, Tim J Senden, Mohammad Saadatfar, and Tomaso Aste. Onset of mechanical stability in random packings of frictional spheres. *Physicsal Review Letters*, 101(1):18301, 2008.

[56] Pablo F Damasceno, Michael Engel, and Sharon C Glotzer. Predictive self-assembly of polyhedra into complex structures. *Science*, 337(6093):453–457, 2012.

[57] David Muir Wood. *Soil mechanics: a one-dimensional introduction.* Cambridge University Press, 2009.

[58] CP Wroth. Soil behaviour during shearexistence of critical voids ratios. *Engineering*, 186:409–413, 1958.

[59] S Fazekas, J Török, and J Kertész. Critical packing in granular shear bands. *Physical Review E*, 75(1):011302, 2007.

[60] Donald W Taylor. Fundamentals of soil mechanics. *Soil Science*, 66(2):161, 1948.

[61] Peter Schall and Martin van Hecke. Shear bands in matter with granularity. *Annual Review of Fluid Mechanics*, 42:67–88, 2010.

[62] Arshad Kudrolli, Geoffroy Lumay, Dmitri Volfson, and Lev S Tsimring. Swarming and swirling in self-propelled polar granular rods. *Physicsal Review Letters*, 100(5): 58001, 2008.

[63] Devaraj Van Der Meer, Ko Van Der Weele, and Detlef Lohse. Sudden collapse of a granular cluster. *Physicsal Review Letters*, 88(17):174302, 2002.

[64] Sung Joon Moon, MD Shattuck, C Bizon, Daniel I Goldman, JB Swift, and Harry L Swinney. Phase bubbles and spatiotemporal chaos in granular patterns. *Physical Review E*, 65(1):011301, 2001.

[65] K Huang, K Röller, and S Herminghaus. Universal and non-universal aspects of wet granular matter under vertical vibrations. *The European Physical Journal-Special Topics*, 179(1):25–32, 2009.

[66] A Fingerle, K Roeller, K Huang, and S Herminghaus. Phase transitions far from equilibrium in wet granular matter. *New Journal of Physics*, 10(5):053020, 2008.

[67] Mario Scheel, Dimitrios Geromichalos, and Stephan Herminghaus. Wet granular matter under vertical agitation. *Journal of Physics: Condensed Matter*, 16(38):S4213, 2004.

[68] HM Jaeger, Chu-heng Liu, and Sidney R Nagel. Relaxation at the angle of repose. *Physicsal Review Letters*, 62(1):40–43, 1989.

[69] Douglas Rubin, Naomi Goldenson, and Greg A Voth. Failure and strengthening of granular slopes under horizontal vibration. *Physical Review E*, 74(5):051307, 2006.

[70] S Nasuno, A Kudrolli, A Bak, and JP Gollub. Time-resolved studies of stick-slip friction in sheared granular layers. *Physical Review E*, 58(2):2161, 1998.

[71] R Albert, MA Pfeifer, A-L Barabási, and P Schiffer. Slow drag in a granular medium. *Physicsal Review Letters*, 82(1):205–208, 1999.

[72] I Albert, P Tegzes, B Kahng, R Albert, JG Sample, M Pfeifer, A-L Barabási, T Vicsek, and P Schiffer. Jamming and fluctuations in granular drag. *Physicsal Review Letters*, 84(22):5122–5125, 2000.

[73] I Albert, JG Sample, AJ Morss, S Rajagopalan, A-L Barabási, and P Schiffer. Granular drag on a discrete object: Shape effects on jamming. *Physical Review E*, 64(6): 061303, 2001.

[74] Ryan D Maladen, Yang Ding, Chen Li, and Daniel I Goldman. Undulatory swimming in sand: Subsurface locomotion of the sandfish lizard. *Science*, 325(5938):314–318, 2009.

[75] Jennifer L Anthony and Chris Marone. Influence of particle characteristics on granular friction. *Journal of Geophysical Research*, 110(B8):B08409, 2005.

[76] Salvatore Torquato and Yang Jiao. Dense packings of the platonic and archimedean solids. *Nature*, 460(7257):876–879, 2009.

[77] Salvatore Torquato and Frank H Stillinger. Jammed hard-particle packings: From kepler to bernal and beyond. *Reviews of Modern Physics*, 82(3):2633, 2010.

[78] Aleksandar Donev, Frank H Stillinger, PM Chaikin, and Salvatore Torquato. Unusually dense crystal packings of ellipsoids. *Physicsal Review Letters*, 92(25):255506, 2004.

[79] Aleksandar Donev, Ibrahim Cisse, David Sachs, Evan A Variano, Frank H Stillinger, Robert Connelly, Salvatore Torquato, and PM Chaikin. Improving the density of jammed disordered packings using ellipsoids. *Science*, 303(5660):990–993, 2004.

[80] Charlles RA Abreu, Frederico W Tavares, and Marcelo Castier. Influence of particle shape on the packing and on the segregation of spherocylinders via monte carlo simulations. *Powder technology*, 134(1):167–180, 2003.

[81] SR Williams and AP Philipse. Random packings of spheres and spherocylinders simulated by mechanical contraction. *Physical Review E*, 67(5):051301, 2003.

[82] Albert P Philipse. The random contact equation and its implications for (colloidal) rods in packings, suspensions, and anisotropic powders. *Langmuir*, 12(5):1127–1133, 1996.

[83] J Blouwolff and S Fraden. The coordination number of granular cylinders. *EPL (Europhysics Letters)*, 76(6):1095, 2007.

[84] Geoffroy Lumay and Nicolas Vandewalle. Compaction of anisotropic granular materials: Experiments and simulations. *Physical Review E*, 70(5):051314, 2004.

[85] Jennifer Galanis, Daniel Harries, Dan L Sackett, Wolfgang Losert, and Ralph Nossal. Spontaneous patterning of confined granular rods. *Physicsal Review Letters*, 96(2): 28002, 2006.

[86] Kevin Stokely, Ari Diacou, and Scott V Franklin. Two-dimensional packing in prolate granular materials. *Physical Review E*, 67(5):051302, 2003.

[87] Kenneth Desmond and Scott V Franklin. Jamming of three-dimensional prolate granular materials. *Physical Review E*, 73(3):031306, 2006.

[88] M Trepanier and Scott V Franklin. Column collapse of granular rods. *Physical Review E*, 82(1):011308, 2010.

[89] Summer Saraf and Scott V Franklin. Power-law flow statistics in anisometric (wedge) hoppers. *Physical Review E*, 83(3):030301, 2011.

[90] Chris R Reid, Tanya Latty, Audrey Dussutour, and Madeleine Beekman. Slime mold uses an externalized spatial memory to navigate in complex environments. *Proceedings of the National Academy of Sciences*, 109(43):17490–17494, 2012.

[91] Rasika M Harshey. Bees aren't the only ones: swarming in gram-negative bacteria. *Molecular microbiology*, 13(3):389–394, 2006.

[92] He-Peng Zhang, Avraham Beer, E-L Florin, and Harry L Swinney. Collective motion and density fluctuations in bacterial colonies. *Proceedings of the National Academy of Sciences*, 107(31):13626–13630, 2010.

[93] Nicholas C Darnton, Linda Turner, Svetlana Rojevsky, and Howard C Berg. Dynamics of bacterial swarming. *Biophysical journal*, 98(10):2082–2090, 2010.

[94] K Bhattacharya and Tamás Vicsek. Collective decision making in cohesive flocks. *New Journal of Physics*, 12(9):093019, 2010.

[95] Michele Ballerini, Nicola Cabibbo, Raphael Candelier, Andrea Cavagna, Evaristo Cisbani, Irene Giardina, Alberto Orlandi, Giorgio Parisi, Andrea Procaccini, Massimiliano Viale, et al. Empirical investigation of starling flocks: a benchmark study in collective animal behaviour. *Animal behaviour*, 76(1):201–215, 2008.

[96] John Toner and Yuhai Tu. Flocks, herds, and schools: A quantitative theory of flocking. *Physical Review E*, 58(4):4828, 1998.

[97] John Hutchinson and Peter M Waser. Use, misuse and extensions of ideal gas models of animal encounter. *Biological Reviews*, 82(3):335–359, 2007.

[98] Larisa Gheber and Zvi Priel. Synchronization between beating cilia. *Biophysical journal*, 55(1):183–191, 1989.

[99] Andrej Vilfan and Frank Jülicher. Hydrodynamic flow patterns and synchronization of beating cilia. *Physicsal Review Letters*, 96(5):58102, 2006.

[100] Salima Rafaï, Levan Jibuti, and Philippe Peyla. Effective viscosity of microswimmer suspensions. *Physicsal Review Letters*, 104(9):98102, 2010.

[101] Andrey Sokolov and Igor S Aranson. Reduction of viscosity in suspension of swimming bacteria. *Physicsal Review Letters*, 103(14):148101, 2009.

[102] Charles W Wolgemuth. Collective swimming and the dynamics of bacterial turbulence. *Biophysical journal*, 95(4):1564–1574, 2008.

[103] Vijay Narayan, Sriram Ramaswamy, and Narayanan Menon. Long-lived giant number fluctuations in a swarming granular nematic. *Science*, 317(5834):105–108, 2007.

[104] Tamás Vicsek, András Czirók, Eshel Ben-Jacob, Inon Cohen, and Ofer Shochet. Novel type of phase transition in a system of self-driven particles. *Physicsal Review Letters*, 75(6):1226–1229, 1995.

[105] Craig W Reynolds. Flocks, herds and schools: A distributed behavioral model. In *ACM SIGGRAPH Computer Graphics*, volume 21, pages 25–34. ACM, 1987.

[106] John Toner and Yuhai Tu. Long-range order in a two-dimensional dynamical xy model: how birds fly together. *Physicsal Review Letters*, 75(23):4326–4329, 1995.

[107] Hugues Chaté, Francesco Ginelli, Guillaume Grégoire, and Franck Raynaud. Collective motion of self-propelled particles interacting without cohesion. *Physical Review E*, 77(4):046113, 2008.

[108] H Chaté, F Ginelli, G Grégoire, F Peruani, and F Raynaud. Modeling collective motion: variations on the vicsek model. *The European Physical Journal B-Condensed Matter and Complex Systems*, 64(3):451–456, 2008.

[109] Michele Ballerini, Nicola Cabibbo, Raphael Candelier, Andrea Cavagna, Evaristo Cisbani, Irene Giardina, Vivien Lecomte, Alberto Orlandi, Giorgio Parisi, Andrea Procaccini, et al. Interaction ruling animal collective behavior depends on topological rather than metric distance: Evidence from a field study. *Proceedings of the National Academy of Sciences*, 105(4):1232–1237, 2008.

[110] Nikolai WF Bode, A Jamie Wood, and Daniel W Franks. The impact of social networks on animal collective motion. *Animal Behaviour*, 82(1):29–38, 2011.

[111] Anton Peshkov, Sandrine Ngo, Eric Bertin, Hugues Chaté, and Francesco Ginelli. Continuous theory of active matter systems with metric-free interactions. *Physicsal Review Letters*, 109(9):98101, 2012.

[112] C Anderson, G Theraulaz, and J-L Deneubourg. Self-assemblages in insect societies. *Insectes Sociaux*, 49(2):99–110, 2002.

[113] Nathan J Mlot, Craig A Tovey, and David L Hu. Fire ants self-assemble into waterproof rafts to survive floods. *Proceedings of the National Academy of Sciences*, 108 (19):7669–7673, 2011.

[114] NIGEL R FRANKS. Thermoregulation in army ant bivouacs. *Physiological entomology*, 14(4):397–404, 2008.

[115] KL Haight. Defensiveness of the fire ant, solenopsis invicta, is increased during colony rafting. *Insectes sociaux*, 53(1):32–36, 2006.

[116] Benjamin J Adams, Linda M Hooper-Bùi, Rachel M Strecker, and Daniel M O'Brien. Raft formation by the red imported fire ant, solenopsis invicta. *Journal of Insect Science*, 11(171):1–14, 2011.

[117] William B Jackson. Microclimatic patterns in the army ant bivouac. *Ecology*, pages 276–285, 1957.

[118] Melanie Mitchell. *Complexity: a guided tour.* Oxford University Press, USA, 2009.

[119] Guy Theraulaz, Eric Bonabeau, Christian Sauwens, Jean-Louis Deneubourg, Arnaud Lioni, François Libert, Luc Passera, and Ricard Solé. Model of droplet dynamics in the argentine ant linepithema humile (mayr). *Bulletin of Mathematical Biology*, 63 (6):1079–1093, 2001.

[120] Eric Bonabeau, Guy Theraulaz, Jean-Louis Deneubourg, Arnaud Lioni, François Libert, Christian Sauwens, and Luc Passera. Dripping faucet with ants. *Physical Review E*, 57(5):5904, 1998.

[121] P Martien, SC Pope, PL Scott, and RS Shaw. The chaotic behavior of the leaky faucet. *Physics Letters A*, 110(7):399–404, 1985.

[122] Michael Henry Hansell. *Animal architecture.* Oxford University Press Oxford, UK:, 2005.

[123] James L Gould and Carol Grant Gould. *Animal architects: building and the evolution of intelligence.* Basic Books, 2007.

[124] David Sloan Wilson and Elliott Sober. Reviving the superorganism. *Journal of theoretical Biology*, 136(3):337–356, 1989.

[125] Bert Hölldobler and Edward O Wilson. *The ants.* Belknap Press, 1990.

[126] Walter R Tschinkel. Subterranean ant nests: trace fossils past and future? *Palaeogeography, Palaeoclimatology, Palaeoecology*, 192(1):321–333, 2003.

[127] Walter Reinhart Tschinkel. *The fire ants.* Belknap Press, 2006.

[128] Walter R Tschinkel et al. Methods for casting subterranean ant nests. *Journal of Insect Science*, 10, 2010.

[129] Nicholas J Minter, Nigel R Franks, and Katharine A Robson Brown. Morphogenesis of an extended phenotype: four-dimensional ant nest architecture. *Journal of The Royal Society Interface*, 9(68):586–595, 2012.

[130] JD Halley, M Burd, and P Wells. Excavation and architecture of argentine ant nests. *Insectes sociaux*, 52(4):350–356, 2005.

[131] Jérôme Buhl, Jean Louis Deneubourg, Anne Grimal, and Guy Theraulaz. Self-organized digging activity in ant colonies. *Behavioral Ecology and Sociobiology*, 58(1): 9–17, 2005.

[132] Jérôme Buhl, Jacques Gautrais, Jean-Louis Deneubourg, and Guy Theraulaz. Nest excavation in ants: group size effects on the size and structure of tunneling networks. *Naturwissenschaften*, 91(12):602–606, 2004.

[133] Jérôme Buhl, Jacques Gautrais, Jean Louis Deneubourg, Pascale Kuntz, and Guy Theraulaz. The growth and form of tunnelling networks in ants. *Journal of theoretical biology*, 243(3):287–298, 2006.

[134] TD Seeley and RA Morse. The nest of the honey bee (apis mellifera l.). *Insectes Sociaux*, 23(4):495–512, 1976.

[135] JM Dangerfield, TS McCarthy, and WN Ellery. The mound-building termite macrotermes michaelseni as an ecosystem engineer. *Journal of Tropical Ecology*, 14 (4):507–520, 1998.

[136] Walter R Tschinkel. The fire ant (solenopsis invida): Still unvanquished. *Biological pollution: the control and impact of invasive exotic species. Indiana Academy of Science, Indianapolis, Ind*, pages 121–136, 1993.

[137] Daniel P Wojcik. Comparison of the ecology of red imported fire ants in north and south america. *Florida Entomologist*, pages 101–111, 1983.

[138] NL Wilson, JH Dillier, and GP Markin. Foraging territories of imported fire ants. *Annals of the Entomological Society of America*, 64(3):660–665, 1971.

[139] D Cassill, WR Tschinkel, and SB Vinson. Nest complexity, group size and brood rearing in the fire ant, *Solenopsis invicta. Insectes Sociaux*, 49(2):158–163, 2002.

[140] Walter R Tschinkel. The organization of foraging in the fire ant, solenopsis invicta. *Journal of Insect Science*, 11, 2011.

[141] Nicole Mazouchova, Nick Gravish, Andrei Savu, and Daniel I Goldman. Utilization of granular solidification during terrestrial locomotion of hatchling sea turtles. *Biology letters*, 6(3):398–401, 2010.

[142] Chen Li, Paul B Umbanhowar, Haldun Komsuoglu, Daniel E Koditschek, and Daniel I Goldman. Sensitive dependence of the motion of a legged robot on granular media. *Proceedings of the National Academy of Sciences*, 106(9):3029–3034, 2009.

[143] Edward McKyes et al. *Soil cutting and tillage.* Elsevier, 1985.

[144] R Candelier and O Dauchot. Creep motion of an intruder within a granular glass close to jamming. *Physicsal Review Letters*, 103(12):128001, 2009.

[145] Junfei Geng, D Howell, E Longhi, RP Behringer, G Reydellet, L Vanel, E Clément, and S Luding. Footprints in sand: the response of a granular material to local perturbations. *Physicsal Review Letters*, 87(3):35506, 2001.

[146] G. Hill, S. Yeung, and SA Koehler. Scaling vertical drag forces in granular media. *EPL (Europhysics Letters)*, 72:137, 2005.

[147] Y. Ding, N. Gravish, and D.I. Goldman. Drag induced lift in granular media. *Physicsal Review Letters*, 106(2):28001, 2011.

[148] A. Seguin, Y. Bertho, P. Gondret, and J. Crassous. Dense granular flow around a penetrating object: Experiment and hydrodynamic model. *Physicsal Review Letters*, 107(4):48001, 2011.

[149] F.Q. Potiguar. Lift force on an asymmetrical obstacle immersed in a dilute granular flow. *Physical Review E*, 84(6):061302, 2011.

[150] Eugenio Hamm, Franco Tapia, and Francisco Melo. Dynamics of shear bands in a dense granular material forced by a slowly moving rigid body. *Physical Review E*, 84 (4):041304, 2011.

[151] E. Kolb, J. Cviklinski, J. Lanuza, P. Claudin, and E. Clément. Reorganization of a dense granular assembly: The unjamming response function. *Physical Review E*, 69 (3):031306, 2004.

[152] DJ Costantino, J. Bartell, K. Scheidler, and P. Schiffer. Low-velocity granular drag in reduced gravity. *Physical Review E*, 83(1):011305, 2011.

[153] J.F. Métayer, D.J. Suntrup III, C. Radin, H.L. Swinney, and M. Schröter. Shearing of frictional sphere packings. *EPL (Europhysics Letters)*, 93:64003, 2011.

[154] Matthias Schröter, Sibylle Nägle, Charles Radin, and Harry L Swinney. Phase transition in a static granular system. *EPL (Europhysics Letters)*, 78(4):44004, 2007.

[155] T. Darnige, A. Bruand, E. Clement, et al. Creep and fluidity of a real granular packing near jamming. *Physicsal Review Letters*, 107(13):138303, 2011.

[156] P.B. Umbanhowar and D.I. Goldman. Low density fragile states in cohesive powders. *American journal of physics*, 74:720, 2006.

[157] R. Ojha, N. Menon, and DJ Durian. Hysteresis and packing in gas-fluidized beds. *Physical Review E*, 62(3):4442, 2000.

[158] P. Richard, M. Nicodemi, R. Delannay, P. Ribière, and D. Bideau. Slow relaxation and compaction of granular systems. *Nature materials*, 4(2):121–128, 2005.

[159] Tomaso Aste, Mohammad Saadatfar, and TJ Senden. Geometrical structure of disordered sphere packings. *Physical Review E*, 71(6):061302, 2005.

[160] D. Chehata, R. Zenit, and CR Wassgren. Dense granular flow around an immersed cylinder. *Physics of fluids*, 15:1622, 2003.

[161] Baptiste Percier, Sebastien Manneville, Jim N McElwaine, Stephen W Morris, and Nicolas Taberlet. Lift and drag forces on an inclined plow moving over a granular surface. *Physical Review E*, 84(5):051302, 2011.

[162] DJ Pine, DA Weitz, PM Chaikin, and E Herbolzheimer. Diffusing wave spectroscopy. *Physicsal Review Letters*, 60(12):1134–1137, 1988.

[163] P. Evesque, D. Fargeix, P. Habib, MP Luong, and P. Porion. Pile density is a control parameter of sand avalanches. *Physical Review E*, 47(4):2326, 1993.

[164] K.A. Dahmen, Y. Ben-Zion, and J.T. Uhl. A simple analytic theory for the statistics of avalanches in sheared granular materials. *Nature Physics*, 7(7):554–557, 2011.

[165] D. Bi, J. Zhang, B. Chakraborty, and RP Behringer. Jamming by shear. *Nature*, 480 (7377):355–358, 2011.

[166] A.J. Liu and S.R. Nagel. The jamming transition and the marginally jammed solid. *Annual Review of Condensed Matter Physics*, 1, 2010.

[167] M.R. Shaebani, T. Unger, and J. Kertész. Unjamming due to local perturbations in granular packings with and without gravity. *Phys. Rev. E*, 78(011308), 2008.

[168] L.E. Silbert, A.J. Liu, and S.R. Nagel. Structural signatures of the unjamming transition at zero temperature. *Phys. Rev. E*, 73, 2006.

[169] M. Guizar-Sicairos, S.T. Thurman, and J.R. Fienup. Efficient subpixel image registration algorithms. *Opt. Lett.*, 33:156–158, 2008.

[170] GDR MiDi. On dense granular flows. *Eur. Phys. J. E.*, 14, 2004.

[171] Franco Tapia, David Espíndola, Eugenio Hamm, and Francisco Melo. Effect of packing fraction on shear band formation in a granular material forced by a penetrometer. *Physical Review E*, 87(1):014201, 2013.

[172] Einat Aharonov and David Sparks. Rigidity phase transition in granular packings. *Physical Review E*, 60(6):6890, 1999.

[173] Vidar Frette, Kim Christensen, Anders Malthe-Sørenssen, Jens Feder, Torstein Jøssang, and Paul Meakin. Avalanche dynamics in a pile of rice. *Nature*, 379(6560): 49–52, 1996.

[174] Yoël Forterre and Olivier Pouliquen. Flows of dense granular media. *Annu. Rev. Fluid Mech.*, 40:1–24, 2008.

[175] Lydie Staron, Farhang Radjai, and Jean-Pierre Vilotte. Granular micro-structure and avalanche precursors. *Journal of Statistical Mechanics: Theory and Experiment*, 2006 (07):P07014, 2006.

[176] S Kiesgen de Richter, G Le Caër, and R Delannay. Dynamics of rearrangements during inclination of granular packings: the avalanche precursor regime. *Journal of Statistical Mechanics: Theory and Experiment*, 2012(04):P04013, 2012.

[177] V Yu Zaitsev, P Richard, R Delannay, Vincent Tournat, and VE Gusev. Pre-avalanche structural rearrangements in the bulk of granular medium: Experimental evidence. *EPL (Europhysics Letters)*, 83(6):64003, 2008.

[178] Axelle Amon, Roman Bertoni, and Jérôme Crassous. Experimental investigation of plastic deformations before a granular avalanche. *Physical Review E*, 87(1):012204, 2013.

[179] M Pailha, M Nicolas, and O Pouliquen. Initiation of underwater granular avalanches: Influence of the initial volume fraction. *Physics of fluids*, 20:111701, 2008.

[180] Félix Bonnet, Thierry Richard, and Pierre Philippe. Sensitivity to solid volume fraction of gravitational instability in a granular medium. *Granular Matter*, 12(3):317–325, 2010.

[181] Réka Albert, István Albert, Daniel Hornbaker, Peter Schiffer, and Albert-László Barabási. Maximum angle of stability in wet and dry spherical granular media. *Physical Review E*, 56(6):6271–6274, 1997.

[182] HG Matuttis, S Luding, and HJ Herrmann. Discrete element simulations of dense packings and heaps made of spherical and non-spherical particles. *Powder technology*, 109(1):278–292, 2000.

[183] Stephane Roux and Farhang Radjai. Texture-dependent rigid-plastic behavior. *NATO ASI Series E Applied Sciences-Advanced Study Institute*, 350:229–236, 1998.

[184] Chu-heng Liu and Sidney R Nagel. Sound in sand. *Physicsal Review Letters*, 68(15):2301–2304, 1992.

[185] Emilien Azéma, Nicolas Estrada, and Farhang Radjaï. Nonlinear effects of particle shape angularity in sheared granular media. *Physical Review E*, 86(4):041301, 2012.

[186] L. Meng, S. Li, P. Lu, T. Li, and W. Jin. Bending and elongation effects on the random packing of curved spherocylinders. *Physical Review E*, 86(6):061309, 2012.

[187] N. Gravish, S.V. Franklin, D.L. Hu, and D.I. Goldman. Entangled granular media. *Physicsal Review Letters*, 108(20):208001, 2012.

[188] E. Brown, H. Zhang, N.A. Forman, B.W. Maynor, D.E. Betts, J.M. DeSimone, and H.M. Jaeger. Shear thickening and jamming in densely packed suspensions of different particle shapes. *Physical Review E*, 84(3):031408, 2011.

[189] N.B. McKeown and P.M. Budd. Exploitation of intrinsic microporosity in polymer-based materials. *Macromolecules*, 43(12):5163–5176, 2010.

[190] N.B. McKeown, P.M. Budd, K.J. Msayib, B.S. Ghanem, H.J. Kingston, C.E. Tattershall, S. Makhseed, K.J. Reynolds, and D. Fritsch. Polymers of intrinsic microporosity (pims): Bridging the void between microporous and polymeric materials. *Chemistry-A European Journal*, 11(9):2610–2620, 2005.

[191] L. Manna, D.J. Milliron, A. Meisel, E.C. Scher, and A.P. Alivisatos. Controlled growth of tetrapod-branched inorganic nanocrystals. *Nature Materials*, 2(6):382–385, 2003.

[192] S. Chen, Z.L. Wang, J. Ballato, S.H. Foulger, and D.L. Carroll. Monopod, bipod, tripod, and tetrapod gold nanocrystals. *Journal of the American Chemical Society*, 125(52):16186–16187, 2003.

[193] S.C. Glotzer and M.J. Solomon. Anisotropy of building blocks and their assembly into complex structures. *Nature materials*, 6(8):557–562, 2007.

[194] G.M. Whitesides and M. Boncheva. Beyond molecules: Self-assembly of mesoscopic and macroscopic components. *Proceedings of the National Academy of Sciences*, 99 (8):4769–4774, 2002.

[195] Eric Brown, Nicholas Rodenberg, John Amend, Annan Mozeika, Erik Steltz, Mitchell R Zakin, Hod Lipson, and Heinrich M Jaeger. Universal robotic gripper based on the jamming of granular material. *Proceedings of the National Academy of Sciences*, 107(44):18809–18814, 2010.

[196] N.G. Cheng, M.B. Lobovsky, S.J. Keating, A.M. Setapen, K.I. Gero, A.E. Hosoi, and K.D. Iagnemma. Design and analysis of a robust, low-cost, highly articulated manipulator enabled by jamming of granular media. In *Robotics and Automation (ICRA), 2012 IEEE International Conference on*, pages 4328–4333. IEEE, 2012.

[197] L. Miao, O. Vanderlinde, J. Liu, R.P. Grant, A. Wouterse, K. Shimabukuro, A. Philipse, M. Stewart, and T.M. Roberts. The role of filament-packing dynamics in powering amoeboid cell motility. *Proceedings of the National Academy of Sciences*, 105(14):5390–5395, 2008.

[198] M.H. Hansell et al. Animal architecture and building behaviour. *Animal architecture and building behaviour.*, 1984.

[199] A. Wouterse, S. Luding, and AP Philipse. On contact numbers in random rod packings. *Granular matter*, 11(3):169–177, 2009.

[200] JC Phillips. Stretched exponential relaxation in molecular and electronic glasses. *Reports on Progress in Physics*, 59(9):1133, 1999.

[201] J. Mattsson, H.M. Wyss, A. Fernandez-Nieves, K. Miyazaki, Z. Hu, D.R. Reichman, and D.A. Weitz. Soft colloids make strong glasses. *Nature*, 462(7269):83–86, 2009.

[202] P. Philippe and D. Bideau. Compaction dynamics of a granular medium under vertical tapping. *EPL (Europhysics Letters)*, 60(5):677, 2007.

[203] D.H. Eberly. *3D game engine design: a practical approach to real-time computer graphics*. Morgan Kaufmann Publishers, 2007.

[204] I. Sánchez, F. Raynaud, J. Lanuza, B. Andreotti, E. Clément, and I.S. Aranson. Spreading of a granular droplet. *Physical Review E*, 76(6):060301, 2007.

[205] E. Brown, A. Nasto, A.G. Athanassiadis, and H.M. Jaeger. Strain stiffening in random packings of entangled granular chains. *Physicsal Review Letters*, 108(10):108302, 2012.

[206] D.M. Raymer and D.E. Smith. Spontaneous knotting of an agitated string. *Proceedings of the National Academy of Sciences*, 104(42):16432–16437, 2007.

[207] IY Wong, ML Gardel, DR Reichman, E.R. Weeks, MT Valentine, AR Bausch, and DA Weitz. Anomalous diffusion probes microstructure dynamics of entangled f-actin networks. *Physicsal Review Letters*, 92(17):178101, 2004.

[208] Jedrzej Szymanski and Matthias Weiss. Elucidating the origin of anomalous diffusion in crowded fluids. *Physicsal Review Letters*, 103(3):38102, 2009.

[209] M.J. Saxton. Anomalous diffusion due to obstacles: a monte carlo study. *Biophysical journal*, 66(2):394–401, 1994.

[210] Iva Marija Tolić-Nørrelykke, Emilia-Laura Munteanu, Genevieve Thon, Lene Oddershede, and Kirstine Berg-Sørensen. Anomalous diffusion in living yeast cells. *Physicsal Review Letters*, 93(7):78102, 2004.

[211] N.T. Tsui, A.J. Paraskos, L. Torun, T.M. Swager, and E.L. Thomas. Minimization of internal molecular free volume: A mechanism for the simultaneous enhancement of polymer stiffness, strength, and ductility. *Macromolecules*, 39(9):3350–3358, 2006.

[212] Bert Hölldobler and Edward O Wilson. *The superorganism: the beauty, elegance, and strangeness of insect societies.* WW Norton & Company, 2009.

[213] David C Queller and Joan E Strassmann. Kin selection and social insects. *Bioscience*, 48(3):165–175, 1998.

[214] Julia C Jones and Benjamin P Oldroyd. Nest thermoregulation in social insects. *Advances in Insect Physiology*, 33:153–191, 2006.

[215] Deborah M Gordon. The organization of work in social insect colonies. *Complexity*, 8(1):43–46, 2002.

[216] Michael J Greene and Deborah M Gordon. Interaction rate informs harvester ant task decisions. *Behavioral Ecology*, 18(2):451–455, 2007.

[217] Walter R Tschinkel. The nest architecture of the florida harvester ant, pogonomyrmex badius. *Journal of Insect Science*, 4, 2004.

[218] Andrew FG Bourke and Nigel R Franks. *Social evolution in ants.* Princeton University Press, 1995.

[219] Valerie S Banschbach and Joan M Herbers. Nest movements and population spatial structure of the forest ant myrmica punctiventris (hymenoptera: Formicidae). *Annals of the Entomological Society of America*, 92(3):414–423, 1999.

[220] Deborah M. Gordon. Nest relocation in harvester ants. *Annals of the Entomological Society of America*, 85(1):44–47, 1992.

[221] Terrence P McGlynn, Ryan A Carr, Johnny H Carson, and Johnathan Buma. Frequent nest relocation in the ant aphaenogaster araneoides: resources, competition, and natural enemies. *Oikos*, 106(3):611–621, 2004.

[222] J Smallwood. Nest relocations in ants. *Insectes Sociaux*, 29(2):138–147, 1982.

[223] JL Deneubourg and NR Franks. Collective control without explicit coding: the case of communal nest excavation. *Journal of insect behavior*, 8(4):417–432, 1995.

[224] Guy Theraulaz, Jacques Gautrais, Scott Camazine, and Jean-Louis Deneubourg. The formation of spatial patterns in social insects: from simple behaviours to complex structures. *Philosophical Transactions of the Royal Society of London. Series A: Mathematical, Physical and Engineering Sciences*, 361(1807):1263–1282, 2003.

[225] Edward O Wilson et al. The sociogenesis of insect colonies. *Science(Washington)*, 228(4707):1489–1495, 1985.

[226] D Nicolas Espinoza and J Carlos Santamarina. Ant tunnelinga granular media perspective. *Granular Matter*, 12(6):607–616, 2010.

[227] Ph Rasse and JL Deneubourg. Dynamics of nest excavation and nest size regulation of lasius niger (hymenoptera: Formicidae). *Journal of Insect behavior*, 14(4):433–449, 2001.

[228] Nan-Yao Su and Sang-Hee Lee. Tunnel volume regulation and group size of subterranean termites (isoptera: Rhinotermitidae). *Annals of the Entomological Society of America*, 102(6):1158–1164, 2009.

[229] JH Sudd. Specific patterns of excavation in isolated ants. *Insectes Sociaux*, 17(4): 253–260, 1970.

[230] Etienne Toffin, David Di Paolo, Alexandre Campo, Claire Detrain, and Jean-Louis Deneubourg. Shape transition during nest digging in ants. *Proceedings of the National Academy of Sciences*, 106(44):18616–18620, 2009.

[231] Etienne Toffin, Jonathan Kindekens, and Jean-Louis Deneubourg. Excavated substrate modulates growth instability during nest building in ants. *Proceedings of the Royal Society B: Biological Sciences*, 277(1694):2617–2625, 2010.

[232] Deby Lee Cassill and Walter R Tschinkel. Task selection by workers of the fire ant solenopsis invicta. *Behavioral Ecology and Sociobiology*, 45(3):301–310, 1999.

[233] Ana Duarte, Franz J Weissing, Ido Pen, and Laurent Keller. An evolutionary perspective on self-organized division of labor in social insects. *Annual Review of Ecology, Evolution, and Systematics*, 42:91–110, 2011.

[234] Sanford D Porter and Walter R Tschinkel. Fire ant polymorphism: the ergonomics of brood production. *Behavioral Ecology and Sociobiology*, 16(4):323–336, 1985.

[235] Paul Schmid-Hempel. Worker castes and adaptive demography. *Journal of evolutionary biology*, 5(1):1–12, 1992.

[236] Edward O Wilson. Division of labor in fire ants based on physical castes (hymenoptera: Formicidae: Solenopsis). *Journal of the Kansas Entomological Society*, pages 615–636, 1978.

[237] Walter R Tschinkel, Alexander S Mikheyev, and Shonna R Storz. Allometry of workers of the fire ant, solenopsis invicta. *Journal of Insect Science*, 3, 2003.

[238] Michael AD Goodisman, Paul D Mack, Devon E Pearse, and Kenneth G Ross. Effects of a single gene on worker and male body mass in the fire ant solenopsis invicta (hymenoptera: Formicidae). *Annals of the Entomological Society of America*, 92(4): 563–570, 1999.

[239] Les Greenberg, DJC Fletcher, and SB Vinson. Differences in worker size and mound distribution in monogynous and polygynous colonies of the fire ant solenopsis invicta buren. *Journal of the Kansas Entomological Society*, pages 9–18, 1985.

[240] George P Markin, J O'Neal, and J Dillier. Foraging tunnels of the red imported fire ant, solenopsis invicta (hymenoptera: Formicidae). *Journal of the Kansas Entomological Society*, pages 83–89, 1975.

[241] DP Jouvenaz, GE Allen, WA Banks, and Daniel P Wojcik. A survey for pathogens of fire ants, solenopsis spp., in the southeastern united states. *Florida Entomologist*, pages 275–279, 1977.

[242] Harvey J Motulsky and Lennart A Ransnas. Fitting curves to data using nonlinear regression: a practical and nonmathematical review. *The FASEB journal*, 1(5):365–374, 1987.

[243] John H Sudd. The excavation of soil by ants. *Zeitschrift für Tierpsychologie*, 26(3): 257–276, 1969.

[244] Marc Barthélemy. Spatial networks. *Physics Reports*, 499(1):1–101, 2011.

[245] Prassede Calabi and Sanford D Porter. Worker longevity in the fire ant¡ i¿ solenopsis invicta¡/i¿: Ergonomic considerations of correlations between temperature, size and metabolic rates. *Journal of Insect Physiology*, 35(8):643–649, 1989.

[246] Allen H Hurlbert, Ford Ballantyne IV, and Scott Powell. Shaking a leg and hot to trot: the effects of body size and temperature on running speed in ants. *Ecological Entomology*, 33(1):144–154, 2008.

[247] Walter R Tschinkel. Colony growth and the ontogeny of worker polymorphism in the fire ant, solenopsis invicta. *Behavioral Ecology and Sociobiology*, 22(2):103–115, 1988.

[248] John T Mirenda and S Bradleigh Vinson. Division of labour and specification of castes in the red imported fire ant *Solenopsis invicta* buren. *Animal Behaviour*, 29 (2):410–420, 1981.

[249] Martin Burd, Debbie Archer, Nuvan Aranwela, and David J Stradling. Traffic dynamics of the leaf-cutting ant, atta cephalotes. *The American Naturalist*, 159(3):283–293, 2002.

[250] Audrey Dussutour, Samuel Beshers, Jean-Louis Deneubourg, and Vincent Fourcassié. Priority rules govern the organization of traffic on foraging trails under crowding conditions in the leaf-cutting ant atta colombica. *Journal of Experimental Biology*, 212(4):499–505, 2009.

[251] Vincent Fourcassié, Audrey Dussutour, and Jean-Louis Deneubourg. Ant traffic rules. *Journal of Experimental Biology*, 213(14):2357–2363, 2010.

[252] Paul Bardunias and Nan-Yao Su. Opposing headings of excavating and depositing termites facilitate branch formation in the formosan subterranean termite. *Animal Behaviour*, 78(3):755–759, 2009.

[253] Paul M Bardunias and Nan-Yao Su. Queue size determines the width of tunnels in the formosan subterranean termite (isoptera: Rhinotermitidae). *Journal of insect behavior*, 23(3):189–204, 2010.

[254] Alberto Colorni, Marco Dorigo, Vittorio Maniezzo, et al. Distributed optimization by ant colonies. In *Proceedings of the first European conference on artificial life*, volume 142, pages 134–142. Paris, France, 1991.

[255] TM Lejeune, PA Willems, and NC Heglund. Mechanics and energetics of human locomotion on sand. *Journal of Experimental Biology*, 201(13):2071–2080, 1998.

[256] K Autumn, ST Hsieh, DM Dudek, J Chen, C Chitaphan, and RJ Full. Dynamics of geckos running vertically. *Journal of Experimental Biology*, 209(2):260–272, 2006.

[257] K Jayaram, D Springthorpe, D Haldane, S McKinley, A Dicorcco, and RJ Full. Running in confined spaces by the american cockroach. SICB, 2013.

[258] R McNeill Alexander. *Principles of animal locomotion.* Princeton University Press, 2002.

[259] Daniel E Koditschek, Robert J Full, and Martin Buehler. Mechanical aspects of legged locomotion control. *Arthropod structure & development*, 33(3):251–272, 2004.

[260] Kiisa Nishikawa, Andrew A Biewener, Peter Aerts, Anna N Ahn, Hillel J Chiel, Monica A Daley, Thomas L Daniel, Robert J Full, Melina E Hale, Tyson L Hedrick, et al. Neuromechanics: an integrative approach for understanding motor control. *Integrative and Comparative Biology*, 47(1):16–54, 2007.

[261] GE Loeb. Control implications of musculoskeletal mechanics. In *Engineering in Medicine and Biology Society, 1995., IEEE 17th Annual Conference*, volume 2, pages 1393–1394. IEEE, 1995.

[262] Monica A Daley and Andrew A Biewener. Running over rough terrain reveals limb control for intrinsic stability. *Proceedings of the National Academy of Sciences*, 103 (42):15681–15686, 2006.

[263] Philip Holmes, Robert J Full, Dan Koditschek, and John Guckenheimer. The dynamics of legged locomotion: Models, analyses, and challenges. *Siam Review*, 48(2): 207–304, 2006.

[264] Robert J Full, Timothy Kubow, John Schmitt, Philip Holmes, and Daniel Koditschek. Quantifying dynamic stability and maneuverability in legged locomotion. *Integrative and comparative biology*, 42(1):149–157, 2002.

[265] Uluc Saranli, Martin Buehler, and Daniel E Koditschek. Rhex: A simple and highly mobile hexapod robot. *The International Journal of Robotics Research*, 20(7):616–631, 2001.

[266] McKee M. Mars rover spirit gets stuck as winter approaches. *New Scientist*, 2012.

[267] OJ Reichman and STAN C Smith. Burrows and burrowing behavior by mammals. *Current mammalogy*, 2:197–244, 1990.

[268] Eviatar Nevo. Adaptive convergence and divergence of subterranean mammals. *Annual Review of Ecology and Systematics*, pages 269–308, 1979.

[269] Craig R White. The allometry of burrow geometry. *Journal of Zoology*, 265(04): 395–403, 2005.

[270] CR White. The energetics of burrow excavation by the inland robust scorpion, urodacus yaschenkoi (birula, 1903). *Australian journal of zoology*, 49(6):663–674, 2001.

[271] BG Lovegrove. The cost of burrowing by the social mole rats (bathyergidae) cryptomys damarensis and heterocephalus glaber: the role of soil moisture. *Physiological Zoology*, pages 449–469, 1989.

[272] David Vleck. The energy cost of burrowing by the pocket gopher *Thomomys bottae*. *Physiological Zoology*, pages 122–136, 1979.

[273] Luis A Ebensperger and Francisco Bozinovic. Energetics and burrowing behaviour in the semifossorial degu octodon degus (rodentia: Octodontidae). *Journal of Zoology*, 252(2):179–186, 2006.

[274] Frans Sluyter, Abel Bult, Carol B Lynch, Geert A Oortmerssen, and Jaap M Koolhaas. A comparison between house mouse lines selected for attack latency or nest-building: evidence for a genetic basis of alternative behavioral strategies. *Behavior genetics*, 25 (3):247–252, 1995.

[275] Jesse N Weber, Brant K Peterson, and Hopi E Hoekstra. Discrete genetic modules are responsible for complex burrow evolution in peromyscus mice. *Nature*, 493(7432): 402–405, 2013.

[276] Richard Dawkins. *The extended phenotype: The long reach of the gene*. Oxford University Press, USA, 1999.

[277] Edward O Wilson. The organization of colony defense in the ant pheidole dentata mayr (hymenoptera: Formicidae). *Behavioral Ecology and Sociobiology*, 1(1):63–81, 1976.

[278] Edward O Wilson. The organization of flood evacuation in the ant genuspheidole (hymenoptera: Formicidae). *Insectes sociaux*, 33(4):458–469, 1986.

[279] Tali Kimchi and Joseph Terkel. Comparison of the role of somatosensory stimuli in maze learning in a blind subterranean rodent and a sighted surface-dwelling rodent. *Behavioural brain research*, 153(2):389–395, 2004.

[280] Audrey Dussutour, Vincent Fourcassié, Dirk Helbing, and Jean-Louis Deneubourg. Optimal traffic organization in ants under crowded conditions. *Nature*, 428(6978): 70–73, 2004.

[281] James FA Traniello. Foraging strategies of ants. *Annual review of entomology*, 34(1): 191–210, 1989.

[282] George F Oster and Edward O Wilson. *Caste and Ecology in the Social Insects.(MPB-12).* Princeton University Press, 1979.

[283] B Hölldobler. Multimodal signals in ant communication. *Journal of Comparative Physiology A: Neuroethology, Sensory, Neural, and Behavioral Physiology*, 184(2): 129–141, 1999.

[284] Glennis E Julian and Wulfila Gronenberg. Reduction of brain volume correlates with behavioral changes in queen ants. *Brain, Behavior and Evolution*, 60(3):152–164, 2002.

[285] F Roces, J Tautz, and B Hölldobler. Stridulation in leaf-cutting ants. *Naturwissenschaften*, 80(11):521–524, 1993.

[286] Hayward G Spangler. Ant stridulations and their synchronization with abdominal movement. *Science*, 155(3770):1687–1689, 1967.

[287] Peggy SM Hill. Vibration and animal communication: a review. *American Zoologist*, 41(5):1135–1142, 2001.

[288] Edward O Wilson. Chemical communication among workers of the fire ant¡ i¿ solenopsis saevissima¡/i¿(fr. smith) 1. the organization of mass-foraging. *Animal behaviour*, 10(1):134–147, 1962.

[289] Brian D Jackson and E David Morgan. Insect chemical communication: pheromones and exocrine glands of ants. *Chemoecology*, 4(3):125–144, 1993.

[290] Nick Gravish, Mateo Garcia, Nicole Mazouchova, Laura Levy, Paul B Umbanhowar, Michael AD Goodisman, and Daniel I Goldman. Effects of worker size on the dynamics of fire ant tunnel construction. *Journal of The Royal Society Interface*, 2012.

[291] Tony Chan and Luminita Vese. An active contour model without edges. *Scale-Space Theories in Computer Vision*, pages 141–151, 1999.

[292] GP Markin, JH Dillier, and HL Collins. Growth and development of colonies of the red imported fire ant, solenopsis invicta. *Annals of the Entomological Society of America*, 66(4):803–808, 1973.

[293] JC Spagna, DI Goldman, PC Lin, DE Koditschek, and RJ Full. Distributed mechanical feedback in arthropods and robots simplifies control of rapid running on challenging terrain. *Bioinspiration & biomimetics*, 2(1):9, 2007.

[294] Eviatar Nevo. *Mosaic evolution of subterranean mammals: regression, progression, and global convergence*, volume 4. Oxford University Press Oxford, 1999.

[295] David Grimaldi and Michael S Engel. *Evolution of the Insects*. Cambridge University Press, 2005.

[296] Ardian Jusufi, Daniel I Goldman, Shai Revzen, and Robert J Full. Active tails enhance arboreal acrobatics in geckos. *Proceedings of the National Academy of Sciences*, 105 (11):4215–4219, 2008.

[297] Leif Ristroph, Attila J Bergou, Gunnar Ristroph, Katherine Coumes, Gordon J Berman, John Guckenheimer, Z Jane Wang, and Itai Cohen. Discovering the flight autostabilizer of fruit flies by inducing aerial stumbles. *Proceedings of the National Academy of Sciences*, 107(11):4820–4824, 2010.

[298] Walter Federle, Werner Baumgartner, and Bert Hölldobler. Biomechanics of ant adhesive pads: frictional forces are rate-and temperature-dependent. *Journal of experimental biology*, 207(1):67–74, 2004.

[299] Walter Federle, Elizabeth L Brainerd, Thomas A McMahon, and Bert Hölldobler. Biomechanics of the movable pretarsal adhesive organ in ants and bees. *Proceedings of the National Academy of Sciences*, 98(11):6215–6220, 2001.

[300] LA Feldkamp, LC Davis, and JW Kress. Practical cone-beam algorithm. *JOSA A*, 1 (6):612–619, 1984.

[301] N Rezvani, D Aruliah, K Jackson, D Moseley, and J Siewerdsen. Su-ff-i-16: Oscar: An open-source cone-beam ct reconstruction tool for imaging research. *Medical Physics*, 34(6):2341–2341, 2007.

[302] Debashish Chowdhury, Ludger Santen, and Andreas Schadschneider. Statistical physics of vehicular traffic and some related systems. *Physics Reports*, 329(4):199–329, 2000.

[303] Takashi Nagatani. The physics of traffic jams. *Reports on Progress in Physics*, 65(9): 1331, 2002.

[304] Alexander John, Andreas Schadschneider, Debashish Chowdhury, and Katsuhiro Nishinari. Collective effects in traffic on bi-directional ant trails. *Journal of theoretical biology*, 231(2):279–285, 2004.

[305] Alexander John, Andreas Schadschneider, Debashish Chowdhury, and Katsuhiro Nishinari. Trafficlike collective movement of ants on trails: Absence of a jammed phase. *Physicsal Review Letters*, 102(10):108001, 2009.

[306] Cécile Leduc, Kathrin Padberg-Gehle, Vladimír Varga, Dirk Helbing, Stefan Diez, and Jonathon Howard. Molecular crowding creates traffic jams of kinesin motors on microtubules. *Proceedings of the National Academy of Sciences*, 109(16):6100–6105, 2012.

[307] Debashish Chowdhury, Andreas Schadschneider, and Katsuhiro Nishinari. Physics of transport and traffic phenomena in biology: from molecular motors and cells to organisms. *Physics of Life Reviews*, 2(4):318–352, 2005.

[308] Martin Burd and Nuvan Aranwela. Head-on encounter rates and walking speed of foragers in leaf-cutting ant traffic. *Insectes Sociaux*, 50(1):3–8, 2003.

[309] Dirk Helbing. Traffic and related self-driven many-particle systems. *Reviews of modern physics*, 73(4):1067, 2001.

[310] Antonio Coniglio, Tiziana Abete, Antonio de Candia, Emanuela Del Gado, and A Fierro. A review of the dynamical susceptibility in different complex systems. *The European Physical Journal-Special Topics*, 161(1):45–54, 2008.

[311] Kerstin N Nordstrom, Jerry P Gollub, and Douglas J Durian. Dynamical heterogeneity in soft-particle suspensions under shear. *Physical Review E*, 84(2):021403, 2011.

[312] Sharon C Glotzer, Vladimir N Novikov, and Thomas B Schrøder. Time-dependent, four-point density correlation function description of dynamical heterogeneity and decoupling in supercooled liquids. *The Journal of Chemical Physics*, 112:509, 2000.

[313] H Katsuragi, AR Abate, and DJ Durian. Jamming and growth of dynamical heterogeneities versus depth for granular heap flow. *Soft Matter*, 6(13):3023–3029, 2010.

# VITA

Nick Gravish was born to Jeff and Cathy Gravish May 8th, 1983 in Santa Clara, CA. Nick attended the University of California at Santa Barbara from 2001-2005 and graduated with a B.S. in Physics. In 2005 Nick moved to Portland, Oregon where he worked in a chain bagel shop. In Spring 2006 Nick responded to a job-posting in the Oregonian newspaper and soon after began work as a research technician in Kellar Autumn's lab at Lewis & Clark college. Nick worked in the Autumn lab from Spring of 2006 to Summer of 2008 garnering seven publications (two first author). In 2008 Nick joined Dan Goldman's lab at Georgia Tech to pursue graduate studies in biological-physics. Nick's work in the Goldman lab has garnered several publications in prominent physics journals and his research has been featured in Physics Today and on journal covers. In 2010 Nick won the Georgia Tech Research and Innovation poster competition. In 2011 Nick was an SAIC student paper competition winner with Yang Ding. Also in 2011 Nick was awarded the Amelio award for *Excellence in Research* from the School of Physics. In 2012 Nick was a recipient of the Georgia Tech Impact scholarship for his positive impact to the Georgia Tech community. In 2012 Nick was awarded the James S. McDonnell postdoctoral fellowship for his past and future work in the study of complex systems science.